Experimentele studie van de belasting en vervorming
van quasistarre en vervormbare objecten bij verticale waterintrede

Experimental Study of the Slamming Induced Pressures,
Forces and Deformations of Quasi-Rigid and Deformable Bodies
during Vertical Water Entry

Diederik Van Nuffel

Promotoren: prof. dr. ir. W. Van Paepegem, dr. ir. I. De Baere
Proefschrift ingediend tot het behalen van de graad van
Doctor in de Ingenieurswetenschappen: Werktuigkunde-Elektrotechniek

Vakgroep Toegepaste Materiaalwetenschappen
Voorzitter: prof. dr. ir. J. Degrieck
Faculteit Ingenieurswetenschappen en Architectuur
Academiejaar 2013 - 2014

UNIVERSITEIT
GENT

ISBN 978-90-8578-683-2
NUR 969, 974
Wettelijk depot: D/2014/10.500/29

The author gives the authorization to consult and to copy parts of this work for personal use only. Any other use is limited by the Laws of Copyright. Permission to reproduce any material contained in this work should be obtained from the author.

De auteur geeft de toelating dit doctoraatswerk voor consultatie beschikbaar te stellen en delen ervan te kopiëren uitsluitend voor persoonlijk gebruik. Elk ander gebruik valt onder de beperking van het auteursrecht, in het bijzonder met betrekking tot de verplichting uitdrukkelijk de bron te vermelden bij het aanhalen van de resultaten van dit werk.

Copyright © D. Van Nuffel and Ghent University
Ghent, February 2014

Promotors:

Prof. dr. ir. Wim Van Paepegem
Ghent University
Faculty of Engineering and Architecture
Department of Materials Science and Engineering

Dr. ir. Ives De Baere
Ghent University
Faculty of Engineering and Architecture
Department of Materials Science and Engineering

Examination Committee:

Prof. L. Taerwe (Chair)	Ghent University, Belgium
Prof. W. Van Paepegem (Promotor)	Ghent University, Belgium
Dr. I. De Baere (Promotor)	Ghent University, Belgium
Prof. J. De Rouck	Ghent University, Belgium
Prof. P. Troch	Ghent University, Belgium
Prof. S. Vanlanduit	Free University of Brussels, Belgium
Dr. S. Schimmels	Forschungszentrum Küste, Germany
Prof. J.P. Kofoed	Aalborg University, Denmark

Research Institute:

Ghent University
Faculty of Engineering and Architecture
Department of Materials Science and Engineering
Mechanics of Materials and Structures
Technologiepark 903
B-9052 Zwijnaarde
Belgium
Tel.: +32 (0)9 331 04 44
Fax.: +32 (0)9 264 58 33
Diederik.VanNuffel@gmail.com

"When dealing with water, first experiment, then use judgment"

Leonardo Da Vinci (1452 - 1519)

"Genius is one percent inspiration, ninety-nine percent perspiration"

Thomas Alva Edison (1847 - 1931)

Acknowledgements

Een doctoraat is als een avontuur, waarvan je niet goed weet hoe het begint en hoe het zal aflopen. Met die drang naar avontuur stortte ik mij vier en een half jaar geleden in een verhaal waarvan de uiteindelijke uitkomst in dit boek is neergeschreven.

Net als een avontuur is een doctoraat op vele momenten erg boeiend, afwisselend en vooral leerrijk zowel op professioneel als op persoonlijk vlak. Ik heb mijn doctoraat dan ook ervaren als een fantastische tijd. Maar terzelvertijd ligt een avontuur vol onverwachte hindernissen die je moet overwinnen om je doel te behalen. En soms kunnen die hindernissen ervoor zorgen dat je een vermoeiende en lange omweg moet maken. Bij momenten vergt een doctoraat dan ook veel doorzettingsvermogen om je einddoel te bereiken.

Uiteraard heb ik dat doorzettingsvermogen niet alleen aan mezelf te danken. Mijn doctoraat was immers niet mogelijk zonder de vele mensen die me gedurende de voorbije jaren gesteund hebben in mijn werk. Met plezier wil ik in dit voorwoord dan ook uitgebreid de kans grijpen om deze mensen stuk voor stuk te bedanken.

Eerst en vooral wil ik mijn promotoren, prof. Wim Van Paepegem en dr. Ives De Baere van harte bedanken voor hun jarenlange gemotiveerde begeleiding. Dag in dag uit kon ik op hun steun, kennis en raadgevingen rekenen als ik met vragen of bedenkingen zat. Telkens weer stond hun deur open. Wim wil ik vooral bedanken voor zijn gedreven inzet, ondanks het feit dat hij zovele doctoraten begeleidt en instaat voor nog vele andere zaken in onze vakgroep. Hoe hij het combineert is voor mij nog steeds een raadsel. Ives wil ik voornamelijk bedanken voor het ter beschikking stellen van zijn encyclopedische mechanische kennis. Op zowat iedere vraag wist hij zowaar uit het vuistje mij onmiddellijk een antwoord te bieden. Verder kon ik bij hem ook altijd terecht voor een leuke babbel over koken, duiken, klimmen, etc.

Ook onze vakgroepvoorzitter prof. Joris Degrieck wil ik graag bedanken voor zijn tips, voor het ter beschikking stellen van de faciliteiten van de vakgroep, en voor de kans die hij me heeft gegeven om een doctoraat aan deze aangename vakgroep te kunnen aanvatten.

Naast deze adequate begeleiding verdient ook de technische en administratieve ondersteuning van onze vakgroep, en van onze onderzoeksgroep in het bijzonder een dikke pluim. In dat kader wil ik vooral Luc, Pascal en Martine heel erg bedanken. In de beginjaren was er enkel Luc die de technische ondersteuning op zich nam. Telkens weer wist hij voor ieder probleem de juiste oplossing uit zijn hoed te toveren. Alles waar je naar vroeg had hij wel ergens liggen in ons labo in het diepe

hart van het Technicum. Later kwam er Pascal bij, na onze verhuis naar het Technologiepark dan, waar hij samen met Luc een sterk team vormde om de goede technische ondersteuning van het groeiend aantal doctoraatsstudenten te kunnen blijven verzekeren. Ook Pascal was technisch zeer sterk en wist in een oogwenk testopstellingen volledig bij te 'tunen' om aan de noden van de onderzoekers te voldoen. En dan was er Martine, die als een moeder voor haar kroost ervoor zorgde dat wij iedere dag opnieuw, klokslag om tien uur de vermoeidheid van al dat harde labeur konden wegslaan met een lekkere koffie. De legendarische koffiepauzes, waarin de lachspieren heel vaak werden getraind, waren een moment van ontspanning en verademing die ervoor zorgden dat we er voor de rest van de dag met een frisse geest opnieuw konden invliegen. Ondertussen is Martine in pensioen en ik wens haar daarbij het allerbeste toe.

Een goede sfeer kan je enkel verwezenlijken als iedereen daartoe zijn steentje bijdraagt. Voor die reden wil ik graag alle collega's die in deze vier en een half jaar de revue zijn gepasseerd heel hartelijk bedanken. Ook al is een doctoraat een vrij individueel werk, toch vond ik dat we telkens weer een sterk team vormden. Ik wil hen graag bedanken voor de goede samenwerking, de vele plezante momenten, de leuke babbels en de interessante gesprekken. In het bijzonder wil ik daarvoor mijn bureaugenoten, Stefan en Joachim heel hartelijk bedanken. Ook Matthias en Nicolas wil ik daarvoor graag bedanken, ook voor de leuke momenten buiten het werk. Verder verwelkom ik Matthias graag als 'nieuwe' collega bij BelV.

Furthermore, I would like to gratefully thank Sridhar, my colleague at UGent who performed the numerical part of the slamming project and whose PhD script is now in progress. I want to thank him for the nice cooperation and fruitful discussions on the project. I wish him all the best back in India together with his wife and daughter and good luck in his further career and life.

I am also very thankful to Alex, the third member of the slamming project and PhD student at the Free University of Brussels (VUB). I thank him for the good cooperation during the many days that we spent together in the dust and darkness of the laboratory Magnel. Eventually, our efforts were rewarded with very nice results of which we may be proud. I also wish Alex the very best in Belgium, back in Romania, or somewhere else, and good luck with his future career and life.

In het kader van samenwerkingen wil ik ook graag de volgende vakgroepen en personen bedanken:

- De onderzoeksgroep Weg-en Waterbouwkunde van de Vakgroep Civiele Techniek van de Universiteit Gent voor het ter beschikking stellen van hun testopstelling. In het bijzonder wil ik prof. Peter Troch en prof. Julien De Rouck

bedanken voor hun revisiewerk als lid van de examencommissie. Ook wil ik heel graag Tom, Herman, Sam en David bedanken voor hun regelmatige hulp en advies. Ik kon er telkens op eender welk moment terecht als ik met vragen zat op hulp nodig had met de testopstelling. Verder wens ik ook prof. Peter Troch, prof. Julien De Rouck en dr. Leen De Vos graag te bedanken voor de kans die ze me hebben gegeven om indrukwekkende slammingtesten te kunnen bijwonen in de grootste golfgoot van Europa in Hannover. En tenslotte wil ik ook graag dr. Griet De Backer bedanken voor haar revisiewerk destijds tijdens mijn masterthesis en voor de nuttige input die zij toen heeft gegeven voor de start van het slammingproject.

- De onderzoeksgroep Akoestiek en Trillingen van deVakgroep Werktuigkunde van de Vrije Universiteit Brussel en in het bijzonder prof. Steve Vanlanduit voor het ter beschikking stellen van hun PIV-opstelling en de apparatuur nodig om modale analyses uit te voeren. Ik wens prof. Steve Vanlanduit ook te bedanken voor zijn revisiewerk als lid van de examencommissie, en voor zijn inzet gedurende de vier en een half jaar voor het opvolgen van het FWO-project.

- De onderzoeksgroep Stromingsmechanica van de Vakgroep Warmte, Stroming en Verbranding van de Universiteit Gent, met in het bijzonder prof. Jan Vierendeels en dr. Joris Degrootte, voor hun inbreng en advies en in het bijzonder voor hun werk met betrekking tot het numerieke luik van het FWO-project.

I also would like to thank the other jury members for their excellent review and for the tips they gave me:

- Dr. Stefan Schimmels, manager of the ForschungsZentrum Küste in Hannover, Germany

- Prof. Jens Peter Kofoed, associate professor at the Department of Civil Engineering of Aalborg University, Denmark

- Prof. Luc Taerwe, Prodecaan van de Faculteit Ingenieurswetenschappen en Architectuur, en Directeur van het Laboratorium Magnel voor Betononderzoek om als voorzitter deel uit te maken van de examencommissie

Ik wil ook graag dr. Chris Blommaert, destijds mijn begeleidster voor mijn master thesis, alsook mijn eigen thesisstudenten van de voorbije vier en een half jaar, nl. Maarten, Mathias, Jonathan, Koen en Anthony bedanken voor de goede samenwerking en hun inzet.

Naast de hulp en steun van alle bovengenoemde personen uit ‘professionele’ kring, mag het belang van de steun van familie, vrienden en kennissen niet onderschat worden.

Ik richt mij daarbij in de eerste plaats tot mijn lieftallige echtgenote, Ellen, zonder wie dit doctoraat vrijwel onmogelijk zou zijn. Ik dank haar voor haar onvoorwaardelijke steun doorheen het hele parcours en voor haar geduld gedurende de momenten dat het werk te veel van mijn tijd ontnam. Ik dank haar ook voor haar medeleven op momenten dat ik het moeilijk had en voor haar stimulans om door te zetten. Vooral het laatste half jaar was erg zwaar en waren de momenten samen eerder schaars. Maar zij bleef echter in mij geloven en ik kon op haar steun blijven rekenen.

Ook zonder mijn ouders, Herman en Nadine, zou dit werk niet mogelijk geweest zijn. Ook hen dank ik voor hun continue steun en voor de kans die ze me hebben gegeven om dit doctoraat aan te vatten. Ik bedank hen ook voor hun geduld tijdens de moeilijke momenten, vooral tijdens mijn studies dan, en tijdens de momenten dat ik nog last minute opdrachten moest voltooien en daardoor bij hen de nodige stress teweegbracht.

Ook mijn schoonouders, Etienne en Hilde, wil ik graag bedanken voor hun steun en voor de ontspannende momenten.

Verder zijn er nog mijn broers met hun respectievelijke echtgenotes en kinderen: Filip en Sofie, en Frederik, Isolde, Sien en Tijs. Ook zij hebben met hun steun hun steentje bijgedragen tot het welslagen van dit werk.

Tot slot zijn er nog de vele vrienden en kennissen, wiens namen ik hier niet zal opsommen om niemand te vergeten. Ik dank hen voor de plezante momenten die we samen konden beleven en op die manier geregeld voor een welkome ontspanning zorgden.

Bedankt aan iedereen!

English summary

This dissertation is situated in a project funded by the FWO (Funds for Scientific Research) which was initiated based on the findings from an earlier PhD work. In that work it was observed experimentally that during the impact of a marine structure on a water surface (i.e. a slamming event) the deformability of the structure had an effect on the slamming loads.

The two main objectives of this research are the following:

- Experimentally investigating the precise effect of the structural deformability on the slamming loads.

- Setting up a rigorous and straightforward procedure for accurately and reliably measuring slamming pressures and forces.

To the author's best knowledge, both objectives are not yet discussed in detail in the available literature before. To achieve these objectives, research was necessary in different fields. Chapter 4, 5 and 6 contain the most relevant information on the stated objectives. Chapters 1, 2, 3 and 7 contain more background information. Chapter 8 finally presents the conclusion of this dissertation and offers an outline for future research. Keeping this in mind, a short overview of the different chapters and the main results is provided below.

Chapter 1 provides a global introduction on this dissertation. More information on the background of this thesis and on the motivations is given. Furthermore, this chapter also presents an overview of the main achievements and innovative aspects characterizing this dissertation.

A comprehensive literature review which is necessary to gain expertise in the field of slamming is presented in chapter 2. This review contains a more general part which deals with a description of the slamming phenomenon and its consequences on ships and other naval constructions. A slamming event is mostly characterized by very large and spiky pressures and forces which are considerably localized in time and space. The duration is typically in the order of milliseconds or even smaller. Since 1929, many theoretical approximations trying to describe these slamming pressures and forces are developed. A detailed description and overview of the most relevant slamming theories is given the second part of chapter 2. Furthermore, the second chapter also provides a simplified theoretical approach on the determination of the effect of structural flexibility on the slamming loads, based on a mass-spring and a mass-spring-damper system, which is useful for the further chapters.

In the third chapter, the used experimental drop weight slamming setup together with is instrumentation is described in detail. Dynamic pressure and force sensors, a

position encoder, an accelerometer and a high speed camera (to perform the digital correlation technique - DIC) are the main instruments. Furthermore, a PIV-setup (particle imaging velocimetry) and a smoke machine have been used in some experiments to visualize the movement of the water and the air flow. All the instruments are triggered at the same time and sampled on the same time basis in order to synchronize the recordings. This chapter also presents the quasi-rigid and deformable cylindrical and flat plate test models which were selected in order to assess the effect of the structural flexibility on the slamming loads.

In order to enable correct measurements and reliable interpretations of the instrumentation described in chapter 3, a comprehensive validation procedure is elaborated in chapter 4. For the dynamic pressure and force transducers, a first validation was performed by identifying all the external parameters affecting these types of recordings. In this way, measurement guidelines could be developed which should be followed in order to enable correct and reliable pressure and force recordings. Next, the dynamic pressure and force transducers were also calibrated with respect to a reference pressure and force. For the pressure transducers, a dynamic calibration technique was therefore developed based on an existing static calibration instrument in series with a valve. For the force sensors, a new and promising calibration method was elaborated based on the split Hopkinson pressure bar setup. Furthermore, also a calibration of the force sensor assembly used during the slamming experiments, consisting of three dynamic force sensors clamped between two circular Aluminium plates, was performed by means of a hydraulic compression machine.

For the accelerometer, the position encoder and the DIC technique, a validation is presented based on the comparison of the position, velocity and acceleration signals obtained or calculated from each of their recordings. The good correspondence among the different sensor types indicated their proper and correct working.

Based on the validation of the instrumentation in chapter 4, slamming experiments could be performed. Chapter 5 and 6 present the results obtained from these experiments. In chapter 5, the results corresponding to the slamming experiments with the cylindrical test objects are discussed. It was observed that rigid cylinder slamming typically starts with very large impact pressures at the bottom which propagate along the cylindrical surface at high speeds. In the very initial stage of the impact, a small air pocket has been observed locally at the bottom of the cylinder which rapidly disappears. A comparison of the measured and theoretically predicted impact pressures learned that the measured pressures are in fact an average of the true pressure distribution, meaning that the true slamming pressures are in fact much

larger than the ones which are recorded. These true pressures can be estimated from Wagner's extending flat plate theory for deadrise angles between 4˚ and 20˚.

Furthermore, it was observed during the slamming experiments with the cylindrical test objects that the sudden water impact caused an excitation of some of the natural frequencies of the setup resulting in oscillations in the force recordings. These oscillations caused a large uncertainty in the recorded slamming forces for rigid cylinder slamming since the frequency of the oscillations was in the same range as the frequency of the true slamming forces. The same has been observed in several other experimental studies available in the literature. This resulted in the important indication that also in real marine constructions vibrations may occur due to slamming events causing forces in the structure which are larger than the ones expected from the pure slamming loads only.

In the second part of chapter 5, the experimental results obtained from the slamming experiments with the deformable cylindrical test objects are discussed. For these test models, no pressures were recorded since the installation of the pressure sensors in the thin-walled cylindrical tubes was difficult and would affect the cylinder's deformation. For the force recordings, oscillations could again be observed due to vibrations in the setup. Though, by combining the strain recordings (which were not affected by the vibrations) together with the force recordings, the exact impact forces for these test objects could be determined.

Similar series of slamming experiments were performed with the flat plate test models and are described in chapter 6. Due to a better load distribution, vibrations in the setup no longer interfered with the measurements. It was observed that the vertical water entry of a flat plate is typically accompanied by the inclusion of a large air pocket under the complete area of the plate in the initial slamming stage. This phenomenon is known under the term air cushioning. Once this air pocket is entrapped by the plate and the air flow under the plate is suddenly stopped, a pressure wave is generated which propagates from the edges of the plate to the centre causing the air pocket to break up into many smaller air bubbles. It is during this stage that a large force builds up.

The test series with the deformable test plates as well as the one with the deformable cylindrical test objects lead to the same observations regarding the effect of the deformability on the slamming loads. These observations and their corresponding conclusions are summarized below:

- It was observed that in general, introducing flexibility into a marine structure which is prone to water slamming in most cases causes a reduction of the impact forces which are passed on to the construction supporting the structure

which is in direct contact with the water. This indicates that a part of the impact energy is absorbed by the deformation causing a softening of the impact.

- The relation between the impact forces and the structural stiffness seems to be proportional to the logarithm of the structural stiffness, in the sense that in the range of small stiffness values (large flexibility), the impact forces increase fast with increasing stiffness, while for larger stiffness values (small flexibility), the impact forces increase much slower with increasing structural stiffness.
- For the stress distribution in the material, no straightforward relation with respect to the structural flexibility is present. This indicates that, in contrast with the impact forces, introducing deformability into a structure may also cause an increase in the internal stresses in the considered structure.
- Besides the flexibility of a structure, also other material parameters may have an effect on the magnitude of the slamming loads (e.g. material damping). However, these effects are smaller than the ones from the structural flexibility.

With respect to these conclusions, it was wondered whether besides the effect of the structural properties of the impacting body on the slamming loads, also the properties of the water had an effect. Experiments, in some extent different than the ones performed in the other chapters were therefore performed and are presented in Appendix A. The effect of the water density/salinity, the water surface tension and the level of water aeration on the slamming loads was investigated. A smaller experimental setup with a smaller water tank was used in order to facilitate a variation of the water properties.

Experiments with normal tap water at 20˚C gave similar experimental results as recorded in other chapters with the original experimental setup. This correspondence was considered as a validation of both experimental setups and as a validation of the working method applied throughout the complete dissertation.

For the experiments with changed water properties, it was observed that a variation in water density/salinity and a variation in water surface tension have no effect on the slamming pressures and forces, except in the case of brine close to the saturation concentration. In that last case, slightly larger impact loads were recorded. For the case of the slamming experiments with the water being aerated, significantly smaller impact loads were observed. However, in this respect it was noticed that it is not only the air concentration in the water which affects the slamming loads, but rather small waves which were introduced by the air bubbles reaching the water surface which caused a more gradual and softer impact.

Finally chapter 8 presents an overview of the conclusions drawn from this thesis and suggests an outline for future research.

Nederlandstalige samenvatting

Deze doctoraatsthesis is gesitueerd in een project gefinancierd door het FWO (Fonds voor Wetenschappelijk Onderzoek) dat werd opgestart op basis van de bevindingen uit een voorgaand doctoraatswerk. In dat werk was experimenteel waargenomen dat tijdens de impact van een maritieme structuur op een wateroppervlak (een slamming incident) de vervormbaarheid van die structuur een effect heeft op de belastingen veroorzaakt door dit slamming incident.

De twee belangrijkste doelstellingen van dit onderzoek zijn de volgende:

- Experimenteel onderzoek naar het preciese effect van de structurele vervormbaarheid op de belastingen veroorzaakt door slamming.

- Het opstellen van een strikte en rechtlijnige procedure om slammingdrukken en -krachten nauwkeurig en betrouwbaar te kunnen opmeten.

Voor zover de auteur weet zijn beide topics tot op heden nog niet in detail behandeld in de beschikbare literatuur. Om deze doelstellingen te bereiken was onderzoek nodig op verschillende vlakken. De hoofdstukken 4, 5 en 6 bevatten de meest relevante informatie met betrekking tot deze doelstellingen. De hoofdstukken 1, 2, 3 en 7 bevatten meer achtergrondinformatie. In hoofdstuk 8 worden tenslotte de conclusies van dit werk voorgesteld en enkele suggesties voor toekomstig onderzoek gegeven. Met dit in het achterhoofd wordt hieronder een kort overzicht gegeven van de verschillende hoofdstukken en hun belangrijkste resultaten.

Hoofdstuk 1 geeft een globale inleiding met betrekking tot dit doctoraatswerk. Meer informatie wordt hierbij verstrekt over de achtergrond van deze thesis en de motivaties voor het onderzoek. Verder geeft dit hoofdstuk een overzicht van de belangrijkste verwezenlijkingen en innovatieve aspecten die dit doctoraat karakterizeren.

Een uitgebreid literatuuronderzoek, nodig om expertise te verwerven op het domein van slamming, is voorgesteld in hoofdstuk 2. Deze review bevat een algemeen deel waarin het slamming fenomeen op zich en de gevolgen ervan op schepen en andere maritieme constructies worden beschreven. Een slamming incident wordt meestal gekarakteriseerd door zeer grote en scherpe drukken en krachten die enkel zeer plaatselijk optreden. Ze duren meestal slechts enkele milliseconden of zelfs korter. Vele theoretische benaderingen zijn ontwikkeld sinds 1929 die deze drukken en krachten theoretisch trachten te beschrijven. Een gedetailleerd overzicht en een preciese beschrijving van de meest relevante theorieën is voorzien in het tweede deel van hoofdstuk 2. Verder geeft het tweede hoofdstuk ook een vereenvoudigde theoretische benadering in verband met het effect van de structurele

vervormbaarheid op de slammingkrachten gebaseerd op een massa-veer en een massa-veer-demper systeem.

In het derde hoofdstuk wordt de gebruikte experimentele valopstelling en de aangewende instrumentatie in detail besproken. Dynamische druk- en krachtopnemers, een positie-encoder, een accelerometer en een hogesnelheids-camera (om de digitale correlatie techniek (DIC) toe te passen) zijn de belangrijkste instrumenten die tijdens de testen gebruikt worden. Verder wordt er ook een PIV-opstelling (particle imaging velocimetry) en een rookmachine gebruikt in een aantal experimenten om de water- en luchtstroming te visualiseren. Al deze instrumenten worden aangestuurd op hetzelfde moment en gesampeld met dezelfde tijdsbasis om the metingen te kunnen synchroniseren. Dit hoofdstuk geeft ook een overzicht van de quasistarre en vervormbare cylindrische en vlakke plaatvormige testobjecten die waren geselecteerd om het effect van de structurele vervormbaarheid op de slammingbelastingen in te schatten.

Om met de instrumentatie beschreven in hoofdstuk 3 correcte en betrouwbare metingen mogelijk te maken werd een uitgebreide validatieprocedure uitgewerkt in hoofdstuk 4. Voor de dynamische druk- en krachtsensoren werd een eerste validatie uitgevoerd door alle extrene parameters te identificeren die deze soort metingen beïnvloeden. Op basis daarvan konden richtlijnen uitgewerkt worden die moeten gevolgd worden om correcte en betrouwbare metingen uit te voeren. Daarnaast werden de dynamische druk- en krachtsensoren ook gecalibreerd ten opzichte van referentiedrukken en –krachten. Voor de drukopnemers werd daartoe een calibratietechniek uitgewerkt gebaseerd op een bestaand calibratietoestel voor statische druksensoren in combinatie met een klep. Voor de krachtsensoren werd een nieuwe en veelbelovende calibratiemethode ontwikkeld die gebaseerd is op de Hopkinson-techniek. Verder werd ook een calibratie uitgevoerd van de krachtsensorcombinatie die werd gebruikt tijdens de slammingexperimenten, bestaande uit drie individuele krachtsensoren geassembleerd tussen twee cirkelvormige aluminiumplaten. Daartoe werd een hydraulische trekbank gebruikt.

Voor de accelerometer, de positie-encoder en de DIC techniek werd een validatie uitgevoerd door de postie-, snelheids- en acceleratiesignalen, bepaald en berekend uit de verschillende metingen, met elkaar te vergelijken. De goede overeenkomst die uit deze vergelijking voortvloeide bevestigde de goede en correcte werking van de verschillende betrokken sensoren.

Na het valideren van de instrumentatie konden betekenisvolle slamming-experimenten uitgevoerd worden. De hoofdstukken 5 en 6 geven de resultaten van deze experimenten weer. In hoofdstuk 5 worden de metingen horende bij de

slammingexperimenten met de testcilinders behandeld. De metingen gaven weer dat het slammingproces van een star cilindrisch object typisch begint met de opbouw van grote impactdrukken aan de onderkant van de cilinder, die zich vervolgens snel langsheen het manteloppervlak voortplanten. Verder werd ook in de vroege beginfase van de impact een smalle en langwerpige luchtbel waargenomen aan de onderkant van de cilinder die zeer snel verdwijnt. Een vergelijking tussen de gemeten en theoretisch voorspelde impactdrukken wees aan dat de gemeten drukken in feite een gemiddelde zijn van de ware drukverdeling over de cilinder. Dit toonde aan dat de ware slammingdrukken dus in feite veel hoger zijn dan diegene die gemeten werden. De ware drukken kunnen ingeschat worden met behulp van de uitgebreide vlakke-plaat-theorie van Wagner voor tilhoeken tussen 4˚ en 20˚.

Verder bleek uit de metingen dat tijdens de slammingexperimenten met de cilindrische testobjecten enkele natuurlijke trillingsfrequenties van de opstelling werden aangeslaan door de plotse waterimpact van de testobjecten. Als gevolg hiervan werden oscillaties in de krachtenmetingen waargenomen die een grote onzekerheid op de gemeten slammingkrachten creëerden, aangezien de geobserveerde oscillatiefrequentie ten gevolge van de trillingen van dezelfde orde was als de frequentie van de werkelijke slammingkrachten. Verschillende andere experimentele studies uit de beschikbare literatuur maken ook melding van een dergelijk fenomeen. Dit toont aan dat ook in echte maritieme structuren trillingen kunnen ontstaan ten gevolge van slamming incidenten die krachten induceren groter dan de krachten die verwacht worden ten gevolge van de waterimpact op zich.

In het tweede deel van hoofdstuk 5 worden de experimentele resultaten van de slammingexperimenten met de vervormbare testcilinders besproken. Tijdens deze experimenten werden geen drukken gemeten aangezien de druksensoren moeilijk in de dunwandige cilinders konden gemonteerd worden en een dergelijke installatie bovendien de vervorming van de betrokken cilinders zou beïnvloeden. Opnieuw vertoonden de krachtmetingen van deze experimenten oscillaties ten gevolge van trillingen in de opstelling. In dit geval konden de impactkrachten toch exact bepaald worden door de krachtmetingen te combineren met de rekmetingen (die niet door de trillingen werden beïnvloed).

Gelijkaardige testreeksen werden ook voor de vlakke testplaten uitgevoerd en zijn beschreven in hoofdstuk 6. Een betere distributie van de impactkrachten vermeed in dit geval de beïnvloeding van de metingen door trillingen van de opstelling. De metingen toonden aan dat de waterintrede van een vlakke plaat in de beginfase typisch gepaard gaat met de insluiting van een grote luchtbel verspreid over de volledige oppervlakte van die plaat. Dit fenomeen staat beter bekend als het ‘air cushioning’-fenomeen. Het kon verder waargenomen worden dat eens de luchtbel

werd ingesloten, de plotse stopzetting van de luchtstroom onder de plaat een drukgolf genereerde die zich voortplantte van de randen naar het centrum van de plaat en hierbij de grote luchtbel opbrak in vele kleinere luchtbelletjes. Het is tijdens deze fase dat een grote kracht zich opbouwt.

De testreeksen van de vervormbare testplaten en testcilinders leidden tot dezelfde observaties met betrekking tot het effect van de structurele vervormbaarheid op de slammingbelasting. Samenvattend kon het volgende waargenomen worden:

- De metingen toonden dat in het algemeen het introduceren van vervormbaarheid in een maritieme structuur die blootstaat aan slamming een reductie teweegbrengt van de impactkrachten die doorgegeven worden naar de constructie die de betrokken structuur ondersteunt. Dit geeft aan dat een deel van de impactenergie geabsorbeerd wordt door de vervorming van de structuur wat leidt tot een verzachting van de impact.

- De relatie tussen de impactkrachten en de structurele stijfheid is evenredig met het logaritme van de structurele stijfheid, in de zin dat voor kleine waarde van de structurele stijfheid (grote graad van flexibiliteit) de impactkrachten snel stijgen met toenemende stijfheid, terwijl voor grote waarden van de structurele stijfheid (lage graad van flexibiliteit) de impactkrachten veel trager stijgen met toenemende structurele stijfheid.

- Geen eenduidige relatie kon worden afgeleid tussen de spanningsverdeling in het materiaal en de stijfheid van de structuur. In tegenstelling tot de impactkrachten geef dit aan dat het introduceren van vervormbaarheid in een maritieme structuur in sommige gevallen ook een verhoging van de interne spanningen kan betekenen.

- Naast de graad van vervormbaarheid van een maritieme structuur hebben ook andere materiaalparameters een effect op de slammingkrachten (bv. materiaaldemping). De effecten van deze parameters zijn echter kleiner dan die van de structurele vervormbaarheid.

In het licht van voorgaande experimentele observaties werd ook de vraag gesteld of, naast het effect van de structurele eigenschappen van het impacterende object, ook de eigenschappen van het water een effect hadden of de slammingbelasting. Om dit te achterhalen werden experimenten uitgevoerd die in zekere mate verschillen van de experimenten die in de andere hoofdstukken zijn besproken. Appendix A beschrijft deze experimenten. De invloed van de densiteit/zoutconcentratie, de oppervlaktespanning en het gehalte aan luchtbellen in het water op de slammingdrukken en –krachten werd onderzocht. Om een variatie van de

watereigenschappen te vergemakkelijken werd in dit kader een kleinere valopstelling gebruikt met een kleinere watertank.

Bij experimenten met normaal kraantjeswater op 20˚C werden gelijkaardige experimentele resultaten bekomen als in de andere hoofdstukken met de originele opstelling. Deze overeenkomst werd beschouwd als een validatie van beide opstellingen en als een validatie van de werkmethode toegepast tijdens het volledige doctoraat.

De experimenten met gewijzigde watereigenschappen toonden aan dat een verandering in de densiteit/zoutconcentratie en een variatie in de oppervlaktespanning geen invloed hadden op de slammingdrukken en -krachten, met uitzondering van het geval waarbij de zoutconcentratie de maximale zoutconcentratie van pekel benadert. In dat geval werden lichte verhoogde slammingdrukken en –krachten opgemeten. Bij de experimenten waarbij luchtbellen onderaan in het water werden toegevoegd werden veel lagere impactdrukken en –krachten opgemeten. Het kon in dit opzicht echter wel waargenomen worden dat de slammingbelasting in dit geval niet zozeer door een verandering van de luchtconcentratie werd beinvloed, maar wel door kleine verstoringen van het wateroppervlak door luchtbellen die het wateroppervlak bereikten. Deze kleine verstoringen van het wateroppervlak zorgden voor een meer graduele waterintrede en dus een verzachting van de waterimpact.

In hoofdstuk 8 worden tenslotte de conclusies van dit werk voorgesteld en worden er suggesties voor verder onderzoek gegeven.

Table of contents

Chapter 1
Introduction 1

1. 1. Background 1
1. 2. Objectives 5
1. 3. Methodology and outline 6
1. 4. Main achievements and innovative aspects 9
1. 5. References 10

Chapter 2
Literature survey and slamming theories 13

2. 1. Description of the slamming phenomenon 13
2. 2. Theoretical problem description 19
2. 3. Literature review 22
2. 4. Slamming load theory 28
2. 4. 1. General considerations 28
2. 4. 2. Impact pressure 29
2. 4. 2. 1. Flat plate slamming 29
2. 4. 2. 1. a. von Karman 29
2. 4. 2. 1. b. Verhagen 30
2. 4. 2. 2. Cylinder slamming 34
2. 4. 2. 2. a. von Karman 34
2. 4. 2. 2. b. Wagner 38
2. 4. 2. 2. c. Wienke 39
2. 4. 3. Impact forces 40
2. 4. 3. 1. Flat plate slamming 40
2. 4. 3. 2. Cylinder slamming 40
2. 4. 3. 2. a. von Karman 40
2. 4. 3. 2. b. Wagner 42
2. 4. 3. 2. c. Wienke 43
2. 4. 3. 2. d. Greenhow and Yanbao 44
2. 4. 3. 2. e. Wellicome 44

2. 4. 3. 2. f. Kaplan and Silbert 44
2. 4. 3. 2. g. Campbell and Weynberg 45
2. 4. 3. 2. h. Miao 46
2. 5. Conclusions 46
2. 6. References 46

Chapter 3
Experimental setup and instrumentation 51

3. 1. Experimental setup 51
3. 2. Instrumentation 53
3. 2. 1. Pressure sensors 53
3. 2. 2. Force sensors 55
3. 2. 3. Accelerometer 58
3. 2. 4. Position encoder 59
3. 2. 5. Strain gauges 61
3. 2. 6. High speed camera 63
3. 2. 7. Particle Image Velocimetry 64
3. 2. 8. Smoke machine 65
3. 3. Data Acquisition 65
3. 4. Test objects 68
3. 4. 1. Cylindrical test objects 68
3. 4. 1. 1. Rigid cylindrical test models 69
3. 4. 1. 1. a. The stiffened cylinder 69
3. 4. 1. 1. b. Concrete and plaster cylinder 70
3. 4. 1. 2. Deformable cylindrical test models 71
3. 4. 2. Flat plates 73
3. 4. 2. 1. Rigid flat plates 73
3. 4. 2. 1. a. Bottom impactor plate 73
3. 4. 2. 1. b. Sandwich panel 74
3. 4. 2. 2. Deformable plates 76
3. 5. Conclusions 78
3. 6. References 78

Chapter 4

Validation and calibration of the experimental instrumentation 81

4. 1. Background 81
4. 2. Dynamic pressure measurements 83
4. 2. 1. Parameters affecting the impact pressure measurements 83
4. 2. 1. 1. The data sampling frequency 83
4. 2. 1. 2. Thermal shock 87
4. 2. 1. 3. Sensor mounting 90
4. 2. 1. 4. Object surface conditions 91
4. 2. 1. 5. Water surface conditions 93
4. 2. 2. Guidelines for measuring dynamic impact pressures 94
4. 2. 3. Calibration methods for dynamic pressure transducers 95
4. 2. 3. 1. Industrial calibration methods for dynamic pressure transducers 96
4. 2. 3. 1. a. The Pistonphone 96
4. 2. 3. 1. b. Hydraulic impulse calibrator 96
4. 2. 3. 1. c. The Aronson step pressure generator 98
4. 2. 3. 1. d. The calibration shock tube 98
4. 2. 3. 2. Calibration method developed in the present dissertation 99
4. 3. Dynamic force measurements 102
4. 3. 1. Parameters affecting the impact force measurements 102
4. 3. 1. 1. The data sampling frequency 102
4. 3. 1. 2. Sensor mounting 103
4. 3. 1. 3. Transient effect at impactor release 105
4. 3. 1. 4. The impactor mass distribution 106
4. 3. 2. Guidelines for measuring dynamic impact forces 107
4. 3. 3. Calibration methods for dynamic force transducers 108
4. 3. 3. 1. Industrial calibration methods for dynamic force transducers ... 108
4. 3. 3. 1. a. Calibrating dynamic force transducers against an oscillation force 109

4. 3. 3. 1. b. Calibrating dynamic force transducers against an impact force 109
4. 3. 3. 1. c. Calibrating dynamic force transducers against a step force 110
4. 3. 3. 2. Calibration methods developed in the present dissertation 110
4. 3. 3. 2. a. Calibration of the individual force transducers 110
4. 3. 3. 2. b. Calibration of the complete load cell combination 115
4. 4. Position, velocity and acceleration measurements 117
4. 4. 1. Methods for calculating the impact velocity 117
4. 4. 2. Validation of the velocity recordings 122
4. 4. 3. Impact velocity values 126
4. 5. Conclusions 127
4. 6. References 128

Chapter 5
Cylinder slamming 131

5. 1. Effect of the cylindrical mass on the slamming pressures and forces 131
5. 2. Rigid cylindrical test objects 135
5. 2. 1. Impact pressures 135
5. 2. 1. 1. Pressure time history 136
5. 2. 1. 2. Impact pressure values 140
5. 2. 2. Impact forces 155
5. 2. 2. 1. Force time history 155
5. 2. 2. 2. Force impact values 165
5. 3. Deformable cylindrical test objects 171
5. 3. 1. Impact forces 171
5. 3. 1. 1. Deformable cylindrical test objects with large diameter ($D \geq 31.5$ cm) 172
5. 3. 1. 1. a. Force time histories 172
5. 3. 1. 1. b. Impact force values 185
5. 3. 1. 2. Deformable cylindrical test objects with small diameter ($D \leq 9$ cm) 188

5. 3. 1. 2. a. Force time histories 188
5. 3. 1. 2. b. Impact force values 193
5. 3. 1. 3. Comparison of the slamming force results for all cylindrical test objects 197
5. 3. 2. Maximum hoop strains and stresses 202
5. 3. 2. 1. Deformable cylindrical test objects with large diameter ($D \geq 31.5$ cm) 203
5. 3. 2. 2. Deformable cylindrical test objects with small diameter ($D \leq 9$ cm) 207
5. 4. Conclusions 210
5. 5. References 212

Chapter 6
Flat plate slamming 215

6. 1. Effect of the flat plate mass on the slamming pressures and forces 215
6. 2. Rigid flat plate test objects 217
6. 2. 1. Sandwich panel 217
6. 2. 2. Bottom impactor plate 224
6. 2. 2. 1. Force time history 224
6. 2. 2. 2. Impact force values 226
6. 3. Deformable flat plate test objects 228
6. 3. 1. Impact forces 229
6. 3. 1. 1. Force time history 229
6. 3. 1. 2. Force impact values 231
6. 3. 2. Impact strains and stresses 237
6. 3. 2. 1. Strain and stress time histories 237
6. 3. 2. 2. Strain and stress impact values 239
6. 4. Hopkinson based flat plate slamming experiments 242
6. 4. 1. Description of the method and materials 243
6. 4. 2. Experimental results 245
6. 5. Conclusions 250
6. 6. References 251

Chapter 7
Conclusions and future research 253

7. 1. Conclusions 253

7. 2. Future work 261

7. 3. References 262

Appendix A
Experimental study on the effect of water properties on the slamming loads 263

A. 1. Background 263

A. 2. Materials and methods 266

A. 2. 1. Experimental test setup and test object 266

A. 2. 2. Test procedure 268

A. 2. 2. 1. Effect of the water density/salinity on the slamming loads 268

A. 2. 2. 2. Effect of the water surface tension on the slamming loads 269

A. 2. 2. 3. Effect of water aeration on the slamming loads 269

A. 3. Experimental results 270

A. 3. 1. Slamming experiments in tap water 270

A. 3. 1. 1. Impact pressures 270

A. 3. 1. 2. Impact forces 274

A. 3. 2. Slamming experiments in water with changed properties 277

A. 3. 2. 1. Effect of the water density/salinity on the impact loads 278

A. 3. 2. 2. Effect of the water surface tension on the impact loads 279

A. 3. 2. 3. Effect of water aeration on the slamming loads 279

A. 4. Conclusions 280

A. 5. References 281

About the author 283

Curriculum vitae 283

List of publications 284

List of symbols

h	Relative vertical distance between a body and the water surface [m]
$\dot{h}$	Relative vertical velocity between a body and the water surface [m/s]
g	Gravitational constant (= 9.81 m/s^2)
λ	Ship length [m]
P	Probability [-]
R_h	Area under the amplitude spectrum of the relative displacement of the foreship with respect to the water surface [m]
$R_{\dot{h}}$	Area under the amplitude spectrum of the relative velocity of the foreship with respect to the water surface [m/s]
T	Ship draught [m]
v	Ship velocity [m/s]
M	Mass [kg]
k	Spring constant [N/m]
t	Time [s]
X	Spring indentation [m]
U	Impact velocity [m/s]
F_z	Gravity force [N]
F_v	Spring force [N]
F_d	Damping force [N]
c	Damping factor [N.s/m]
ω	Natural frequency of the system [rad/s]
ς	Dimensionless damping factor [-]

$[x,y,z]$	Cartesian coordination system with z perpendicular on the water surface, and (x,y) in the plane of the water surface
R	Flat plate radius / cylinder radius [m]
V	Drop speed as function of time [m/s]
θ	Deadrise angle according to von Karman [°]
θ_b	Deadrise angle according to Wagner [°]
b	Half wetted width [m]
L	Length of test object [m]
D	Flat plate diameter / Cylinder diameter [m]
C_s	Slamming coefficient [-]
F_M	Inertia force [N]
F_D	Drag force [N]
F_B	Buoyancy force [N]
F_I	Slamming force [N]
M_w	Added mass of water [kg]
ρ_w	Water density [kg/m³]
A	Area [m²]
γ_w	Velocity of sound in water [m/s]
$p_{I,}$	Impact pressure [Pa]
$\vec{W} = [w1, w2, w3]$	Velocity vector of the fluid [m/s]
φ	Velocity potential [m²/s]
p	Pressure [Pa]
p_a	Atmospheric air pressure [Pa]
ρ_a	Air density [kg/m³]

l	Half width of a test object [m]
h	Relative vertical distance between a body and the water surface [m]
h_0	Relative vertical distance between a body and the water surface at an arbitrary time t_0 [m]
u	Horizontal air velocity [m/s]
γ_a	Velocity of sound in air [m/s]
h_1	Relative vertical distance between a flat plate and the water surface at the moment of the first contact of the plate with the water [m]
p_1	Pressure in the air pocket during flat plate impact at the moment of the first contact of the plate with the water [Pa]
$\mathcal{M}$	Mass per unit length [kg/m]
χ	Ratio between the specific heat at constant pressure and that at constant volume [-]
$W_{s,1}$	Average downward velocity of the water surface under an impacting plate at the moment of first contact [m/s]
C_p	Pressure coefficient [-]
$\mathcal{F}_I$	Impact force per unit length [N]
C_s	Slamming coefficient [-]
$\mathcal{M}_w$	Added mass per unit length [kg/m]
K	Flexural stiffness [Pa.m^3]
E	Elasticity modulus [Pa]
d	Plate thickness / cylinder thickness [m]
ν	Coefficient of Poisson [-]
δ	Plate deflection / cylinder deflection [m]

V_A	Output voltage [V]
Z	Resistance [Ω]
V_B	Supply voltage [V]
S	Gauge factor for strain gauges [-]
ε	Strain [-]
E_{33}	Elasticity modulus in the thickness direction [Pa]
F_{sens}	Sum of the forces measured by the individual force transducers [N]
ε_i	Incident strain [-]
ε_r	Reflected strain [-]
ε_t	Transmitted strain [-]
σ_m	Average stress history [Pa]
A_s	Cross sectional area of a Hopkinson bar [m^2]
A_p	Cross sectional area of a test specimen [m^2]
E_s	Elasticity modulus of a Hopkinson bar [Pa]
n	Number of data points [-]
i	index number [-]
a	acceleration [m/s^2]
H	Drop height [m]
$\Delta\theta$	The angle corresponding with the sensor area [˚]
d_{sens}	Diameter of the pressure sensor diapraghm [m]
K_c	Cylinder stiffness [N/m]
A,B and C	Empirical variables [-]

List of abbreviations

WEC	Wave energy convertor
LNG	Liquefied natural gas
FPSO	Floating production storage and offloading unit
RoRo	Roll-on-Roll-off
BP	British Petroleum
DNV	Det Norske Veritas
P	Plate
VK	Von Karman
VH	Verhagen
W	Wagner
Wi	Wienke
C	Cylinder
GY	Greenhow and Yanbao
We	Wellicome
KS	Kaplan and Silbert
CW	Campbell and Weynberg
M	Miao
ICP	Integrated circuit piezoelectric
MOSFET	Metal-oxide-semiconductor field-effect transistor
PZT	Lead ziconate titanate
DTC	Discharge time constant
PVC	Polyvinylchloride
GFRP	Glass fiber reinforced plastics

PE	Polyethylene
PP	Polypropylene
GR&R	Gauge repeatability and reproducibility
SPL	Sound pressure level
SHPB	Split Hopkinson pressure bar
CAD	Computer aided drawing
FEM	Finite element method
PIV	Particle image velocimetry

Chapter 1

Introduction

Overview

This chapter gives a global overview of the underlying PhD dissertation. The background and the objectives of this thesis are presented. Furthermore, the research methodology is introduced and an outline of the chapters is provided. Finally, a description on the innovative aspects related to this dissertation is given.

1. 1. Background

The current research is based on the observations done during an earlier PhD work which was performed at the 'Mechanics of Materials and Structures'-group at Ghent University. In this work, which was performed by Blommaert [1], a survivability design has been developed for composite floating 'point absorbers' for the FO^3 wave energy convertor (WEC) [2].

The FO^3 WEC was one of the many designs in the ultimate quest for finding a cost- and power-efficient wave energy convertor which can compete with conventional renewable energy techniques (e.g. wind energy, hydropower) or even with traditional energy sources (e.g. oil and gas plants, nuclear plants) [3]. In this type of convertor, energy is generated from the waves by the vertical motion of cone-cylinder-cone shaped 'point absorbers' or buoys relative to an offshore floating platform. A matrix of about 20 buoys is intended to be placed on one platform to

combine their generated power into one power station. A sketch of the working principle and a rendering of a FO^3 wave farm are depicted in Figure 1-1.

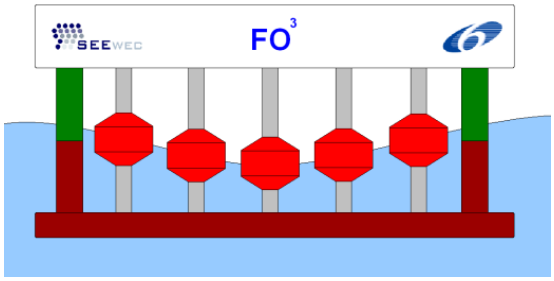

(a)

(b)

Figure 1-1: (a) Sketch of the FO^3-WEC; (b) Rendering of a FO^3 wave farm [4]

A critical aspect in the design of these wave energy convertors is the survivability in extreme weather conditions. In fact, this has been identified as one of the main design criteria for all types of wave energy convertors [5]. After all, in order to remain cost-efficient, these energy devices should stay at their location in open sea even during heavy storms. Towing the platforms into safe harbours is not an option since it would raise the exploitation costs tremendously.

However, this means that during storms the platform and its components should withstand large waves and wave speeds. To prevent the point absorbers from being swayed back and forth rapidly and being slammed against the platform structure, the device is then switched in safe modus by preventing the buoys moving with respect to the platform. In these circumstances, the WEC is thus not generating power.

But even in this condition, damage may occur when waves with high speed collide upon the side walls of the buoys. Especially when a wave starts to break at the moment that it hits a point absorber, the loads can be very large. This event not only

occurs with respect to these point absorbers, but it is a widely known phenomenon in the field of marine hydrodynamics and offshore and coastal engineering which is called lateral or breaking wave slamming. In the field of coastal engineering, specific structures (e.g breakwaters, storm walls) are designed to absorb the energy corresponding to breaking waves in order to protect the underlying coastal structures from damage [6].

Furthermore, it is also possible that in situations with large wave heights and wave lengths the point absorbers exit the water and enter again. In this situation it is more at the bottom that large loads will occur due to the impact of the object with the water surface. In technical terms, this event is called bottom slamming. Also this type of water slamming is commonly known in the field of marine and offshore engineering. Figure 1-2 shows a sketch of the two main types of slamming on the buoys. Both slamming types cause very large local and global loads which are characterized by a short duration in the order of milliseconds or even shorter. In order to design the point absorbers of the FO^3 to let them survive even the heaviest storms, it was necessary to estimate these loads and the damage they may produce.

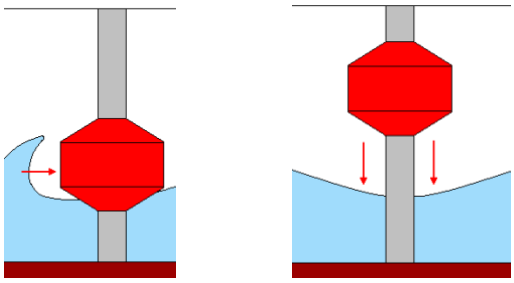

(a) (b)

Figure 1-2: (a) Breaking wave slamming; (b) Bottom slamming

In a finite element analysis on the buoys, Blommaert [1] used a uniform static pressure over a certain sector of the area to estimate the slamming forces. This load was chosen according to the standard of Det Norske Veritas [7], a classification society which is an authority in the field of marine and offshore regulation. However, it is clear that this approximation lies too far from reality since slamming may not be considered as a static event, but a highly dynamic one.

In order to have a more precise estimation of the loads acting on the point absorbers during lateral and bottom slamming, Blommaert [1] and De Backer [8] performed slamming experiments on scale models of the point absorbers which were made of composite material. Two models with scaling 1:2.29 with respect to the original dimensions were produced for this purpose (diameter 1.75 m). The difference

between the two models comprised a difference in the composition of the buoy wall. For the first buoy, the wall was built up of four layers with the following stacking sequence (from inside to outside): filament wound layer (glass fibre - polyester) / foam / filament wound layer (glass fibre - polyester) / isotropic glass fibre layer (glass fibre-polyester). The second buoy had only two layers: filament wound layer (glass fibre-polyester) / isotropic glass fibre layer (glass fibre-polyester). The structural stiffness of this latter buoy was thus much smaller than the first one. Figure 1-3 shows the wall composition for both point absorber models.

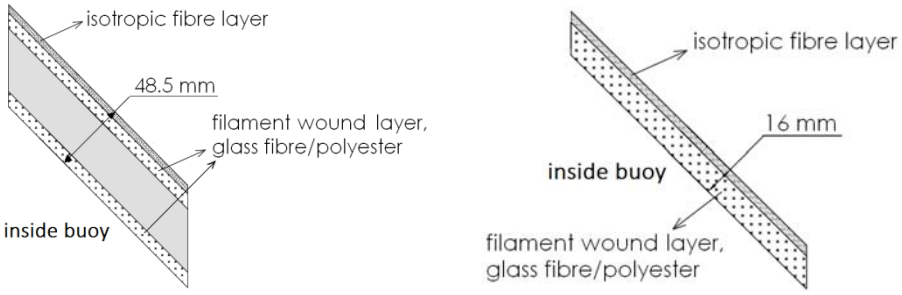

(a) (b)

Figure 1-3: Wall composition for (a) the buoy with foam and (b) the buoy without foam

Slamming experiments on the buoys were performed by dropping them on a nearly flat water surface for different drop heights corresponding to different impact velocities. Lateral slamming was investigated by dropping the buoys on their side onto the water while bottom slamming was tested by dropping them with the bottom onto the water. A picture at the moment of impact for both types of tests is depicted in Figure 1-4.

(a) (b)

Figure 1-4: Large scale drop tests on (a) lateral slamming and (b) bottom slamming

During the lateral slamming tests, impact pressures were measured with pressure transducers located at the bottommost point of the falling buoys. For the buoy without foam an average impact pressure over ten tests of 22.3 bar was observed. For the buoy with foam, the impact pressures were beyond the range limit of the sensors of 34.5 bar. This observation indicated that structural flexibility must play an important role with respect to the loads which occur during water slamming. The fact that for the most flexible buoy smaller impact loads are measured may be explained by the fact that a larger part of the impact energy is absorbed by deformation. The larger deformation thus causes a sort of softening of the slamming impact. This type of impact softening may occur for all types of naval constructions where deformability comes into picture.

Nowadays, fibre reinforced composites are used very frequently in the shipbuilding and offshore industry (e.g. sailing yachts, catamarans, high speed boats). Due to their high specific strength and stiffness, less material is required in the construction and this often results in thin-walled deformable structures. At one hand, this deformability is advantageous since it thus causes a softening of the impact during water slamming. But at the other hand, attention should be paid to the possible occurrence of fatigue damage when repeated slamming is present.

1. 2. Objectives

According to the author's best knowledge, the precise effect of the deformability on the slamming loads has never been investigated in detail before. It is the main objective in this work to provide fundamental experimental results on slamming of simple object geometries in order to precisely examine the effect of the deformability on the impact loads during water slamming and to understand the physics behind the obtained relation.

In order to draw reliable conclusions from the experimental results, it deemed necessary to verify the correctness of the experimental recordings. Reliable results are only possible if the transducers are reliable and the interpretation of the recordings is correct. Hence, the second aim of this thesis is to develop a rigorous test procedure for recording slamming loads which guarantees accurate and reliable experimental results. This procedure contains elements regarding the experimental setup, installation requirements of the sensors and interpretation guidelines of the measured signals. According to the author's knowledge, no such experimental framework for performing slamming load recordings has ever been published before. However, this is a very important issue.

1. 3. Methodology and outline

The methodology which is followed in this PhD is chosen according to the objectives stated in the previous paragraph.

The study starts with a literature survey on marine hydrodynamics and water slamming in particular in chapter 2, to gain expertise in the field. First, some general considerations on water slamming are introduced. This is followed by a more thorough description of the slamming theory. Since the characteristics of the slamming phenomenon and the corresponding theories depend on the geometry of the impacting object, it was necessary at this stage to make a choice for the objects which were planned to be tested.

The main concern in this selection is the issue that the objects should be easily available in both rigid and deformable condition. Moreover, it is necessary to have different degrees in flexibility for the same shape. Two types of objects were found to satisfy the previous requirements, i.e. flat plate models and cylindrical models.

The flat plate models were realized as circular plates to avoid edge effects and to obtain axisymmetric conditions. However, as will be also shown in a later stage of this dissertation, a specific phenomenon was present during slamming of these flat plates. It was observed that at impact, air was entrapped under the plate since not all the air could escape from the gap between the plate and the water surface in the moments just before the slamming impact. It is assumed that this air pocket causes a damping of the water impact. A sketch of this air pocket damping or air cushioning effect is shown in Figure 1-5. It was expected that this air cushioning would have a large effect on the measured impact pressures and forces, and thus also on the relation between the impact loads and the plate's flexibility.

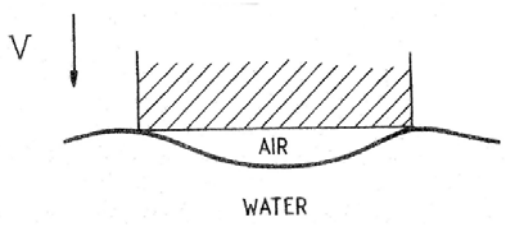

Figure 1-5: Air cushioning or air pocket damping [9]

To investigate the relation between a structure's flexibility and the slamming loads without the air cushioning effect playing a role, it was decided to start the research with the cylindrical test objects. It was assumed that for these test models the air between the objects and the free water surface could escape a lot easier during a

slamming event, and the slamming pressures and forces would thus not be influenced by an air cushion. Moreover, the advantage of using a cylinder is that it has a deadrise angle which varies along the circumference of the object. As such, pressure measurements are possible at different deadrise angles. The deadrise angle is defined as the angle between the object's surface and the water surface at the location where the object penetrates the water. An explaining illustration is given in Figure 1-6.

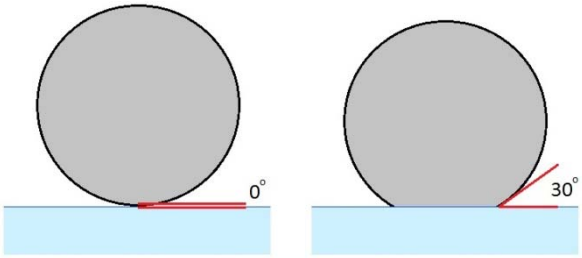

Figure 1-6: The penetration of a cylindrical model corresponding to a deadrise angle of 0° and 30°

A description of the different tested models is provided in chapter 3. This chapter also gives an overview of the experimental setup and the various types of instrumentation which is used. It is important to mention that the slamming setup is a drop weight setup and that thus all the slamming data which was obtained during this thesis was generated by a vertical drop of the objects on a calm free water surface.

This type of testing is a good physical approximation for bottom slamming, but not really for breaking wave slamming. For this latter slamming type, the experimental approach can be considered as the case wherein an infinite steep wave collides with a fixed structure. However, in the tests it is not the wave which is moved towards the object but the object which is moved towards the wave surface. The difference between the real situation and the experimental approach for breaking wave slamming is illustrated in Figure 1-7. In reality, waves with infinite steepness (i.e. the ratio of the wave height H_s to the wave length L_w) do not exist [10, 11]. Hence, the impact load results measured during this thesis can be considered as upper limits for the breaking wave case.

Figure 1-7: The real slamming situation compared to the experimental approach for breaking wave slamming

Before performing the planned slamming experiments, it was first necessary to verify if the results generated by the various instruments were accurate and reliable. For this purpose, a validation of the used instrumentation was done in chapter 4. Moreover, chapter 4 provides guidelines which should be followed in order to enable correct pressure and force recordings. Great care should be carried out in how and where to place the sensors for measuring impact pressure and impact force, and how to handle them and interpret their results. By controlling the parameters affecting the pressure and force recordings, correct results could be guaranteed. Chapter 4 is thus an important step in the current experimental study. Most of the aspects discussed in this chapter have never been reported before in the available literature.

By using the guidelines defined in chapter 4, precise and reproducible measurements could be performed. Chapters 5 and 6 comprehensively report the experimental results from the slamming experiments on the rigid and deformable cylindrical and flat plate models. The obtained test results are compared in detail with the existing literature. Relations with respect to the effect of the deformability of the cylindrical and flat plate test objects on the slamming loads are identified and precisely investigated.

Although the examination of the structural properties of an object on the slamming loads was one of the main objectives of this thesis, it was also interesting to investigate the effect of the water properties on the slamming loads. Therefore, experiments using another test setup as described in chapter 3 were performed. They are described in Appendix A. The effect of the water density/salinity, the water surface tension and the water aeration level on the slamming pressures and forces was investigated. By comparing the results from both setups, an extra validation of some of the measurements described in the earlier chapters could be performed.

The conclusions of this work are presented in chapter 7. Moreover, this chapter provides an outline for some future research.

1. 4. Main achievements and innovative aspects

The list below presents the main achievements and innovative aspects which characterize the underlying work:

- A rigorous review of the slamming theories concerning rigid cylinder and rigid flat plate slamming has been elaborated. All the available theories concerning this matter have been gathered and presented in a clear and concise way. According to the author's best knowledge, this has never been published before.

- A widely instrumented experimental setup has been used, with state-of-the-art equipment in order to record the slamming pressures and forces as accurately as possible. The properties of the sensors are chosen well-considered in order to meet the requirements, and are documented properly in this dissertation.

- Well documented measurement guidelines on how to perform accurate and reliable slamming pressure and force recordings were realized. Therefore, all the parameters introducing parasitic effects on the impact pressures and forces were identified. In this way, controlled experiments could be performed and a correct interpretation of the recordings could be guaranteed. No such guidelines were presented yet in the available literature. This part of the research has been published in *Experimental Mechanics* [12].

- A fast, mobile and effective calibration technique for calibrating dynamic pressure transducers has been developed. Up to now, calibration of dynamic pressure transducers could only be performed in specialized laboratories using large and expensive installations.

- A new calibration technique for calibrating dynamic force transducers was elaborated, which makes use of a reference instrument which is easy to calibrate (strain gauges). The current commercial calibration techniques are all based on reference instruments which are on their turn difficult to calibrate or which need complex calibration techniques. The developed technique was presented at the *15th International Conference on Experimental Mechanics* [13]

- A comprehensive and detailed validation of all the experimental instrumentation has been performed. This is an important step in the

working process of an experimental research. However, its importance is too often neglected in the available literature.

- Extensive experimental research was performed on rigid cylinder and rigid flat plate slamming. The obtained experimental results were carefully compared with the available existing analytical and experimental work from the literature. Agreements and differences with the literature are discussed and explained. The experimental study on the impact pressures generated during vertical water entry of a rigid cylinder is published in *Ocean Engineering [14]*. The study on the impact forces generated during vertical water entry of a rigid cylinder is submitted to *Marine Structures* [15].

1. 5. References

[1] C. Blommaert, "Composite floating 'point absorbers' for wave energy convertors: survivability design, production method, and large-scale testing," *PhD dissertation, Ghent University, Department of Materials Science and Engineering,* 2010.

[2] J. De Rouck and V. Meirschaert, "SEEWEC: Publishable final activity report," 2009.

[3] J. Brooke, "Wave energy conversion," 2003.

[4] Seewec. (2013). *Official website Seewec project*. Available: http://www.seewec.org at 15/02/2014

[5] Parmeggiani S. and Kofoed J.P., "Survivability mode and extreme loads on the mooring lines of the Wave Dragon energy convertor," *DCE Technical Reports, No. 108, Aalborg University, Department of Civil Engineering,* p. 51, 2011.

[6] K. Van Doorslaer, J. De Rouck, K. Trouw, J. W. van der Meer, and S. Schimmels, "Wave forces on storm walls, small and large scale experiments," *8th International Conference on Coastal and Port Engineering in Developing Countries, IIT Madras, Chennai, India,* 2012.

[7] Det Norske Veritas, "Environmental conditions and environmental loads," *Classification notes no. 30.5,* 2010.

[8] G. De Backer, M. Vantorre, P. Frigaard, C. Beels, and J. De Rouck, "Bottom slamming on heaving point absorber wave energy devices," *Journal of Marine Science and Technology,* vol. 15, pp. 119-130, 2010.

[9] O. M. Faltinsen, "Sea loads on ships and offshore structures," 1990.

[10] R. Miche, "Mouvement ondulatoires de la mer en profondeur constante ou decroissante," *Annales des Ponts et Chaussees,* 1944.

[11] J. N. Newman, "Marine hydrodynamics," 1977.

[12] D. Van Nuffel, K. S. Vepa, I. De Baere, J. Degrieck, J. De Rouck, and W. Van Paepegem, "Study on the Parameters Influencing the Accuracy and Reproducibility of Dynamic Pressure Measurements at the Surface of a

Rigid Body During Water Impact," *Experimental Mechanics*, pp. 1-14, 2012/05/01 2012.

[13] D. Van Nuffel, J. Peirs, I. De Baere, P. Verleysen, J. Degrieck, and W. Van Paepegem, "Calibration of dynamic piezoelectric force transducers using the Hopkinson bar technique," *Proceedings of the 15th International Conference on Experimental Mechanics*, pp. 1-12, 2012.

[14] D. Van Nuffel, K. S. Vepa, I. De Baere, P. Lava, M. Kersemans, J. Degrieck, *et al.*, "A comparison between the experimental and theoretical impact pressures acting on a horizontal quasi-rigid cylinder during vertical water entry," *Ocean Engineering*, 2013.

[15] D. Van Nuffel, K. S. Vepa, I. De Baere, P. Lava, J. Degrieck, and W. Van Paepegem, "An experimental and theoretical study on the impact loads acting on a horizontal quasi-rigid cylinder during vertical water entry," *submitted to Marine structures*, 2013.

Chapter 2

Literature survey and slamming theories

Overview

The current chapter starts with a description of the slamming phenomenon and with some general considerations concerning this topic. This is followed by a theoretical approach of the basic goal of this thesis: a comparison of the impact loads related with rigid and deformable impacting bodies. Next, a comprehensive review of the work done on wave slamming in general, and on flat plate and cylinder slamming in particular is presented. Finally, a detailed description of the existing slamming theories of flat plates and cylinders is provided.

2. 1. Description of the slamming phenomenon

Water slamming is known as one of the most important loads which naval constructions have to deal with. The load caused by the collision of the structure with the water highly depends on how the water hits the body surface and with which velocity this occurs. The slamming event is mostly characterized by very large and spiky pressures and forces which are considerably localized in time and space. The duration of the event is in the order of milliseconds or even smaller.

Different types of water slamming exist and they are divided in two main categories: bottom slamming and breaking wave slamming. Pure bottom, straight or vertical slamming mostly occurs when a floating structure falls with its bottom on the water surface. This type of slamming mostly occurs with small vessels at high speed (e.g.

high speed boat, sailing yachts) when they are swept out of the water and come down again on the waves. Some examples are depicted in Figure 2-1.

Figure 2-1: Pure bottom slamming of small vessels

Also larger vessels (e.g. tankers, bulk carriers) can experience pure bottom slamming but this is more likely to happen in ballast condition and in extreme sea state. For these types of vessels this is a dangerous situation in which the vessel suffers from excessive slamming loads. Some examples of pure bottom slamming for larger vessels are given in Figure 2-2.

Figure 2-2: Pure bottom slamming of large vessels

A special type of bottom slamming is bow flare slamming which is typical for larger vessels [1, 2]. The bottom of the ship stays under water and slamming occurs at the bow flares by the vertical motion of the ship. Figure 2-3 shows some bow flare slamming events.

Figure 2-3: Bow flare slamming

Finally, a third slamming type which occurs from the bottom is wetdeck slamming [3]. It occurs at the underside of the wetdeck of multihulls and offshore platforms.

In the breaking wave slamming or lateral slamming case, water impact occurs when a wave starts to break just at the moment that it reaches the side wall of a marine construction [4-6]. Some pictures of lateral slamming are depicted in Figure 2-4.

Figure 2-4: Examples of pure breaking wave slamming

Lateral wave impact on the superstructure or equipment on deck of a ship is a special case of this slamming type, known as green water impact [7, 8]. Some observations of green water are represented in Figure 2-5.

Figure 2-5: Examples of green water slamming

Lateral slamming can also occur inside tanks which contain liquids, for example in the tanks of an LNG-carrier. This type of slamming is called sloshing [9, 10]. Figure 2-6 shows an impression of the sloshing phenomenon.

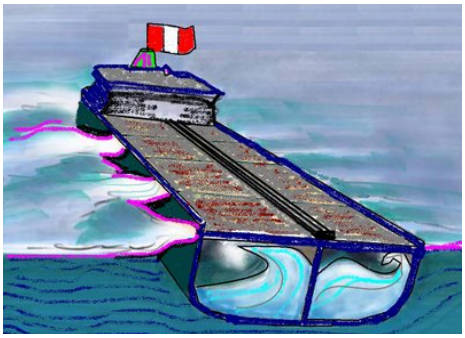

Figure 2-6: Impression of sloshing in a large tanker

Al these types of slamming have negative consequences for the structures upon which they act. First of all, there is the economical aspect that these powerful impacts cause a large increase in sailing resistance and consequently a large increase in fuel consumption and corresponding costs [11].

Furthermore, slamming loads can cause transient hull girder vibrations which might reduce the structure's life time. These vibrations can be often felt and heard by the passengers of the considered floating structures and it is called the whipping phenomenon. For vessels, the 2-node and 3-node vertical vibration modes will be the most important during these whipping events. For catamarans and monohulls with large deck openings, torsion/twisting vibrations should also be taken into consideration [12].

Eventually, in harsh weather conditions, waves can contain so much energy that they can introduce a lot of damage to the structure when they clash with a marine

construction. A reported example of damage due to slamming is the *Schiehallion* floating production, storage and offloading unit (FPSO) where a steep wave caused an indentation of the bow, which finally resulted in an evacuation of all personnel [13] (see Figure 2-7). In the case of the German roll-on-roll-off (RoRo) vessel *Linda Buck* it was green water impact which caused windows breaking at the ship bridge. As a result, the control over the ship was lost and the vessel stranded on a Dutch beach [14] (see Figure 2-8). A last example of damage due to wave slamming is mentioned by Attfield [15], who reports the failure of a horizontal structural member in the splash zone of the BP's West Sole offshore platform in the southern North Sea in 1972. The splash zone of an offshore platform is the region where structural members repeatedly enter and exit the water due to the surface waves.

Figure 2-7: Bow indentation due to slamming at the *Shiehallion* FPSO [13]

Figure 2-8: Consequences of green water impact for the *Linda Buck* [14]

To avoid slamming on ships, the sailing direction can be altered towards calmer seas or shelter can be searched in protective ports. If these measures are not possible and the ship is in the middle of a turbulent sea, it is recommended to reduce the ship's speed [16]. This voluntary speed reduction is operative when there are more than four obstructive slams out of hundred heave oscillations [17]. A slam is considered obstructive when the relative speed at impact between the water surface and the ship increases the threshold velocity. This threshold velocity is expressed by the following equation [16]:

$$\frac{\dot{h}_*}{\sqrt{g\lambda}} = 0.14 \qquad \textbf{(2.1)}$$

With:
- $\dot{h}$ = relative vertical velocity between the keel of the foreship and the water surface [m/s]
- g = gravitational constant (= 9.81 m/s^2)
- λ = ship length [m]

The probability that a slam occurs corresponding with this threshold velocity $\dot{h}_*$ is given by [16]:

$$P[slam] = e^{-\left(\frac{T^2}{R_h} + \frac{\dot{h}_*^2}{R_{\dot{h}}}\right)} \qquad \textbf{(2.2)}$$

With:
- R_h = area under the amplitude spectrum of the relative displacement of the foreship with respect to the water surface [m]
- $R_{\dot{h}}$ = area under the amplitude spectrum of the relative velocity of the foreship with respect to the water surface [m/s]
- T = ship draught [m]

R_h and $R_{\dot{h}}$ can be calculated from the ship velocity *v*. The ship velocity for which *P*[*slam*] = 0.04 determines the speed reduction which should be applied in rough sea state [16].

However, fixed marine constructions have no option to search for shelter or to decrease their speed. The sea waves can be so rough that even in this standstill position these structures suffer from severe slamming. They should thus be designed in order to withstand the slamming loads.

The present dissertation originates from the observation done for the point absorbers of the FO^3 wave energy convertor, that introducing flexibility in the point absorbers apparently reduces the large slamming loads. After all, it is intuitively expected that by introducing deformability into the structure, the slamming loads and thus the material stresses would decrease since a part of the impact energy is then absorbed by the deformation. In this way, instant impact damage may be prevented but fatigue can then start playing a role. The next paragraph further elaborates on the effect of the deformability of the structure on the impact loads by a more theoretical and simplified approach in order to get more insight into the mechanism.

2. 2. Theoretical problem description

Consider a large vessel with mass *M* which slams onto a water surface. If the hull of the vessel would be extremely elastic (e.g. elastic rubber), then the slamming forces are expected to be much smaller as in the conventional case since it is supposed that the elastic hull softens the impact by its deformation. If this is the case for a vessel hitting a water surface, then this behaviour is also expected for the imaginary case of a vessel hitting a rigid surface.

If the vessel is now considered as a rigid mass *M* and the hull as a massless spring with a spring constant *k*, then an extremely simplified problem is obtained which is shown in Figure 2-9.

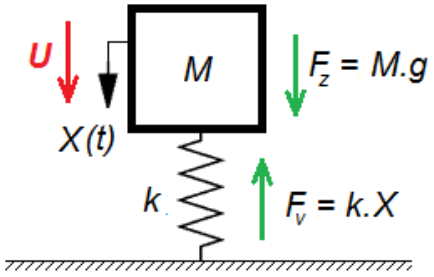

Figure 2-9: A mass-spring system as model for the impact of a ship with a rigid surface

The equation of motion of this system is well known as:

$$M\frac{d^2X(t)}{dt^2} + k\,X(t) - Mg = 0 \qquad \textbf{(2.3)}$$

A solution of this equation is of the form:

$$X(t) = A\sin\left(\sqrt{\frac{k}{M}}t\right) + B\cos\left(\sqrt{\frac{k}{M}}t\right) + \frac{Mg}{k} \qquad \textbf{(2.4)}$$

If the moment of the first contact of the ship's hull with the rigid surface is taken as starting point, then there is no displacement at $t = 0$, and the relative velocity at that moment equals the impact velocity *U*:

$$\begin{cases} X(0) = 0 \\ \dot{X}(0) = U \;\; (= \dot{h}_{\text{impact}}) \end{cases}$$

This gives:

$$A = \sqrt{\frac{M}{k}}U\,; \quad B = -\frac{Mg}{k} \tag{2.5}$$

And thus:

$$X(t) = \sqrt{\frac{M}{k}}U\sin\left(\sqrt{\frac{k}{M}}t\right) - \frac{Mg}{k}\cos\left(\sqrt{\frac{k}{M}}t\right) + \frac{Mg}{k} \tag{2.6}$$

The force which is exerted on the ship mass *M* is then given by:

$$F_v = k \cdot X(t) = \sqrt{kM}U\sin\left(\sqrt{\frac{k}{M}}t\right) - Mg\cos\left(\sqrt{\frac{k}{M}}t\right) + Mg \tag{2.7}$$

From Equation (2.7) it can be observed that the amplitude of the force acting on the ship mass *M* is proportional with the square root of the spring constant. This confirms the premise that flexible structures will encounter smaller impact forces.

The model can now be extended in order to consider also the dampening effect of the ship's hull. The model then becomes a mass-spring-damper system as illustrated in Figure 2-10.

The equation of motion is now:

$$M\frac{d^2X(t)}{dt^2} + c\frac{dX(t)}{dt} + k\,X(t) - Mg = 0 \tag{2.8}$$

Or:

$$\frac{d^2X(t)}{dt^2} + 2\varsigma\omega\frac{dX(t)}{dt} + \omega^2X(t) - g = 0 \tag{2.9}$$

With: - $\omega = \sqrt{\frac{k}{M}}$ = natural frequency of the system [rad/s] **(2.10)**

- $\zeta = \frac{c}{2\sqrt{kM}}$ = dimensionless damping factor [-] **(2.11)**

- c = damping factor [N.s/m]

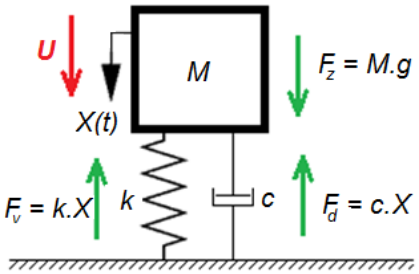

Figure 2-10: A mass-spring-damper system as model for the impact of a ship with a rigid surface

If $\zeta < 1$, then the solution is of the form:

$$X(t) = e^{-\zeta\omega t}\left(A\sin\left(\sqrt{1-\zeta^2}\,\omega t\right) + B\cos\left(\sqrt{1-\zeta^2}\,\omega t\right) + \frac{g}{\omega^2}\right) \quad \textbf{(2.12)}$$

The initial conditions result in:

$$A = \frac{\sqrt{1-\zeta^2}\,(\zeta g - U\omega)}{\sqrt{\zeta^2-1}\,\omega^2}; \qquad B = -\frac{g}{\omega^2} \quad \textbf{(2.13)}$$

And thus:

$$X(t) = e^{-\zeta\omega t}\left(\frac{\sqrt{1-\zeta^2}\,(\zeta g - U\omega)}{\sqrt{\zeta^2-1}\,\omega^2}\sin\left(\sqrt{1-\zeta^2}\,\omega t\right)\ldots \right. \\ \left. \ldots - \frac{g}{\omega^2}\cos\left(\sqrt{1-\zeta^2}\,\omega t\right) + \frac{g}{\omega^2}\right) \quad \textbf{(2.14)}$$

The force on the structure is then:

$$F_v(t) = k\cdot X(t) = ke^{-\zeta\omega t}\left(\frac{\sqrt{1-\zeta^2}\,(\zeta g - U\omega)}{\sqrt{\zeta^2-1}\,\omega^2}\sin\left(\sqrt{1-\zeta^2}\,\omega t\right)\ldots \right. \\ \left. \ldots - \frac{g}{\omega^2}\cos\left(\sqrt{1-\zeta^2}\,\omega t\right) + \frac{g}{\omega^2}\right) \quad \textbf{(2.15)}$$

Or:

$$F_v(t) = k \cdot X(t) = e^{-\zeta\omega t}\left[-\frac{M\left(\frac{cg}{2\sqrt{kM}} - U\sqrt{\frac{k}{M}}\right)}{\sqrt{1-\frac{c^2}{4kM}}}\sin\left(\sqrt{1-\zeta^2}\,\omega t\right)... \right. \\ \left. ... - Mg\cos\left(\sqrt{1-\zeta^2}\,\omega t\right) + Mg \right] \quad \textbf{(2.16)}$$

Equation (2.16) shows that the amplitude of the impact force is thus not only dependent on the spring constant k, but also on the damping factor c of the ship's hull. However, for small values of c this effect is negligible.

The main objective of this dissertation consists of investigating the precise effect of the deformability on the slamming loads and of understanding the obtained relation. In addition, it will also be verified whether material damping plays any role in this relation.

2. 3. Literature review

The precise effect of deformability on the slamming loads has never been studied before. Only a few authors have been found which present studies concerning the slamming of an elastic body but to the author's best knowledge no studies exist which compare the impact loads for a range of flexibility degrees. The present section gives a comprehensive overview of the work which has already been done during the past years on wave slamming in general and on flat plate slamming and cylinder slamming in particular.

Research on the water slamming phenomenon was started in the first half of the 20th century. The pioneer in the field was Th. von Karman [18] who investigated the ditching of wedge-shape seaplane floats in 1929 in order to estimate the stress in the floats and in the members connecting the floats to the fuselage. In his theoretical study, he calculated the pressure and force acting on the wedge during impact by applying the momentum theorem, which states that the original momentum of the body is partly transferred to a certain mass of water, called the added mass. Hereby, he assumed that this added mass of water equals the one associated with a flat plate with variable width which corresponds at each moment with the body width at the intersection of the water surface (wetted width). This type of theory is called the flat plate theory.

By taking the width of the plate equal to the width of the body at the intersection of the body with the water, von Karman [18] did not consider the local water uprise at the surface of the body, causing an increase in the true wetted width and thus an

increase in the added mass of water affected by the impact. Wagner [19] extended the flat plate theory in 1932 to take this effect into account.

The difference between the von Karman [18] and the Wagner [19] approach is illustrated in Figure 2-11. This figure clearly shows that in the theoretical approach of Wagner [19] the wetted width $2b$ and the deadrise angle θ_b, which is defined as the local angle between the object's surface and the water surface, is larger than in the case of von Karman [18].

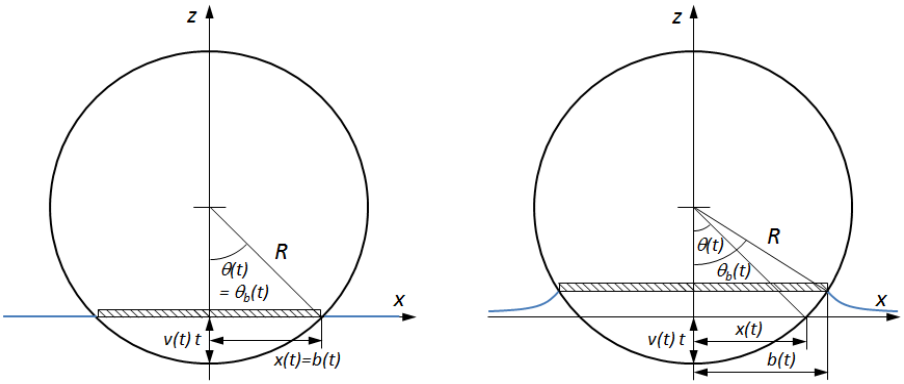

Figure 2-11: Comparison of the von Karman [18] (a) and Wagner [19] (b) approach for a cylinder penetrating the water

Because of the flat plate approach, both theories are only applicable for small deadrise angles ($\theta < 20°$). However, the water is assumed incompressible in both theories. This makes that both theories are also not valid for very small deadrise angles since it has been observed by Egorov [20] that compressibility plays a role during the initial stages of the impact. It has been shown by Malleron et al. [21] that the validity of both theories is hence restricted to deadrise angles $\theta > 4°$.

The water uprise was further investigated in detail by Cointe and Armand [22], who included the effect of nonlinear jet flow in the intersection region between the body and the free surface. Dobrovol'skaya [23] derived an analytical similarity solution for wedges entering with constant velocity which was also applicable for deadrise angles beyond 20°. Unfortunately, this solution was not available in explicit form and hence must be solved numerically. Based on the analytical formulation of Dobrovol'skaya [23], Zhao and Faltinsen [24] developed another numerical method for studying water entry of two-dimensional bodies of symmetric cross-section, which was applicable on deadrise angles between 4° and 81°. The numerical solution technique was different than the one developed by Dobrovol'skaya [23] in

order to handle also smaller deadrise angles more accurately. Zhao and Faltinsen [24] extended their research by including flow separation at larger penetration depths and by investigating general two-dimensional bodies [25] and axysimmetric bodies [26]. Inspired by Zhao's work, Mei et al. [27] developed an analytical solution for the water impact problem of general two-dimensional bodies. The main difference with the Wagner's approach is that the exact boundary conditions are fulfilled, instead of approximating the body by a flat plate.

Several studies have also been performed to describe the impact behaviour for deadrise angles $\theta < 4°$ by taking into account the compressible character of the water in the initial stages of the water impact. Von Karman [18] already built the foundations for these studies. Based on von Karman's findings, this study was extended by Egorov [20], Skalak and Feit [28], Iafrati and Korobkin [29] and Campana et al. [30].

The latter studies also investigated the limiting case of a flat plat impacting the water which can be considered as the case of a wedge with zero deadrise angle. However, it has to be noted that flat plate slamming is totally different from the case of water impact of a wedge with small deadrise angle. That is because the air in the gap between the body and the water just before impact is allowed to escape in the case of wedge slamming, while this is not the case during flat plate slamming. This causes a compressible volume of air to be entrapped under the plate and forced into the water. This phenomenon is called the air cushioning effect since it is expected to soften the impact. The previous studies did not consider this effect.

Verhagen [31] was the first one in 1967 to study horizontal slamming of a rigid flat plate while taking the air cushion formed in the initial stage of the impact into account. He elaborated a rigorous theoretical description to predict the pressure acting upon the plate during the initial stages of water penetration. Korobkin and Pukhnachov [32], Howison et al. [33] and Ermanyuk and Okhusu [34] presented some extra theoretical considerations on the air cushion effect. Experimental work was performed by Oh et al. [35] in order to visualize the air pocket formation during impact. Other experimental work focussing more on the measurement of the impact loads during water entry was performed by Verhagen [31] and Chuang [36].

Only little research was found on the study of slamming of deformable plates. According to the author's knowledge, Faltinsen et al. [37] were the only investigators who studied the horizontal slamming of a deformable plate. They performed a theoretical and experimental investigation on the stresses and strains acting on two different flexible plates during water impact. Research on the impact of inclined deformable plates is reported in Huera-Huarte et al. [38], Smith et al.

[39] and Battley et al. [40]. However, the results of these latter studies are difficult to compare with the measurements obtained during the horizontal drop tests done in the present dissertation, since even small differences in deadrise angle may have a large effect on the slamming loads. Moreover, the water impact of horizontal plates differs from the impact of inclined plates concerning the presence of an air cushion at the moment of impact, which also has an important effect on the impact forces and pressures. Hence, it is quite irrelevant to compare the results from the considered studies with the ones obtained from this research within the scope of this thesis (finding a relation between the impact forces and the degree of deformability).

For the second slamming case considered in the present work, i.e. water impact of a horizontal cylinder, a lot of work has been done in the past. Cylinder slamming has gained much attention during the last decades since it is very important for the design of offshore platforms. That is because many of these platforms are built upon jackets which contain a lot of cylindrical structural elements vulnerable to wave slamming as can be seen in Figure 2-12. The oil and gas industry therefore made large investments in the study of this problem.

Figure 2-12: Examples of jacket based offshore platforms

For cylinder slamming, the air cushion effect should not be considered, since the air is allowed to escape just before contact of the cylinder with the water. This was observed in the photographs of Greenhow and Lin [41], and was also reported by Greenhow and Yanbao [42].

Basic solutions on the cylinder water entry problem can be obtained from the flat plate theory [18, 19], where the varying plate half width $b(t)$ during water penetration now follows the contours of a circle. The formulations of $b(t)$ in the case of the von Karman-theory (without water uprise correction) and in the case of the Wagner theory (with water uprise correction) are presented by Sun and Faltinsen [43]. However, due to the restrictions in deadrise angle applicable for these theories as mentioned before, they are not valid for large penetration depths and neither at the very initial stage of the impact since the water acts as a compressible fluid at that

moment. However, most of the analytical studies which further elaborated these basic solutions still assumed incompressible water.

To improve the estimation of the wetted part of the cylinder during water penetration, Fabula [44] fitted an ellipse to the submerged portion of the cylinder to match its wetted width and draught. This approach was inspired on the ellipsoid fitting technique of Shiffman and Spencer [45] for the impact of three-dimensional spheres.

Further improvements in estimating the added mass of the cylinder during water slamming were presented by Kaplan and Silbert [46] who treated the body shape exactly instead of approximating the cylindrical body by an extending flat plate. Their findings were also reported by Greenhow and Yanbao [42] and Garrison [47]. The results of this exact body approach were still not valid for large penetration depths.

Faltinsen et al. [48] numerically expanded the previous theory to larger penetration depths. Therefore, they used a special numerical technique based on a distribution of sources and dipoles over the averaged wetted body surface. This technique is explained by Newman [49].

Further on, Wienke and Oumeraci [6] determined a theory for breaking wave slamming of vertical monopiles by approaching the slamming as the impact of a vertical wall of water on a fixed vertical cylinder. This approach is in fact the same as the one of a horizontal cylinder being forced with a constant velocity onto a flat water surface as was the case in all studies mentioned before, except for the gravity which is not playing a role for the vertical cylinder. Wienke and Oumeraci [6] elaborated a piecewise function for the slamming load, depending on the penetration depth, which was partly based on Fabula's formulation [44].

Several numerical algorithms were introduced based on the analytical formulations presented above, such as the ones performed by Ionina [50] and Sun and Faltinsen [43].

Many experimental results are also available on rigid cylinder slamming. Sollied [51] and Nøttveit [52] were the first ones to conduct experiments on horizontal cylinders which were forced with constant velocity through an initially calm free surface. Their results were reported by Faltinsen et al. [48]. Greenhow and Lin [41] performed free fall experiments where high speed images were taken in order to understand the physics and dynamics of the impact phenomenon. Lin and Shieh [53] performed similar experiments and extended the results with local pressure measurements along the surface of the cylinder. Also Colicchio et al. [54] reported

local pressure measurements during cylinder impact. Lange and Rung [55] performed pressure and force measurements with a cylindrical model in pure and aerated water, in order to investigate the effect of the gas content of the water on the impact loads. Very important forced impact experiments were carried out by Campbell and Weynberg [56]. An empirical relation for the global slamming forces derived from their experiments is still used as the basis for the description of slamming on slender structures in the DNV standard [57]. Another empirical formula derived from forced cylinder slamming experiments and which deviates from Campbell and Weynberg [56] was developed by Miao [58]. This latter work also provided an overview of important and less important experimental test campaigns measuring the global impact forces throughout the years. The presented list is depicted in Table 2-1. Hereby, Miao made a distinction between cylinder drop tests and cylinder slamming tests in wave flumes. For the present dissertation, the reported drop experiments are the most important. The following notations are used in the presented table:

- L/D = length to diameter ratio of the cylinder = aspect ratio [-]
- $C_{s,max}$ = dimensionless maximum impact force [-]
  = maximum slamming coefficient [-]

Finally, it has to be mentioned that also for cylindrical structures little information is available on the effect of flexibility on the impact loads. Moreover, the available presented results show large scatter in the load recordings. According to the author's best knowledge, Sun and Faltinsen [43] and Ionina and Korobkin [50, 59] are the only ones who numerically studied the impact of deformable cylinders. No experiments on this matter were performed yet.

The previous literature survey shows the relevancy of the present work. Very little research has been found concerning the study of the effect of deformability on slamming loads. For the object geometries tested in this dissertation, only a few studies are available which investigate slamming loads on deformable bodies. However, none of them copes with a rigorous comparison between the impact loads acting on the concerned object geometries for a wide range of deformability degrees.

Table 2-1: Overview of experimental campaigns measuring global impact forces during cylinder slamming [58]

Investigator	Test	L/D [-]	$C_{s,max}$ [-]
Arhan and Deleuil [60]	Drop test	1	2.4-6.9
Campbell and Weynberg [56]	Drop test	6-16	3.5-6.5
Schnitzer and Hathaway [61]	Drop test	3.6	3.5
Sollied [51]	Drop test	1.1-1.5	4.1-6.4
Watanabe [61]	Drop test	0.5	6.2
Souter et al. [62]	Drop test	3.62-4.63	5.2-6.8
Bergren [63]	Regular waves	40-100	1-3.1
Canham [61]	Regular waves	15	-
Dalton and Nash [64]	Regular waves	20	1-4.5
Homes et al. [61]	Regular and irregular	24-108	0.7-2.9
Miller [65]	Irregular wave packet	15	avg. 3.5
Webb [61]	Irregular waves full	30	3-4
Sarpkaya [66]	Rising water surface	-	3.2

2. 4. Slamming load theory

This section describes the most important slamming theories which are elaborated over the years for flat plate slamming and cylinder slamming. The formulas provided here for the impact pressures and impact forces will be compared with the performed experiments later in this work.

2. 4. 1. General considerations

When an object slams on the water surface under free fall, then the following dynamic force equilibrium applies [6, 17, 67]:

$$F_M + F_D + F_B + F_I = 0 \qquad \textbf{(2.17)}$$

With:
- F_M = inertia force [N]
- F_D = drag force [N]
- F_B = buoyancy force [N]
- F_I = slamming force [N]

The drag force is only important at large submergences, when the fluid shears along the complete cylindrical surface. For the initial stages of the impact, the drag force can thus be neglected. In these stages, the submerged volume of the object is very small, and hence also the buoyancy force can be neglected. The force which the test object feels (inertia force) thus reduces to the slamming force for the initial stages of the impact, which is the stage under consideration in the present dissertation. Hence, only the slamming force F_I and the slamming pressure p_I will be described in the present section, which are the result of a certain mass of water which is suddenly accelerated due to the water impact.

2. 4. 2. Impact pressure

2. 4. 2. 1. Flat plate slamming

For objects with deadrise angles smaller than 4° it has been observed that during the initial stage of the water penetration the area of contact between the water and the object expands with a velocity which is larger than the velocity of sound in water. Due to this supersonic perturbation in the water, the compressibility of the water plays a role and should be taken into account [18, 20, 28-30, 32, 33]. Only theories assuming the water to be compressible can thus be used for comparison with the experimental results obtained from the present dissertation.

2. 4. 2. 1. a. <u>von Karman</u>

Besides his impact theory for wedge-shaped floats of seaplanes which was based on incompressible water, von Karman [18] also investigated the impact of a flat body by assuming the water to be compressible. He assumed that due to the supersonic perturbation in the water during the initial stage of the impact, the fluid mass which is accelerated during a time dt is $\rho_w A \gamma_w dt$ with A being the body surface area, ρ_w being the water density (1000 kg/m^3 at 4°C) and γ_w being the velocity of sound in water (1497 m/s at 25 °C). Since the velocity of this mass is increased from zero to U (= constant impact velocity of the flat plate) in the time dt, the force which corresponds to the acceleration of this added mass of water is:

$$F_{I,P,VK} = \frac{d}{dt}\left(M_w V(t)\right) = \rho_w A \gamma_w \frac{d}{dt}\left(V(t)dt\right) = \rho_w A \gamma_w U \qquad \textbf{(2.18)}$$

Following notations are hereby used:

- P = plate
- VK = von Karman
- M_w = added mass of water [kg]

- *V(t)* = speed of the flat plate as function of time [m/s]. Von Karman assumed a constant water entry *U*

Thus, the pressure acting upon the plate during the initial stage of the impact is:

$$p_{I,P,VK} = \rho_w \gamma_w U \qquad \textbf{(2.19)}$$

However, von Karman [18] did not take the air pocket into account which is usually formed during flat plate impact. Verhagen [31] tried to improve von Karman's theory by doing so.

2. 4. 2. 1. b. Verhagen

To solve the problem incorporating the air cushioning effect, Verhagen [31] assumed that the effect of a compressible air pocket was much more important than the effect of the compressibility of the water, and hence he considered the water as being an incompressible fluid. Furthermore, he assumed a two-dimensional flow and the fluid to be ideal, which means that viscous effects are neglected. As a consequence, no shear stresses act within the fluid. Newman [68] showed that this assumption together with the incompressibility of the water results in the motion of the fluid to be irrotational:

$$\vec{\nabla} \times \vec{W} = 0 \qquad \textbf{(2.20)}$$

With $\vec{W}$ = velocity vector of the fluid [m/s].

In Cartesian coordinates, this becomes:

$$\frac{\partial w_1}{\partial y} - \frac{\partial w_2}{\partial x} = 0; \quad \frac{\partial w_2}{\partial z} - \frac{\partial w_3}{\partial y} = 0; \quad \frac{\partial w_3}{\partial x} - \frac{\partial w_1}{\partial z} = 0 \qquad \textbf{(2.21)}$$

The left hand side of Equation (2.20) and Equation (2.21) represents the vorticity, or the curl of the velocity. Saying that the flow is irrotational is equivalent to saying that the vorticity is zero throughout the fluid [68]. Morse and Feshbach [69] showed that an irrotational vector can be represented as the gradient of a scalar φ, and thus:

$$\vec{W} = \vec{\nabla}\varphi \qquad \textbf{(2.22)}$$

The scalar φ is called the velocity potential. Describing the flow by means of a velocity potential and using the corresponding assumptions to enable its use is regularly done in the theoretical description of water slamming. A flow which is

described by a velocity potential is called a potential flow and the corresponding theory is called the potential theory.

Using this velocity potential, the hydrodynamic pressure distribution on the impacting object can then be calculated by Bernouilli's equation:

$$p(x,z,t) = -\rho_w \frac{\partial \varphi}{\partial t}(x,z,t) - \rho_w g z - \frac{\rho_w}{2}\vec{W}\cdot\vec{W} + C \qquad \textbf{(2.23)}$$

The first term on the right hand side gives the pressure contribution due to the rate of change of velocity potential with time. For slamming problems, this will be typically a large contribution and hence, it is considered as the hydrodynamic pressure. The second term on the right hand side represents the hydrostatic pressure due to a submergence *z*. The last term in the pressure gives the dynamic pressure due to the fluid motions.

Figure 2-13 shows a sketch of the stage just before water impact of a flat plate as described by Verhagen [31].

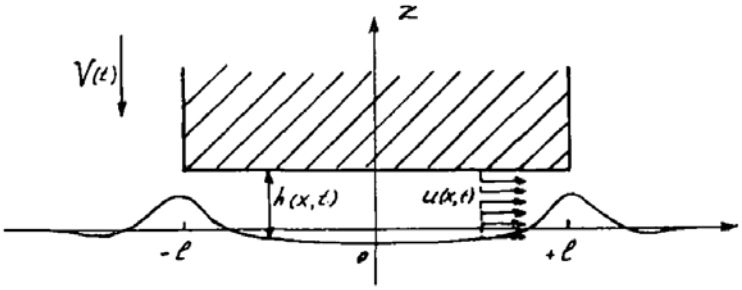

Figure 2-13: The stage just before impact of a plate as described by Verhagen [31]

By choosing the appropriate velocity potential and boundary conditions, Verhagen [31] could calculate the pressure distribution on the plate just before impact as:

$$p(x,t) = p_a + \rho_a \frac{l^2 - x^2}{h^2}\left[\left(\frac{dh}{dt}\right)^2 - \frac{h}{2}\frac{d^2h}{dt^2}\right] \qquad \textbf{(2.24)}$$

With:
- p_a = atmospheric air pressure (1 atm) [Pa]
- ρ_a = air density (1.18 kg/m³ at 25°C) [kg/m³]
- $h(t)$ = distance between the flat plate and the water surface [m]:

$$h(t) = h_0 - \int_0^t V(t)dt \qquad \textbf{(2.25)}$$

With h_0 = the air gap thickness at an arbitrary time t_0.

Figure 2-13 also illustrates the small surface waves which are generated by the rapid air flow in the gap between the object and the water just before impact. These were experimentally investigated by Oh et al. [35]. Verhagen assumed that the moment t_1 at which the plate touches these surface waves and the air layer under the plate is locked coincides with the moment that the escape velocity of the air $u(x,t)$ at the plate edges $x = \pm l$ attains the acoustic sound velocity of the air γ_a (343.2 m/s in dry air at 20 °C). The velocity of the air $u(x,t)$ under the plate is given by:

$$u(x,t) = -\frac{x}{h}\frac{dh}{dt} \qquad \textbf{(2.26)}$$

The assumption at t_1 is thus translated into the following equation:

$$u(\pm l, t_1) = -\frac{l}{h_1}\frac{dh}{dt}(t_1) = \gamma_a \qquad \textbf{(2.27)}$$

With h_1 = the air gap thickness at a time t_1.

From Equations (2.25) and (2.27), the air thickness layer h_1 and the time t_1 at first contact of the plate with the water can be calculated. The situation at that moment is depicted in Figure 2-14.

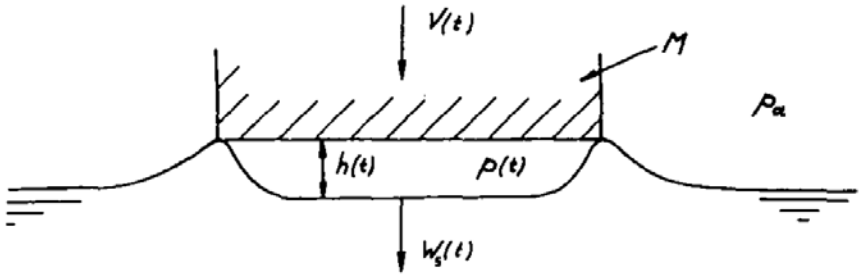

Figure 2-14: The impact stage at the moment of first contact of the plate with the water [31]

Furthermore, Verhagen [31] assumed that from this moment on the pressure in the enclosed air bubble is place-independent. Using this assumption and by choosing

appropriate boundary conditions and a velocity potential at this stage, he could solve Equation (2.23) for times $t > t_1$. After complicated mathematics, he obtained:

$$\frac{d\left(\frac{p_{1,P,VH}}{p_1}\right)}{d\left(\frac{\gamma_w t}{l}\right)} = \pm\left(\frac{p_{1,P,VH}}{p_1}\right)^{\frac{1+\chi}{\chi}}\left[\frac{\frac{\pi}{2}l^2\rho_w + \mathcal{M}}{\mathcal{M}}\cdot\frac{8\chi l\rho_a}{\pi h_1\rho_w}\ldots\right.$$
$$\ldots\times\left[\frac{p_1}{p_a(\chi-1)}\cdot\left(1-\left(\frac{p_{1,P,VH}}{p_1}\right)^{\frac{\chi-1}{\chi}}\right)+1-\left(\frac{p_{1,P,VH}}{p_1}\right)^{-\frac{1}{\chi}}\right]\ldots \quad \textbf{(2.28)}$$
$$\left.\ldots+\frac{\chi^2 l^2}{h_1^2}\left(\frac{W_{s,1}-U}{\gamma_w}\right)\right]^{\frac{1}{2}}$$

With:
- VH = Verhagen
- p_1 = pressure in the air pocket at moment t_1, obtained from Equation (2.24) [Pa]
- χ = ratio between the specific heat at constant pressure and that at constant volume (1.40 at normal atmospheric conditions) [-]
- $\mathcal{M}$ = mass of the impacting plate per unit length (rectangular plate) [kg/m]
- $W_{s,1}$ = average downward velocity of the water surface under the plate at the time moment t_1 [m/s]

The average downward velocity of the water surface under the plate is calculated according to:

$$\frac{\partial W_s}{\partial t} = -\frac{1}{\pi\rho_w}\int_0^t d\tau\int_{-\infty}^{\infty}\frac{\frac{\partial p}{\partial\xi}d\xi}{x-\xi} \quad \textbf{(2.29)}$$

With p evaluated from Equation (2.24).

The positive sign in Equation (2.28) corresponds to a pressure increase and has to be taken before the maximum pressure is reached. Afterwards, the negative sign must be used.

Finally, Verhagen [31] derived a relation from Equation (2.28) to obtain the maximum of the impact pressure:

$$\frac{1}{\chi-1}\frac{p_1}{p_a}\left[1-\left(\frac{p_{\max}}{p_1}\right)^{\frac{\chi-1}{\chi}}\right]+1-\left(\frac{p_{\max}}{p_1}\right)^{-\frac{1}{\chi}}\ldots$$

$$\ldots=-\frac{\pi}{8}\frac{\rho_w}{\rho_a}\frac{\chi l}{h_1}\frac{\mathcal{M}}{\frac{\pi}{2}l^2\rho_w+\mathcal{M}}\left(\frac{W_{s,1}-U}{\gamma_w}\right)^2 \qquad \textbf{(2.30)}$$

2. 4. 2. 2. Cylinder slamming

2. 4. 2. 2. a. <u>von Karman</u>

Although the flat plate theory as initially described by von Karman [18] was developed for wedge shaped bodies, it can easily be adopted for circular cylinders by adjusting the variable plate half width *b(t)* to the contours of a circle instead of a wedge (see Figure 2-11). This extension was already partly done by Faltinsen [17] and is described here more into detail.

The following assumptions were made to simplify the calculations:

- The flow under the plate is two-dimensional.
- The water is incompressible.
- The water is non-viscous.
- Gravity effects can be neglected due to the large entry speeds of the cylinder.
- The entry velocity *U* of the cylinder is constant.

Hence, the potential theory is applicable. Furthermore, it has been shown by Newman [68] that under these circumstances, the flow can be described by a complex velocity potential of the following form:

$$\varphi=-iU\sqrt{(x+iz)^2-b(t)^2} \qquad \textbf{(2.31)}$$

Thus, the velocity components of the flow are given by:

$$[W_1, W_2] = \left[\frac{\partial\varphi}{\partial x}, \frac{\partial\varphi}{\partial z}\right] = \left[iU\frac{(x+iz)}{\sqrt{(x+iz)^2 - b(t)^2}}, -U\frac{(x+iz)}{\sqrt{(x+iz)^2 - b(t)^2}}\right] \quad \textbf{(2.32)}$$

In the plane of the plate (z=0), this yields for the fluid particles besides the plate ($|x| > b(t)$):

$$\begin{aligned}[W_1, W_2] &= \left[iU\frac{x}{\sqrt{x^2 - b(t)^2}}, -U\frac{x}{\sqrt{x^2 - b(t)^2}}\right] \\ &= \left[0, -U\frac{x}{\sqrt{x^2 - b(t)^2}}\right]\end{aligned} \quad \textbf{(2.33)}$$

For the fluid particles on the plate ($|x| < b(t)$), this finally results in:

$$\begin{aligned}[W_1, W_2] &= \left[-U\frac{x}{\sqrt{b(t)^2 - x^2}}, -iU\frac{x}{\sqrt{b(t)^2 - x^2}}\right] \\ &= \left[-U\frac{x}{\sqrt{b(t)^2 - x^2}}, 0\right]\end{aligned} \quad \textbf{(2.34)}$$

Equations (2.33) and (2.34) show that the fluid particles in contact with the plate only have a velocity component in the x-direction, while just next to the plate the fluid particles only have a velocity component in the y-direction. The streamlines corresponding to this type of flow are shown in Figure 2-15.

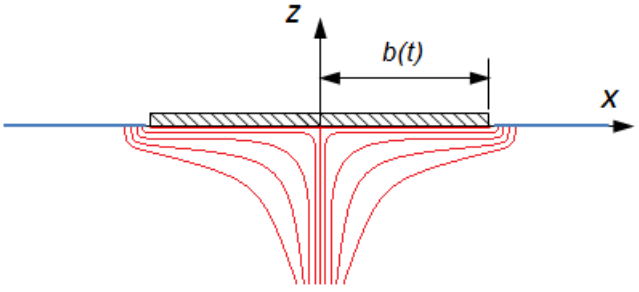

Figure 2-15: Streamlines corresponding to the velocity potential in the flat plate theory

Now, Bernouilli's Equation (2.23) for the pressure distribution on the plate is considered again. Since the focus lies on the initial contact of the cylinder with the

water, the submergence of the body is rather small in this stage and therefore the hydrostatic term $-\rho_w g z$ can be neglected. Furthermore, the dynamic pressure term can be written as:

$$-\frac{\rho_w}{2}\vec{W}\cdot\vec{W} = -\frac{\rho_w}{2}\left(\left(\frac{\partial\varphi}{\partial x}\right)^2 + \left(\frac{\partial\varphi}{\partial z}\right)^2\right) \qquad \textbf{(2.35)}$$

The pressure distribution in the plane of the plate (z=0) then becomes:

$$p(x,t) = -\rho_w \frac{\partial\varphi}{\partial t}(x,t) - \frac{\rho_w}{2}\left(\left(\frac{\partial\varphi}{\partial x}\right)^2 + \left(\frac{\partial\varphi}{\partial z}\right)^2\right) + C \qquad \textbf{(2.36)}$$

If a point infinitely far away from the plate and in the plane of the plate ($x \to \infty$, $z = 0$) is considered, then the time rate of change of the velocity potential is zero, and also the pressure is zero. To evaluate the dynamic pressure term on this location, the following limits are taken into account:

$$\lim_{x\to\infty}\frac{\partial\varphi}{\partial x}(x, z=0, t) = 0 \qquad \textbf{(2.37)}$$

$$\lim_{x\to\infty}\frac{\partial\varphi}{\partial z}(x, z=0, t) = \lim_{x\to\infty}\left(-U\frac{x}{\sqrt{x^2 - b(t)^2}}\right) = -U \qquad \textbf{(2.38)}$$

Equation (2.36) then yields:

$$C = \frac{\rho_w}{2}U^2 \qquad \textbf{(2.39)}$$

If this latter value for the constant C and the velocity potential (2.31) is now substituted into the pressure distribution on the plate ($|x| < b(t)$, z=0) according to Equation (2.36), then the following pressure formulation is obtained:

$$p(x,t) = \rho_w U\frac{b(t)\frac{db}{dt}(t)}{\sqrt{b(t)^2 - x^2}} - \frac{\rho_w}{2}U^2\frac{x^2}{b(t)^2 - x^2} + \frac{\rho_w}{2}U^2 \qquad \textbf{(2.40)}$$

From Figure 2-11(a), it can be observed that for the bottom point of a cylinder, if the water uprise is not taken into account, the submergence z can be calculated as:

$$z = R - \sqrt{R^2 - b(t)^2} \qquad \textbf{(2.41)}$$

This can be approximated by the following series [6]:

$$z = R - \sqrt{R^2 - b(t)^2} = \frac{1}{2R} b(t)^2 + \frac{1}{8R^3} b(t)^4 + \ldots \qquad \textbf{(2.42)}$$

For small submergences and consequently for small b(t), only the first term of the series must be considered. Furthermore, the submergence can also be formulated as $z = Ut$. This results in:

$$z = Ut \approx \frac{1}{2R} b(t)^2 \qquad \textbf{(2.43)}$$

And thus:

$$b(t) \approx \sqrt{2RUt} \qquad \textbf{(2.44)}$$

$$\frac{db}{dt}(t) = \sqrt{\frac{UR}{2t}} \qquad \textbf{(2.45)}$$

Substituting Equations (2.44**)** and (2.45**)** into (2.40**)** gives:

$$\begin{aligned} p_{I,C,VK}(x,t) &= \frac{\rho_w U^2 R}{\sqrt{2URt - x^2}} - \frac{\rho_w}{2} U^2 \frac{x^2}{2URt - x^2} + \frac{\rho_w}{2} U^2 \\ &= \frac{1}{2} \rho_w U^2 \left[\frac{1}{\sqrt{\frac{1}{2}\frac{Ut}{R} - \frac{1}{4}\left(\frac{x}{R}\right)^2}} - \frac{x^2}{2URt - x^2} + 1 \right] \end{aligned} \qquad \textbf{(2.46)}$$

Where the subscript C stands for cylinder.

The dimensionless pressure, which is defined as the pressure coefficient C_p [17], for the von Karman theory is then finally given by:

$$C_{p,C,VK} = \frac{p_{I,C,VK}}{\frac{1}{2}\rho_w U^2} = \frac{1}{\sqrt{\frac{1}{2}\frac{Ut}{R} - \frac{1}{4}\left(\frac{x}{R}\right)^2}} - \frac{x^2}{2URt - x^2} + 1 \quad \textbf{(2.47)}$$

2. 4. 2. 2. b. *Wagner*

Wagner [19] tried to improve von Karman's theory by taking the water uprise along the surface of the cylinder into account. Therefore, he assumed that for small submergences, the wetted width is √2 times the wetted width which was assumed by von Karman. As a result, the half width of the expanding plate *b(t)* is now:

$$b(t) = 2\sqrt{RUt} \quad \textbf{(2.48)}$$

$$\frac{db}{dt}(t) = \sqrt{\frac{UR}{t}} \quad \textbf{(2.49)}$$

The pressure given by Equation (2.40**)** now becomes:

$$p_{I,C,W}(x,t) = \frac{2\rho_w U^2 R}{\sqrt{4URt - x^2}} - \frac{\rho_w}{2}U^2 \frac{x^2}{4URt - x^2} + \frac{\rho_w}{2}U^2 = \frac{1}{2}\rho_w U^2 \left[\frac{4}{\sqrt{4\frac{Ut}{R} - \left(\frac{x}{R}\right)^2}} - \frac{x^2}{4URt - x^2} + 1 \right] \quad \textbf{(2.50)}$$

Where the subscript *W* stands for the Wagner theory. The dimensionless pressure coefficient for the Wagner theory is then:

$$C_{p,C,W} = \frac{4}{\sqrt{4\frac{Ut}{R} - \left(\frac{x}{R}\right)^2}} - \frac{x^2}{4URt - x^2} + 1 \quad \textbf{(2.51)}$$

2. 4. 2. 2. c. Wienke

Both theories of von Karman and Wagner are only valid for small submergences (with exception from the very initial impact stage), due to the approximation of the cylindrical circumference as in Equation (2.44) and (2.48). Wienke [6] tried to improve this by defining a piecewise description for the cylindrical circumference:

$$\begin{cases} z = \dfrac{1}{4R} b(t)^2 & \text{for} \quad 0 \le b(t) \le \dfrac{R}{\sqrt{2}} \\ z = \dfrac{3}{8R^3} b(t)^4 & \text{for} \quad \dfrac{R}{\sqrt{2}} < b(t) \le R \end{cases} \qquad \textbf{(2.52)}$$

This resulted in the following expressions for the half width of the expanding plate:

$$\begin{cases} b(t) = 2\sqrt{URt} & \text{for} \quad 0 \le b(t) \le \dfrac{R}{\sqrt{2}} \\ b(t) = \sqrt[4]{\dfrac{8}{3} UR^3 t} & \text{for} \quad \dfrac{R}{\sqrt{2}} < b(t) \le R \end{cases} \qquad \textbf{(2.53)}$$

The piecewise dimensionless pressure according to Wienke is thus given by:

$$C_{p,C,Wi} = \begin{cases} \dfrac{4}{\sqrt{4\dfrac{Ut}{R} - \left(\dfrac{x}{R}\right)^2}} - \dfrac{x^2}{4URt - x^2} + 1 \quad \text{for } 0 \le b(t) \le \dfrac{R}{\sqrt{2}} \\ \dfrac{1}{2}\left(\dfrac{R^3}{\sqrt{UR^3 t}\sqrt{\sqrt{\dfrac{3}{8}UR^3 t} - \dfrac{3}{8}x^2}} - \dfrac{x^2}{\sqrt{\dfrac{8}{3}UR^3 t - x^2}} + 1 \right) \\ \qquad\qquad \text{for } \dfrac{R}{\sqrt{2}} < b(t) \le R \end{cases} \qquad \textbf{(2.54)}$$

As long as the wetted half width $b(t)$ of the cylinder is not larger than $R/\sqrt{2}$ the solution of Wienke [6] coincides with the one from Wagner [19]. This value for $b(t)$ corresponds with a penetration depth of $z = R/8$ and a deadrise angle of 45°. The solution of Wienke [6] thus adjusts Wagner's formulation [19] only for larger penetration depths.

2. 4. 3. Impact forces

2. 4. 3. 1. Flat plate slamming

The impact forces acting on flat plates during slamming can be calculated by integrating the pressure distributions over the area of the plate. Since both theories presented for flat plate slamming assume the impact pressure to be independent of the location under the plate, the slamming force can be simply calculated by multiplying the pressure with the plate area. For example for the von Karman theory, this results in Equation (2.18).

2. 4. 3. 2. Cylinder slamming

2. 4. 3. 2. a. von Karman

Similarly to the case of flat plate slamming, the impact force acting on a cylinder during cylinder water entry can be calculated by integrating the pressure distribution over the equivalent flat plate with varying half width *b(t)*. The force per unit length $\mathcal{F}$ according to von Karman [18] can thus be calculated by the following formula:

$$\mathcal{F}_{I,C,VK} = \int_{-b(t)}^{b(t)} p_{I,C,VK}(x,t)dx$$

$$= \int_{-\sqrt{2URt}}^{\sqrt{2URt}} \frac{1}{2}\rho_w U^2 \left[\frac{1}{\sqrt{\frac{1}{2}\frac{Ut}{R} - \frac{1}{4}\left(\frac{x}{R}\right)^2}} - \frac{x^2}{2URt - x^2} + 1 \right] dx \qquad \textbf{(2.55)}$$

However, it has been observed that this integral cannot be solved analytically due to singularities occurring at the borders of the integration interval ($x = \pm b(t)$). These borders closely correspond to the roots of the water jets which are generated as the cylinder penetrates the water. Consequently, they also correspond at any time *t* closely with the *x*-values where the maximum impact pressures are reached. In order to determine an approximate solution of the above integral, the integration interval is hence restricted to the *x*-values for which the maximum pressure is reached. The difference between the half width of the expanding plate $b(t)$ and the location of the maximum of the impact pressure $x_{max}(t)$ is illustrated in Figure 2-16.

In order to find a solution for the integral (2.55), the location of the impact pressure maxima as function of time $x_{max}(t)$ should thus be found at first. The impact pressure

reaches its maximum for a certain time t when its derivative with respect to x is zero. The following x-values satisfy this condition:

$$x_{\max,VK}(t) = \pm\sqrt{-4U^2t^2 + 2RUt} \qquad \textbf{(2.56)}$$

A close approximation of the impact force per unit length according to von Karman [18] can thus be found by:

$$\mathcal{F}_{I,C,VK} = \int_{-x_{\max,VK}(t)}^{x_{\max,VK}(t)} p_{I,C,VK}(x,t)dx$$

$$= \rho RU^2\left[2\arctan\left(\frac{\sqrt{1-2\frac{Ut}{R}}}{\sqrt{2\frac{Ut}{R}}}\right) + 2\sqrt{2\frac{Ut}{R}\left(1-2\frac{Ut}{R}\right)}\ldots \right. \qquad \textbf{(2.57)}$$

$$\left. \ldots - \sqrt{2\frac{Ut}{R}}\operatorname{arctanh}\left(\sqrt{1-2\frac{Ut}{R}}\right)\right]$$

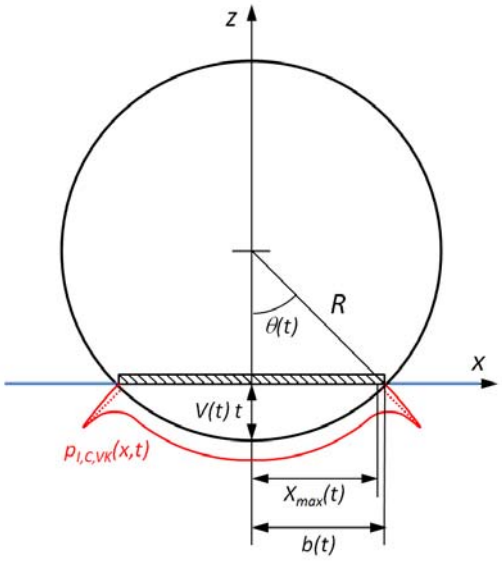

Figure 2-16: The flat plate theory of von Karman [18] showing the difference between the varying half width of the expanding plate $b(t)$ and the location of the maximum impact pressure $x_{max}(t)$

The corresponding dimensionless impact force, called the slamming coefficient is given by:

$$C_{s,C,VK} = \frac{\mathcal{F}_{I,C,VK}}{\rho_w R U^2}$$

$$= 2\arctan\left(\frac{\sqrt{1-2\frac{Ut}{R}}}{\sqrt{2\frac{Ut}{R}}}\right) + 2\sqrt{2\frac{Ut}{R}\left(1-2\frac{Ut}{R}\right)}... \qquad \textbf{(2.58)}$$

$$... - \sqrt{2\frac{Ut}{R}}\operatorname{arctanh}\left(\sqrt{1-2\frac{Ut}{R}}\right)$$

This slamming coefficient is maximum at the moment of first contact of the cylinder with the water. Although the von Karman theory is not completely valid for these very initial phases of the slamming impact, it is interesting to quantify the initial slamming coefficient which corresponds with this theory. The initial value of the slamming coefficient can be calculated as:

$$C_{s,0,C,VK} = \lim_{t\to 0} C_{s,C,VK} = \pi \qquad \textbf{(2.59)}$$

This initial value of the slamming coefficient has been also reported in many other publications [6, 32, 42, 47, 48, 58].

2. 4. 3. 2. b. <u>*Wagner*</u>

The same method for calculating the impact forces from the impact pressures is now applied for the Wagner theory [19]. For this case, the following locations of the maximum impact pressures as function of time are found:

$$x_{\max,W}(t) = \pm 2\sqrt{-U^2t^2 + RUt} \qquad \textbf{(2.60)}$$

This yields in the following formulation for the impact force per unit length:

$$\mathcal{F}_{I,C,W} = \int_{-x_{\max}}^{x_{\max}} p_{I,C,W}(x,t)dx$$

$$= 2\rho RU^2\left[2\arctan\left(\frac{\sqrt{1-\frac{Ut}{R}}}{\sqrt{\frac{Ut}{R}}}\right)+2\sqrt{\frac{Ut}{R}\left(1-\frac{Ut}{R}\right)}...\right. \qquad \textbf{(2.61)}$$

$$\left. ...-\sqrt{\frac{Ut}{R}}\operatorname{arctanh}\left(\sqrt{1-\frac{Ut}{R}}\right)\right]$$

And for the slamming coefficient:

$$C_{s,C,W} = \frac{\mathcal{F}_{I,C,W}}{\rho_w RU^2}$$

$$= 4\arctan\left(\frac{\sqrt{1-\frac{Ut}{R}}}{\sqrt{\frac{Ut}{R}}}\right)+4\sqrt{\frac{Ut}{R}\left(1-\frac{Ut}{R}\right)}... \qquad \textbf{(2.62)}$$

$$...-2\sqrt{\frac{Ut}{R}}\operatorname{arctanh}\left(\sqrt{1-\frac{Ut}{R}}\right)$$

Again, the slamming coefficient is maximum at the start of the slamming process. Now, the initial slamming coefficient is double the one as calculated for the von Karman theory [18]:

$$C_{s,0,C,W} = \lim_{t\to 0} C_{s,C,W} = 2\pi \qquad \textbf{(2.63)}$$

Also this value has been repeatedly reported before in [6, 32, 42, 47, 48, 58].

2. 4. 3. 2. c. Wienke

For the piecewise pressure function of Wienke [70], the same calculation can be applied. For the case that $0 \le b(t) \le \frac{\sqrt{2}}{R}$, the same impact force and slamming coefficient as for Wagner [19] is obtained (Equation (2.57) and (2.58)). For the case that $\frac{\sqrt{2}}{R} < b(t) \le R$, an analytical solution for the slamming coefficient is given by Wienke [70]:

$$C_{s,C,Wi} = \frac{\mathcal{F}_{I,C,Wi}}{\rho_w R U^2}$$
$$= \pi \sqrt{\frac{1}{6}\frac{1}{\frac{U}{R}\left(t - \frac{1}{32}\frac{R}{U}\right)}} - \sqrt[4]{\frac{8}{3}\frac{U}{R}\left(t - \frac{1}{32}\frac{R}{U}\right)}\ldots \qquad \textbf{(2.64)}$$
$$\ldots \cdot \operatorname{arctanh}\sqrt{1 - \frac{U}{R}\left(t - \frac{1}{32}\frac{R}{U}\right)} \cdot \sqrt{6\frac{U}{R}\left(t - \frac{1}{32}\frac{R}{U}\right)}$$

2. 4. 3. 2. d. Greenhow and Yanbao

Based on the findings of von Karman [18], Greenhow and Yanbao [42] proposed a formulation for the slamming coefficient which is initially the same as calculated by von Karman [18], but which diminishes faster after the first contact of the cylinder with the water. The following expression for the slamming coefficient was obtained:

$$C_{s,C,GY} = \pi\left(1 - \frac{Ut}{R}\right) \qquad \textbf{(2.65)}$$

2. 4. 3. 2. e. Wellicome

The same was done by Wellicome [71], now based on the force solution of Wagner [19]. Wellicome obtained a slamming coefficient of the following form:

$$C_{s,C,We} = \frac{2\pi}{1 + \frac{3}{2}\frac{Ut}{R}} \qquad \textbf{(2.66)}$$

2. 4. 3. 2. f. Kaplan and Silbert

Kaplan and Silbert [46] calculated the added mass $\mathcal{M}_w$ per unit length for a cylinder penetrating the water. They treated the body shape exactly instead of approximating the cylinder's submerged section by a flat plate. Assuming a constant entry velocity U, they could convert this added mass to a slamming coefficient using the following relation:

$$\begin{aligned}\mathcal{F}_I &= \frac{d}{dt}\left(\mathcal{M}_w V(t)\right)\\ &= U\frac{d\mathcal{M}_w}{dt}\\ &= U\frac{d\mathcal{M}_w}{dh}\frac{dh}{dt}\\ &= U^2\frac{d\mathcal{M}_w}{dh}\\ &= \rho_w R U^2\left(\frac{1}{\rho_w R}\frac{d\mathcal{M}_w}{dh}\right)\\ &= \rho_w R U^2 C_s\end{aligned} \qquad \textbf{(2.67)}$$

And thus:

$$C_s = \frac{1}{\rho_w R}\frac{d\mathcal{M}_w}{dh} \qquad \textbf{(2.68)}$$

They obtained:

$$C_{s,C,KS} = \left[\frac{2\pi^3}{3}\left(\frac{\sin\left(2\arccos\left(1-\frac{Ut}{R}\right)\right)}{\left(2\pi-2\arccos\left(1-\frac{Ut}{R}\right)\right)^2}+\frac{2\left(1-\cos\left(2\arccos\left(1-\frac{Ut}{R}\right)\right)\right)}{\left(2\pi-2\arccos\left(1-\frac{Ut}{R}\right)\right)^3}\right)\ldots\right.$$
$$\left.\ldots+\frac{\pi}{3}\sin\left(2\arccos\left(1-\frac{Ut}{R}\right)\right)+\cos\left(2\arccos\left(1-\frac{Ut}{R}\right)\right)-1\right]\ldots \qquad \textbf{(2.69)}$$
$$\ldots\cdot\left(1-\left(1-\frac{Ut}{R}\right)^2\right)^{\frac{1}{2}}$$

2. 4. 3. 2. g. *Campbell and Weynberg*

An empirical relation from cylinder drop experiments was obtained by Campbell and Weynberg [56]. Up to know, this relation plays an important role in the design of cylindrical marine constructions since it is used in the DNV standard [57]. The empirical relation found by Campbell and Weynberg [56] is given by:

$$C_{s,C,CW} = \frac{5.15}{1+\frac{8.5Ut}{R}} + \frac{0.275Ut}{R} \qquad \textbf{(2.70)}$$

2. 4. 3. 2. h. Miao

Another empirical relation for the slamming coefficient is provided by Miao [58]. This relation was also obtained from cylinder drop experiments. From pressure and force measurements, he obtained:

$$C_{s,C,M} = 6.1e^{-6.2\frac{Ut}{R}} + 0.4 \qquad \textbf{(2.71)}$$

2. 5. Conclusions

This chapter provides a succinct and comprehensive introduction in the field of wave slamming in general, and in the field of flat plate slamming and cylinder slamming in particular. All the necessary terminology to understand the next chapters of this dissertation has been presented. A concise literature survey has been performed giving an overview of the work which has already been done throughout the years. This literature survey shows that very little research has yet been performed concerning the matter which is dealt in this dissertation.

Furthermore, this chapter gives a complete overview of the existing slamming theories concerning flat plate and cylinder slamming. These theoretical models have been comprehensively summarized. To the author's best knowledge, such a review has never been performed before and it is hence of great value also for future research.

Finally, this chapter contains a simplified theoretical approximation on the effect of deformability on the impact loads generated during water slamming. This simplified glance on the problem confirmed the basic assumptions made at the start of this research, i.e. that the slamming impact loads on a structure diminish with increasing deformability.

2. 6. References

[1] H. Kihara, "A numerical study for bow flare slamming using boundary element model."

[2] H. Sun and O. Faltinsen, "Water entry of a bow-flare ship section with roll angle," *Journal of Marine Science and Technology,* vol. 14, pp. 69-79, 2009.

[3] O. M. Faltinsen, "Slamming on the wetdeck of multihulls," in *7th International Workshop on Water Waves and Floating Bodies*, France, 1992.

[4] J. De Rouck, K. Van Doorslaer, T. Versluys, K. Ramachandran, S. Schimmels, and M. Kudella, "Full scale impact tests on a vertical wall in the large wave flume in Hannover," *33rd International Conference on Coastal Engineering, Santander, Spain,* 2012.

[5] D. Kisacik, P. Troch, and P. Van Bogaert, "Experimental study of pressure distributions due to breaking wave impacts," *33rd International Conference on Coastal Engineering, Santander, Spain,* 2012.

[6] J. Wienke and H. Oumeraci, "Breaking wave impact force on a vertical and inclined slender pile--theoretical and large-scale model investigations," *Coastal Engineering,* vol. 52, pp. 435-462, 2005.

[7] B. Buchner, "The impact of green water on FPSO design," in *Offshore Technology Conference*, Houston, Texas, 1995.

[8] M. Greco, "A two-dimensional study of green-water loading," Department of marine hydrodynamics, Norwegian University of Science and Technology, Trondheim, 2001.

[9] O. Faltinsen and A. Timokha, *Sloshing*: Cambridge University Press, 2009.

[10] G. X. Wu, Q. W. Ma, and R. Eatock Taylor, "Numerical simulation of sloshing waves in a 3D tank based on a finite element method," *Applied Ocean Research,* vol. 20, pp. 337-355, 1998.

[11] R. Dallinga, M. Flikkema, and R. Grin, "Challenging wind and waves: their impact on fuel consumption," *Maritilme Reporter & Engineering News*.

[12] O. M. Faltinsen, *Hydrodynamics of high-speed marine vehicles*, 1 ed.: Cambridge University Press, 2005.

[13] K. M. T. Kleefsman, "Water impact loading on offshore structures," Faculty of Mathematics and Natural Sciences, RUG University Groningen, Groningen, 2005.

[14] f. Systema. *Storm en schepen*. Available: http://members.multimania.nl/fokke6/stormenschepen.htm

[15] K. Attfield, "Gas Platforms - How designers underestimated the North Sea," *Offshore Technology,* pp. 12-22, 1975.

[16] M. Van Torre, "Manoeuvreer- en zeegangsgedrag van maritieme constructies," *Course at Ghent University*.

[17] O. M. Faltinsen, "Sea loads on ships and offshore structures," 1990.

[18] T. von Karman, "The impact of seaplane floats during landing," *Technical note no. 321, National Advisory Committe for Aeronautics,* 1929.

[19] H. Wagner, "Über Stoß- und Gleitvorgänge an der Oberfläche von Flüssigkeiten," *ZAMM - Journal of Applied Mathematics and Mechanics / Zeitschrift für Angewandte Mathematik und Mechanik,* vol. 12, pp. 193-215, 1932.

[20] I. T. Egorov, "Impact on a compressible fluid," *Technical Memorandum 1413, National Advisory Commitee for aeronautics,* vol. 20, 1956.

[21] N. Malleron, Y.-M. Scolan, and A. A. Korobkin, "Some aspects of a generalized Wagner model," *22nd International Workshop on Water Waves and Floating Bodies,* pp. 137-140, 2007.

[22] R. Cointe and J. L. Armand, "Hydrodynamic impact analysis of a cylinder," *Journal of offshore mechanics and Arctic engineering,* vol. 109, p. 237, 1987.

[23] Z. N. Dobrovol'skaya, "On some problems of similarity flow of fluid with a free surface," *Journal of Fluid Mechanics,* vol. 36, pp. 805-829, 1969.

[24] R. Zhao and O. Faltinsen, "Water entry of two-dimensional bodies," *Journal of Fluid Mechanics,* vol. 246, pp. 593-612, 1993.

[25] R. Zhao and O. M. Faltinsen, "Water entry of arbitrary two-dimensional sections with and without flow separation," in *21st Symposium on Naval Hydrodynamics*, Trondheim, Norway, 1996, pp. 408-423.

[26] R. Zhao and O. M. Faltinsen, "Water entry of axisymmetric bodies with and without flow separation," in *22nd Symposium on Naval Hydrodynamics*, Washington DC, 1998, pp. 651-664.

[27] X. M. Mei, Y. M. Liu, and D. K. P. Yue, "On the water impact of general two-dimensional sections," *Applied Ocean Research,* vol. 21, pp. 1-15, Feb 1999.

[28] R. Skalak and D. Feit, "Impact on the surface of a compressible fluid," Office of Naval Research, New York1963.

[29] A. Iafrati and A. A. Korobkin, "Hydrodynamic loads during early stage of flat plate impact onto water surface," *Physics of Fluids,* vol. 20, Aug 2008.

[30] E. Campana, A. Carcaterra, E. Ciappi, and A. Iafrati, "Some insights into slamming forces: compressible and incompressible phases," *Proceedings of the Institution of Mechanical Engineers, Part C: Journal of Mechanical Engineering Science,* vol. 214, pp. 881-888, 2000.

[31] J. H. G. Verhagen, "The impact of a flat plate on a water surface," *Journal of Ship Research,* pp. 211-223, 1967.

[32] A. A. Korobkin and V. V. Pukhnachov, "Initial stage of water impact," *Annual Review of Fluid Mechanics,* vol. 20, pp. 159-185, 1988.

[33] S. D. Howison, J. R. Ockendon, and S. K. Wilson, "Incompressible water-entry problems at small deadrise angles," *Journal of Fluid Mechanics,* vol. 222, pp. 215-230, 1991.

[34] E. V. Ermanyuk and M. Ohkusu, "Impact of a disk on shallow water," *Journal of Fluids and Structures,* vol. 20, pp. 345-357, 2005.

[35] S. H. Oh, S. H. Kwon, and J. Y. Chung, "A close look at air pocket evolution in flat impact," *24th International Workshop on Water Waves and Floating Bodies,* 2009.

[36] S. L. Chuang, "Experimental investigation of rigid flat-bottom body slamming," *Report 2041, David Taylor Model Basin,* 1965.

[37] O. Faltinsen, J. Kvålsvold, and J. Aarsnes, "Wave impact on a horizontal elastic plate," *Journal of Marine Science and Technology,* vol. 2, pp. 87-100, 1997.

[38] F. J. Huera-Huarte, D. Jeon, and M. Gharib, "Experimental investigation of water slamming loads on panels," *Ocean Engineering,* vol. 38, pp. 1347-1355, Aug 2011.

[39] N. J. Smith, P. K. Stansby, and J. R. Wright, "The slam force on a flat plate in free flight due to impact on a wave crest," *Journal of Fluids and Structures,* vol. 12, pp. 183-196, Feb 1998.

[40] M. A. Battley, T. Allen, P. Pehrson, I. Stenius, and A. Rosen, "Effects of panel stiffness on slamming responses of composite hull panels," in *17th International Conference on Composite Materials*, Edinburgh, 2009.

[41] M. Greenhow and W.-M. Lin, "Nonlinear free surface effects: experiments and theory," *Report 83-19 of Massachusetts Institute of Technology, Department of Ocean Engineering,* 1983.

[42] M. Greenhow and L. Yanbao, "Added masses for circular cylinders near or penetrating fluid boundaries—review, extension and application to water-entry, -exit and slamming," *Ocean Engineering,* vol. 14, pp. 325-348, // 1987.

[43] H. Sun and O. M. Faltinsen, "Water impact of horizontal circular cylinders and cylindrical shells," *Applied Ocean Research,* vol. 28, pp. 299-311, 2006.

[44] A. G. Fabula, "Ellipse-fitting approximation of two-dimensional normal symmetric impact of rigid bodies on water," *Fifth Midwestern Conference on fluid Mechanics,* pp. 299-315, 1957.

[45] M. Shiffman and D. C. Spencer, "The force of impact on a sphere striking a water surface," *Applied Mathematics Panel, National Defense Research Committee U.S.,* 1945.

[46] P. Kaplan and M. H. Silbert, "Impact forces on platform horizontal members in the splash zone," in *Offshore Technology Conference*, Houston, 1976, p. Paper No. OTC 2498.

[47] C. J. Garrison, "Water impact loads on circular structural members," *Applied Ocean Research,* vol. 18, pp. 45-54, 1996.

[48] O. M. Faltinsen, "Water impact loads and dynamic response of horizontal circular cylinders in offshore structures," in *9th annual Offshore Technology Conference*, Houston, Texas, 1977, pp. 191 - 123.

[49] J. N. Newman, "Distributions of sources and nomal dipoles over a quadrilateral panel," *Journal of Engineering Mathematics,* vol. 20, pp. 113-126, 1986.

[50] M. F. Ionina, "Penetration of an elastic circular cylindrical shell into an incompressible liquid," *Journal of Applied Mechanics and Technical Physics,* vol. 40, 1999.

[51] Sollied, "Student project: Beregning av Krefter pa Stag ved Slagaktige Pakjenninger," Division of Ship Hydrodynamics, NTNU, Trondheim1976.

[52] A. Nøttveit, "En undersøkelse av slagaktige påkjenninger fra bølger på horisontale stag på bore- og produksjonsplattformer," Master thesis, Divison of Port and Ocean Engineering, NTNU, Trondheim, 1975.

[53] M.-C. Lin and L.-D. Shieh, "Flow visualization and pressure characteristics of a cylinder for water impact," *Applied Ocean Research,* vol. 19, pp. 101-112, 1997.

[54] G. Colicchio, M. Greco, M. Miozzi, and C. Lugni, "Experimental and numerical investigation of the water-entry and water-exit of a circular cylinder," in *International Workshop on Water Waves and Floating Bodies*, Zelegonorsk, Russia, 2009.

[55] N. A. Lange and T. Rung, "Impact tests in pure and aerated water," presented at the 30th International Conference on Ocean, Offshore and Arctic Engineering, Rotterdam, The Netherlands, 2011.

[56] J. M. C. Campbell and P. A. Weynberg, "Measurements of parameters affecting slamming," in *Report No. 440*, Wolfson Unit for Marine Technology, Southampton, United Kingdom, 1980.

[57] Det Norske Veritas, "Environmental conditions and environmental loads," *Classification notes no. 30.5,* 2010.

[58] G. Miao, "Hydrodynamic forces and dynamic responses of circular cylinders in wave zones," *PhD dissertation, Norwegian University of Science and Technology,* 1988.

[59] M. F. Ionina, "Water impact on cylindrical shells," in *14th International Workshop on Water Waves and Floating Bodies*, Port Huron, MI, USA, 1999.

[60] M. Arhan and G. Deleuil, "Experimental study of the impact of horizontal cylinders on a water surface," *Offshore Technology Conference, paper 3107,* 1978.

[61] B. L. Miller, "Wave slamming on offshore structures," *NMI Report no. R81 OT-R-8041,* 1980.

[62] K. Souter, N. Mahale, and H. Krachman, "Water impact tests of rigid and flexible cylinders," *EPRI NP-798, Electrical Power Institute,* 1978.

[63] B. P.A., "Water impact loads on horizontal members in the splash zone," *Master thesis, Norwegian University of Science and Technology,* 1977.

[64] C. Dalton and S. M. Nash, "Wave slam on horizontal members of an offshore platform," *Offshore Technology Conference, paper 2500,* 1976.

[65] B. L. Miller, "Wave slamming loads on horizontal circular elements of offshore structures," *Journal of the Royal Institute of Naval Architecture, paper no. 5,* 1977.

[66] T. Sarpkaya, "Wave impact loads on cylinders," *Offshore Technology Conference, paper 3065,* 1978.

[67] J. Morison, M. P. O'Brien, J. W. Johnson, and S. A. Schaaf, "The force exerted by surface waves on piles," *Petrloeum Transactions (American Institute of Mining engineers),* vol. 189, pp. 149-154, 1950.

[68] J. N. Newman, "Marine Hydrodynamics," *Massachusetts Institute of Technology,* 1977.

[69] P. M. Morse and H. Feshbach, "Methods of theoretical physics," 1953.

[70] J. Wienke, *Druckschlagbelastung auf schlanke zylindrische bauwerke durch brechende wellen*, 2001.

[71] J. M. C. Campbell, J. F. Wellicome, and P. A. Weynberg, "An investigation into wave slamming loads on cylinders," *Wolfson Marine Craft Unit Report No. 317,* 1977.

Chapter 3

Experimental setup and instrumentation

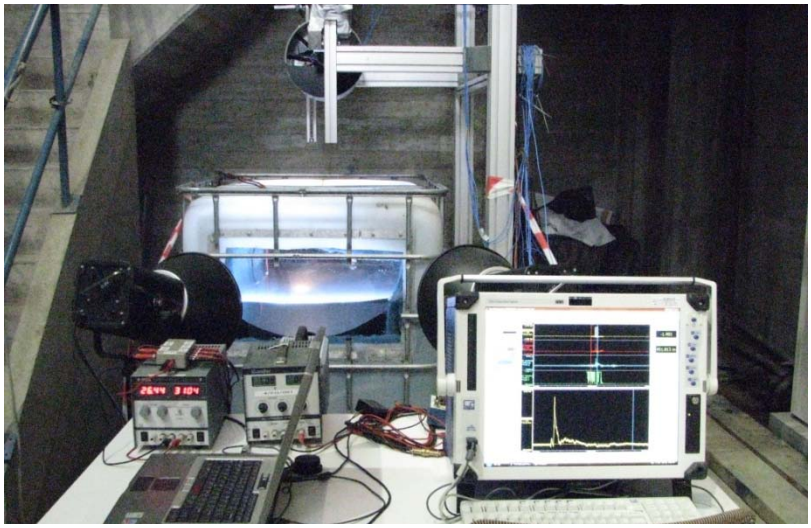

Overview

The present chapter describes the experimental setup and the instrumentation which is used during the slamming experiments. Furthermore, an overview of the data acquisition is provided. Finally, the characteristics of the used test specimens are discussed.

3. 1. Experimental setup

Water slamming is experimentally investigated in this dissertation by means of slamming drop experiments. Therefore, a vertical drop weight test rig was used, which was originally designed and built by the division Ocean Engineering of the Department of Civil Engineering of Ghent University [1-5]. It is basically composed of an Aluminium framework, firmly fixed to a concrete wall and floor. This framework contains two vertical rails of 3 m long which are used to guide a T-shaped impactor towards a water basin at the bottom. The test object is fixed at the bottom of the impactor and falls due to gravity into the water reservoir.

The water basin is a 1000 litre plastic industrial barrel which is equipped with two transparent Plexiglas panels in order to allow visualisation of the slamming process from two sides of the test object. The water tank measures 1 m by 1 m and the water level has been fixed at 0.6 m. The experimental setup is visualized in Figure 3-1.

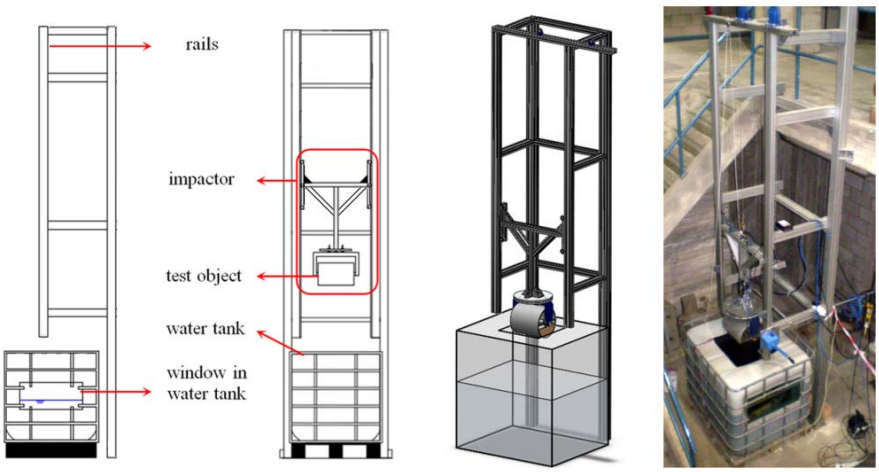

Figure 3-1: The experimental slamming drop weight setup used in this dissertation

During this dissertation, the setup has been extended with extra components and instrumentation to improve the precision and reproducibility of the experiments. A manual hoist has been added to the setup to facilitate the lifting of the test objects, and to improve the tuning of the drop height (and thus the impact velocity) of the experiments. Furthermore, a mechanical release mechanism has been introduced which is based on pneumatic and hydraulic tube clutches. Finally, the damping of the impactor motion after the test object has slammed the water surface has been improved by using industrial dampers in combination with elastic foam material. Figure 3-2 shows a few photographs of the main changes of the existing setup.

(a) (b) (c)

Figure 3-2: (a) the manual hoist; (b) the mechanical release system; (c) the industrial dampers

3. 2. Instrumentation

A schematic overview of the main instruments with their location on the setup is depicted in Figure 3-3 for the case of cylinder slamming experiments. All of these are discussed in the following sections.

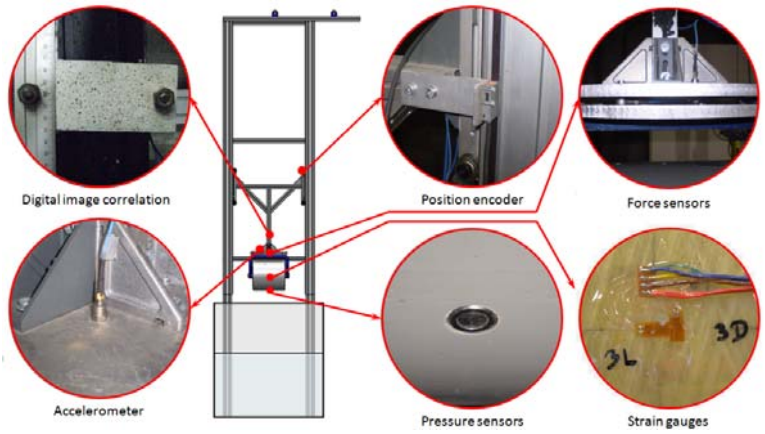

Figure 3-3: Schematic overview of the experimental instrumentation

The literature survey from chapter2 learned that slamming loads are typically highly dynamic with short rise times and short durations. For acquiring these signal types, two criteria in the selection process of the transducers for measuring the slamming loads then become very important, i.e. the resonance frequency and the minimum rise time. Piezoelectric based sensors are known to be the best choice when applying these selection criteria. The reason for this is that piezoelectric materials typically exhibit very high natural frequencies (in the order of 100 kHz or more) and have an excellent linear behaviour over a wide amplitude range [6]. Examples of common piezoelectric crystals are quartz, tourmaline (crystal materials) and lead zirconate titanate (PZT – a ceramic material). It is for this reason that the chosen pressure sensors, force sensors and accelerometer are from the piezoelectric type.

3. 2. 1. Pressure sensors

Pressure sensors are used to measure the local loads acting at a certain location of the object surface during water penetration. The pressure sensors used are dynamic integrated circuit piezoelectric sensors (ICP sensors) from *PCB Piezotronics*. They incorporate piezoelectric quartz crystals which generate an electrostatic charge when being loaded and thus compressed. This charge output is proportional to the input pressure and is converted into a low impedance voltage signal by a built-in MOSFET microelectronic amplifier. A low impedance signal is required to prevent triboelectric cable noise in the output signal [6].

In contrast with their excellent dynamic behaviour, piezoelectric crystal based sensors are unable to measure static loads. Even though the transducers are very well electrically insulated, the electrostatic charge generated by compression will eventually leak to zero through the lowest resistance path. This makes that when a static load is applied on a piezoelectric sensor, the output will decrease to zero after some time, while the load is still present on the transducer. The rate at which the charge leaks back to zero is characterized by the discharge time constant (DTC) and is considered as the second important parameter of dynamic gauges. This DTC is defined as the time required for a sensor to discharge its signal to 37% of the original value from a step input load. The DTC is thus a measure for the low frequency limit of a dynamic transducer. The typical discharge curve due to a step pressure input for a dynamic pressure transducer is depicted in Figure 3-4.

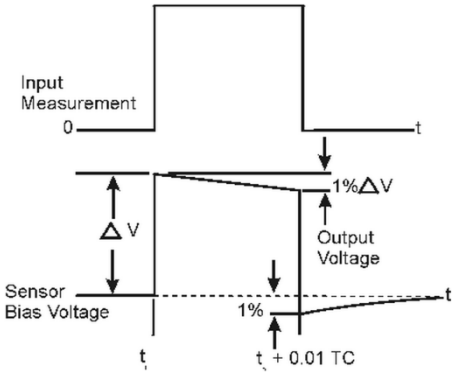

Figure 3-4: Typical discharge of a piezoelectric transducer [7]

A photograph of a typical ICP pressure sensor with its internal configuration is given in Figure 3-5. It can be observed that at the side of the sensor diaphragm, metric thread is provided in order to facilitate the mounting of the sensor into the test specimen.

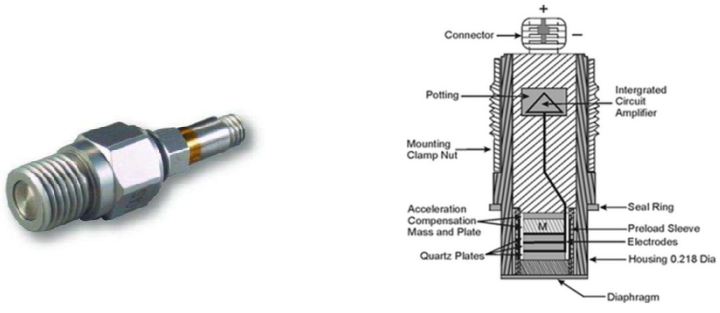

(a) (b)

Figure 3-5: (a) Photograph of an ICP pressure sensor and (b) schematic view on its internal configuration [7]

For the experiments performed in this dissertation, three types of pressure sensors are used. Their main characteristics are provided in Table 3-1.

Table 3-1: Characteristics of the used pressure sensors [8]

Characteristics	Pressure sensor types		
	102A06/102B06	102A07	102A08
Measurement range [bar]	34.5	3.45	3.45
Sensitivity [mV/kPa]	1.45	14.5	14.5
Resonant Frequency [kHz]	≥ 500	≥ 250	≥ 430
Minimal rise time [µs]	≤ 1.0	≤ 2.0	≤ 2.0
Temperature coefficient of Sensitivity [%/°C]	≤ 0.054	≤ 0.05	≤ 0.05
Discharge time constant [s]	≥ 50	≥ 1	≥ 1
Excitation voltage [VDC]	20 to 30	20 to 30	24 to 30
Constant current excitation [mA]	2 to 20	2 to 20	2 to 20
Sensing element material	Quartz	Quartz	Quartz
Diaphragm diameter [mm]	5	5	5

3. 2. 2. Force sensors

Besides pressure sensors, force sensors are used to measure the global response of the complete test model during water impact. The used force sensors are also dynamic integrated circuit piezoelectric sensors (ICP sensors) from *PCB Piezotronics*. Their working principle is exactly the same as for the dynamic pressure transducers. A photograph and schematic overview of their internal configuration is given in Figure 3-6. Table 3-2 gives an overview on the main characteristics.

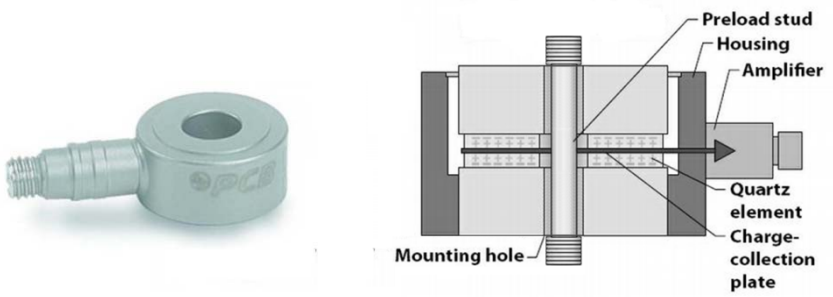

(a) (b)

Figure 3-6: (a) Photograph of an ICP force sensor and (b) schematic view on its internal configuration [9]

Table 3-2: Characteristics of the used force sensors [9]

Characteristics	Force sensor type 201B05
Measurement range [kN]	22.24
Sensitivity [mV/kN]	224.8
Resonant Frequency [kHz]	90
Temperature coefficient of Sensitivity [%/°C]	≤ 0.054
Discharge time constant [s]	≥ 2000
Excitation voltage [VDC]	20 to 30
Constant current excitation [mA]	2 to 20
Stiffness [kN/µm]	2.1
Sensor diameter [mm]	16.5

The force cells are located between the test object and the T-shaped top structure of the impactor. Three identical transducers are used which are configurated in an equilateral triangle with the centre of gravity of the impactor lying on the vertical axis through the midpoint of this triangle. As such, an even load distribution on the load cells is obtained. A schematic view on the location of the force sensors on the impactor is shown in Figure 3-7. A similar force sensor installation is reported in Faltinsen et al. [10] and Huera-Huarte et al. [11].

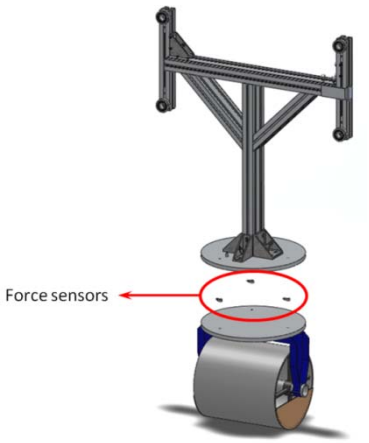

Figure 3-7: Schematic view on the location of the force sensors on the impactor containing a cylindrical test object

To enable the installation of the force sensors between the T-shaped top structure of the impactor and the test object, two circular plates are provided to clamp the force

sensors in between. It is very important to avoid bending of these plates under the loads caused by the water impact. Such deformations would lead to asymmetric load distributions over the individual force sensors causing disturbed and wrong force recordings, as illustrated in Figure 3-8. Hence, the used impactor plates should be thick and made from a stiff material. However, the use of too thick plates would lead to a large impactor mass which is difficult or impossible to handle. Hence, a compromise was found between the stiffness and the mass of the impactor plates. It was decided to restrict the mass of the plates to 10 kg, to enable slamming experiments also with heavy test models. Aluminium was chosen as material since it has a high value for the specific stiffness. A maximum mass of 10 kg resulted in two Aluminium plates with a diameter of 40 cm and a thickness of 1.5 cm. The corresponding flexural stiffness K of these plates is then:

$$K = \frac{Ed^3}{12\left(1-\nu^2\right)} = 21635\ \text{Pa}\cdot\text{m}^3 \qquad \textbf{(3.1)}$$

With:
- E = Elasticity modulus of the material [Pa] (70 GPa for Aluminium)
- d = plate thickness [m]
- ν = Poisson's ratio [-] (0.3 for Aluminium)

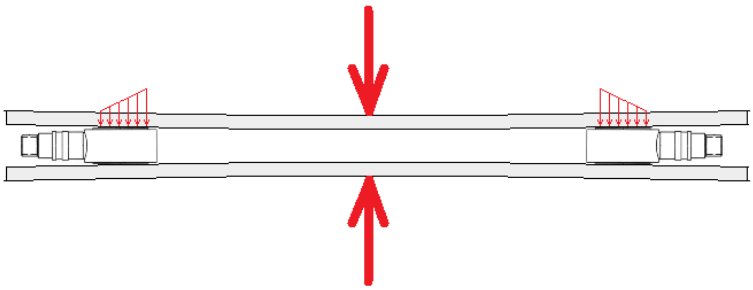

Figure 3-8: Force sensors loaded in bending

To attach a physical meaning to this latter value for the flexural stiffness, the plate is considered to be simply supported at its edges and loaded with a mass of 1000 kg, evenly distributed over the entire area of the plate (see Figure 3-9). In this loading case, the deflection of the plate in the centre can be calculated by the following formulation [12]:

$$\delta = \frac{pR^4}{64K}\frac{5+\nu}{1+\nu} \qquad \textbf{(3.2)}$$

With:
- p = the uniform pressure acting on the plate

- R = plate radius

For the considered load, the maximum deflection in the middle of the plate δ becomes 0.375 mm. This is a very small value considering the large load acting on the plate. Hence, the impactor bottom plates were considered rigid enough to avoid large asymmetric load distributions on the force sensors.

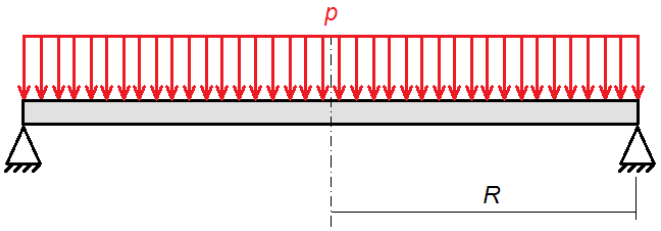

Figure 3-9: A circular plate simply supported at its edges and subjected to a uniform load

The complete combination (Al plate – 3 force sensors – Al plate) can be interpreted as one big load cell measuring the global force on the cylinder. In the following, it will be denoted as the 'load cell combination'.

3. 2. 3. Accelerometer

An accelerometer is used to measure the accelerations and decelerations of the impactor during the slamming tests. The transducer used in this work is again a piezoelectric one. It is an ICP sensor from *Kistler*. However, the working principle is now somewhat different than the one for the used pressure and force sensors. Instead of being compressed, the piezoelectric quartz crystals are now loaded in shear. Two of these quartz crystals are therefore clamped horizontally with one of their sides to the internal structure of the accelerometer. At the other side of the crystals, small masses are installed. When a change in velocity occurs, the inertia of the small masses causes the crystals to shear. These shear deformations are then subsequently converted into electrical charges and voltages. This type of design provides very low sensitivity to transverse accelerations which makes this sensor very well suited for measuring accelerations in one direction [13]. A picture of the accelerometer and a schematic view on its internal configuration is provided in Figure 3-10. An overview of its main characteristics is given in Table 3-3.

The accelerometer in the slamming experiments is located on top of the upper Aluminium plate of the load cell combination (see Figure 3-3). This enables a good comparison between the measured accelerations and the forces measured by the force sensors. Newton's second law of motion is used to perform this comparison.

Furthermore, the data from this transducer can also be converted to velocity and position by integration. As such, the impact velocity can be determined and the moment of water contact can be assessed.

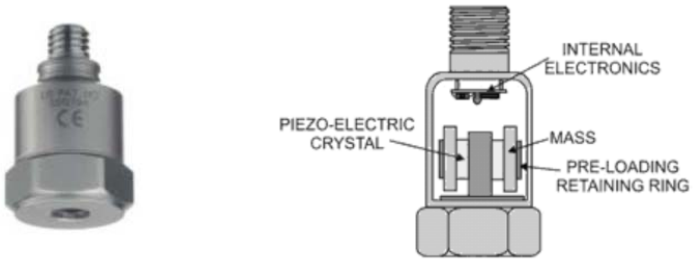

(a) (b)

Figure 3-10: (a) Photograph of the ICP accelerometer and (b) schematic view on its internal configuration [13]

Table 3-3: Characteristics of the used accelerometer [13]

Characteristics	Force sensor type
	8704B500
Measurement range [g]	± 500
Sensitivity [mV/g]	10
Resonant Frequency [kHz]	54
Temperature coefficient of Sensitivity [%/°C]	0.00174
Discharge time constant [s]	1
Excitation voltage [VDC]	20 to 30
Constant current excitation [mA]	4
Sensing element material	Quartz
Nut dimensions	1/2” HEX

3. 2. 4. Position encoder

A position sensor in the form of a linear encoder is used to know the exact position of the test object at any time. It is placed on top of the T-shaped upper structure of the impactor as is depicted in Figure 3-3. The encoder is an inductive sensor which moves very closely, without making contact, to a magnetic strip which is mounted along one of the vertical rails of the setup. This strip contains a sequence of magnetic north and south poles along its length as illustrated in Figure 3-11 (a).

During a drop test, the inductive coil in the encoder detects these magnetic changes and decodes them to a set of output square waves as is depicted in Figure 3-11 (b). These output signals are then converted to an output voltage proportional to the position by a counter device. A photograph of the position encoder and the corresponding counter is shown in Figure 3-12.

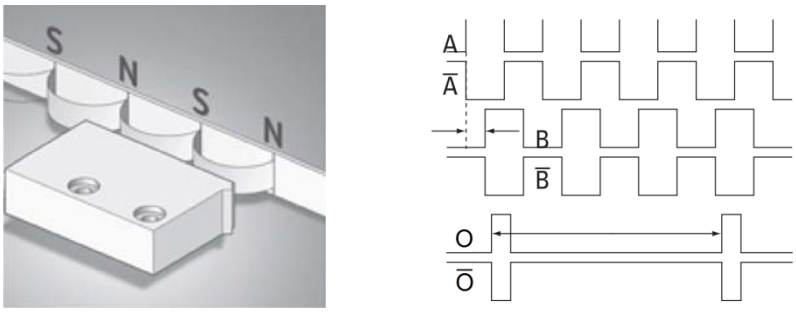

(a) (b)

Figure 3-11: (a) Schematic view on the sequence of north and south poles of the magnetic strip; (b) typical sensor output signals [14]

(a) (b)

Figure 3-12: Photograph of the position encoder (a) and its corresponding counter device (b) [14]

The position encoder plays an important role during the experiments since the position measurement is used to trigger the complete measuring system. The trigger system has been selected as the time moment at which the test object makes the first contact with the water surface. More information on the triggering of the recordings is given in section 3.3.

Furthermore, the encoder is also used to measure the impact velocity by differentiation of the position signal. An attempt is also made to calculate the impact force from the position signal by performing a second differentiation of the signal to acceleration and then using Newton's second law. However, as will be shown in

chapter 4, this attempt failed due to large noise effects which were caused by an amplification of the original noise during the two differentiations.

The most important technical details of the position encoder, which is of the type Limes LI20/B1 from *Kübler* are provided in Table 3-4.

Table 3-4: Characteristics of the used position encoder and corresponding counter device [14]

Characteristics	Sensor type
	Encoder Limes LI20/B1
Excitation voltage [VDC]	4.8 to 30
Resolution [µm]	10
Maximum speed [m/s]	6.5
Dimensions [mm]	10 x 25 x 40
	LED Counter 572
Output voltage [V]	-10..10
Sensitivity [m/V]	set to 0.2

3. 2. 5. Strain gauges

In order to find a relation between the slamming loads and the degree of deformability of a certain object, it is necessary to measure the deformation during slamming impact. Therefore, strain gauges are used on different locations of the test objects.

A strain gauge typically consists of a long, thin conductive strip in a zig-zag pattern of parallel lines. This conductor contains a certain resistance which changes when the conductor is stretched or compressed. This change in resistance is proportional to the strain which is applied on the strain gauge. If such a strain gauge is placed in one branch of a Wheatstone bridge circuit of which the other branches have a resistance which equals the resistance of the undeformed strain gauge, then the output voltage of the bridge circuit is directly proportional to the resistance change of the strain gauge, and thus to the applied strain. Following relation is then applicable [15]:

$$V_A = \frac{1}{4}\frac{\Delta Z}{Z} V_B = \frac{1}{4} S\, \varepsilon V_B \qquad \textbf{(3.3)}$$

With: - V_A = output voltage [V]

- Z = resistance of the undeformed strain gauge [Ω]
- ΔZ = change in the resistance of the strain gauge [Ω]
- V_B = supply voltage to the strain gauge [V]
- S = gauge factor of the strain gauge (sensitivity) [-]
- ε = strain applied to the strain gauge [-]

More strain gauges can be placed in one Wheatstone bridge in order to increase the resolution. In this dissertation, only bridges containing one strain gauge are used. These are called quarter Wheatstone bridges. An illustration on the composition of a strain gauge and a schematic view on a quarter Wheatstone bridge circuit is provided in Figure 3-13.

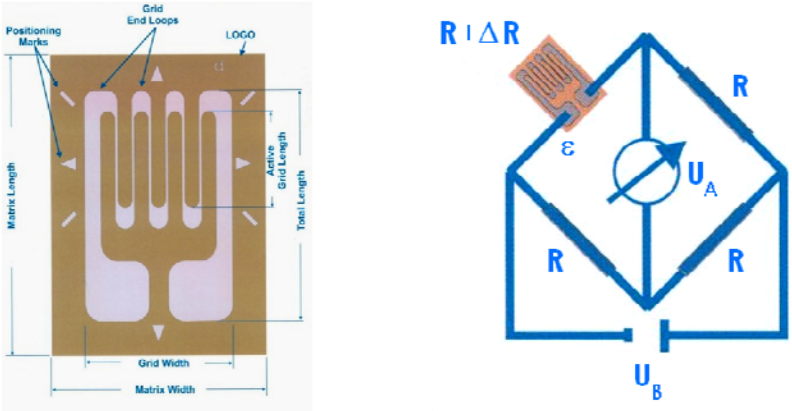

(a) (b)

Figure 3-13: (a) Composition of a strain gauge [16]; (b) Schematic view of a Wheatstone bridge circuit [15]

In this dissertation, uniaxial strain gauges of type CEA-06-250UN-350 from *Vishay* are used. An overview on the main characteristics is given in Table 3-5.

Table 3-5: Characteristics of the used strain gauges [17]

Characteristics	Sensor type
	CEA-06-250UN-350
Active grid length [mm]	6.35
Resistance [Ω]	350
Gauge factor [-]	2.12

3. 2. 6. High speed camera

The slamming events occur so fast that it is impossible for the human eye to distinguish the different stages of the impact event. Hence, a high speed camera has been used. These types of cameras can take thousands of frames per second which enables to investigate every detail of the impact and which helps to have a better understanding of the phenomenon. In this work a high speed camera of type APX-RS has been used from *Photron* (see Figure 3-14). Table 3-6 provides the main characteristics.

Figure 3-14: Photograph of the *Photron* APX-RS high speed camera

Table 3-6: Characteristics of the used high speed camera [18]

Characteristics	Camera type
	APX-RS
Memory [GB]	8
Maximum recording time	6 s at 1000 fps
Maximum resolution [pixels]	1024 x 1024
Maximum frame rate at full resolution [fps]	3000
Maximum frame rate [fps]	250000
Sensor	10 bit CMOS
Minimum shutter time [μs]	2

Furthermore, the camera is also used to measure the position of the cylinder at any time. This has been done by using the digital correlation technique (DIC) [19]. This is a non-interferometric optical technique which is widely accepted as a powerful tool for measuring surface displacements and surface deformations. To calculate the displacement of the test object, the signature of each pixel of a feature within the images is tracked throughout the list of images. The signature of a pixel is a unique value that characterizes that pixel, e.g. the grey value. It can also be calculated using

properties of the neighbouring pixels, e.g. the grey value of the neighbouring pixels. To improve the precision of the digital image correlation technique, a random speckle pattern consisting of a white paint surface layer and black speckles is applied on the test object which is then used as a feature to track throughout the images. In the experiments performed in this work, a white and black speckle pattern is applied on the vertical beam of the T-shaped top structure of the impactor as can be seen in Figure 3-3. The software used to process the images in order to obtain the displacement of the test object versus time is *MatchID* [20].

Finally, this position data as measured by the DIC technique can again be converted to impact velocity and impact force. However, similarly as for the case of the position signal as measured by the linear encoder, the conversion to impact force failed due to noise effects.

3. 2. 7. Particle Image Velocimetry

In this work, the particle image velocimetry (PIV) technique is only used for the experiments with the deformable cylinders. The technique represents an optical method to visualize flow and to obtain the velocity field of the fluid at any time of the impact event. This can be done by seeding the water basin with a large number of reflecting particles. In the experiments performed in the present dissertation, hollow glass spheres of 10 μm diameter are used which have the property to drift for a long time on the same level in the water tank before eventually sinking to the bottom. By taking high speed images during the water impact, the position of these particles can be tracked throughout the complete slamming event. In order to visualize the particles, a high energetic laser plane is generated perpendicular to the view direction of the camera. The camera then captures the laser light which is reflected by the particles towards the camera lens.

During the experiments performed with the deformable cylinders, the PIV setup was provided by the Department of Mechanical Engineering at the Free University of Brussels (VUB). It was mainly used in the framework of the PhD dissertation of Nila [21], which deals with the development of an adaptive PIV method for estimating slamming loads and which is in progress yet. The technical details of this setup can thus be found in [21]. A view on the PIV setup and on the laser plane is presented in Figure 3-15.

The knowledge of the velocity field of the fluid particles versus time makes it possible to calculate the 2D velocity potential of the flow. By using Bernoulli's equation (Equation (2.23)), the impact pressures and integrated impact forces on the test object can then be calculated. The working method and the results of this

technique are precisely explained in [21] and hence fall out of the scope of this dissertation.

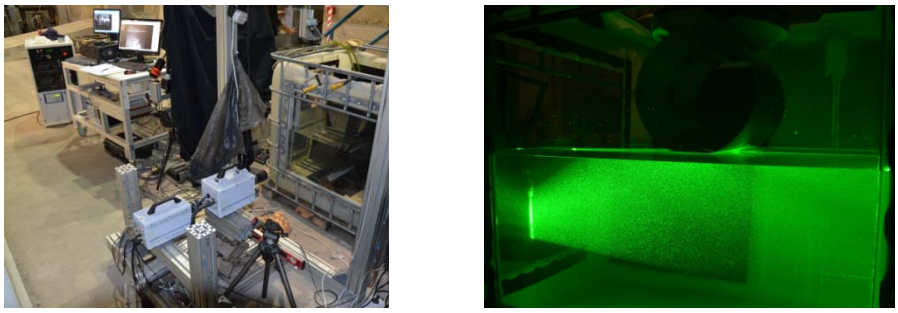

(a) (b)

Figure 3-15: (a) Overview of the PIV setup; (b) View on the 2D laser plane

3. 2. 8. Smoke machine

Besides the fluid flow, it is also interesting to investigate the air flow around the test object just before and during water penetration. In this way, it is possible to verify if all the air has escaped under the test object at the moment of impact and to estimate the air cushion effect. For this purpose, an industrial smoke machine is used during the drop tests to fill the experiment chamber partly with fog for visualizing the air stream.

3. 3. Data Acquisition

Figure 3-16 shows an overview of the data acquisition process used in this dissertation.

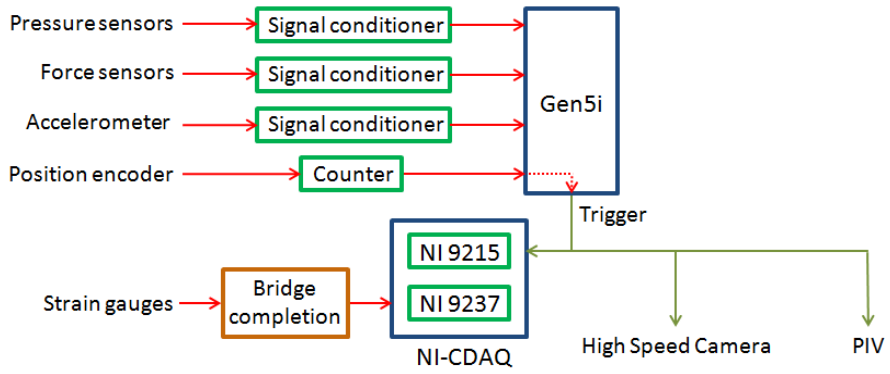

Figure 3-16: Overview of the data acquisition

The data acquisition process mainly consists of two stages. In the first stage, the sensors are provided with the appropriate supply power generated by a signal conditioner, and the sensor returns a voltage or current output which is amplified by the same conditioner. In the second step, this conditioned signal is sent to a data acquisition system which saves the generated data.

For the pressure and force transducers, and for the accelerometer, a signal conditioner of type 480C02 from *PCB Piezotronics* is used. It is important to mention that this signal conditioner also exhibits charge leakage throughout time. The discharge time constant which characterizes this conditioner is close to, but larger than 7 s [22]. This has important implications on the DTC of the complete measurement chain. It is known that in the data acquisition sequence it is the instrument with the smallest DTC which determines the DTC of the complete chain [7]. This indicates that for the force sensors, the DTC reduces from a value larger than 2000 s to a value somewhere close to but larger than 7 s. For the pressure sensors of type 102A06 and 102B06, the DTC reduces from a value larger than 50 s to a value ≥ 7 s. For the other pressure sensors and for the accelerometer, the DTC remains unchanged since the DTC for these sensors themselves is smaller than 7 s. The use of the signal conditioner of type 480C02 thus restricts the measurements to purely dynamic phenomena. However, this presents no problems for the highly dynamic slamming experiments performed in the present dissertation. Figure 3-17 shows a photograph of the used conditioner.

Figure 3-17: Photograph of the signal conditioner of type 480C02 from *PCB Piezotronics* [22]

For the position encoder, it is the counter (see Figure 3-12 (b)) which provides the sensor with the appropriate power and which amplifies the output signal.

For the four aforementioned sensor types, the conditioned signals are subsequently read out by one of the two types of data acquisition systems which are used in this thesis, i.e. the Genesis Gen5i. This is a portable all-in-one multichannel oscilloscope, data acquisition system and industrial computer which can be

considered as the state of the art in its domain. The system can obtain data at a frequency up to 100 MHz, and all channels are electrically insulated from each other to prevent crosstalk. Crosstalk is the phenomenon where the signal input channels are mutually affected by each other, due to a lack of electrical insulation. The Genesis Gen5i is depicted in Figure 3-18.

Figure 3-18: The Genesis Gen5i portable data acquisition system

Internally in the Genesis oscilloscope, a trigger goes off when the position signal crosses the zero level, i.e. when the test object touches the water surface. This trigger starts the recording of the four types of transducers connected to this system and is simultaneously sent to the second data acquisition system used, i.e. the National Instruments C-DAQ data acquisition system. A small pretrigger is used in order to enable also the acquisition of the recordings in a small time span before the first contact of the test objects with the water.

This second type of data acquisition system is used to acquire the strain gauge signals. It consists of a main C-DAQ chassis in which specific modules can be plugged. For the tests performed in this work, two types of modules are used: the general purpose module NI 9215 and the strain gauge module NI 9237. The general purpose module is used to acquire the trigger signal. Internally in the C-DAQ, which is controlled by the software LABVIEW, this trigger signal starts the acquisition of the strain gauges by the strain gauge module. Besides operating as a data acquisition system, this latter module also serves as the signal conditioner for the strain gauges since it acts as voltage supply and amplifier for these gauges. However, the voltage signal which is acquired by the strain gauge module does not come directly from the strain gauge sensors, but from the bridge completion kits NI 9945 which are necessary to complete the quarter Wheatstone bridges for each strain gauge. The absence of this bridge completion in the Genesis oscilloscope is the reason why another acquisition system was necessary to acquire the strain gauges signals. The NI C-DAQ system is shown in Figure 3-19.

The trigger, which has been generated by the Gen5i oscilloscope and which is sent to the NI C-DAQ has also been sent to the high speed camera and the PIV system to

start the recordings of these instruments. This trigger system thus causes all the instruments to be started simultaneously so that the different types of recordings can be compared with each other on the same time basis. Especially for fast occurring phenomena such as slamming, the trigger has a crucial role for the correct interpretation of the different measured signals. In the experiments of this thesis, also a pretrigger recording has been set up, which means that a part of the complete recording is situated before the trigger event. As such, the slamming stage just before impact can also be studied in detail.

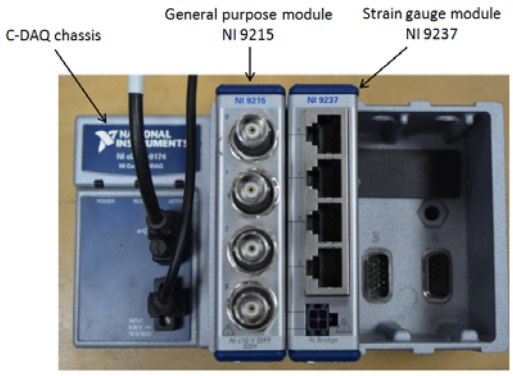

Figure 3-19: The NI C-DAQ data acquisition system

Finally, it must be mentioned that a delay is present within this data acquisition process. The biggest delay can be found between the moment that the Genesis Gen5i internally triggers and the moment that a trigger out signal is sent towards the C-DAQ, the camera and the PIV system. This delay will be taken into account during the experiments in order to enable the synchronisation of the measurements.

3. 4. Test objects

As was mentioned in chapter 1, two types of test objects were chosen which are easily available in both rigid and deformable condition, i.e. cylinders and circular flat plates. The following sections give an overview of the used test objects.

3. 4. 1. Cylindrical test objects

The horizontal cylindrical test objects are the first test objects which will be examined in this dissertation since it is expected that no air cushion will occur during the slamming experiments with these test objects. Hence, the impact pressures and impact forces purely related to hydrodynamic impact can be measured and the effect of the deformability of the cylindrical models on these hydrodynamic loads can be investigated.

3. 4. 1. 1. Rigid cylindrical test models

3. 4. 1. 1. a. The stiffened cylinder

The first cylindrical test model was developed for measuring simultaneously slamming pressures and forces. It consists of a hollow tube made of polyvinylchloride (PVC) with steel frameworks inserted inside the tube to enhance the rigidity of the object. Figure 3-20 illustrates the geometry of these inserts. The steel inserts are connected with a central axis which is suspended on a U-shaped stiffened beam to connect the cylinder with the load cell combination. The cylinder including the U-shaped beam weighs 10 kg. The complete impactor with the cylinder as test model is shown in Figure 3-21.

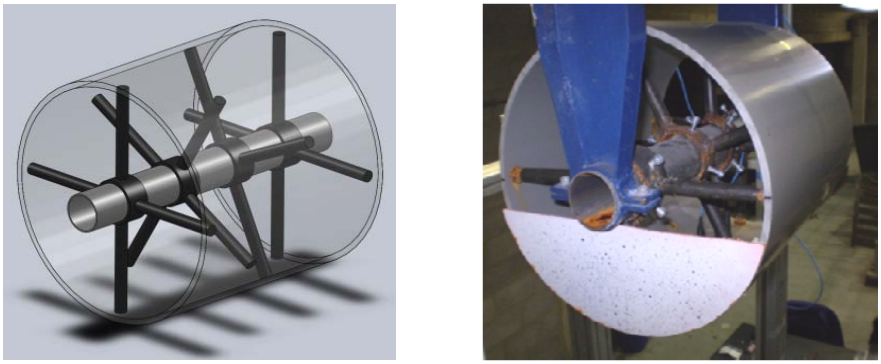

Figure 3-20: The stiffened cylindrical test object

Figure 3-21: The complete impactor including the stiffened cylindrical test object

The dimensions of the cylinder are chosen according to the dimensions of the experimental setup and the availability of the material, namely a length of 350 mm, an external diameter of 315 mm and a wall thickness of 6.2 mm. The space inside the tube enabled the mounting of pressure sensors in the cylindrical wall. Two

pressure sensors are placed in parallel on the same meridian of the cylinder in order to have two simultaneous measurements. One sensor is placed exactly in the middle of the cylinder's length, while the other one is placed 8 cm from the side. Pressure measurements at different positions on the circumference of the cylinder are possible by rotating the whole cylindrical tube including the mounted pressure sensors around its central axis over the desired angle, as shown in Figure 3-22.

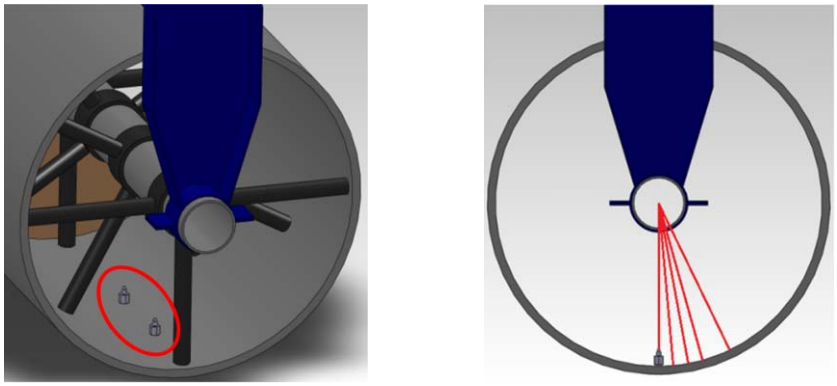

Figure 3-22: CAD drawing showing the position of the pressure sensors and the tested angles

3. 4. 1. 1. b. Concrete and plaster cylinder

In order to have impact load measurements also on solid rigid cylinders, two types of rigid cylindrical test models were developed: a concrete and a plaster cylindrical segment. Figure 3-23 depicts these test specimens.

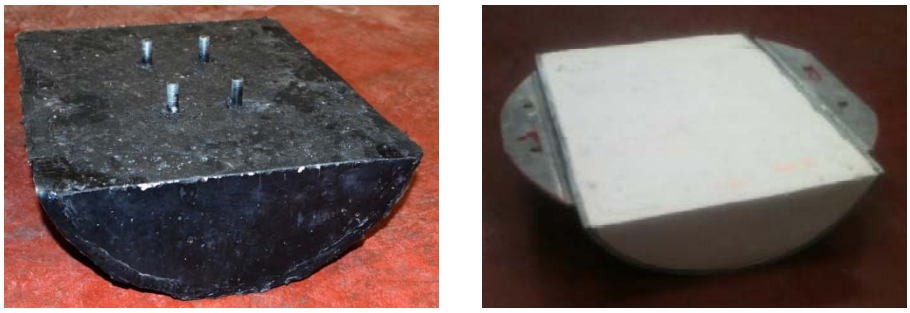

(a) (b)

Figure 3-23: (a) the concrete cylindrical test object and (b) the plaster one

The cylinder segments are respectively 11.4 cm and 12.2 cm high and weigh 19 kg and 10 kg respectively. The outer diameter of the cylindrical segments is the same as the outer diameter of the stiffened cylinder mentioned before (315 mm).

The cylindrical segments are connected with their flat side to the bottom Aluminium plate of the load cell combination. Potential gaps between the latter two entities due to irregularities in the flat surface of the cylindrical segments are eliminated by filling them with extra plaster material in order to distribute the impact load evenly over the complete contact area.

Finally, due to space restrictions, pressure sensors could not be mounted and hence no pressure measurements are performed for these test objects.

3. 4. 1. 2. Deformable cylindrical test models

Several types of deformable cylindrical test objects are used in order to find a relation between the degree of deformability and the magnitude of the loads acting upon a horizontal cylinder during vertical water entry. The deformability has been varied by changing the material, the wall thickness and the diameter of the hollow cylindrical test models. Table 3-7 gives an overview of the examined cylinders. This table does not list the material properties of the used cylindrical test objects, since they were not provided by the manufacturers. They will be experimentally obtained in chapter 5.

Table 3-7: Overview of the properties of the deformable cylindrical test objects

Cylinder	Material	d [mm]	Diameter D [cm]	Length L [cm]	M [kg]
C1	PVC	9.4	31.5	35	4.25
C2	PVC	6.6	31.5	35	3
C3	PVC	2.95	31.5	35	1.15
C4	GFRP	3.325	32.17	39	2.24
C5	GFRP	1.85	31.87	40	1.12
C6	GFRP	1.2	31.74	35	0.38
C7	PVC	4.7	9	35	0.62
C8	PVC	3.15	9	35	0.42
C9	PVC	1.5	8.9	35	0.30
C10	PE	5.83	9	35	0.51
C11	PE	3.3	9	35	0.21
C12	PP	3.1	9	35	0.276

The following notations are hereby used:

- PVC = Polyvinylchloride
- GFRP = Glass fibre reinforced plastics

- PE = Polyethylene
- PP = Polypropylene

The three glass fibre reinforced composite cylinders are manufactured by filament winding using the winding machine of the Department of Material Science and Engineering at Ghent University. Filament winding is a composite production technique which is a very successful technique for making axisymmetric composite objects (e.g. composite pressure vessels, fuel tanks, pipelines) [23]. It typically consists of a rotating mandrel on which a fibre impregnated with resin is wound according to a specific winding pattern [24]. The filament winding process is schematically illustrated in Figure 3-24.

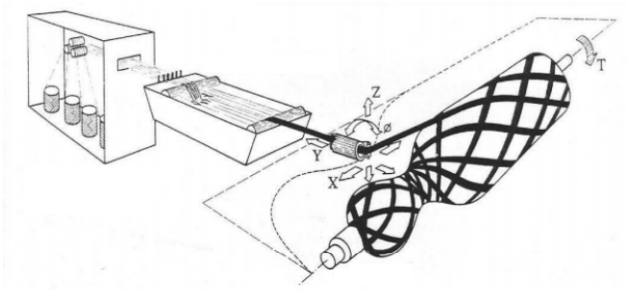

Figure 3-24: Schematic illustration of the filament winding process

The deformable cylinders which are produced with this machine are wound by using a helical winding. With this type of winding, the mandrel rotates at a constant speed while the fibre feed carriage transverses back and forth at a speed regulated to generate the desired helical angles. For the manufactured cylinders in this dissertation, the machine was tuned to produce a helical angle of +89°/-89°, in order to obtain a maximum strength in the hoop direction. The used mandrel was a PVC tube similar to one of the PVC test cylinders. This explains why the diameter of the composite cylinders is slightly larger than the diameter of the PVC cylindrical test models.

The flexible cylindrical test models are directly connected with the bottom plate load cell combination by using three bolts on the same meridian. Figure 3-25 shows a photograph of the impactor with the GFRP cylinder C4.

The deformations of the flexible cylinders are measured by two strain gauges which are directed in the hoop direction. For the large cylinders ($D \geq 31.5$), one strain gauge is installed at the bottom of the cylinder while the other one is mounted at the side (90° angular shift with respect to the bottom strain gauge). For the small cylinders, both strain gauges are mounted at the side (one on each side).

Figure 3-25: The impactor containing the GFRP cylinder with D = 32.17 cm and d = 3.325 mm

Finally, no pressure measurements were performed during the experiments with the deformable cylinders. This is due to the fact that the holes necessary for mounting the pressure sensors would largely affect the deformation of the cylinders. Moreover, some of the cylinders were too thin to guarantee a firm fixture of the pressure transducers.

3. 4. 2. Flat plates

Circular flat plates were chosen as the second type of test objects to be investigated, since these models are also easy available in both rigid and deformable condition. The next sections describe the used flat plate test models.

3. 4. 2. 1. Rigid flat plates

3. 4. 2. 1. a. Bottom impactor plate

It has been shown in section 3.2.2 that the circular Aluminium impactor plates from the load cell combination exhibit a large flexural stiffness K. It can consequently be considered as a quasi-rigid plate. Hence, the bottom impactor plate has been used as a test object in the current test series. However, since the plate's surface was quite rough containing periodic ribbles from the production process, a smooth and undisturbed PVC circular plate of 8 mm thickness was glued to the bottom Aluminium plate to make it one combined rigid and smooth test object. It made the test object even more rigid. The mass of this combined rigid flat plate model is 6.4 kg. A photograph and a schematic section view of the impactor in this configuration are given by Figure 3-26 and Figure 3-27 respectively.

Figure 3-26: Photograph of the impactor plate combined with a PVC plate as being a rigid flat plate test object

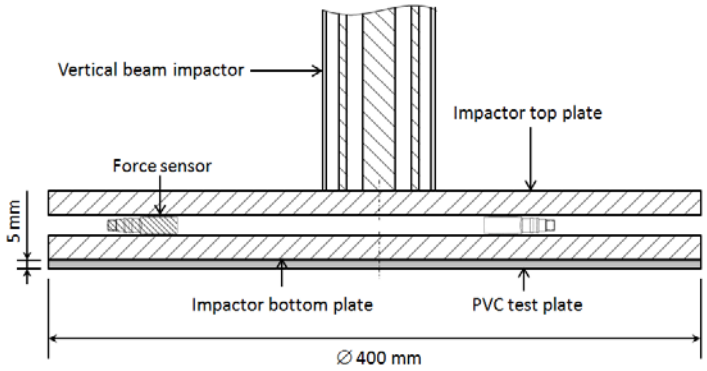

Figure 3-27: Schematic section view on the impactor plate combined with a PVC plate as being a rigid flat plate test object

3. 4. 2. 1. b. Sandwich panel

It was very difficult to install pressure sensors in the previous test object. Hence, no pressure measurements were performed on this model. In order to enable pressure measurements during the water impact of a rigid plate, another flat plate test model was developed. It consists of a circular sandwich panel of type HD60 from the company *Acrosoma* [25] which is glued to a support ring of the same material. The sandwich material has a thickness of 30 mm and contains a foam inner core of 28 mm thick which is at both sides covered with a 1 mm thick layer of aramide fibre reinforced composite. Its mass and that of the ring is 2.24 kg. Figure 3-28 depicts a schematic section view of the impactor with the sandwich panel as the test plate.

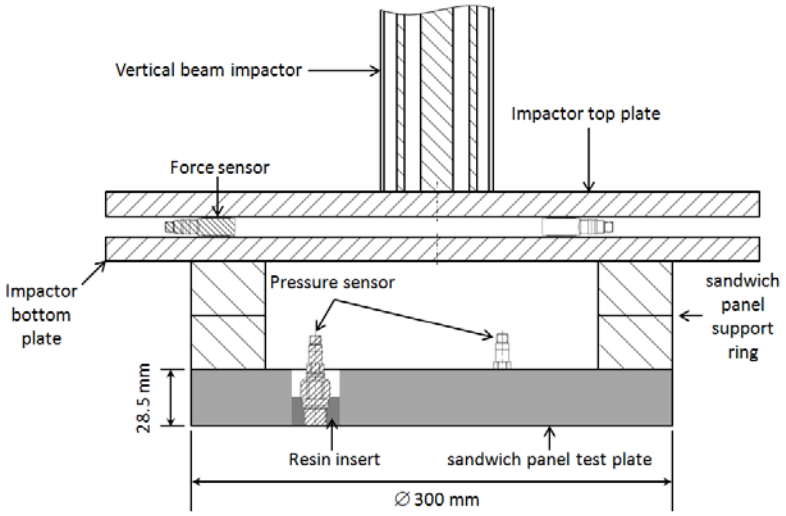

Figure 3-28: Schematic section view on the impactor with the sandwich test panel

The advantage of using a sandwich panel as a rigid plate test model is that it has a large flexural stiffness for a limited weight. An average E-modulus of 29 GPa has been reported in the technical sheet [25] (30 GPa in the weft direction and 28 GPa in the warp direction). This results in a bending stiffness K of at least 65250 Pa.m^3, when a zero Poisson's ratio has been taken into account (no information on the Poisson's ratio is available). This value is even larger than the flexural stiffness of the bottom impactor plate. Hence, this plate is considered a suitable test model within the current test series.

However, it has to be mentioned that the stiffness of the sandwich panel in the thickness direction is more than 36 times smaller than the E-modulus in the directions in the plane of the plate (E_{33} = 800 MPa). Contrary to the previous flat plate test object, this makes that also deformations through the plate thickness might play a role. Energy absorption during slamming impact due to a compression of the plate thickness should therefore be considered. Though, it is assumed that this effect is limited when considering that for a plate of 30 cm diameter a force of 188 kN is necessary for compressing the plate's thickness with 0.1 mm according to the modulus E_{33}.

Finally, by using the support ring, space was generated above the plate to enable the pressure sensors to be mounted into the test plate. Resin inserts were casted into the plate to mount the pressure transducers. Three pressure sensors were provided at a radius of 100 mm from the centre of the plate, and at an angle of 120° from each

other. A photograph of the test plate including the three pressure sensors is depicted in Figure 3-29.

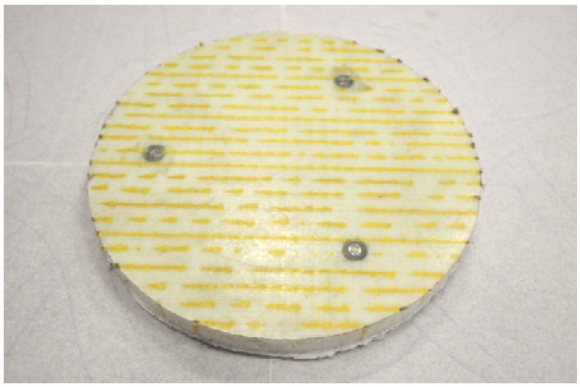

Figure 3-29: Sandwich panel test plate with the pressure sensors installed

3. 4. 2. 2. Deformable plates

Several circular deformable plates were tested. The deformability of the plates was varied by changing the material and the thickness of the plates, and thus by varying the flexural stiffness K (see Equation (3.1)). An overview of the tested plates is given in Table 3-8.

Table 3-8: Overview of the properties of the deformable plate test objects

Plate	Material	d [mm]	Radius R [cm]	E [Gpa]	ν [-]	K [Pa.m^3]	m [kg]
P1	Steel	5	15.75	210	0.3	2174.91	3.08
P2	Steel	1.97	15.75	210	0.3	133.03	1.28
P3	Steel	1	15.75	210	0.3	17.4	0.70
P4	Aluminium	1.02	15.75	70	0.3	6.8	0.29
P5	Ertalon	5.1	16	3.3	0.405	43.64	0.79
P6	Ertalon	2.1	16	3.3	0.405	3.05	0.27
P7	Ertalon	1.1	16	3.3	0.405	0.44	0.17

The test configuration for the deformable plates is based upon the one which is used for the experiments with the sandwich panel. It is schematically illustrated in Figure 3-30. To match the dimensions of the deformable plates, the support ring is now replaced by a very stiff steel support ring with a diameter of 32.3 cm, a wall thickness of 1.2 cm and a height of 6.2 cm. The weight is 5.4 kg. During testing, the

considered plates are positioned against that ring. They are not fixed nor glued to the ring to allow the plates to deform freely under the slamming loads without any resistance. A simply supported boundary condition is thus created. However, measures should be taken to prevent the plates from loosing contact with the ring due to gravity before they touch the water. Therefore, small ring connectors are fixed to the top surface of the deformable plates which are pulled up by nylon wires under little tension. These nylon wires are fixed with bolts at the impactor top plate as shown in Figure 3-30. It is assumed that these wires and the ring connectors do not affect the deformation of the plates.

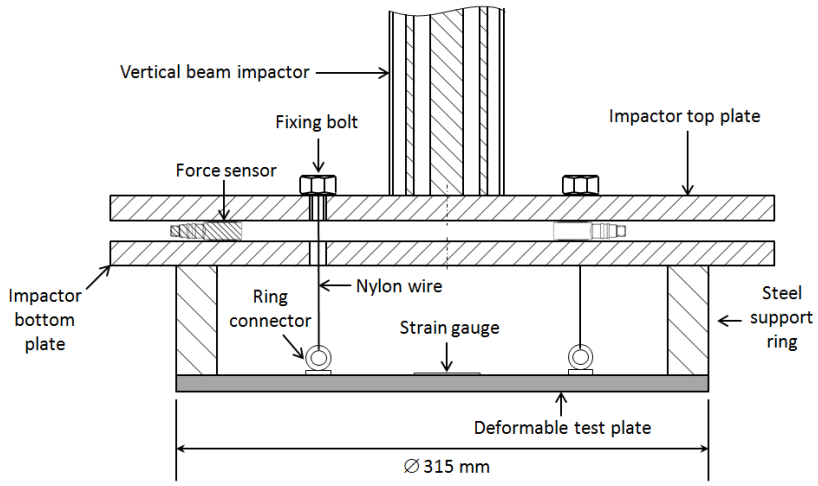

Figure 3-30: Schematic section view on the impactor configuration for the circular deformable plates

The deformation of the plates during the slamming experiments is measured by four strain gauges on each plate. Two gauges are placed near the plates' centre perpendicularly oriented to each other, and the two others are mounted in the same configuration at a radius of 13 cm from the centre. As such, the radial and tangential strains are measured on two locations of the plate. The strain recordings give information on the local stresses occurring in the plate material which can be correlated with the measured global impact forces. A photograph of the strain gauges installed on plate P7 is depicted in Figure 3-31.

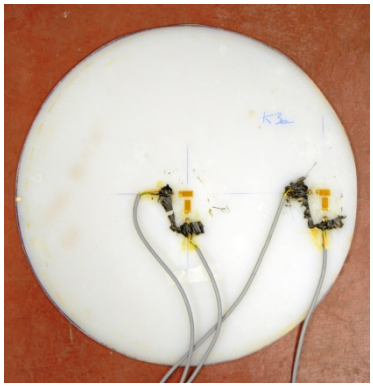

Figure 3-31: The plate P7 with the strain gauges installed

Similarly to the deformable cylindrical test objects, pressure sensors could not be mounted into the deformable flat plates since it was not possible to obtain a firm fixture of these sensors into some of the plates and since the sensors themselves could affect the deformation of the plates. Hence, no impact pressures were recorded for the test objects considered in this section.

3. 5. Conclusions

The present chapter gives a complete overview of the experimental test setup used in this thesis. State-of-the-art equipment has been used which is carefully selected to meet the requirements characteristic for highly dynamic experiments. Selecting the appropriate instrumentation is the first important step in an experimental research programme since it determines the accurateness of the experimental results.

Finally, this chapter also presents the different test objects which have been used during the experiments. A variety of deformability degrees have been applied for the cylinders as well as for the flat plate test objects in order to precisely investigate the effect of the flexibility on the slamming loads corresponding with these object types in particular, and with all types of constructions in general

3. 6. References

[1] G. De Backer, "Hydrodynamic design optimization of wave energy convertors consisting of heaving point absorbers," *PhD dissertation, Ghent University, Department of Ocean Engineering,* 2009.

[2] G. De Backer, M. Vantorre, C. Beels, J. De Pré, S. Victor, J. De Rouck*, et al.*, "Experimental investigation of water impact on axisymmetric bodies," *Applied Ocean Research,* vol. 31, pp. 143-156, 2009.

[3] G. De Backer, M. Vantorre, J. De Pré, J. De Rouck, P. Troch, C. Beels*, et al.*, "Experimental study of bottom slamming on point absorbers using drop

tests," in *International Conference on the Application of Physical Modelling to Port and Coastal Protection*, Bari, Italy, 2008.

[4] J. Depré, "Experimenteel onderzoek naar slammingsverschijnselen bij point absorbers," *Master thesis, Ghent University, Department of Coastal Engineering,* 2008.

[5] S. Victor, "Study of the slamming phenomena occurring on point absorbers: experiments and literature review," *Master thesis, Ghent University, Department of Coastal Engineering,* vol. Master in civil engineering, 2007.

[6] PCB Piezotronics. (2013). *General Piezoelectric theory and specific information on piezoelectric pressure sensors*. Available: http://www.pcb.com/techsupport/tech_gen.php and http://www.pcb.com/techsupport/tech_pres.php at 15/02/2014

[7] PCB Piezotronics. *Introduction to piezoelectric sensors*. Available: http://www.pcb.com/techsupport/tech_force.php at 15/02/2014

[8] PCB Piezotronics, "Operating manuals dynamic pressure sensors 102A06, 102B06, 102A07, 102A08."

[9] PCB Piezotronics, *Operating manual dynamic force sensor 201B05*.

[10] O. Faltinsen, J. Kvålsvold, and J. Aarsnes, "Wave impact on a horizontal elastic plate," *Journal of Marine Science and Technology,* vol. 2, pp. 87-100, 1997.

[11] F. J. Huera-Huarte, D. Jeon, and M. Gharib, "Experimental investigation of water slamming loads on panels," *Ocean Engineering,* vol. 38, pp. 1347-1355, Aug 2011.

[12] P. Verleysen, "Mechanica van werktuigkundige constructies," *Master course, Ghent University*.

[13] Kistler, "Operating manual dynamic accelerometer 8704B500."

[14] Kuebler, "Operating manual Kuebler position encoder Limes LI20/B1 and LED counter 572."

[15] Vishay, "Errors due to Wheatstone Bridge Nonlinearity," *Tech Note TN-507-1*.

[16] Vishay, "Strain Gauge Selection: Criteria, Procedures, Recommendations.," *Tech Note TN-505-4*.

[17] Vishay, "Precision Strain Gauges: Interactive Data Book."

[18] Photron, "Operating manual high speed camera APX-RS."

[19] S. Palanivelu, S. De Pauw, W. Van Paepegem, J. Degrieck, J. Van Ackeren, D. Kakogiannis*, et al.*, "Validation of digital image correlation technique for impact loading applications," vol. 1, pp. 373-379, 2009.

[20] P. Lava, "MatchID - Image Correlation & Material Identification," ed. Gent: Catholic University College Ghent, department of Mechanical Engineering, 2012.

[21] A. Nila, "An adaptive PIV method for estimating slamming loads," *PhD dissertation, VUB Brussels, under progress,* 2013.

[22] PCB Piezotronics, "Operating manual signal conditioner 480C02."

[23] M. S. Babu and G. Srikanth. (2000). *Composite fabrication by filament winding, an insight*. Available: www.tifac.org.in at 15/02/2014

[24] F. H. Abdalla, S. A. Mutasher, Y. A. Khalid, S. M. Sapuan, A. M. S. Hamouda, B. B. Sahari*, et al.*, "Design and fabrication of low cost filament winding machine," *Materials & Design,* vol. 28, pp. 234-239, // 2007.

[25] Acrosoma, "Technical sheet for the Acrosoma HD-60 sandwich panel," 2013.

Chapter 4

Validation and calibration of the experimental instrumentation

Overview

Chapter 4 deals with a thorough investigation of the correctness, accuracy and interpretation of the instrumentation used in this thesis. It starts with a description of the motivation for dedicating a separate chapter to this study. Next, the dynamic pressure and force measurements are examined in detail and test procedures for measuring accurate and reproducible dynamic slamming pressures and forces are developed. Furthermore, some calibration methods are presented for both types of instruments. In the second part of this chapter, the recordings from the accelerometer, the position encoder and the DIC technique are investigated and the method for obtaining the impact velocity is explained. A validation of these latter three sensor types is achieved by comparing the acceleration, velocity and position signals obtained from each of these sensors with each other.

4. 1. Background

Preliminary slamming experiments during the early stages of this research resulted in extremely large scatter in the impact force and pressure measurements and revealed some particular load evolutions, e.g. extremely large positive pressures

which last for several seconds, and non-zero forces which are present before the moment of water impact. Instead of these types of load histories, only one single slamming pressure or force peak with short duration was expected. In the initial stage of this research, no physical explanations could be related to these peculiar phenomena, and a more detailed investigation was needed.

The problem regarding the large scatter in the impact load results can be translated into the problem of limited reproducibility of the slamming experiments. Reproducibility and repeatability of experimental data has been a challenge for decades in all types of testing. Several studies already investigated relevant aspects concerning this topic. These studies are known under the name gauge repeatability and reproducibility studies (GR&R) [1-4]. In these studies, repeatability is defined as the ability of the same gauge to give consistent measurement readings no matter how many times the same operator of the gauge repeats the measurement process. Reproducibility is described as the ability of the same gauge to give consistent measurement readings regardless of who performs the measurements [1, 3].

Large scatter in the slamming load measurements were already reported in some earlier publications. Lin and Shieh [5] presented pressure measurements during vertical drop experiments of rigid horizontal cylinders and reported large scatter in the maximum pressure values. The scatter was observed to be larger for pressure recordings at small deadrise angles, which was also the case for the initial experiments performed in this dissertation.

It was the question whether the large scatter and the particular load histories are inherent to the physics of the complete system, or whether they are caused by a misuse and corresponding misinterpretation of the instrumentation.

In order to find out the answer, an assessment was started to find all instrumental and environmental parameters which could influence the pressure and force measurements and to have a better view on the complete physics of the dropping impactor. By identifying the parameters which could have an effect on the slamming load measurements, a test procedure for performing correct, accurate and reproducible pressure and force recordings could be developed. In this way, the proper working of the pressure and force transducers could be validated. According to the authors' knowledge, no other publication is available in the open literature which performs such a study.

A similar validation is also necessary for the other instrumentation, i.e. the accelerometer, the position encoder and the DIC technique. For these latter instruments, the validation is realized by comparing the instrument outputs in terms

of position, velocity and acceleration with each other. This has been done in the second part of this chapter.

4. 2. Dynamic pressure measurements

4. 2. 1. Parameters affecting the impact pressure measurements

The identification of the parameters which can affect the local slamming pressure recordings is presented in the present section by using the initial slamming experiments done in this thesis. In order to exclude the air cushion effect, which certainly has an influence on the pressure measurement but which is inherent to the slamming process, the current study is focused on the slamming of a horizontal cylinder, i.e. the stiffened cylinder described in section 3.4.1.1.a.

4. 2. 1. 1. The data sampling frequency

During the initial slamming tests performed in this work, it has been observed that the slamming pressure pulses travel very fast over the surface of the object penetrating the water. The pressure peak duration at a fixed point of the object surface only lasts for a time in the order of a few milliseconds or even shorter. This is especially the case for locations characterized by small deadrise angles. Therefore, it is necessary to use a sufficiently large sampling rate of the data acquisition system in order to measure the real pressure peak value. If the selected sampling rate is too small, the recorded peak values may vary since the true pressure peak is situated between two sampling points, as is visualized in Figure 4-1(a) and (b).

The minimum deviation is zero bar, and takes place when one of the samples just corresponds with the maximum in the pressure history (see Figure 4-1(c)). The maximum deviation between the measured and the true pressure peak value occurs when two data points are situated at either side of this true maximum having the same pressure value (see Figure 4-1(a)). The peak of the recorded signal then exists of two data points of equal amplitude. When using an insufficient sampling rate, the deviation between the measured maximum and true maximum will vary between the latter two extreme cases, introducing scatter in the measurement results.

Figure 4-2 depicts the pressure history recorded during a slamming test of the stiffened cylinder for a drop height of 0.7 m and the pressure sensor placed at the bottom of the cylinder. In this experiment, a sampling rate of 100 MHz was used and it is clear that more than enough data points cover the top of the pressure peak to be sure of the peak value. This makes a data sampling rate of 100 MHz more than sufficient.

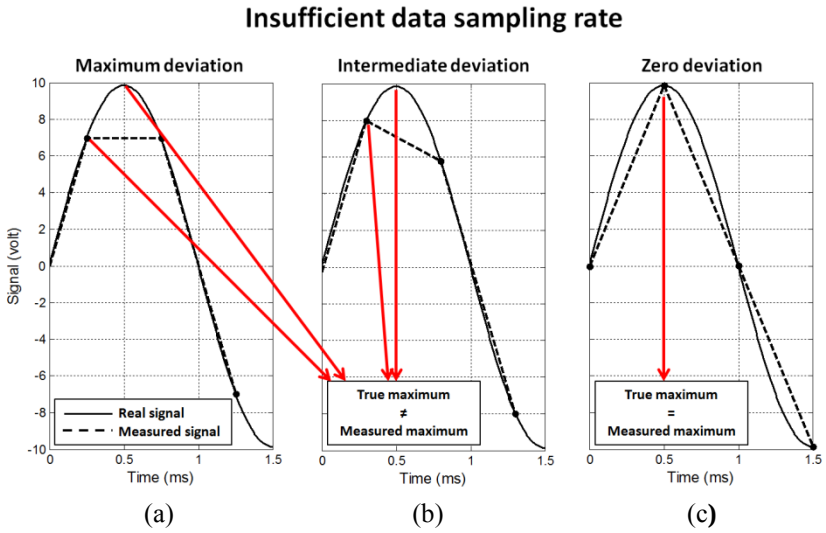

Figure 4-1: Insufficient data sampling rate causing scatter in the slamming pressure measurements

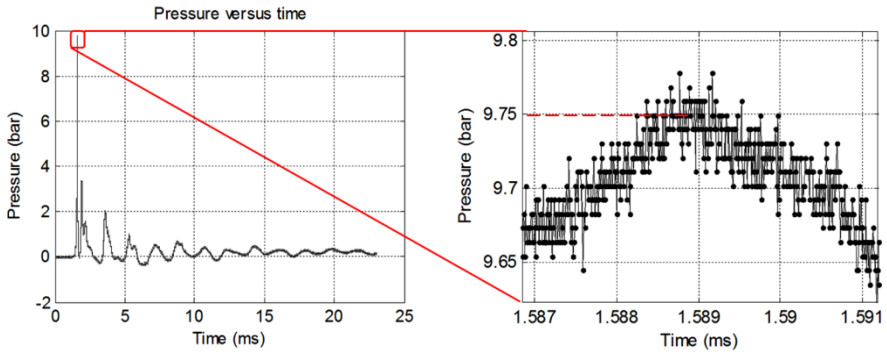

Figure 4-2: Pressure history at the bottom of the stiffened cylinder at a drop height of 0.70 m, measured at 100 MHz sampling rate

Repalle et al. [6] already recognized the effect of the sampling rate on measured slamming pressures. However, his study was focused on water impact caused by sloshing. The sloshing event is highly stochastic and the impact pressure varies significantly even for a simple harmonic excitation in one direction. The measured pressure peaks varied between 13 kPa and 100 kPa, which are significantly smaller than the pressure peaks inherent to bottom slamming, as can be observed from Figure 4-2, where a drop height of only 0.7 m causes pressure peaks of almost 10 bar at the bottom of a slamming cylinder. The duration of the pressure pulses in [6] was also much longer than as measured in Figure 4-2. This allowed the use of a smaller sampling rate. Repalle et al. [6] concluded from a series of experiments that

a sampling rate of 40 kHz was sufficient to capture the sloshing pressure peaks accurately. However, strange observations were made at higher sampling rates. Experiments performed at 100 kHz showed impact pressures being 10-15% smaller than those measured at 40 kHz and 60 kHz, which is quite unexpected if one assumes the same physical conditions with consequently the same pressure pulses. The dynamic response of the sensor used was assumed to be the reason for this phenomenon, as stated by Repalle et al [6]. In the present work, this problem has been excluded by selecting pressure sensors with sufficiently large frequency ranges (resonance frequencies ≥ 250 kHz, see section 3.2.1).

In the following discussion, a minimum threshold value of the sampling rate will be determined for the bottom slamming case, which will be further used in this dissertation in order to accurately capture the true pressure peak values. This threshold has been determined by taking a 1% limit for the deviation between the measured and real pressure peak value. Furthermore, the maximum deviations which correspond with two data points of equal amplitude at either side of the true maximum will be considered in this analysis to illustrate the worst case scenario.

Each graph of Figure 4-3 and each line of Table 4-1 shows the slamming pressure peak which is measured at the bottom of the stiffened cylinder for a drop height of 0.7 m, as was already depicted in Figure 4-2. In the consecutive graphs of Figure 4-3, this pressure peak is presented with another sampling rate, achieved by resampling the original signal using a Matlab routine. The sampling time has been selected in this way that the top of the pressure pulses consists of two samples of the equal magnitude. In the successive graphs, resampling rates of 400 kHz, 300 kHz, 200 kHz, 100 kHz, 25 kHz and 16 kHz are used. It can be seen that for a sampling rate below 300 kHz, the deviation between the measured and the true pressure peak value is larger than 1% and the pressure curve loses its smoothness. Further experiments showed analogue phenomena for other drop heights corresponding to impact speeds up to 5 m/s. Hence it can be concluded that, especially for small deadrise angles, for impact speeds up to 5 m/s, a sampling rate of at least 300 kHz should be used in order to obtain correct and reproducible pressure measurements.

In normal sea conditions, wave celerities up to 5 m/s are quite common [7]. Previous analysis thus indicates that slamming pressure measurements at sea in normal conditions should thus also be performed with a minimum sampling frequency of 300 kHz. For larger wave celerities which can occur in storm conditions, larger data sampling rates might become necessary.

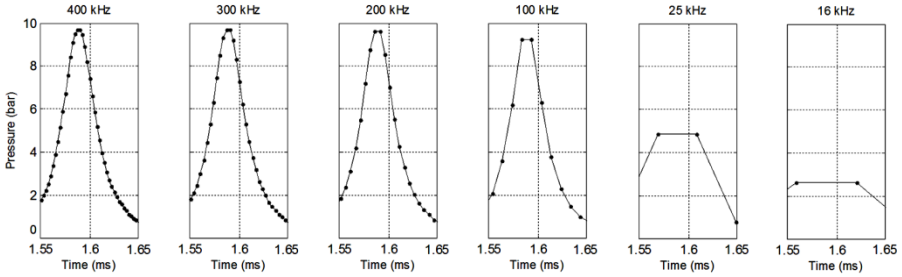

Figure 4-3: Slamming pressure peak at the bottom of the stiffened cylinder at a drop height of 0.7 m, resampled at 400 kHz (a), 300 kHz (b), 200 kHz (c), 100 kHz (d), 25 kHz (e) and 16 kHz (f)

Table 4-1: Slamming pressure peak value at the bottom of the quasi-rigid cylinder at a drop height of 0.7 m for several sampling rates, and the corresponding deviation with the true pressure peak

Sampling rate [Hz]	Pressure peak value [bar]	Deviation with respect to true pressure peak value [%]
100 MHz	9.75	0
400 kHz	9.70	0.51
300 kHz	9.68	0.72
200 kHz	9.63	1.23
100 kHz	9.23	5.33
25 kHz	4.87	50.05
16 kHz	2.61	73.23

Two publications are available in the literature dealing with vertical drop experiments of rigid horizontal cylinders which report the used data sampling rate. Lin and Shieh [5] performed slamming drop experiments on cylinders with a diameter of 200 mm and 300 mm and impact speeds up to 1.98 m/s. Pressure measurements were done at 30°, 15°, 7.5° and 0° deadrise angle. They report a data sampling rate of 25 kHz during the pressure recordings, which is much smaller than the suggested minimum sampling frequency of 300 kHz. Analogue experiments were performed by Colicchio et al. [8], who used a stainless steel ring with a diameter of 300 mm to investigate the loads acting on it during water-entry and exit. Only one impact velocity was tested (2.55 m/s), and no statistics were reported. A

data sampling rate of 16 kHz was used to measure the pressure peaks. This is even smaller than the sampling rate used by Lin and Shieh [5].

Resampling the slamming pressure peak from Figure 4-2 to the data sampling frequencies used by Lin and Shieh [5] and Colicchio et al. [8], results in the graphs plotted in Figure 4-3 (e) and Figure 4-3 (f) respectively. Only a few data points cover the impact pressure pulses in these cases which makes that the measured impact pressures differ significantly from the true impact pressures. In a worst case, a 50% reduction is found for the data sampling rate used by Lin and Shieh [5] (see Figure 4-3 (e)), which becomes 73% for the case of the sampling rate used by Colicchio [8] (see Figure 4-3 (f)). The fact that each experiment has a different reduction rate between 0% and the maximum reduction rate leads to scatter in a complete test series and a reduction of the global average impact pressure.

This explains the large scatter which is observed by Lin and Shieh [5] for the pressure measurements at the bottom of the horizontal cylinder.

4. 2. 1. 2. Thermal shock

Although a sufficiently large data sampling rate was crucial in the slamming experiments, it did not solve the problem of large scatter in the pressure results and certainly not the problem of the peculiar pressure histories. This was observed from slamming experiments performed with the stiffened cylinder at a data sampling rate of 100 MHz.

The peculiar pressure histories consisted of the pressure drifting away both in the positive and negative direction just after the first slamming pressure peak. Only after several seconds the pressure returned to the initial zero level. These singularities were not consistent and varied from time to time. Figure 4-4 shows an experiment with the stiffened cylinder dropped from 0.25 m where a pressure increase is observed after the first slamming pulse which reaches a pressure value of about 8 times higher than the slamming pressure itself, and which lasts for more than 7 seconds after the impact of the cylinder on the water. No physical phenomenon could be related to these types of pressure profiles. Hence, it was assumed that the origin of the unexpected phenomenon was inherent to the pressure transducers and had no external cause.

After a coincidental drop of a pressure transducer into cold water, it became clear that a temperature difference between the sensor and the water, causing a thermal shock in the pressure sensor at the moment of water entry, was related with these peculiar pressure profiles. It was observed that when submerging a sensor adjusted to room temperature gently into colder water, the pressure increased although no

physical load was applied to the sensor diaphragm. Figure 4-5 (a) illustrates this event in the case of the water being 8°C colder than the sensor. The temperature of the sensor was hereby measured with an infrared temperature sensor while the water temperature was measured with an alcohol thermometer. At the other hand, when the sensor at room temperature was submerged into warmer water, it was discovered that a pressure decrease occurred instead of an increase. This last observation is depicted in Figure 4-5 (b) for the water being 13.8°C warmer than the sensor.

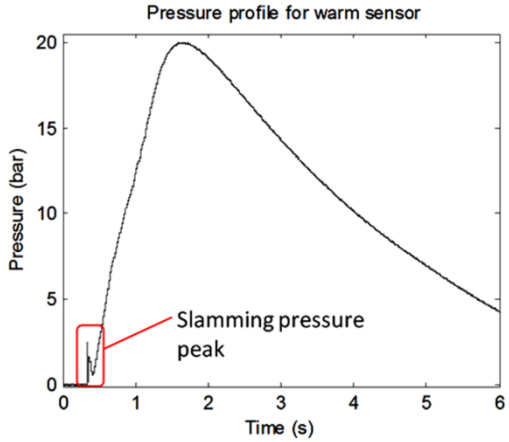

Figure 4-4: Pressure history for a drop impact test with the stiffened cylinder at a drop height of 0.25 m and the pressure sensor at the bottom of the cylinder

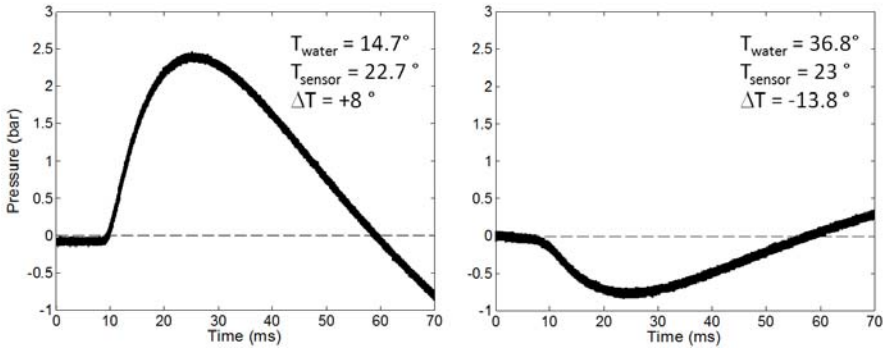

(a) (b)

Figure 4-5: (a) Pressure increase observed when submerging a pressure sensor into colder water; (b) Pressure decrease when submerging a pressure sensor into warmer water

Experiments similar to the ones performed in Figure 4-5 were done for other water temperatures in order to determine the temperature sensitivity of the pressure

transducers. Figure 4-6 presents the evolution of the maxima of the parasitic pressure changes as function of the temperature difference between the sensor and the water. Positive pressure values indicate pressure increases while negative values designate pressure drops. Positive temperature differences indicate a sensor being warmer than the water, while the opposite is applicable for negative values. It can be observed that the pressure is affected even for small temperature differences. However, pressure changes as large as illustrated in Figure 4-4 (20 bar increase) are not encountered in these tests. This indicates that also the rate at which the thermal shock acts plays a role. This means that if the transition from a warm into a cold medium or vice versa occurs more sudden, larger magnitudes of parasitic pressure changes will occur.

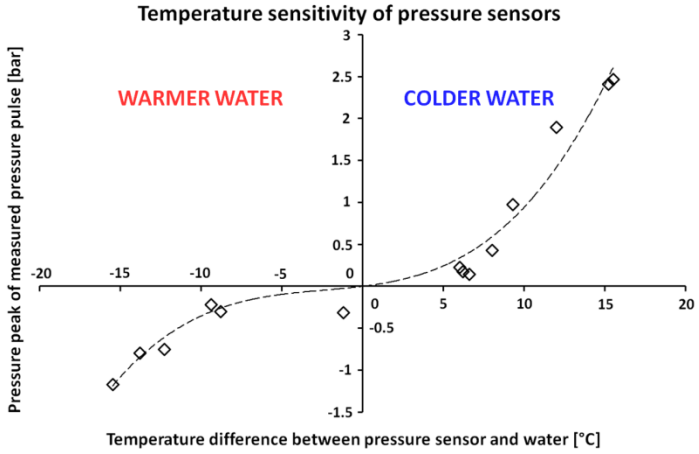

Figure 4-6: The evolution of the parasitic pressure change as function of the temperature difference between the sensor and the water

The effect of a thermal shock on the pressure sensor output can be explained by considering the preloaded state of the piezoelectric crystal in the steel housing of the piezoelectric pressure transducers. Since the thermal expansion coefficient of the crystal is about 20 times smaller than the thermal expansion coefficient of the steel housing (α_{quartz} = 0.59.10^{-6}/°C; α_{steel} = 12.10^{-6}/°C), the steel casing will contract much more than the quartz crystal when the sensor is subjected to a sudden cooling (e.g. by slamming in cold water). As a result, the preload acting on the quartz crystal will increase causing a positive signal output which is interpreted as a positive pressure. On the other hand, if the sensor is suddenly heated, the steel housing will expand more than the quartz crystal, causing a decrease of the preload force on the crystals and a negative signal output. This effect is more pronounced when the rate of the thermal shock increases since the deformations of the crystal and the steel housing relative to each other occur then in a shorter time span. This explains why at

large impact speeds, large pressure changes are observed. This thermal shock effect has not been reported in the manual of the pressure sensors. Moreover, according to the author's best knowledge, no other literature source reports this problem.

Thermal shocks should thus be avoided when using piezoelectric pressure transducers with a preloaded crystal. This can be achieved by adjusting the transducers to the water temperature before performing an experiment in order to eliminate the temperature difference. This technique will thus be applied further on in this thesis.

4. 2. 1. 3. Sensor mounting

With the thermal shocks avoided, no pressure singularities were found anymore after the first slamming peak. However, large scatter in the measured impact pressures was still present.

It is known that the sensor mounting could play an important role here. To test this, three types of experiments were performed: one experiment with the sensor diaphragm as close as possible to the cylindrical surface, and two experiments with the sensors being deliberately mounted out of plane with the cylindrical surface of the stiffened cylindrical test object. In the last two experiments, the sensor diaphragms were placed 1.5 mm inside (Figure 4-7 (a)) or outside (Figure 4-7 (b)) compared to its correct position. The experiments were performed with a drop height of 1 m. With the sensor in its normal position, an average impact pressure of 14.7 bar was measured. With the sensors in the wrong position, this was 6.2 bar and 6.5 bar respectively. This indicates that even small installation deviations with respect to the correct position result in large errors in the pressure measurements. A repeated sensor installation and a lack on special attention on this matter during the initial experiments performed in this thesis can explain the large scatter from the early experiments.

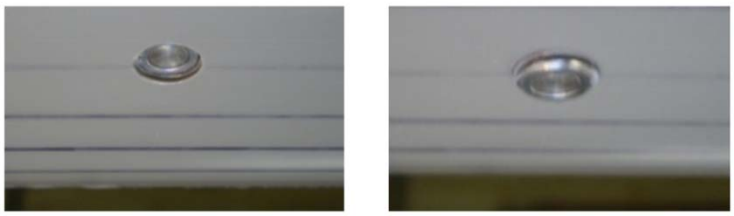

(a) (b)

Figure 4-7: Wrong position of the sensor diaphragm: the diaphragm positioned 1.5 mm inside (a) and 1.5 mm outside (b) the cylindrical surface

A precise and adequate mounting of the sensors in the test object is thus an essential requirement to be capable to perform good and reproducible measurements. Adequate mounting can be achieved by placing the sensors with the diaphragm surfaces as coincident as possible with the body surface. In this case, the flow over the sensor diaphragms will be undisturbed, and flow turbulences and air cavities affecting the pressure load on the sensor diaphragm will be avoided. This type of mounting is called flush mounting and is shown in Figure 4-8 (b).

To verify whether the sensors are flush mounted, a high speed camera can be used which is focused on the sensor diaphragm during the water impact. Water bubbles or turbulences occurring in front of the diaphragm then indicate that the sensor is not flush mounted and that its position should be adjusted.

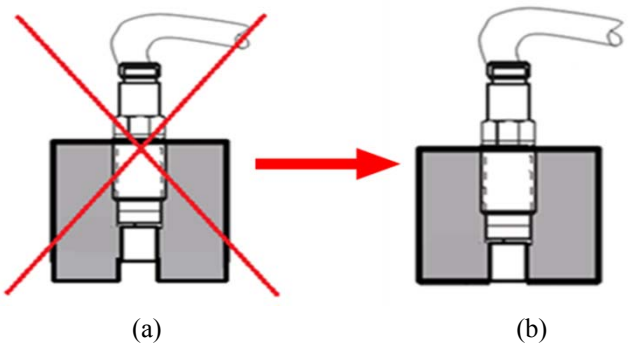

Figure 4-8: (a) Wrong mounting of the pressure sensor due to a gap between the sensor diaphragm and object surface; (b) Flush mounting

4. 2. 1. 4. Object surface conditions

It was observed that after paying precise attention to the flush mounting of the sensors, avoiding thermal shocks and using a sufficiently large sampling rate, the scatter in the measured slamming pressure peaks decreased, but still remained large. The new experiments revealed that the scatter in the pressure results from drop tests which were performed quickly after each other (one or two minutes interval) was larger than for experiments performed with a larger intermediate time interval (close to ten minutes interval or larger). The main difference between these two cases is thus the time span between the successive tests allowing the test object to dry more or less by the water dripping of the test object or by evaporation of the water on the object's surface.

To investigate the effect of a dry and wet object surface condition on the impact pressures, two experiment series were performed. In the first experiment series, tests were done relatively quickly (± two minutes interval) after each other to make sure

that the object surface was wet at water impact. In the second test series, the object was dried before executing the next drop test. Figure 4-9 compares the pressure results for ten consecutive slamming tests with the stiffened cylindrical test object with respectively wet and dry surface conditions at a drop height of 0.7 m. It is clear that the scatter for wet conditions is much larger than in dry conditions and that the average pressure peak in wet conditions is much smaller than in dry conditions. The larger scatter and smaller average in wet conditions can be explained by the presence of water droplets sticking to the sensor diaphragm after each consecutive test. These droplets affect the pressure recordings since the medium between the pressure sensor diaphragm en the water surface just before impact has then changed to water instead of air. Moreover, due to the cohesion force between the water molecules, water from the droplet and the water tank will merge together just before impact causing a softening of the loads acting locally on the cylindrical surface, as illustrated in Figure 4-10.

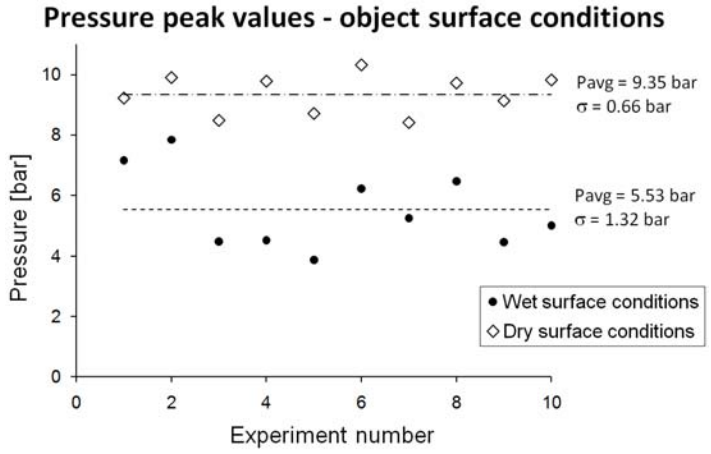

Figure 4-9: Pressure peak values for ten consecutive tests in wet and dry object surface conditions for a drop height of 0.7 m

Since the effect of the water droplets on the pressure will vary from test to test, due to the varying position of the water droplets on the diaphragm, scatter will be introduced. To increase the reproducibility and the correctness of the pressure results, the object surface should thus be dried before each experiment.

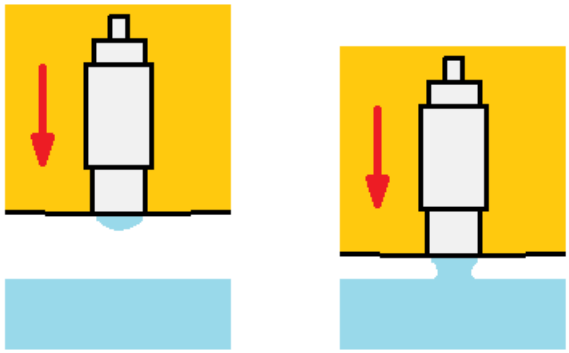

Figure 4-10: Water droplet and water surface merging together causing a softening of the local impact.

4. 2. 1. 5. Water surface conditions

A dry object surface introduced a large improvement in the reproducibility of the experiments. However, now and then large deviations occurred in the measurement results. It was observed that during these aberrant measurements, the water surface of the tank was not completely calm at the moment of impact of the cylinder on the water surface. Small waves or wrinkles on the water surface were present due to droplets falling into the water or accidental vibrations of the water tank. These wrinkles were thus assumed to be the reason for the occasional singularities.

This can be explained by looking into detail what happens if a small wrinkle on the water surface just passes when the cylinder hits the water. Locally, at the interface between the sensor diaphragm and the water surface, a change in deadrise angle is then introduced. This causes large deviations in the impact pressures. Even very small wrinkles reflect in very different pressure results.

Figure 4-11 presents impact pressures at the bottom of the cylinder for ten consecutive tests measured with a slightly deliberately disturbed water surface and a dry object surface, and the results from ten consecutive tests performed at completely calm water surface for a drop height of 0.7 m.

First of all, it can be observed that for the experiments with a deliberately disturbed water surface, the scatter is large and the mean impact pressure is small compared to the pressure measurements from Figure 4-9 with a dry object, but no attention paid to the presence of small wrinkles on the water surface. Though, the experimental conditions are the same. The reason for this is that the deliberately introduced wrinkles in the water in the current test series are much larger in amplitude than the wrinkles which occurred now and then due to small vibrations or falling droplets in

the test series of the previous paragraph. Hence, the deviations on the measured impact pressures are larger.

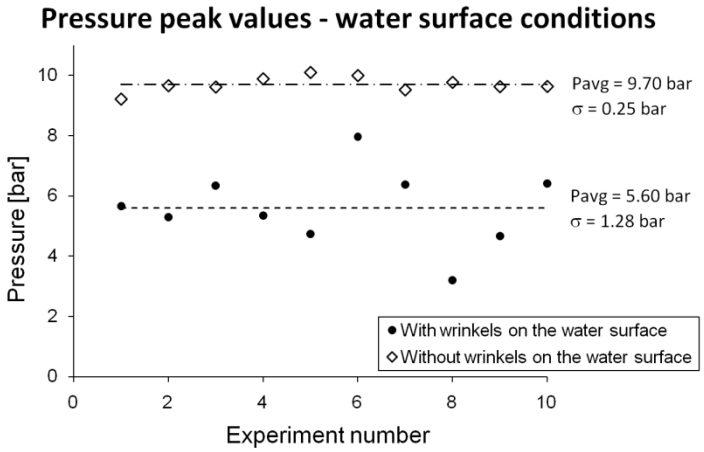

Figure 4-11: Pressure peak values for ten consecutive tests for drop height of 0.7 m with a calm water surface and a water surface containing wrinkles

When finally comparing the impact pressures measured for a calm water surface and dry object from Figure 4-11 with these presented in Figure 4-9 for a possibly slightly disturbed water surface and a dry object, then it is observed that the scatter is even more reduced and the average pressure is slightly increased. Hence, it is very important to make sure that before the execution of each measurement the water surface is completely calm.

4. 2. 2. Guidelines for measuring dynamic impact pressures

The findings done in the previous sections have lead to a test procedure for performing accurate and reproducible dynamic impact pressures during slamming drop experiments:

- The sampling rate of the data acquisition system of the pressure sensors should be chosen sufficiently high in order to obtain the peak value of the pressure pulses. Especially when performing pressure measurements at small deadrise angles, a data sampling rate of at least 300 kHz should be used.

- The pressure sensors should be precisely flush mounted. Flush mounting can be verified by confirming the absence of water bubbles or turbulences at the sensor diaphragms during water impact by using a high speed camera.

- Pressure sensors using a preloaded piezocrystal should be adjusted to the water temperature before an experiment can be performed to prevent parasitic pressures in the pressure signals. Alternatively, sensors based on other sensing technologies can be used.

- The object surface should be dry before testing.

- The water surface should be completely calm at the start of each experiment.

To summarize, Figure 4-12 recapitulates the pressure results done during the last three experiment series with the stiffened cylindrical test object, which clearly show the improvement in reproducibility when these guidelines are followed.

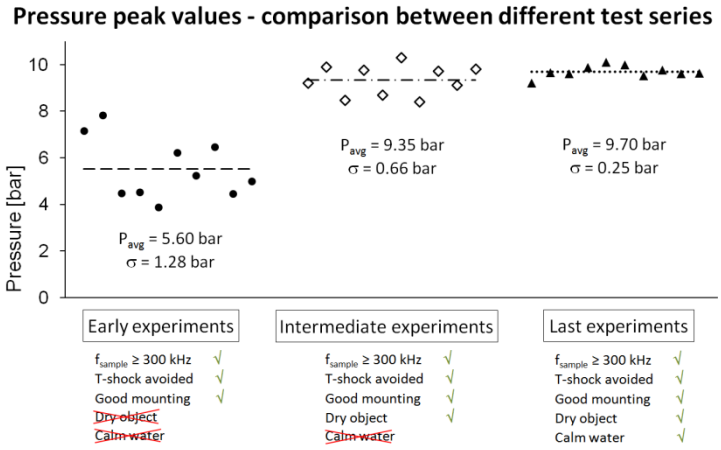

Figure 4-12: Comparison of the pressure peak values for ten consecutive tests of the last three experiment series with the stiffened cylindrical test object for a drop height of 0.7 m

4. 2. 3. Calibration methods for dynamic pressure transducers

During the examination of the large scatter and the particular pressure histories encountered during the early experiments, it was not excluded that these problems could be caused by a deficiency of the pressure transducers. In order to verify the pressure transducers of operating properly, a calibration method based on existing industrial calibration methods was developed.

Dynamic pressure sensors are much more difficult to calibrate than static ones, due to the charge leakage they exhibit. The challenge in calibrating dynamic pressure sensors is thus to generate a known pressure pulse with a short duration in order to prevent the sensors from discharging in considered time.

Following section gives an overview of the existing industrial calibration methods for dynamic pressure sensors.

4. 2. 3. 1. Industrial calibration methods for dynamic pressure transducers

The existing industrial calibration techniques for dynamic pressure sensors can be divided into two categories [9]:

- Periodic pressure pulse generation
- Aperiodic pressure pulse generation

4. 2. 3. 1. a. The Pistonphone

The Pistonphone [10-12] is the most common periodic pressure pulse generator. It is mostly used for the calibration of sensitive microphones. The principle [10] relies on a piston which is mechanically driven at a specified sinusoidal cyclic rate by a rotating cam disc, pushing on a fixed volume of air to which the microphone under test is coupled. The air is assumed to be compressed adiabatically and the pressure in the test chamber can be calculated from the adiabatic gas law. By comparing the microphone's signal output by the calculated pressure, a calibration factor can be allocated. The maximum frequency of the sinusoidal pressure changes is restricted to 250 Hz, and the pressure pulse magnitudes are limited to 125 dB [10, 11]. According to the equation for sound pressure level [10]:

$$SPL = 10\log\left(\frac{p^2}{p_{ref}^2}\right) \qquad \textbf{(4.1)}$$

With p_{ref} = 20 μPa for the case of air, this maximum pressure level becomes 35 Pa, which is much smaller than the range of the pressure sensors used in this thesis. This makes this type of pressure sensor calibration not suited in this dissertation. A photograph of a typical Pistonphone and its internal configuration is depicted in Figure 4-13.

4. 2. 3. 1. b. Hydraulic impulse calibrator

The principle of the hydraulic impulse calibrator [12, 13] is also based on a piston which compresses a volume of air or a hydraulic fluid at which the tested sensor is attached. This occurs by dropping a mass from a specified height onto the piston. The pressure in the pressure tank can be calculated based on the stroke of the piston or may be measured by another calibrated pressure sensor.

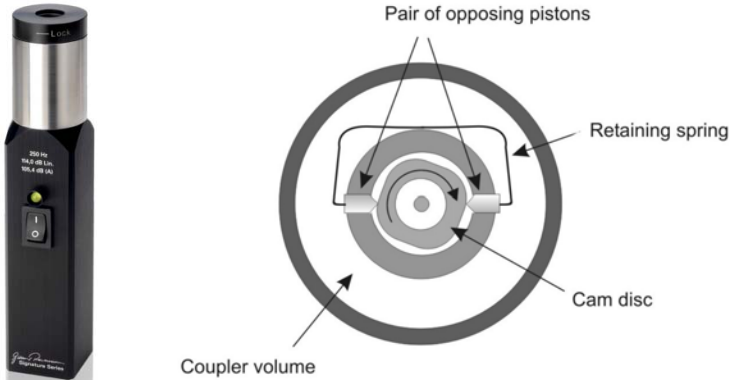

(a) (b)

Figure 4-13: (a) Photograph of a typical Pistonphone [10]; (b) Schematic view on its internal configuration [10]

This type of calibrator is an example of an aperiodic pressure pulse generator. The stroke of the piston and the speed at which it compresses the air can be varied by varying the drop height and the weight of the mass. This allows calibration tests at a wide variety of input frequencies and pressure levels. The minimum rise time and minimum pulse duration of the pressure pulses is 3 ms and 6 ms respectively, and pressures up to 860 MPa can be generated [13]. However, during the slamming experiments, pressure pulse durations of less than 1 ms are possible. A photograph and a schematic overview of the hydraulic impulse generator is given by Figure 4-14.

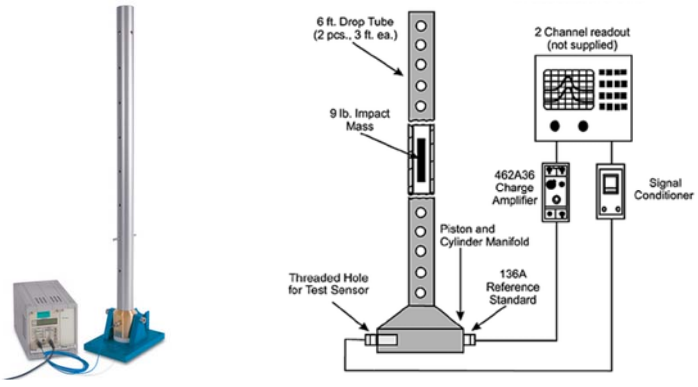

(a) (b)

Figure 4-14: Photograph [12] (a) and schematic overview [13] (b) of the hydraulic impulse generator

4. 2. 3. 1. c. The Aronson step pressure generator

Another example of an aperiodic pressure sensor calibrator is the Aronson step pressure generator [12, 13]. In this type of calibration device, a static pressure is generated in a test chamber at which the sensor under test is attached. This test chamber is mostly filled with Helium. Initially, the sensor is disconnected from the test chamber by a valve and a small volume in front of the sensor diaphragm. Subsequently, a guided mass impacts a plate, which quickly opens the valve. This exposes the sensor under test to a step reference pressure. The effect of the small volume between the valve and the sensor diaphragm on the pressure in the test chamber can be assumed negligible. The static pressure inside the test chamber is measured by another calibrated static pressure transducer.

The drop height and the mass of the drop weight determine the rate at which the valve opens and thus the rise time of the pressure step. The device can typically generate pressures up to 14 MPa at minimum rise times of 50 μs [13]. Figure 4-15 shows a photograph and the internal configuration of the Aronson calibrator.

(a) (b)

Figure 4-15: Photograph (a) and a schematic view on the internal configuration [12] (b) of the Aronson step pressure generator [13]

4. 2. 3. 1. d. The calibration shock tube

In the calibration shock tube [12, 13], a gas such as air, helium or nitrogen is pressurized at one side of a test chamber which is divided by a diaphragm into two parts. At the other side of the diaphragm, the pressure sensor under test is attached to the test chamber. The driver section of the shock tube is pressurized until the diaphragm bursts sending a known shock pressure wave into the test section of the shock tube.

By generating a shock wave, this calibration device enables pressure pulses with nanoseconds rise times. By changing the material and the thickness of the diaphragm, the pressure level of the calibrator can be tuned. Pressures up to 7 MPa can be generated [13]. A schematic view on the calibration shock tube is given in Figure 4-16.

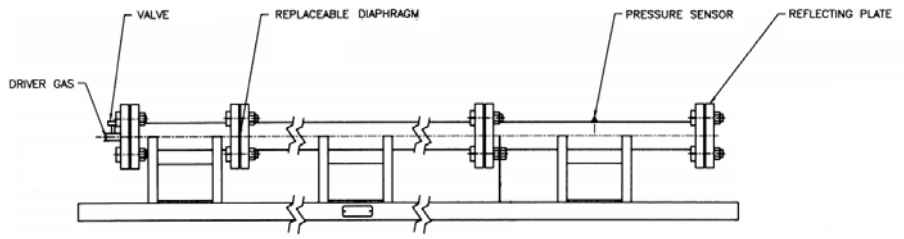

Figure 4-16: A schematic view on the calibration shock tube [13]

4. 2. 3. 2. Calibration method developed in the present dissertation

Most of the aforementioned suited industrial calibration devices are extremely expensive and difficult to transport. Moreover, the corresponding calibration processes are time consuming. In order to verify the proper working of the pressure transducers during water slamming impact, it was preferred to use a relatively cheap calibration method which can be quickly performed, and which is compact and easy portable in order to perform calibrations on the test site.

The calibration technique developed in this dissertation which meets these requirements was based on the Aronson calibration technique and on the working principle of an existing calibration device for static calibration of pressure sensors, namely the calibration hand pump from *GE Druck* (type PV 411A).

This last calibration device exists of a small pressure chamber at which the sensor under test and a static reference pressure sensor (*GE Druck* – type PMP 4000) is attached. By manually pressing the handles of the pressure pump, a certain volume of air or hydraulic fluid is pumped into the test chamber and consequently its internal pressure is increased. The pressure increase can be coarsely tuned by the stroke restrictor which limits the volume of air or fluid pumped into the test chamber, and can be fine-tuned using the volume adjuster of the test chamber. When a hydraulic fluid is used as medium in the test chamber, maximum pressures of 70 MPa can be reached. For air being the pressurized medium, this becomes 4 MPa. Since the slamming pressures are not expected to transcend 4 MPa, air was used as the test medium. An overview of the calibration hand pump is given by Figure 4-17.

Figure 4-17: The pressure hand pump for static calibration of pressure sensors

During calibration with the pressure hand pump, the reference sensor and sensor under test are coupled with the pressurized chamber at all times. Since the maximum pressure step by pressing the handles once at maximum stroke is 1 bar, it is impossible to calibrate the dynamic sensors for pressures larger than 1 bar since they will have leaked charge by the next time the handles are pressed. Moreover, the minimum rise time of a pressure step depends on how fast one can push on the handles of the pump. Especially for larger calibration pressures, large effort is needed to press the handles and the time duration of pressing the handles becomes too large in order to simulate rise times corresponding to slamming pressure pulses.

To solve these problems, inspiration was found with the Aronson step calibrator, and the calibration hand pump was extended with a valve between the tested sensor and the test chamber (see Figure 4-18(a)). By pulling the valve down at location C, the volume of the pressure chamber at B was connected with a small volume of air in front of the sensor diaphragm at A. This allowed the generation of fast rising pressure pulses also larger than 1 bar by rapidly opening the valve after the test chamber was pressurized to the desired pressure level. Minimum rise times of 10 ms could be achieved. Figure 4-18 depicts a schematic view of the valve and the calibrator-valve combination.

Figure 4-19 shows the calibration of the pressure sensor 102A06 at 10 bar. Initially, the pressure chamber is pressurized at 10 bar. The reference sensor which is directly coupled with the pressure chamber reads out 10 bar while the output of the dynamic pressure sensor which is uncoupled from the test chamber by the valve is zero (i.e. the atmospheric pressure). At time t_1, the valve starts to open en air enters the small volume between the valve and the pressure sensor diaphragm. At time t_2, the

generated pressure wave reaches the sensor diaphragm and the pressure recorded by the sensor under test is maximum. Due to an increase in the volume of the test chamber due to the small added volume between the valve and the sensor diaphragm the pressure subsequently drops again. At time t_3, the new equilibrium state has been settled. For this calibration device, the small volume between the valve and the sensor diaphragm is thus not negligible.

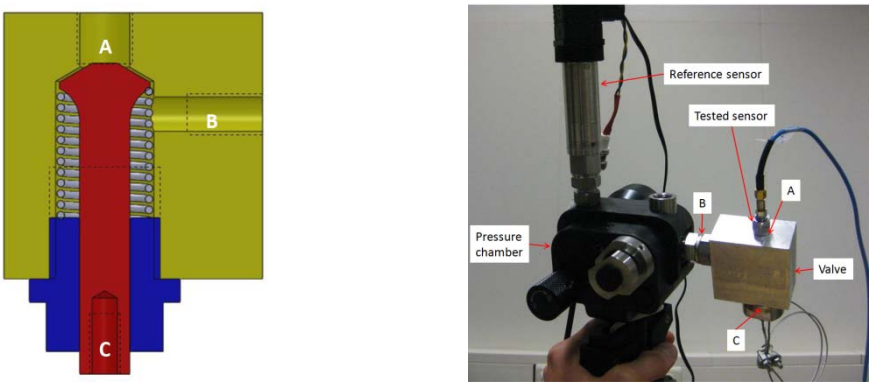

(a) (b)

Figure 4-18: (a) Schematic view of the valve which extends the pressure hand pump; (b) The combination of the pressure pump and the valve

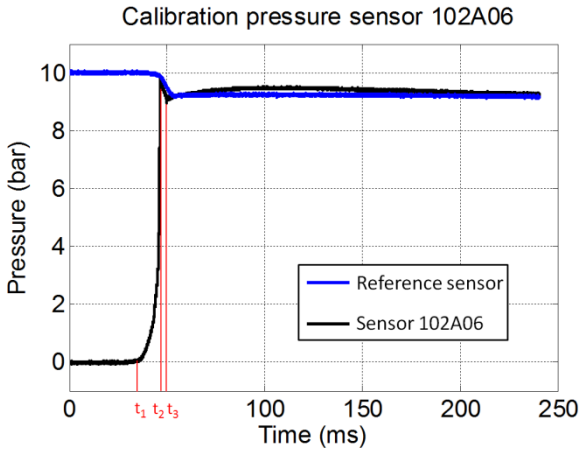

Figure 4-19: Calibration of pressure sensor 102A06

It can be observed that from the time moment t_2, the pressure which is measured by the dynamic pressure sensor under test almost completely coincides with the pressure as measured by the reference sensor. From this, it can be concluded that the pressure sensor 102A06 is working properly and that its sensitivity factor as

presented in section 3.2.1 can be used. The same findings were done for the other pressure sensors.

4. 3. Dynamic force measurements

4. 3. 1. Parameters affecting the impact force measurements

In the present section the same process as done for the dynamic pressure measurements is presented for the dynamic force recordings, in order to find a procedure to perform accurate and reproducible impact force measurements. Results from the experiments with the rigid flat plates as well as with the rigid cylindrical test objects will be presented to find all the parameters which have an influence on the measured impact forces.

4. 3. 1. 1. The data sampling frequency

Similarly to the case of the impact pressures, a sufficiently large data sampling rate should be used to enable the recording of the force peaks during the slamming events. Since the slamming forces are typically larger in duration than the slamming pressures, a smaller data sampling rate can be applied. In order to find a minimum threshold sampling frequency, the attention is focused on the slamming forces obtained during the experiments with the flat plate test objects since these are expected to be the shortest in duration and the largest in magnitude. Figure 4-20 shows the impact force measured during the water entry of the bottom impactor plate as described in section 3.4.2.1.a, for a drop height of 0.4 m. This impact force was originally measured at 100 kHz, and it can be observed from Figure 4-20 (a) that for this sampling frequency more than enough data points cover the peak of the force pulse. In Figure 4-20 (b) – (f), the latter force pulse is resampled to sampling frequencies of respectively 20 kHz, 10 kHz, 8 kHz, 6 kHz and 4 kHz. Table 4-2 gives the largest possible deviations of the force peak values of the resampled signals with respect to the original value. From these values and from the graphs in Figure 4-20, it can be observed that for data sampling rates below 8 kHz, the deviation with respect to the original force peak value transcend 1% and the force curves lose their smoothness. Hence, it was concluded that a minimum sampling frequency of 8 kHz will be used during the slamming force measurements.

Table 4-2: Slamming force peak values during water entry of the bottom impactor plate for a drop height of 0.4 m for several sampling rates, and the corresponding deviation with the true force peak

Sampling rate [Hz]	Force peak value [N]	Deviation with respect to the true force peak value [%]
100 kHz	18762	0
20 kHz	18735	0.14
10 kHz	18649	0.6
8 kHz	18600	0.86
6 kHz	18443	1.7
4 kHz	18050	3.79

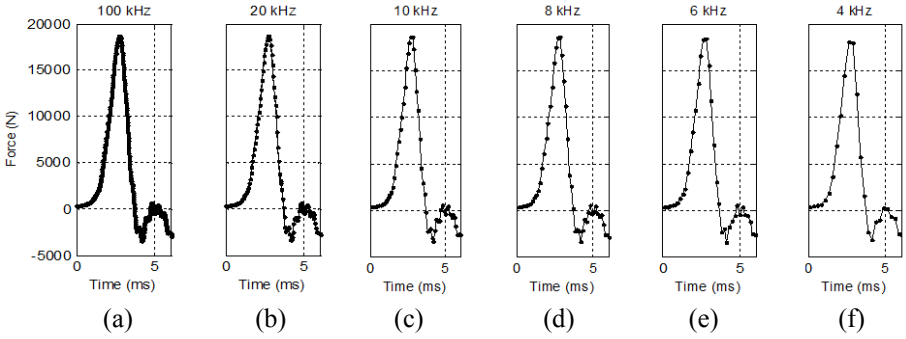

Figure 4-20: Slamming force pulse on the bottom impactor plate for a drop height of 0.4 m, originally measured at 100 kHz (a), and resampled at 20 kHz (b), 10 kHz (c), 8 kHz (d), 6 kHz (e) and 4 kHz (f)

4. 3. 1. 2. Sensor mounting

An adequate mounting of the force sensors in the experimental setup is as important as it is for the pressure sensors in order to obtain accurate measurements. The following section describes the mounting instructions which are provided by the manufacturer [14] and which should be followed carefully.

The force rings of type 201B05 from *PCB Piezotronics* which are used in this dissertation are meant to be installed between two parts of the test structure. As mentioned in section 3.2.2, three of these sensors are installed between two stiff Aluminium plates. In order to ensure output linearity also in the lower operating range, the transducers should be preloaded with a force of 4500 N [14]. This

preloading can be established by installing a supplied elastic beryllium-copper stud or a customer supplied bolt through the hole of the force ring. Both arrangements are illustrated in Figure 4-21.

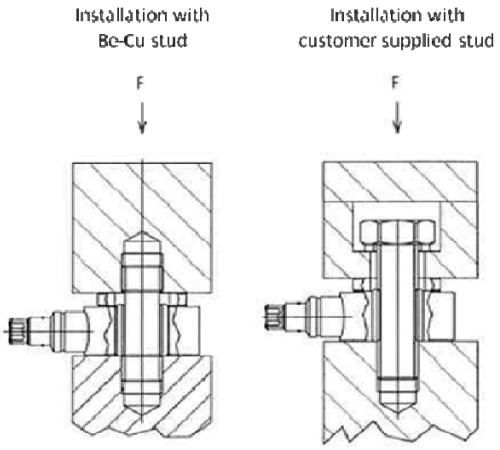

Figure 4-21: Installation types for the dynamic force transducers [14]

In the typical installation using the beryllium-copper stud, a part of the force applied on the force sensor is shunted through this mounting stud. The amount of force shunted may be up to 5% of the total force. The sensitivity factor as provided by *PCB* is based on this mounting arrangement and thus takes into account this force shunting effect of the beryllium-copper stud.

The non-typical installation in Figure 4-21 on the right differs from the arrangement described above in the sense that the customer supplied bolt is not directly connected to the top part of the construction with its threads since there is a clearance in the hole between the stud and the construction. In this installation, the bolt which is used to preload the sensor does not shunt part of the externally applied force. It is mentioned by *PCB* [14] that in this configuration the sensitivity will not match the standard calibration value which is provided in the specification sheet. A calibration of the sensor in the specific installation arrangement should then be performed.

Since three force sensors are applied in the experimental setup in this dissertation, it is impossible to use the beryllium-copper pretensioning studs. This is due to the fact that once one force sensor is installed with the beryllium-copper stud, the impactor plates are fixed with respect to each other which makes the installation of the second stud between the plates impossible. Hence, M5 steel bolts are used which fit in the holes of the force transducers. Calibration of the sensors and, more important, of the complete load cell combination is thus necessary. This clearly shows that the

mounting of the load cells comprehends much more than just installing them on the correct position and reading out the output signals. Impropriate sensor installation and calibration will result in wrong measurements. The calibration of the force sensors and the complete load cell combination will be described further in section 4.3.3.2.

During the tests, the pretensioning of the force transducers was done by the application of a torque wrench on the installation bolts. By reading out the output of the force sensors during the pretensioning process, it has been determined that a torque of 5 Nm was necessary to preload the transducers with 4500 N.

4. 3. 1. 3. Transient effect at impactor release

During the slamming experiments, it was observed that at the moment just before the first contact of the test objects with the water, the force sensors already measured a positive force although no physical contact had occurred yet. A more detailed investigation of the force recordings over a longer time span revealed that this non-zero initial force was the result of a sort of noisy force step which occurred at a time several dozens of milliseconds before the slamming impact. It was noticed that this time moment corresponded with the moment of impactor release. Figure 4-22 (a) shows this initial force step together with the slamming force pulse which occurs at t = 0 ms for the slamming experiment with the bottom impactor plate for a drop height of 0.05 m. Figure 4-22 (b) Shows this initial force step more into detail.

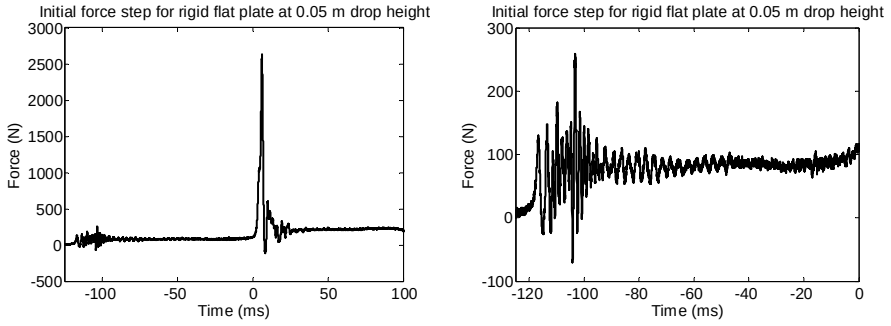

(a) (b)

Figure 4-22: (a) Force recording for the bottom impactor plate for a drop height of 0.05 m, regarded over a long time span before and after the slamming impact; (b) Detailed view of the initial force step

The explanation of this initial unexpected force history must thus be related with the release of the impactor at the start of the slamming experiment. Just before the moment of release, the complete impactor is suspended at the cable which is connected to the hoist in order lift the test object. The impactor is then vertically

stretched due to gravity force acting upon it. This also applies for the bolts which are used to preload the force transducers since the gravity load acting upon the complete bottom part of the impactor (below the force transducers) is divided over these three bolts. As a result, the preload on the force sensors reduces.

At the moment of impactor release, the suspension boundary condition disappears, and the preload on the force transducers recovers till the original value. It is this sudden increase in the preload force which is recorded at the start of the slamming experiment. Since this force step is not a result of the slamming event, it will be subtracted from the force measurements for all slamming experiments performed in this thesis.

4. 3. 1. 4. The impactor mass distribution

Even with the sensors being correctly installed and calibrated, the force as measured by the force sensors may not be interpreted as the force which acts on the test object. Figure 4-23 (a) and (b) can be used to gain this insight.

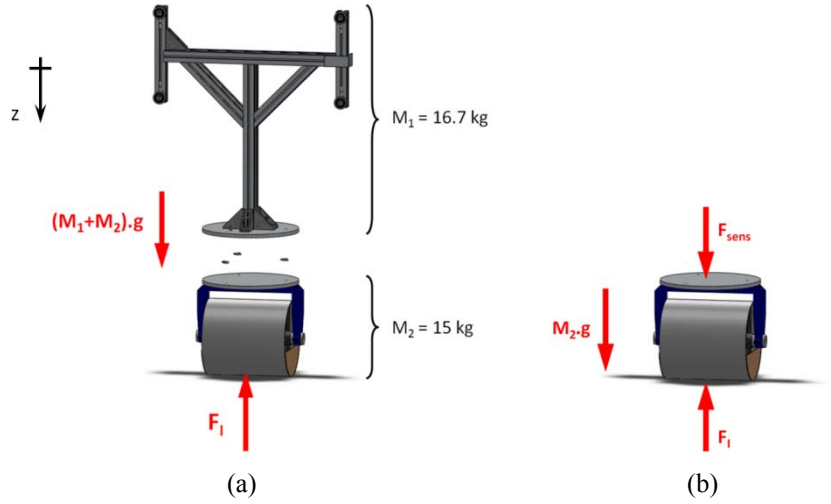

Figure 4-23: (a) Forces acting on the complete impactor; (b) Forces acting only on the bottom part of the impactor

Figure 4-23 (a) shows the impactor with the stiffened cylinder as being the test object. It can be divided into two parts: the T-shaped top structure with mass M_1 and the bottom part containing the test object with mass M_2. Assuming that all parts are rigid, then the overall equation of motion at the moment of water impact can be written as:

$$\begin{aligned} (M_1 + M_2)\cdot \ddot{z} &= F_I - (M_1 + M_2)\cdot g \\ \Rightarrow \qquad F_I &= (M_1 + M_2)\cdot(\ddot{z} + g) \end{aligned} \tag{4.1}$$

The equation of motion of only the bottom part gives the following result:

$$\begin{aligned} M_2 \cdot \ddot{z} &= F_I - F_{sens} - M_2 \cdot g \\ \Rightarrow \qquad F_{sens} &= F_I - M_2(\ddot{z} + g) \\ &\overset{(4.1)}{=} (M_1 + M_2)\cdot(\ddot{z} + g) - M_2(\ddot{z} + g) \\ &= M_1 \cdot (\ddot{z} + g) \end{aligned} \tag{4.2}$$

This shows that the force sensors only measure the force acting on the top structure with mass M_1. To obtain the impact force acting on the test object F_{impact}, Equation (4.1) and (4.2) can be combined to the following result:

$$F_I = \left(\frac{M_1 + M_2}{M_1}\right) F_{sens} \tag{4.3}$$

The force acting on the test object is thus larger than the force measured by the force sensors. This conversion will be performed for the force recordings for all slamming experiments in this thesis. An experimental confirmation of the validity of this conversion method is given in section 5.1.

Although force sensor installations similar to the one as used in this thesis are reported in the literature (Faltinsen et al. [15] and Huera-Huarte et al. [16]), the previous conversion method has never been reported in the literature before, according to the author's best knowledge. However, it is very important to consider the previous conversion factor in order to correctly interpret the test results.

4. 3. 2. Guidelines for measuring dynamic impact forces

The aforementioned parameters influencing the dynamic impact forces lead again to guidelines which should be carefully followed in order to obtain accurate and reproducible test results:

- The sampling frequency of the acquisition system for measuring slamming forces should be chosen larger than 8 kHz to enable a reliable measurement of the peak value of the slamming force pulses.

- The installation of the force sensors should be performed exactly as is recommended in the mounting instructions. Any change with respect to the

standard installation should be calibrated precisely. The preloading of the force sensors during installation is also vital in order to ensure the output linearity.

- It is important to consider the initial force step caused by releasing the impactor when evaluating the slamming force peak value. This initial force should be subtracted from the impact force since it is not a part of the slamming event.

- Finally, it is essential to understand that the impact force acting on the test object differs from the force output of the sensors due the distribution of the impactor mass above and below the force transducers. A mass conversion factor should be applied on the force recordings in order to obtain the slamming force acting at the bottom of the test object.

4. 3. 3. Calibration methods for dynamic force transducers

A calibration of the complete load cell combination is necessary since the installation arrangement of the three force transducers in the present dissertation differs from the standard installation as described by *PCB* [14]. Furthermore, an individual calibration of each sensor separately is also interesting to verify the proper working of the sensors after some series of tests.

Similarly to the case of dynamic pressure sensors, dynamic force sensors are much more difficult to calibrate than static ones, due to the charge leakage they exhibit. The calibration process is thus again a challenge in applying force pulses on the transducers with a pulse duration which is short enough to prevent the sensors from discharging.

The following section first gives an overview of the existing industrial calibration techniques.

4. 3. 3. 1. Industrial calibration methods for dynamic force transducers

According to Fujii [17], the existing industrial calibration methods can be divided into three categories:

- Methods for calibrating dynamic force transducers against an oscillation force.

- Methods for calibrating transducers against an impact force.

- Methods for calibrating transducers against a step force.

4. 3. 3. 1. a. Calibrating dynamic force transducers against an oscillation force

The calibration method using oscillating forces was first introduced by Kumme in 1998 [18]. He proposed a calibration method in which he connected a mass in series with the force sensor to be calibrated. By shaking both the mass and the transducer with a harmonic excitation by means of a shaker, the inertial force of the mass was applied on the transducer. Calibration of the force sensor was then obtained by comparing the output of this sensor with the output of a reference force sensor, also connected to the system. Later on, Bruns et al. [19] adjusted this procedure by using calibrated accelerometers on the mass instead of a calibrated force sensor as reference instrument. Park et al. [20, 21] used this method for dynamic investigation of multi-component force-moment sensors.

Due to the limited power of the available shakers, this calibration method is only suited for force transducers with small range and for low frequency ranges [19]. It is thus not so well suited for calibration of sensors used for measuring slamming forces. Furthermore, it makes use of other sensors which should be calibrated as well. Consequently, the calibration problem is shifted to other sensors which are on their turn difficult to calibrate.

4. 3. 3. 1. b. Calibrating dynamic force transducers against an impact force

Fujii [22] was the first in 1999 to propose another calibration procedure based on a known impact force. In this method, a force pulse was applied on the force sensor by making a mass collide with the transducer. After collision, the mass was immediately reflected making the duration of the force pulse very short. The position of the mass was hereby measured using an optical interferometer. This position was derived to velocity and acceleration and subsequently converted to impact force using the mass of the colliding object. Calibration could then be achieved by comparing this force value with the electrical output of the tested transducer. Fujii [23, 24] improved this method during the years, by measuring directly the acceleration of the mass by means of an accelerometer, instead of calculating the acceleration from the mass position. In the meantime, Bruns et al. [19] developed a similar procedure, which they called the Mass Impact Module. The difference with the latter method is that the force pulse was now generated by the central collinear impact of two masses with the transducer placed in between, instead of one mass.

With this type of calibration method, transducers could now be calibrated up to 20 kN and with pulse durations of 1 ms and less, which makes it more suited to calibrate the force sensors used in this thesis. However, calibrated reference

instruments are again necessary which makes the problem shift to other complex calibration techniques for these instruments.

4. 3. 3. 1. c. Calibrating dynamic force transducers against a step force

The third category of calibration procedures uses a known step force as a reference. Fujii [17] introduced a method in which a heavy mass, which was initially suspended on a wire just above the transducer, was dropped on the transducer. Since the height of the mass above the transducer was small, it did not bounce up again. The inertia force and the weight of the mass were thus used as the calibration input. An optical interferometer was once more applied in order to evaluate the velocity and the acceleration of the mass during impact.

Another calibration method which uses a step force as calibration input is developed by *PCB Piezotronics* [25]. This method uses hydraulic press stand which quickly applies and removes a certain force. The applied force is measured by reference load cells in the hydraulic machine. Dynamic force sensors with operating ranges up to 444,8 kN can be calibrated by this method. However, this calibration method again needs reference sensors which need to be calibrated, and shifts the calibration problem thus again to other transducers.

4. 3. 3. 2. Calibration methods developed in the present dissertation

The calibration procedures found in the literature and presented in the previous section all need reference instruments which need on their turn other complex and time consuming calibration techniques. For the calibration of the individual force sensors, a technique is developed in this section using reference sensors which are easy to calibrate. The need for other complex calibration techniques is hence avoided. For the complete load cell combination, a calibration technique based on the one developed by *PCB Piezotronics* [25] has been used since the load cell combination has too large dimensions to be calibrated by the individual force sensor calibration technique.

4. 3. 3. 2. a. Calibration of the individual force transducers

The calibration method for the individual force transducers is developed in this dissertation in order to verify the proper working of each sensor. The developed calibration method is a fast and precise technique which can be used for most types of dynamic force sensors, and has been presented in the 15th International Conference on Experimental Mechanics [26].

It makes use of a split Hopkinson pressure bar setup (SHPB), which is usually applied as a device to investigate the mechanical properties of materials at high

strain rate. This setup consists of two thin and long circular bars which are supported at regular distances over their entire length by linear bearings which allow the bars to move freely in their longitudinal direction. The test specimen is placed in between these two bars. The load which is applied to this test specimen is measured by means of the Hopkinson measuring technique [27], whereby stress waves in long elastic bars are measured by using strain gauges. Kolsky [28] was the first one to use this technique to test materials at high strain rate in the Hopkinson setup. In these tests, one bar was called the incident bar (longer bar), while the other one was called the transmitter bar (shorter bar).

At the start of such a high strain rate test, a longitudinal stress and strain wave ε_i is generated at the free side of the incident bar by means of a hammer of a longer striker bar. This wave propagates further in the incident bar with the speed of sound of the bar's material. The duration of the wave is determined by the length of the hammer or striker bar, while the magnitude is determined by the impact velocity U. A part of the wave is reflected back into the incident bar at the interface between the incident bar and the test specimen (ε_r). The other part is transmitted through the test specimen and propagates further in the transmitter bar (ε_t).

Under certain conditions, it is possible to calculate the time history of the strain ε, the strain rate $\dot{\varepsilon}$ and the stress σ in the test specimen from the measured time histories of ε_i, ε_r and ε_t. Two assumptions are therefore necessary [29]:

- The stress states in the Hopkinson bars and in the test piece are uniaxial.
- The Hopkinson bars deform in the elastic region.

In reality, there might be some disturbing effects which make the calculations more complex, i.e. dispersion of the stress wave in the bars, and inertia and friction of the test piece. Dispersion effects arise from the wave propagation in the Hopkinson bars, but when the transversal dimensions of the bars are much smaller than the longitudinal dimensions, these effects may be neglected. Inertia and friction effects may also be neglected since the test specimens are mostly very small and are firmly fixed to the incident and transmitter bar.

All the above mentioned assumptions lead to a fairly easy calculation of the average stress history in the test specimen [29]:

$$\sigma_m(t) = \frac{A_s E_s}{2A_p}\left(\varepsilon_t(t) + \varepsilon_r(t) + \varepsilon_i(t)\right) \qquad \textbf{(4.4)}$$

In this formulation, A_s and A_p are the cross-sectional areas of respectively the Hopkinson bars and the test specimen, and E_s is the Young's modulus for the material of the bars.

Since the two Hopkinson bars have the same material and the same intersectional areas, and if we assume the test specimen to be sufficiently short, then an additional equilibrium equation applies [29]:

$$\varepsilon(t) = \varepsilon_t = \varepsilon_i(t) + \varepsilon_r(t) \tag{4.5}$$

The average stress in the test specimen then reduces to:

$$\sigma_m(t) = \frac{A_s E_s}{A_p} \varepsilon_t(t) \tag{4.6}$$

And the force acting on the test specimen becomes:

$$F(t) = A_s E_s \varepsilon_t(t) \tag{4.7}$$

This indicates that, when measuring the strain just behind the short test specimen on the transmitter bar, the force acting on that test piece can be measured.

For the calibration test as described in this section, the individual force sensors are the test specimens which are placed in between the Hopkinson bars. By comparing the output of the force transducer under test with the force as measured by a strain gauge just behind that transducer, the sensitivity of the sensor can be determined.

In this work the SHPB-setup of the 'Mechanics of Materials and structures'-group of Ghent University has been used. It has bars of Aluminium with a length of 6m and 3 m and with diameters of 25 mm. The used setup is depicted in Figure 4-24. A schematic view on this setup is given by Figure 4-25. For this thesis, the strain on the transmitter bar is measured by two strain gauges in a half bridge configuration. They are of type FLA-2-11 from *Tokyo Sokki Kenkyujo*, with a gauge factor of 2.11 and a resistance of 120 Ω. The distance between the gauges and the force transducer is 10 cm.

The sensor under calibration is mounted in the setup by using the non-standard installation with an M5 steel bolt. This bolt clamps two Aluminium pieces against the force sensor with the required preload. The Aluminium pieces are firmly glued to the incident and transmitter bar. Figure 4-26 illustrates a schematic view and a photograph of a force sensor installed between the incident and transmitter bar.

Figure 4-24: Photograph of the used split Hopkinson pressure bar test setup

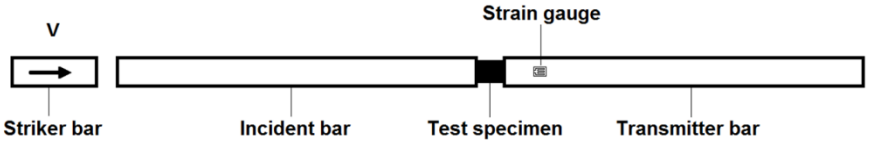

Figure 4-25: Schematic overview of the split Hopkinson pressure bar setup

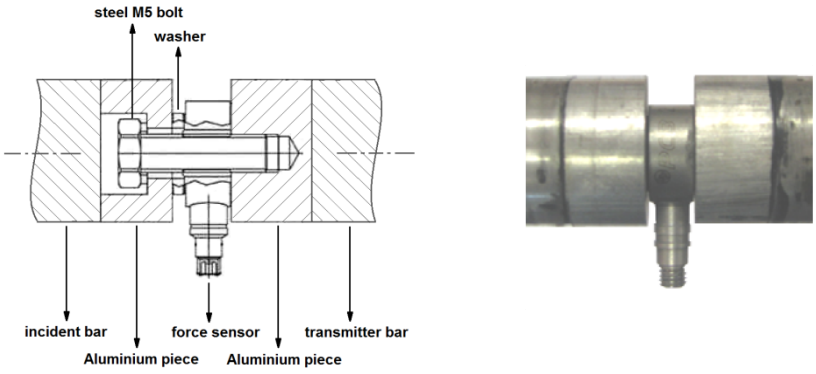

(a) (b)

Figure 4-26: A force transducer installed between the incident and transmitter bar of the Split Hopkinson Pressure Bar setup: (a) schematic view; (b) real setup

The required stress waves were generated both by a hammer and a longer striker bar. Figure 4-27 shows the ratio of the peak values of the forces as measured by the reference strain gauges and by using Equation (4.7), to the maximum voltage outputs of one of the tested force transducers for forty calibration experiments.

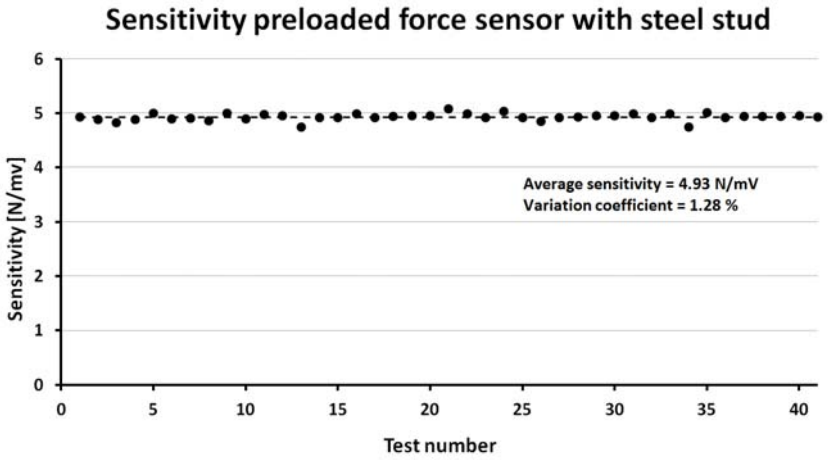

Figure 4-27: Calibration result for one of the force sensors of type 201B05

It can be observed that this ratio varies with a small variation coefficient of 1.28% around a constant average value of 4.93 N/mV. This value represents the calibrated sensitivity factor of the force transducer preloaded with a steel stud. Compared to the sensitivity factor as provided by the manufacturer (4.45 N/mV, see section 3.2.2), a difference of almost 10% is found. This difference is due to the fact that the manufacturer has determined the sensitivity based on the standard installation using the beryllium-copper stud.

For two tests out of these forty calibration experiments, Figure 4-28 compares the force history obtained from the strain gauges and Equation (4.7) with the force history obtained by multiplying the voltage output of the force transducer with the calibrated sensitivity factor. The first graph shows a force pulse generated by a longer striker bar (50 cm), while in the second graph the pulse is generated using a short hammer (10 cm). It can be observed that in both cases, both signals exactly coincide.

Previous examples show that the proposed method is an appropriate technique to precisely calibrate dynamic force transducers. Since it makes use of a force pulse as calibration input, it falls under the category of calibration techniques using an impact force [17]. The advantage of this procedure with respect to the existing industrial calibration techniques is that a calibration of the reference strain gauge sensors is fast and straightforward, since it occurs simply by shunting these strain gauges with a known resistance. No other complex calibration techniques are thus needed to calibrate the reference instrument. With the setup used, maximum forces of 40 kN and minimum rise times of 50 μs can be obtained [29] which makes this setup very well suited for calibration of the force sensor types used in this thesis.

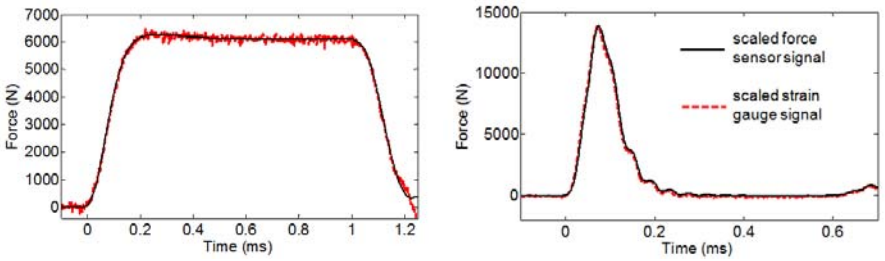

(a) (b)

Figure 4-28: Comparison of the force history obtained from the reference strain gauges and the force history obtained from the force transducer: (a) test with a long striker bar; (b) test with a short hammer

4. 3. 3. 2. b. Calibration of the complete load cell combination

For the present dissertation, a calibration of the complete load cell combination (Al plate – three sensors – Al plate) is more interesting since it is this combined instrument which will be used during all the experiments in order to record the impact forces. Calibration by using the SHPB-setup is not possible, since the size of the load cell combination is too large. Hence, another calibration method is used, which is similar to the step force calibration method developed by *PCB* [25] using a hydraulic press stand. For the calibration in this dissertation, a servo-hydraulic Instron 8801 tensile machine with a fastTrack 8800 digital controller and a dynamic 100 kN load cell [30] was used. The developed calibration procedure, which is visualised in Figure 4-29 proceeds as following:

Step 1: The calibration procedure starts by applying a known compression force with the machine grips on the Aluminium plates by using rigid steel blocks between the machine grips and the load cell combination which spread out the load over a large part of the plates. Input forces of 5 kN, 10 kN, 15 kN and 20 kN are applied.

Step 2: In the next step, as time elapses, the sensors are allowed to discharge due to the charge leakage they exhibit. The input force is hereby still present on the Aluminium plates, but the output signal falls back to zero.

Step 3: Finally, the force is released very fast by imposing a downward displacement step on the hydraulic plunger. As a result, the force sensors show a negative output. By comparing the applied force as measured by the calibrated load cell of the tensile machine with the sum of the voltage outputs of each force sensor individually, a calibration factor for the complete load cell combination can be obtained.

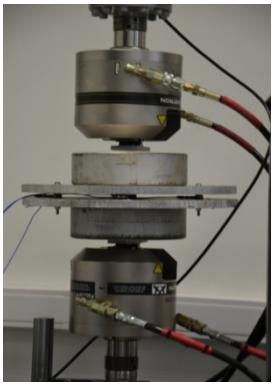

Figure 4-29: Calibration of the load cell combination using a hydraulic compression machine

The graph in Figure 4-30 shows the calibration results of this procedure. It shows the ratio of the static force applied by the hydraulic machine as measured by the machine's load cell, to the maximum of the sum of the voltage outputs of the force sensors under calibration. With a variation coefficient of 2%, it can be concluded that this calibration value is also reproducible. An average sensitivity factor of 14.47 N/mV is obtained. This calibration factor will be applied further on for all the experiments performed in this thesis.

It can be concluded that this last calibration method is thus also an appropriate method to calibrate dynamic force sensors. With the method used in this thesis, step forces up to 20 kN were generated with minimal decay times of 20 ms.

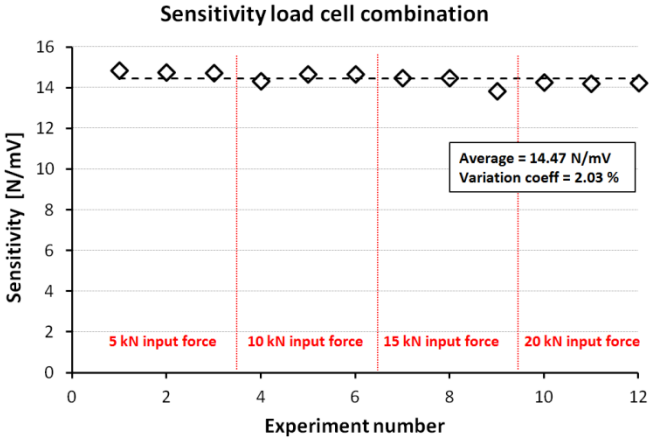

Figure 4-30: Calibration result for the load cell combination

4. 4. Position, velocity and acceleration measurements

From the three parameters which determine the motion of a test object (position, velocity and acceleration), it is only the position and the acceleration which are directly recorded during the experiments. This is done by three types of instruments: the position encoder, the DIC technique (position) and the accelerometer. However, the main purpose of these measurements is to determine the velocity of the test objects at the moment of first water contact, i.e. the impact velocity. That is because the impact velocity is the dominant parameter in the determination of the slamming load level since it represents the initial kinetic energy that the test models have when entering the water. A precise recording of the impact speed is thus crucial in the study of the slamming pressures and forces. Similarly as for the dynamic pressure and force recordings, a validation of the velocity measurements is thus necessary to guarantee the correctness and the reliability of the recorded impact velocity values.

In the following sections, a description is first given on the method which is used to calculate the impact velocity out of the recorded position and acceleration signals. Next, a comparison is performed between the recordings of the different instruments in order to validate the correctness of the measured impact velocities. Finally, the relation of the recorded impact velocities with respect to the applied drop heights is investigated. In all this, the recorded data from the stiffened cylindrical test object is used. The same conclusions are valid for the other test objects.

4. 4. 1. Methods for calculating the impact velocity

The position encoder was intended to be the main sensor for the determination of the impact velocity. Figure 4-31 shows the position history for the complete slamming experiment with the stiffened cylinder for a drop height of 1 m as measured by the encoder. The moment t = 0 ms corresponds with the trigger and thus with the moment of first contact of the test object with the water.

At the start of this typical position time history, the test object is positioned at the desired drop height (1 m). When the object is released, the position starts to decrease quadratically as the test object accelerates under gravity. At t = 0 ms, the object touches the water surface and the slamming event starts. Next, the cylinder penetrates the water and at a position of about 40 cm below the water surface its movement is stopped by the action of the shock absorbers at the bottom of the vertical rails.

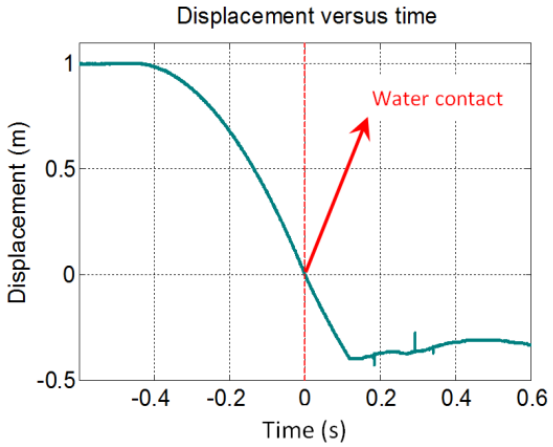

Figure 4-31: Time history of the position of the stiffened cylinder for a slamming experiment with 1 m drop height

The velocity profile of the test model can be calculated by numerically differentiating this position profile with respect to time. A linear differentiation satisfying the following equation is therefore used:

$$V_i = \frac{h_{i+1} - h_i}{t_{i+1} - t_i}, \qquad i = 1 \ldots n \qquad \textbf{(4.8)}$$

With:
- n = number of data points
- h_i = the position of the test object with respect to the water level at $t = t_i$

An unprocessed differentiation of the encoder signal leads to the result of Figure 4-32 (a). This graph shows only a band of noise instead of a realistic velocity profile. This is caused by the large amplification of the signal noise of the encoder output due to the differentiation operation. The most common measure to eliminate this noise is the application of a signal filter. The filter type which is used in this dissertation is a low pass butterworth filter, which is the most common filter in signal processing [31, 32]. It is an all pole filter type which means that the nulls are infinitely far away. Consequently, the enumerator of the transfer function is constant and this causes a magnitude response which is maximally flat in the passband. In the stopband, the magnitude response is characterized by a monotonic decrease of -20dB per decade and per order. Larger orders thus result in sharper magnitude responses which cause a larger suppression of the higher frequencies in the stopband.

The velocity derived from the encoder signal contains noise over a large frequency range. Figure 4-32 (b) shows the time history of the impact velocity as calculated

from the encoder data with a butterworth filter of order 3 and cutoff frequency 500 Hz. Now, a realistic velocity profile can be recognized in the depicted graph, but even at this cutoff frequency a large level of noise is present. Figure 4-32 (c) – (f) show the same velocity profile with decreasing cutoff frequency to respectively 250 Hz (c), 175 Hz (d), 100 Hz (e) and 75 Hz (f), with the velocity filtered at 500 Hz at the background as a reference. It can be observed that the noise level decreases until a curve is obtained which is smooth enough to determine the impact velocity for the experiment.

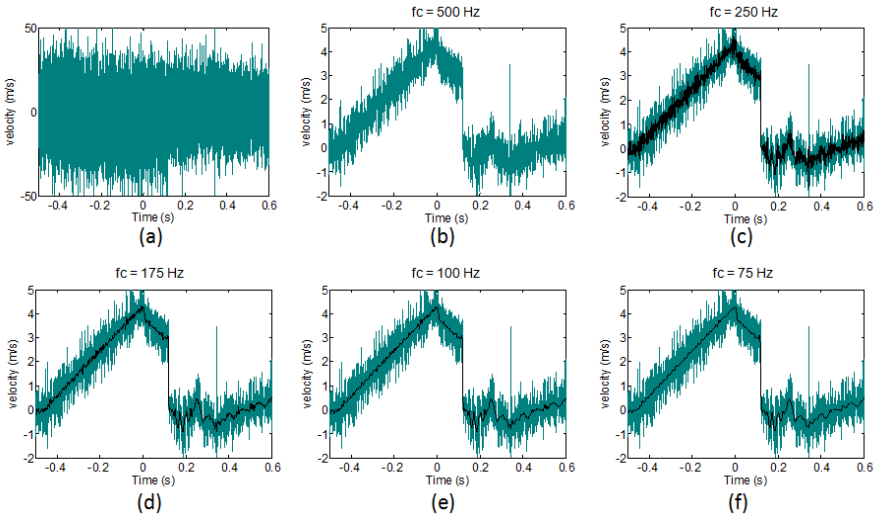

Figure 4-32: Time history of the velocity of the stiffened cylinder for a slamming experiment with 1 m drop height calculated from the position encoder data: original data (a) and filtered with 500 Hz (b), 250 Hz (c), 175 Hz (d), 100 Hz (e) and 75 Hz (f)

Each filter causes a phase shift and a corresponding time shift in its output which makes it difficult to compare data calculated from different transducers on the same time basis. This has been avoided by using a zero-phase digital filtering technique which processes the input data both in the forward and in the reverse direction. This is done by using the Matlab command *filtfilt* [33].

The finally extracted velocity profile starts increasing linearly from zero at the moment that the test object is released. At the moment of first water contact, the velocity reaches a maximum and commences to decrease due to the initial decelerating impact force and for larger penetration depths also due to the buoyancy and drag force. At the moment that the shock absorbers are activated ($t \cong 100$ ms), the velocity suddenly drops to zero and the motion is stopped.

The impact velocity value is determined as the velocity of the test object just at the moment of the first water contact. The impact velocity thus corresponds with the velocity of the test model at the time that the trigger is activated, and can thus be determined by evaluating the velocity time history at t = 0 ms. For the current example, the moment at which the maximum impact speed is reached corresponds with the maximum of the velocity. However, for small drop heights it has been observed that the impact force is so small that the object keeps accelerating even if it starts penetrating the water.

The method to extract the impact velocity from the data obtained from the DIC technique with the high speed camera is similar as the one applied for the position encoder since this technique also results in a position measurement of the test object. The noise-to-signal ratio of the latter signal is smaller than for the encoder signal and hence, no filtering is needed to obtain the velocity out of the position for the DIC data. However, the time span of this recording is much smaller and restricted to the time zone of impact since the camera can only record a limited part of the complete traveled distance of the test object. Only in this way a sufficient image resolution for the DIC algorithm can be guaranteed.

In order to convert the accelerometer signal to velocity, a numerical linear integration instead of a differentiation is performed with respect to time. The following equation represents this type of numerical operation:

$$V_{i+1} = a_i\left(t_{i+1} - t_i\right) - V_i + C, \qquad i = 1\ldots\text{n} \qquad \textbf{(4.9)}$$

An integration constant C is necessary for this operation. The velocity value at the moment of object release, which is zero, has therefore initially been used. The advantage of an integration is that the noise present on the acceleration signal is attenuated which makes that no filter has to be used to extract the velocity out of the integrated signal. However, it appeared impossible to obtain the impact velocity from the acceleration signal due to the dynamic character of the accelerometer. It was observed that in the time span from release till impact of the test object, charge leakage of the accelerometer caused the measured acceleration to drift slightly away from the gravity constant g (9.81 m/s^2), and thus caused the calculated velocity to drift away from the real velocity profile. This is illustrated in Figure 4-33.

The velocity as calculated from the accelerometer can thus only be considered in a limited time zone at the moment of water impact, since the rate of change of the acceleration is then large with respect to the discharge time constant of the sensor. Although it is not possible to determine the impact speed value from the accelerometer output, it is still interesting to compare the velocity history of the

integrated acceleration with the velocity calculated from the encoder and the DIC technique during a small time span after the impact. Therefore, the impact velocity value as measured with the encoder at the moment of impact is used as the integration constant.

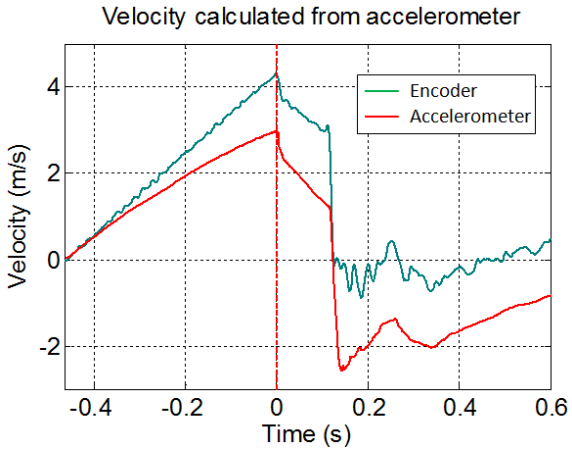

Figure 4-33: The drop velocity integrated from the accelerometer compared with the velocity derived from the position encoder

Finally, it is also possible to calculate the object's velocity from the recorded force histories. Therefore, the global force acting on the test object is first converted to acceleration using the Newton's second law of motion ($F = M.a$) and the object's mass M. Next, the same integration process as performed on the accelerometer output is applied. Figure 4-34 shows the integration result.

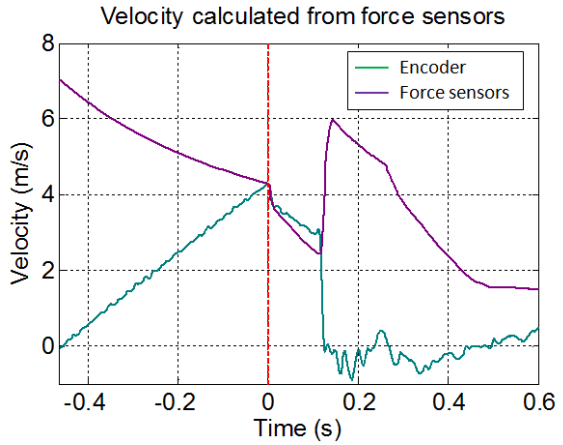

Figure 4-34: The drop velocity calculated from the force sensors compared with the velocity derived from the position encoder

However, the same problems as for the accelerometer can be observed due to the dynamic character of the sensors. Moreover, due to the initial force step at the release of the test object as is described in section 4.3.1.3, the calculated velocity is completely different from the true velocity in the time before the impact (see Figure 4-34). Analogous to the case of the accelerometer, it is however still interesting to compare the velocity profile as calculated from the force sensors with these converted from the other sensors in a small time frame at the moment of the slamming impact.

4. 4. 2. Validation of the velocity recordings

Figure 4-35 shows the velocity for a small time frame around the moment of water impact as calculated from the four aforementioned instrument types: the encoder, the accelerometer, the force sensors and the DIC technique. It can be observed that for this small time span, the shapes of the different velocity histories match very well. However, the velocity profile calculated from the position encoder differs in some extent from the ones calculated from the other sensors. The reason for this is the strong filtering of the encoder signal which does not only filter away the noise but apparently also some true vibrations in the velocity signal. However, the correspondence is still good. Furthermore, it can also be observed that the impact velocity value as calculated from the position encoder signal and from the DIC technique coincides very well.

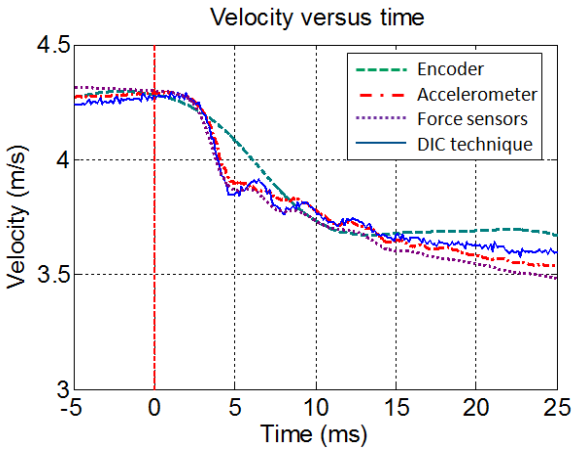

Figure 4-35: Comparison of the velocity history calculated from the encoder, the accelerometer, the force sensors and the DIC technique for a small time span around the time of water impact

From the previous correspondences in velocity evolution and velocity values (only from position encoder and DIC technique) it can thus be concluded that the measured impact velocity at t = 0 ms is correct and reliable. This comparison can thus be considered as a validation of the four involved instruments. It shows that all of the four described measurement sources lead to a similar result. This conclusion can confirmed even more when also the position time history and the force time history as calculated from the four sensor types are compared with each other. Following conversion scheme is than applicable:

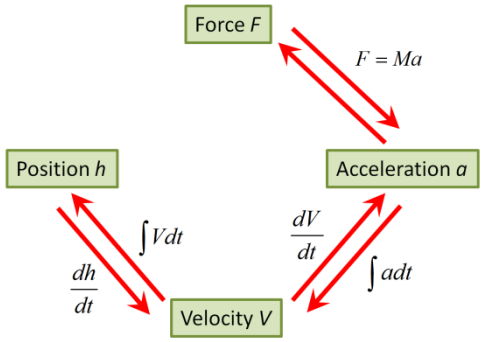

Figure 4-36: Conversion scheme for comparison of position, velocity, acceleration and force

Figure 4-37 compares the position histories calculated from the four types of recordings around the moment of water impact. No filtering has been applied to these data. A perfect match can be observed.

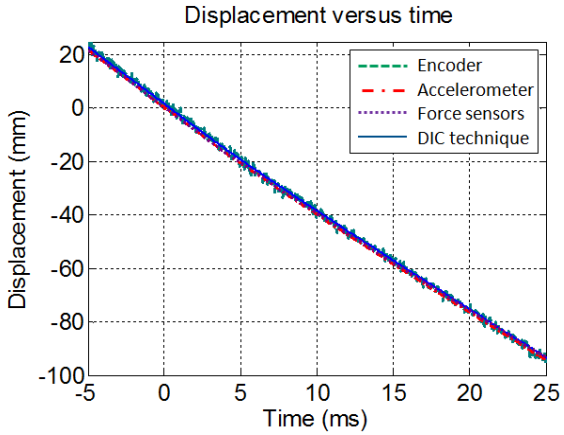

Figure 4-37: Comparison of the position history calculated from the encoder, the accelerometer, the force sensors and the DIC technique for a small time span around the moment of slamming impact

A comparison of the impact forces calculated from the four sensor types is more difficult since large noise levels play a role here. First of all, there is the large noise level on the forces calculated from the encoder and the DIC data due to the double differentiation and the corresponding intense amplification of the noise. Furthermore, it has also been observed that the raw acceleration signal contains a lot of noise. This noise is measurement noise due to an initial overestimation of the accelerometer range. As a consequence, the measured acceleration amplitudes are similar to the noise level of the sensor. Low pass butterworth filters will thus be applied for the force signals calculated from the encoder signal, the DIC measurement and the acceleration recording. To determine the cutoff frequency of these filters, the frequency content of the force sensor recordings is considered.

Figure 4-38 shows the Fourier spectrum of the portion of the force signal as measured by the force sensors from the moment of impact till the moment that the shock absorbers are activated. It can be observed that beyond a frequency of 500 Hz, the signal contains almost no frequency content anymore. A cutoff frequency of 500 Hz will therefore be applied to the other signals.

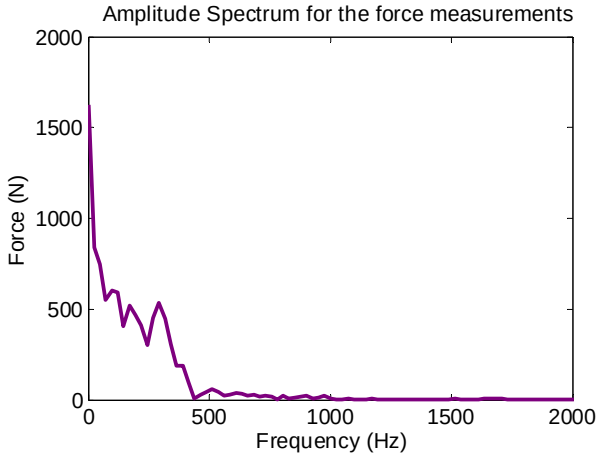

Figure 4-38: Fourier spectrum of the force sensor signal

Figure 4-39 depicts the frequency content of the force signals obtained from the position encoder, the DIC technique and the accelerometer before and after filtering. It can be observed that the filter results in the elimination of the high frequent noise for the force signal obtained from the DIC measurement and the acceleration recording. For the force signal obtained from the position encoder the initial large noise level is not eliminated completely. Moreover, it can be noticed that for this signal the frequency content below 500 Hz is also not corresponding with the frequency content of the force sensors' output. The force time history calculated

from the encoder is thus also contaminated with low frequent noise. Hence, it is not possible to calculate the impact force from the encoder recordings.

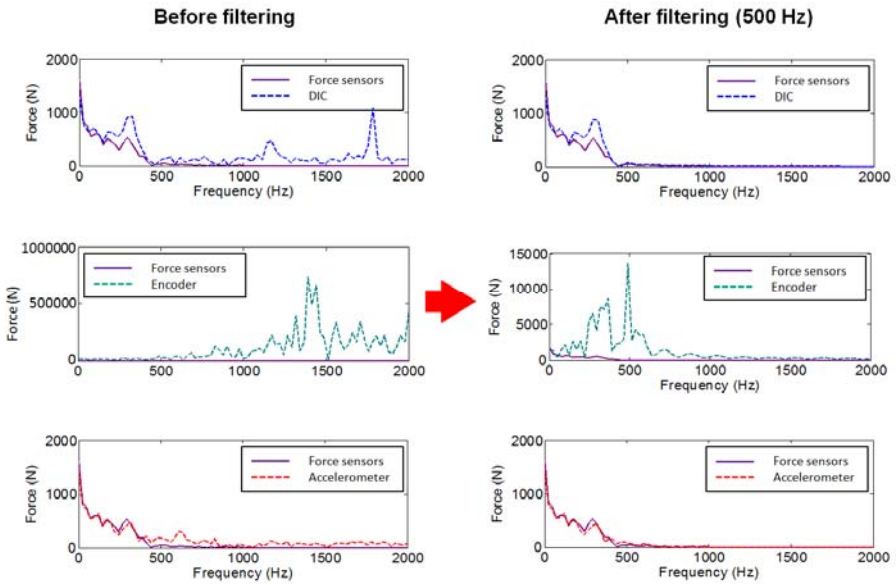

Figure 4-39: Fourier spectra of the force obtained from the DIC technique, the encoder measurement and the acceleration recording before and after filtering

Figure 4-40 compares the filtered impact force histories according to the three remaining sensors. The three plots have a similar shape in time and a good agreement in magnitude. The magnitude of the force signal as calculated from the DIC data is slightly larger than the other two force histories but still in the acceptable range to conclude a good agreement. The reason for this small difference is the presence of a small amount of low frequent noise in the DIC signal which is intensively amplified by the two differentiation operations.

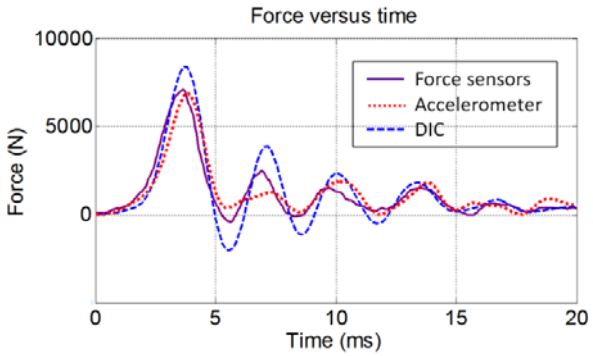

Figure 4-40: Comparison of the force sensor histories obtained from the force sensors, and as calculated from the DIC technique and from the accelerometer

4. 4. 3. Impact velocity values

The previous comparisons confirmed the validity of the calculated velocity histories and thus of the calculated impact velocity values. Figure 4-41 gives an overview of the measured impact velocity values for the complete test series with the stiffened cylinder, as function of the applied drop heights. Each data point is an average value of the velocities measured by the encoder and the DIC technique for three slamming experiments. Table 4-3 gives the numeric values of these data points as well as the standard deviation on the measurements. It can be observed that the standard deviation is very small. Hence, it can be concluded that the impact velocity measurements are reproducible.

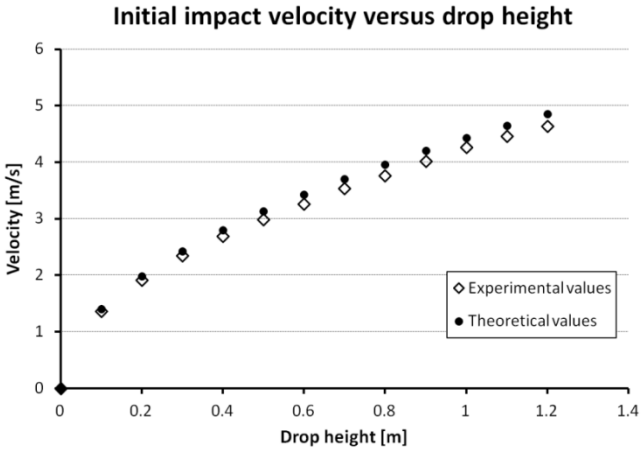

Figure 4-41: Overview of the experimentally obtained impact velocities

The graph in Figure 4-41 also shows the theoretical expected impact velocities which can be calculated from the drop height H and the assumption of the conservation of energy:

$$U = \sqrt{2gH} \tag{4.10}$$

A small difference can be observed between both curves which grows with increasing drop height. This is the result of energy losses which occur due to the friction of the wheels of the impactor with the vertical rails of the experimental setup and air drag which is proportional to the square of the velocity.

The impact velocity curves will be determined in this thesis for each type of test object. In the following chapters, the impact loads will be presented as function of these measured impact velocities. After all, a description of the impact loads as function of the drop height would lead to a wrong interpretation of the initial energy

of the test object due to the energy losses which build up during the drop. A presentation of the impact loads as function of the impact velocity makes it possible to compare the results obtained with this test rig with the ones from other setups which are characterized by other friction losses.

Table 4-3: Overview of the experimental and theoretical impact velocities

H [m]	U_{theo} [m/s]	U_{avg} [m/s]	σ_{Uavg} [.10^{-3} m/s]
0	0.000	0	0.000
0.1	1.401	1.365	1.041
0.2	1.981	1.912	15.019
0.3	2.426	2.347	10.506
0.4	2.801	2.689	5.608
0.5	3.132	2.988	5.082
0.6	3.431	3.263	4.661
0.7	3.706	3.533	4.801
0.8	3.962	3.768	6.352
0.9	4.202	4.022	7.243
1	4.429	4.261	10.121
1.1	4.646	4.458	5.764
1.2	4.852	4.643	9.646

4. 5. Conclusions

The current chapter presents a validation of the experimental instrumentation used in this thesis. This validation represents a necessary step in an experimental research in order to guarantee correct and reliable recordings.

In the first part of this chapter, the dynamic pressure and force recordings are discussed. It was observed that recording slamming pressures and forces comprehends much more than just installing the sensors and reading out the output signals. A correct interpretation of what exactly is measured is of crucial importance in the study of water slamming. A detailed examination of the early slamming experiments performed in this thesis identified several parameters leading to incorrect pressure and force measurements or to a reduced reproducibility. The knowledge of these parameters helped in understanding the preliminary experimental recordings and resulted in guidelines which should be followed in

order to obtain correct and reproducible pressure and force measurements. According to the author's knowledge, such guidelines have never been reported in the literature. The author's findings concerning the guidelines for measuring slamming pressures have hence been published in the *Journal of Experimental Mechanics* [34].

The validation of the dynamic pressure and force recordings was realized by calibrating the used pressure and force transducers. The calibration methods which were developed for calibrating the individual pressure and force sensors were elaborated in order to have a fast and straightforward method for the verification of the proper working of the considered transducers. Besides, also a calibration method for the complete load cell combination was developed. The calibration of this load cell combination was compulsory since it did not match the typical installation satisfying the manufacturer standards.

In the second part of this chapter, the position, velocity and acceleration measurements are investigated in detail. A comparison was made between the position, velocity and acceleration histories calculated from the encoder, the accelerometer and the force sensors signals and from the position recording obtained from the DIC technique. A very good agreement was observed among the different sensors. This indicates that the position sensor, the accelerometer and the DIC technique all give proper and correct results. Consequently, the considered instruments can be assumed validated.

4. 6. References

[1] W. Kappele and J. Raffaldi, "An introduction to gauge R&R," *Quality,* vol. 44, pp. 24-25, 2005.

[2] J. Raffaldi and W. Kappele, "Improving gauge R&R ratios," *Quality,* vol. 43, pp. 48,50,52,54, 2004.

[3] siliconfareast.com. (2005). *Gauge repeatability and reproducablility (GR&R).* Available: http://www.siliconfareast.com/grr.htm at 15/2/2014

[4] R. R. Smith, S. W. McCrary, and R. N. Callahan, "Gauge repeatability and reproducibility studies and measurement system analysis: a multimethod exploration of the state of practice," *Journal of Industrial engineering,* vol. 23, 2007.

[5] M.-C. Lin and L.-D. Shieh, "Flow visualization and pressure characteristics of a cylinder for water impact," *Applied Ocean Research,* vol. 19, pp. 101-112, 1997.

[6] N. Repalle, T. Truong, K. Thiagarajan, D. Roddier, R. K. M. Seah, and T. Finnigan, "The Effect of Sampling Rate on the Statistics of Impact Pressure," *ASME Conference Proceedings,* vol. 2010, pp. 565-572, 2010.

[7] C. Blommaert, "Composite floating 'point absorbers' for wave energy convertors: survivability design, production method, and large-scale

testing," *PhD dissertation, Ghent University, Department of Materials Science and Engineering,* 2010.

[8] G. Colicchio, M. Greco, M. Miozzi, and C. Lugni, "Experimental and numerical investigation of the water-entry and water-exit of a circular cylinder," in *International Workshop on Water Waves and Floating Bodies*, Zelegonorsk, Russia, 2009.

[9] D. Cummiskey and J. Lally, "Dynamic pressure calibration," *Technical Note - PCB Piezotronics,* 2005.

[10] Endevco, "Endevco model EM42AA pistonphone manual," 2013.

[11] Brüel and Kjaer, "Pistonphone Type 4228, operating manual," 2013.

[12] PCB Piezotronics. (2009). *Dynamic pressure calibration setups*. Available: http://www.pcb.com/products/browse_productlist.asp?RequestType=Filter&CategoryType=Product%20Type&CategoryId=362&app=939&tech=&config=&SearchCriteriaWithin= at 15/2/2014

[13] The electric online. (2010). *Dynamic pressure calibration*. Available: http://tijarohonline.blogspot.be/2010/11/dynamic-pressure-callibration.html at 15/2/2014

[14] PCB Piezotronics, *Operating manual dynamic force sensor 201B05*.

[15] O. Faltinsen, J. Kvålsvold, and J. Aarsnes, "Wave impact on a horizontal elastic plate," *Journal of Marine Science and Technology,* vol. 2, pp. 87-100, 1997.

[16] F. J. Huera-Huarte, D. Jeon, and M. Gharib, "Experimental investigation of water slamming loads on panels," *Ocean Engineering,* vol. 38, pp. 1347-1355, Aug 2011.

[17] Y. Fujii, "Proposal for a step response evaluation method for force transducers," *Measurement Science and Technology,* vol. 14, pp. 1741-1746, 2003.

[18] R. Kumme, "Investigation of the comparison method for the dynamic calibration of force transducers," *Measurement,* vol. 23, pp. 239-245, 1998.

[19] T. Bruns and M. Kobusch, "Impulse force calibration: design and simulation of a new calibration device," *Proceedings of the 17th IMEKO TC3 Conference, Istanbul, Turkey,* pp. 85-91, 2001.

[20] Y. K. Park, R. Kumme, and D. I. Kang, "Dynamic investigation of a three-component force-moment sensor," *Measurement Science and Technology,* vol. 13, pp. 654-659, 2002.

[21] Y. K. Park, R. Kumme, and D. I. Kang, "Dynamic investigation of a binocular six-component force-moment sensor," *Measurement Science and Technology,* vol. 13, pp. 1311-1318, 2002.

[22] Y. Fujii and H. Fujimoto, "Proposal for an impulse response evaluation method for force transducers," *Measurement Science and Technology,* vol. 10, pp. N31-N33, 1999.

[23] Y. Fujii, "Measurement of impulse response of force transducers," *Review of Scientific Instruments,* vol. 72, pp. 3108-3111, 2001.

[24] Y. Fujii, "Measurement of steep impulse response of a force transducer," *Measurement Science and Technology,* vol. 14, pp. 65-69, 2003.

[25] PCB Piezotronics. *Introduction to piezoelectric sensors*. Available: http://www.pcb.com/techsupport/tech_force.php at 15/2/2014

[26] D. Van Nuffel, J. Peirs, I. De Baere, P. Verleysen, J. Degrieck, and W. Van Paepegem, "Calibration of dynamic piezoelectric force transducers using the Hopkinson bar technique," *Proceedings of the 15th International Conference on Experimental Mechanics*, pp. 1-12, 2012.

[27] B. Hopkinson, "A method of measuring the pressure produced in the detonation of high explosives or by impact of bullets," *Philosofical Transactions of the Royal Society*, vol. A, pp. 437-456, 1914.

[28] H. Kolsky, "An investigation of the mechanical properties of materials at very high rates of loading," in *Proceedings of the Physical Society*, 1949, pp. 676-700.

[29] J. Peirs, "Development of impact-dynamic compression experiments," Master Master thesis, Department of Materials Science and Engineering, Ghent University, Ghent, 2007.

[30] Instron, "Technical sheet and manual of the hydraulic tensile machine of type 8801," 2013.

[31] S. K. K. Mitra, "Digital signal processing: a computer based approach," 2000.

[32] T. W. Parks and C. S. Burrus, "Digital filter design," 1987.

[33] Matlab Documentation. (2013). *Documentation on the Matlab commmand filtfilt*. Available: http://www.mathworks.nl/help/signal/ref/filtfilt.html at 15/2/2014

[34] D. Van Nuffel, K. S. Vepa, I. De Baere, J. Degrieck, J. De Rouck, and W. Van Paepegem, "Study on the Parameters Influencing the Accuracy and Reproducibility of Dynamic Pressure Measurements at the Surface of a Rigid Body During Water Impact," *Experimental Mechanics*, vol. 53, pp. 131-144, 2013.

Chapter 5

Cylinder slamming

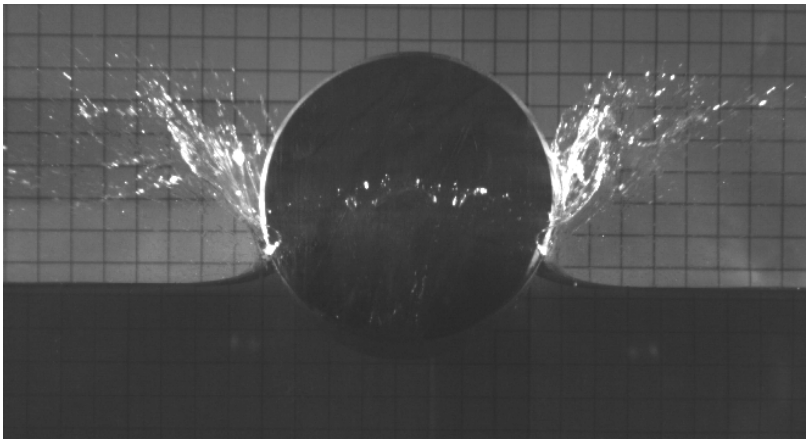

Overview

The present chapter presents and compares the impact pressure and impact force results for the rigid and deformable cylindrical test models. The chapter starts with investigating the effect of the mass on the impact loads generated during cylinder slamming. Further, the water slamming of the rigid cylindrical test objects is investigated and discussed in detail. The obtained force and pressure measurements are compared with the literature. Next, the recordings from the deformable cylinders are presented and compared with the results from the rigid test models. A relation between the degree of deformability and the magnitude of the impact loads acting on these cylindrical objects is searched. Finally, the internal impact stresses in the deformable cylindrical test objects are investigated and their evolution with respect to the degree of cylinder deformability is discussed.

5. 1. Effect of the cylindrical mass on the slamming pressures and forces

In the available literature concerning rigid and deformable cylindrical slamming, no attention has ever been paid to the fact whether the mass of the cylindrical test objects has an effect on the slamming pressures and forces in drop weight impact testing. However, this appears intuitively to be important when considering that in

the case of a cylindrical object falling under gravity on a calm water surface, a small mass will decelerate much more than an object which approaches an infinite mass and is expected to be hardly decelerated. This expected difference in deceleration would then also indicate a difference in the slamming forces, and thus also in the slamming pressures.

Chapter 3 mentions the masses of the different individual test cylinders. The corresponding impactor masses, which represent the actual test object masses, are provided in Table 5-1. It can be observed that the different cylindrical test objects vary in a reasonable wide mass range. A possible effect of the object's mass on the impact loads would indicate that the slamming load results from the different cylindrical test objects cannot be compared directly with each other.

Table 5-1: Impactor masses for the different cylindrical test objects

Test object	Impactor mass [kg]	Test object	Impactor mass [kg]
Stiffened cylinder	31.70	C6, GFRP	32.55
Plaster cylinder	30.30	C7, PVC	25.60
Concrete cylinder	39.50	C8, PVC	22.87
C1, PVC	31.84	C9, PVC	22.75
C2, PVC	31.60	C10, PE	22.66
C3, PVC	32.32	C11, PE	22.96
C4, GFRP	32.40	C12, PP	22.73
C5, GFRP	32.29		

In this section, the effect of the mass of the cylindrical test objects on the slamming loads is evaluated experimentally. Therefore, impact forces were recorded during slamming experiments with the deformable cylindrical test object C1 (PVC, D = 31.5 cm, d = 9.4 mm), for which the mass has been varied by adding mass to the complete impactor construction. A distinction has hereby been made between mass which is added to the impactor construction in the part above the force transducers and in the part below the force transducers. The total masses of these parts have been denoted as M_1 and M_2 respectively, as depicted in Figure 4-23. Mass has been added to both parts by adding circular sheets of steel just above the Aluminium top plate or just below the Aluminium bottom plate of the load cell combination. Figure 5-1 shows as an example a number of these steel sheets added just above the top plate of the load cell combination.

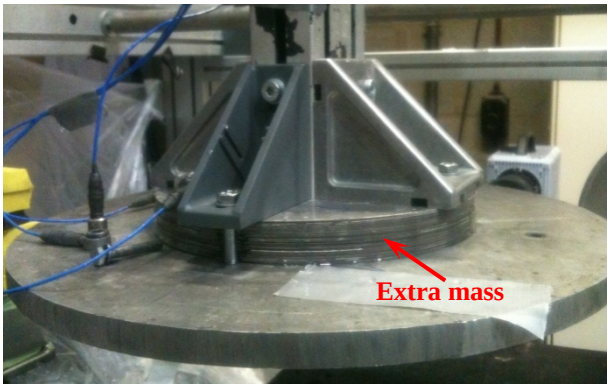

Figure 5-1: Extra mass added to the top part of the impactor construction

Seven mass combinations have been tested in order to estimate the effect of the mass and also the mass distribution of the impactor on the impact forces. The masses M_1 and M_2 corresponding to these mass combinations are presented in Table 5-2. This table also presents the total mass of the impactor and the mass factor for the conversion of the measured force to slamming impact force (see Equation (4.3)). It can be observed that the first four mass combinations correspond with increasing total mass, but a constant mass conversion factor. The last four test cases correspond with constant total impactor mass, but a varying mass conversion factor.

Table 5-2: Overview of the tested mass combinations

Mass combination	M_1 [kg]	M_2 [kg]	M_1+M_2 [kg]	$\frac{M_1+M_2}{M_1}$ [-]
1	15.4	10.3	25.7	1.67
2	16.7	11.2	27.9	1.67
3	18.0	12.1	30.1	1.67
4	19.4	13.0	32.4	1.67
5	22.1	10.2	32.4	1.46
6	15.4	17.0	32.4	2.10
7	18.1	14.3	32.4	1.79

Slamming drop experiments at two drop heights were performed, i.e. at 0.2 and 0.5 m. The procedure for determining the impact force values from the force recordings is explained further on in the following sections. Figure 5-2 and Figure 5-3 show the impact force values at the two tested drop heights. From both graphs, it

can be observed that the recorded impact force values F_{impact} remain reasonably constant for increasing total mass of the impactor. The maximum amount of added mass corresponds to 25% of the initial impactor mass. This indicates that for the mass range which is applicable in this dissertation, the impactor mass has no effect on the global impact force acting on the cylindrical model attached to the impactor.

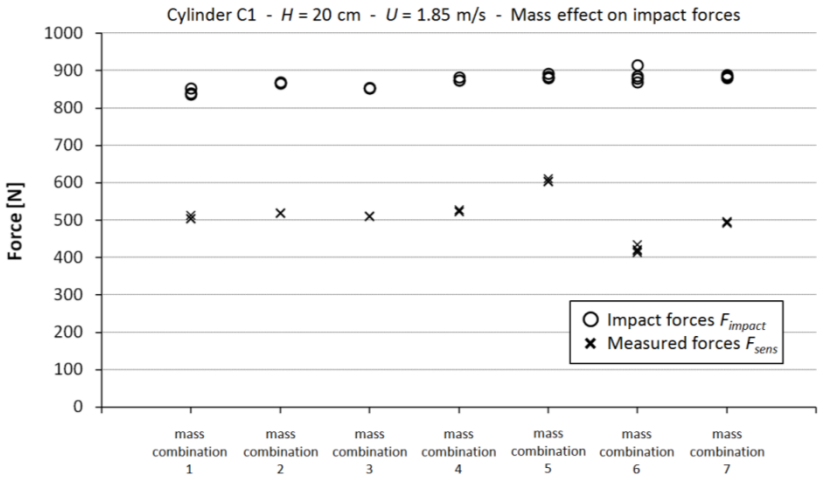

Figure 5-2: Overview of the maxima of the impact forces and the measured forces for the seven applied mass combinations during the slamming experiments with cylinder C1 at a drop height of 0.2 m

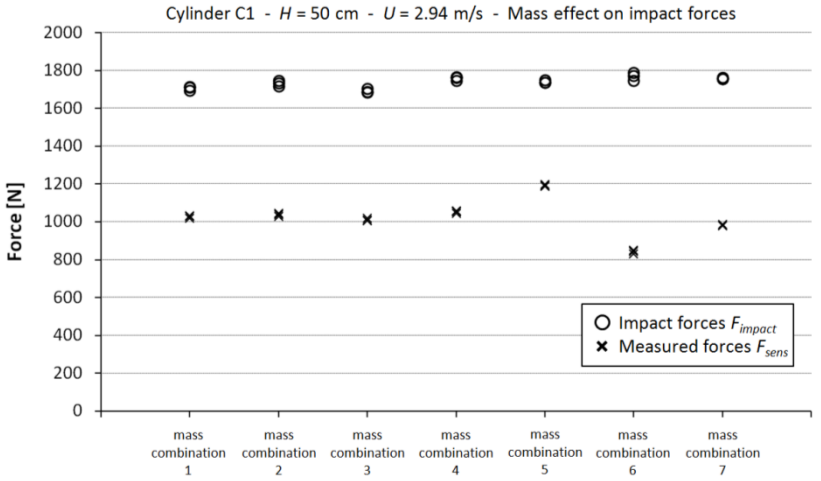

Figure 5-3: Overview of the maxima of the impact forces and the measured forces for the seven applied mass combinations during the slamming experiments with cylinder C1 at a drop height of 0.5 m

This indicates that in the mass range of this dissertation, since the slamming force is constant as function of the mass, also the inertia force corresponding to the complete impactor is independent from the impactor mass (the inertia force of the test object equals the slamming force for slamming experiments with a free fall, see section 2.4.1). This shows that when a larger (smaller) cylindrical mass slams on a flat water surface in a drop weight slamming event, then its speed will be less (more) decelerated due to its increased inertia and the product of its mass with the deceleration will be the same, resulting in the same impact force independent from the mass.

Furthermore, it can be concluded that, since the cylindrical slamming forces are independent from the mass in the mass range of this dissertation, the same is valid for the impact pressures.

In Figure 5-2 and Figure 5-3, also the maxima of the forces F_{sens} (see section 4.3.1.4) have been depicted in the graphs. These forces represent the forces obtained at the location of the force sensor, thus without applying the mass conversion factor to convert these results to impact forces acting at the bottom of the test object. It can be observed that for the first four test cases in which the mass conversion factor remains constant, the maxima of these forces also remain constant. For the cases in which the mass conversion factor has been varied, but the total mass has been kept constant, it can be observed that this altered distribution of the mass between the top part and the bottom part of the impactor does have a pronounced effect on the maxima of the measured forces although the impact forces are constant. Also the impact forces calculated from the measured forces using the mass conversion factor are constant. This observation leads to the conclusion that the method for converting the measured forces to slamming impact forces as discussed in section 4.3.1.4 is valid.

5. 2. Rigid cylindrical test objects

With the knowledge that differences in mass of the used cylindrical objects have no effect on the impact forces, the impact pressures and forces can be presented for each test object and compared with each other and with the theory. In the present section, the impact pressures and forces measured for the rigid cylindrical test objects are described and discussed.

5. 2. 1. Impact pressures

The present section describes the slamming pressures characteristic for rigid cylindrical drop weight slamming. At first, the evolution of the recorded pressures with respect to time is described in detail and is correlated with the physical impact

stages. Later on, the focus will be concentrated only on the maximum impact pressure values in order to estimate the maximum pressures occurring during rigid cylindrical drop weight slamming.

5. 2. 1. 1. Pressure time history

Slamming pressures were only recorded for the stiffened cylindrical test object since it was only for this test object that pressure sensors could be installed at the cylindrical surface. Impact pressures at the surface of the stiffened cylinder were measured at five different deadrise angles and at two positions on the same meridian (see section 3.4.1.1.a). Figure 5-4 shows the time plots for the pressures acting on the cylinder during a slamming drop test with an impact velocity of 4.1 m/s which corresponds with a drop height of 1 m. The recordings are obtained from the pressure sensor in the middle of the cylinder's length. From top to bottom, the deadrise angle is increased from 0° till 25° and the time scale is the same for every graph.

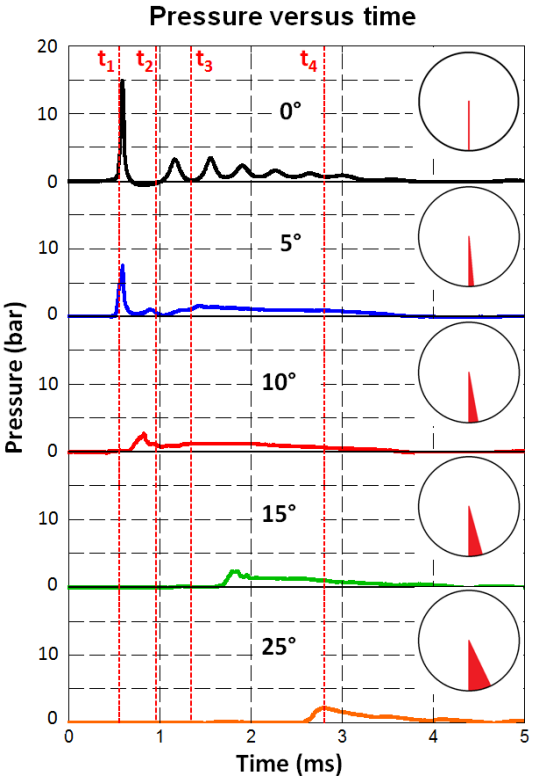

Figure 5-4: Time plots for the pressure measurements at five different deadrise angles (0°, 5°, 10°, 15° and 25°) at the surface of the stiffened cylinder for a slamming drop test with a drop height of 1 m and an impact speed of 4.1 m/s.

From these graphs it can be observed that the impact of the cylinder on the water starts with a high pressure pulse (in the order of 15 bar) with a very short duration (in the order of 200 μs) at the bottom of the cylinder. As the cylinder penetrates the water, this pressure peak travels further along the surface of the cylinder while its peak value reduces and its duration increases. This reduction is mainly due to the increasing deadrise angle. A small part of the reduction may also be contributed to the slightly decreasing velocity after impact. However, in the short time span which is considered, the velocity of the cylinder does not change much (see Figure 5-5).

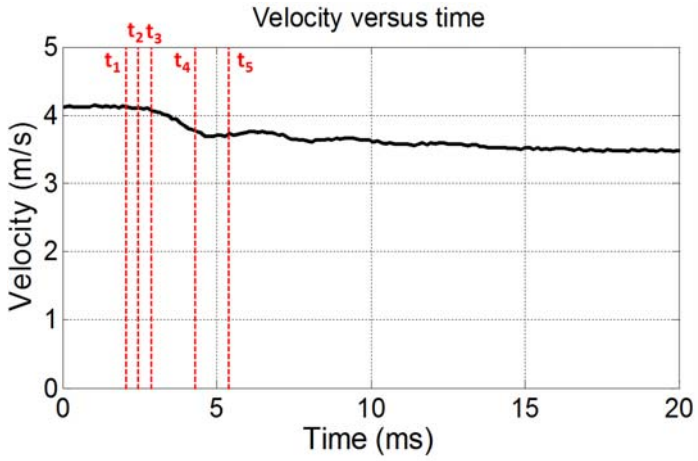

Figure 5-5: Time plot of the velocity of the stiffened cylinder for a slamming drop test with a drop height of 1 m and an average impact speed of 4.1 m/s

The pressure peak always occurs in the intersection zone of the cylindrical surface and the water surface, i.e. at the root of the water jet. In this zone, called the inner domain [1], the water is compressed and forms a water jet which propagates along the surface of the cylinder. Finally, for larger penetration depths, this water jet will separate from the cylinder and no pressure pulse will be registered anymore at the surface of the cylinder for larger deadrise angles. The time moments t_1 and t_4 correspond with the high speed images depicted in Figure 5-6. It can be observed that at the time t_4, when the pressure reaches its peak in the pressure measurement at 25°, the physical deadrise angle exactly matches 25° indicating that the pressure peak is thus reached in the spray root of the jet.

From Figure 5-4, it can further be observed that for the pressure time history at 0° deadrise angle also smaller pressure peaks are observed after the first slamming peak, which occur at a periodic time interval of about 0.35 ms and which dampen out in time. A similar oscillatory pressure time history for the pressure recording at the bottom of the cylinder has also been observed by Lin and Shieh [2]. Such

oscillations are not observed in the pressure time histories recorded at the other deadrise angles. A detailed investigation was carried out to find an explanation for these oscillations.

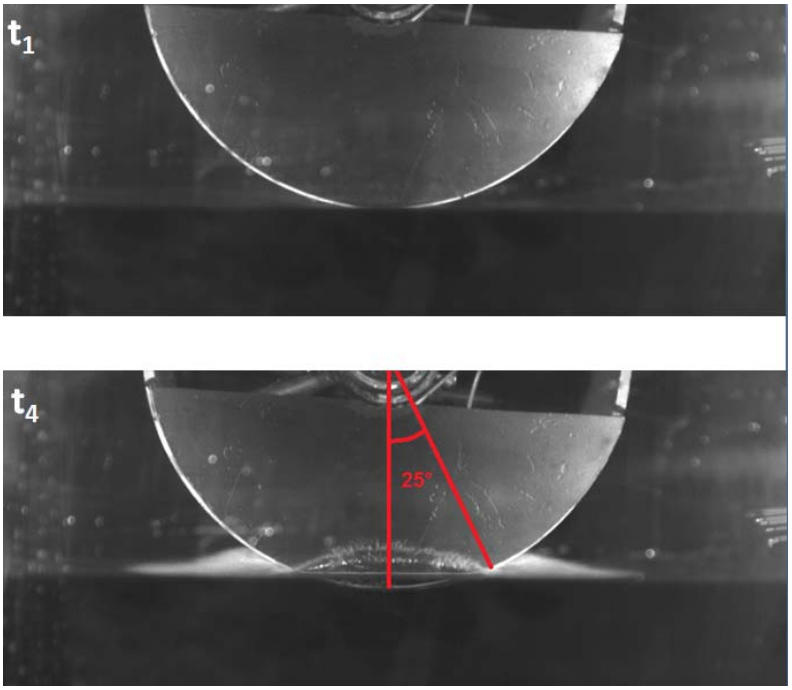

Figure 5-6: Camera images at two different time frames. t_1: first contact of the cylinder with the water; t_4: pressure peak at 25°

If the oscillations were caused by structural vibrations of the cylinder due to the sudden impact, then these oscillations in the impact pressure would also be expected in the recordings at the other deadrise angles. Hence, this possibility seems unlikely as an explanation.

Another hypothesis is that the secondary pressure peaks are caused by the pressure waves which are generated in the water tank due to the impact, which reflect at the bottom of the tank and then again reach the diaphragm of the sensors. The back and forth travelling of these pressure waves would then explain the oscillatory peaks in the pressure recording of the pressure sensor at the bottom. However, this hypothesis is also very unlikely since the generated pressure waves propagate with a cylindrical wave front in the tank and rapidly decay in magnitude. When they travel twice the distance from the point of impact till the bottom of the water tank, it is expected that the magnitude of the pressure wave has decreased so much that it has no significant effect in the pressure recordings. Moreover, it has been observed that the time which

the pressure wave needs to travel twice the depth J of the water tank does not match with the time interval between two pressure pulses. This travelling time can be calculated by dividing the travel distance by the velocity of sound in the water since this is the speed the pressure wave travels with. The travelling time of the pressure wave is thus:

$$\Delta t = \frac{2J}{\gamma_w} = \frac{2 \cdot 0.6\,\text{m}}{1497\,\text{m/s}} = 0.80\,\text{ms} \qquad \textbf{(5.1)}$$

This value is more than double the value which is observed in the pressure recordings.

Although the air was expected to escape completely due to the cylinder's shape and the presence of an air cushion has always been neglected in the literature, camera images though showed that a small air pocket is formed at the initial moment of the impact locally at the bottom of the cylinder. Figure 5-7 presents a sequence of high speed images with the camera positioned at the window of the water tank looking to the underside of the cylinder under the water level, as illustrated in Figure 5-8.

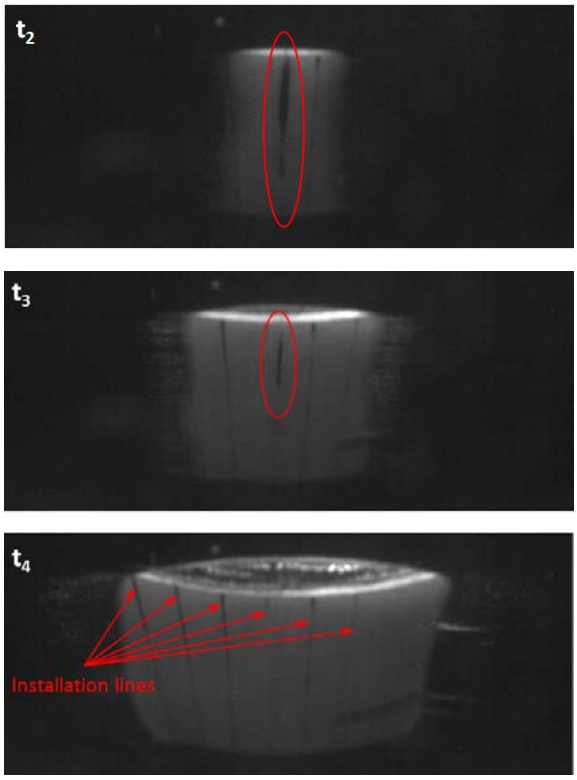

Figure 5-7: Camera images from the bottom of the cylinder during water impact

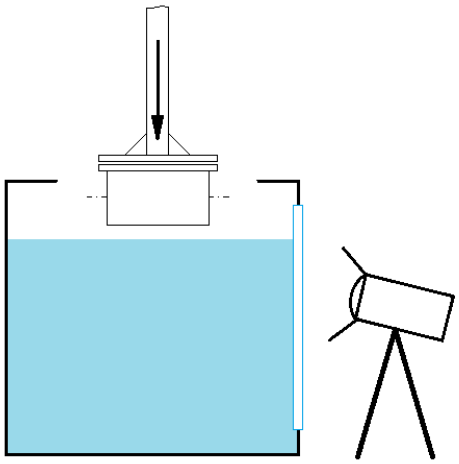

Figure 5-8: Schematic view of the camera position during for the impact videos from Figure 5-7

The black zone which is present locally at the bottom of the cylinder in the very initial stage of the impact represents the air pocket. The black lines on the cylinder represent lines which are drawn on the cylinder in order to assist the pressure sensors to be positioned under the correct test angles. The observed air pocket exists only for a few milliseconds and disappears rapidly, but it is assumed to have a contribution to the oscillatory pressure time history. Since it only occurs at the bottom of the cylinder, this might explain the difference in pressure time history for the pressure sensor at the bottom and for the pressure sensor placed at the other tested deadrise angles. The fact that pressure recorded at the bottom oscillates may be explained by a repeated compression and expansion of the air bubble in front of the pressure sensor at the bottom of the cylinder before it disappears. Also Lin and Shieh [2] assumed the compression of an air pocket in front of the pressure sensor diaphragm as being the reason for the oscillatory pressure time history for the recordings at the bottom of the cylinder, but they could not confirm this assumption. The high speed recordings from Figure 5-7 thus seem to do so.

5. 2. 1. 2. Impact pressure values

Before presenting the impact pressure values on the basis of the average pressure maxima of three recordings per drop height, it is important to consider the difference in the recorded slamming pressure between the two used pressure transducers, which are located at the same deadrise angle, but at another position with respect to the cylinder's length. As such, the effect of the three-dimensionality of the flow around the cylindrical test model on the impact pressures during water impact can be investigated. After all, it is important to take into account any effect of the flow in

the longitudinal direction of the cylinder on the measured impact pressures and forces to make the results from this study also representative for cylinders with larger aspect ratios (*l*/*D*-ratios), since these are more often used in industrial offshore constructions.

Figure 5-9 shows the impact pressure values for both pressure sensors located at 0˚ deadrise angle for all experiments as function of impact velocity. The transducer of type 102A06 is the sensor located in the middle of the cylinder's length, while the sensor 102B06 is the sensor located 8 cm from the side on the same meridian. It is observed that the deviations of the impact pressure values between both pressure transducers are within the scatter level of the overall pressure results. Hence, no significant differences are found which indicate large three-dimensional flow effects.

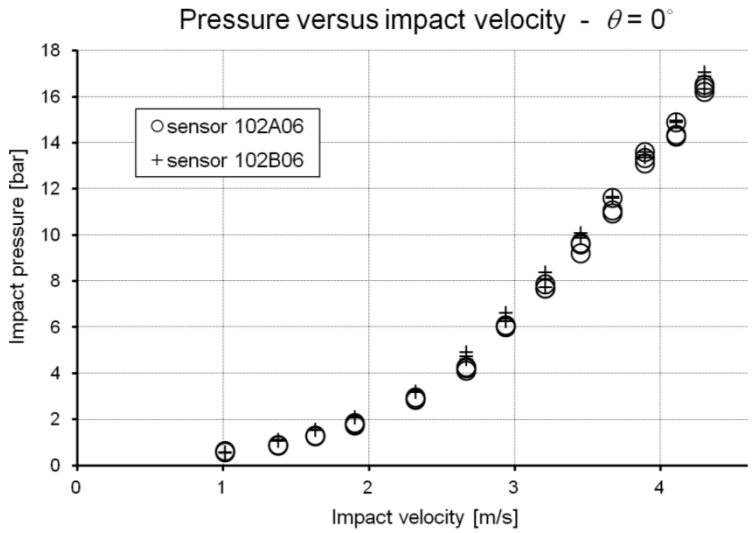

Figure 5-9: Impact pressure measurements for sensor 102A06 and 102B06 for all experiments with the sensors located at 0˚ deadrise angle as function of impact velocity

The effect of the flow in the longitudinal direction of the cylinder has also been investigated in detail by Nila [3]. In his dissertation, the velocity vector field of the water flow in the longitudinal direction could be measured using the PIV technique. Figure 5-10 shows an extraction of these results for the deformable cylindrical test object C1, for a slamming test at 3.74 m/s. Similar results were obtained for all other cylindrical test objects. The figure depicts the velocity vectors of the flow at a large variety of locations in the fluid. The colours in the diagram represent a contour map of the velocity component in the longitudinal direction of the cylinder. It can be

observed that it is only at the very edges that large velocity components in the longitudinal direction of the cylinder exist. Hence, it is assumed further in this dissertation that the effect of the flow in the longitudinal direction on the slamming pressures and forces acting on the tested cylinders is negligible.

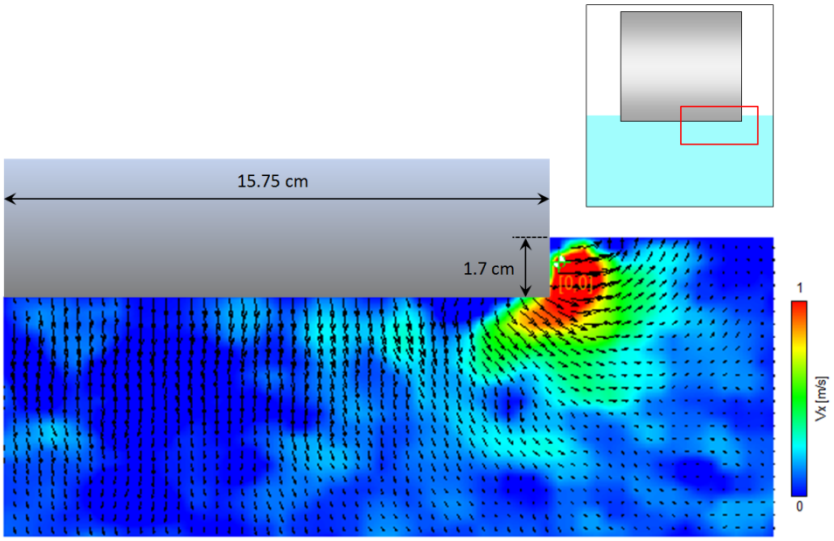

Figure 5-10: Velocity vectors of the flow and contour map of the velocity component in the longitudinal direction of cylinder C1 for a slamming experiment with an impact speed of 3.74 m/s [3]

Since there is no significant difference in the pressure recordings of both pressure transducers, no distinction will be made between them and their average value will be used further in this paragraph. Figure 5-11 and Table 5-3 show an overview of the average measured pressure peak values as function of impact velocity for the different tested deadrise angles. For the deadrise angles 10°, 15° and 25°, the measurements are very close to each other. Figure 5-12 gives a detailed view on these results. The uncertainty has been expressed in the graphs in terms of error bars, based on the standard deviation as reported in Table 5-3. The standard deviation indicates a good reproducibility for the pressure measurements at 0° and 5° deadrise angle, but more scatter for the recordings at larger angles.

For the pressure peaks measured at 0° and 5° deadrise angle, a clear trend can be observed. The data points follow a fourth order relationship rather than a second order trend, which shows that the local loads acting on the cylinder rise very fast with increasing impact velocity. For waves breaking at cylindrical structures with a very large wave celerity, extremely large local pressures will thus occur during the first contact. For the measurements at 10°, 15° and 25°, no clear trend can be

observed but the rate at which the impact pressures rise as function of impact speed is smaller.

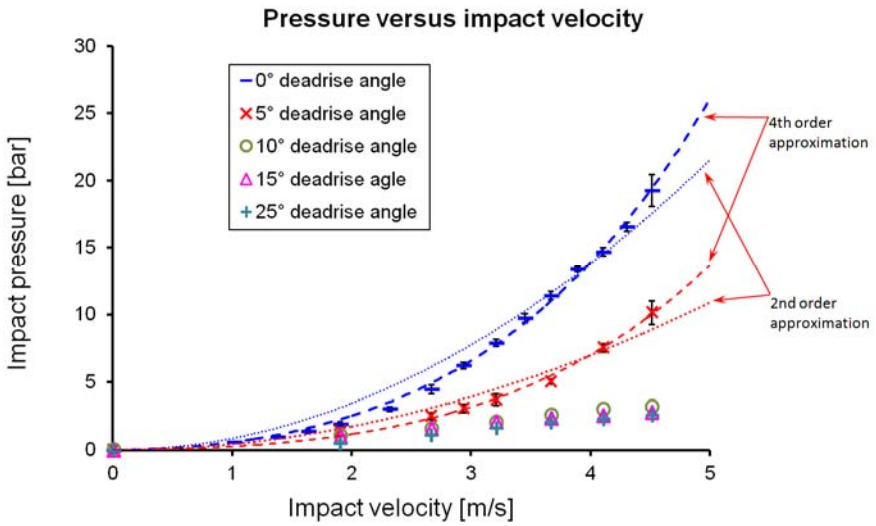

Figure 5-11: Overview of the measured pressure peak values for the slamming drop tests with the stiffened cylinder as function of impact velocity for different deadrise angles

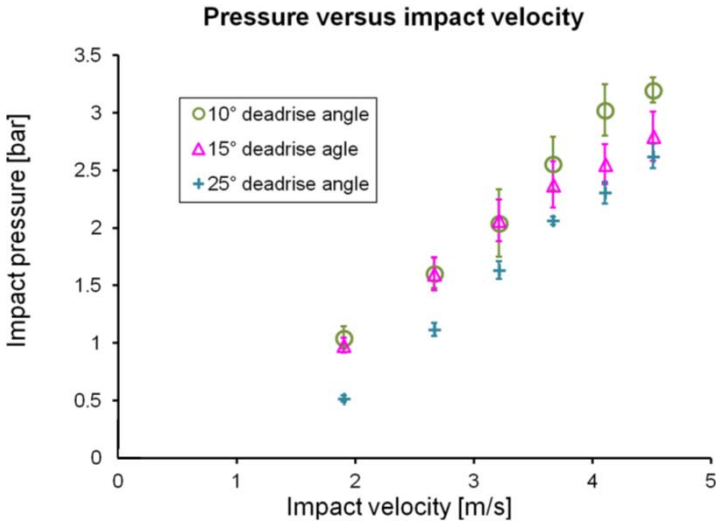

Figure 5-12: Overview of the measured pressure peak values for the slamming drop tests with the stiffened cylinder as function of impact velocity for deadrise angles 10°, 15° and 25°

Table 5-3: Overview of the measured pressure peak values for the slamming drop tests with the stiffened cylinder as function of impact velocity and deadrise angles

H [m]	U_{ava} [m/s]	Average impact pressures [bar]											
		0° deadrise angle		5° deadrise angle		10° deadrise angle		15° deadrise angle		25° deadrise angle	
		$p_{I,C}$ [bar]	σ_p [bar]	$p_{I,P}$ [bar]	σ_p [bar]	$p_{I,P}$ [bar]	σ_p [bar]	$p_{I,P}$ [bar]	σ_p [bar]	$p_{I,P}$ [bar]	σ_p [bar]
0	0	0	0	0	0	0	0	0	0	0	0
0.05	1.01	0.59	0.029								
0.1	1.37	1	0.121								
0.15	1.63	1.42	0.148								
0.2	1.9	1.94	0.171	1.41	0.68	1.05	0.097	0.98	0.064	0.52	0.027
0.3	2.32	3.06	0.167								
0.4	2.66	4.49	0.323	2.52	0.261	1.61	0.130	1.6	0.144	1.12	0.056
0.5	2.93	6.24	0.236	3.09	0.311						
0.6	3.21	7.92	0.273	3.72	0.425	2.04	0.293	2.07	0.182	1.63	0.076
0.7	3.45	9.75	0.321								
0.8	3.67	11.4	0.327	5.06	0.195	2.56	0.230	2.38	0.200	2.06	0.034
0.9	3.89	13.4	0.187								
1	4.1	14.7	0.317	7.55	0.288	3.03	0.223	2.55	0.175	2.31	0.094
1.1	4.3	16.6	0.336								
1.2	4.51	19.3	1.184	10.2	0.858	3.2	0.111	2.8	0.215	2.62	0.106

The fact that the relationship between the impact pressures and the impact velocity increases steeper than a second order curve for small deadrise angles causes the dimensionless pressure coefficient C_p to increase as function of impact velocity. This is depicted in Figure 5-13. For larger deadrise angles, the pressure coefficient tends to decrease with growing impact velocity. However, Lin and Shieh [2] concluded from their slamming drop experiments with two cylindrical test models of diameter 20 cm and 30 cm that for deadrise angles larger than 0˚, the pressure coefficient is constant with respect to the impact velocity. This contrast can probably be explained by the fact that the level of detail of the measurements performed by Lin and Shieh [2] is rather poor when considering the sampling frequency of 25 kHz which is much smaller than the minimum required sampling rate of 300 kHz as discussed in section 4.2.1.1. Since the peak pressure is thus not well captured, Lin and Shieh [2] found dimensionless pressure coefficients which seemed constant with respect to the impact velocity.

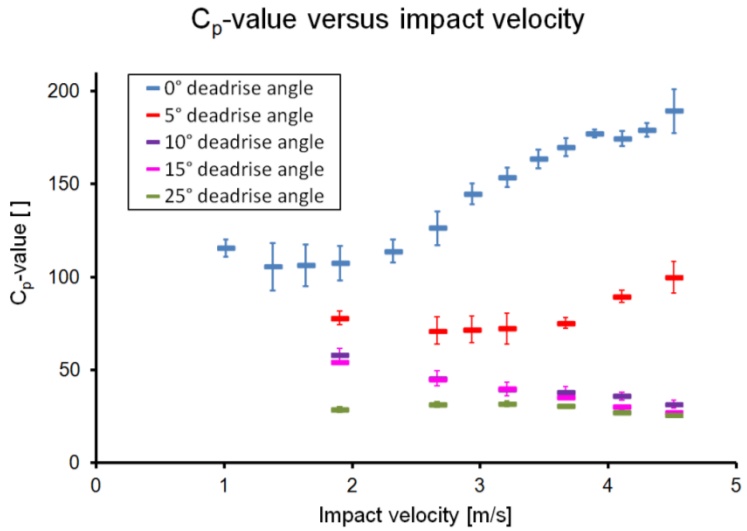

Figure 5-13: Overview of the dimensionless pressure coefficient for the slamming drop tests of the stiffened cylinder as function of impact velocity for different deadrise angles

The previous experimentally obtained slamming pressures will now be compared with the existing theories and available experimental data from the literature. It is important to notice beforehand that in all these publications, a constant entry velocity has been used to study cylindrical slamming, which is not the case for the experiments performed in this dissertation. However, it can be observed from Figure 5-5 that for the tests with the rigid cylindrical test objects the velocity during the first impact stages hardly changes, and thus can be assumed constant.

Theoretical formulations of the slamming pressures corresponding with cylindrical slamming are provided by von Karman [4], Wagner [5] and Wienke [6] (see Equations (2.46), (2.50) and (2.54)). These formulations can be converted to cylindrical coordinates using the following transformation equation (see Figure 2-11):

$$x(t) = R\sin(\theta(t)) \qquad \textbf{(5.2)}$$

$\theta(t)$ represents the deadrise angle as function of elapsed time after the first contact of the cylinder with the water. This transformation makes it possible to determine the theoretical pressure time history at a certain position of the cylindrical surface corresponding to a certain deadrise angle.

Figure 5-14 compares the time history of the experimentally recorded pressure with the theoretical calculated ones at the cylindrical surface for a deadrise angle of 5° and at an impact velocity of 4.1 m/s. The theoretical curves according to Wagner [5] and Wienke [6] are in this case the same since the considered deadrise angle is much smaller than the threshold deadrise angle of 45° for which the formulation of Wienke [6] alters (see Equation (2.54)).

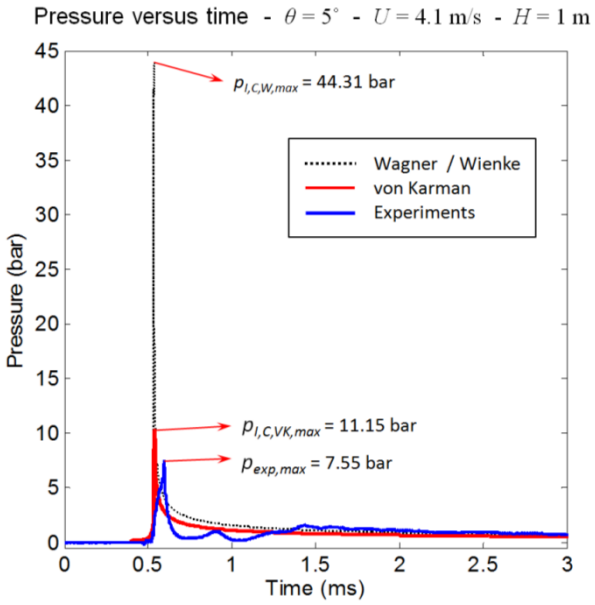

Figure 5-14: Pressure history at the cylindrical surface for an impact velocity of 4.1 m/s at a deadrise angle of 5°: Wagner, Wienke and von Karman theory compared with experiments

It can be observed that the shape of the experimental curve corresponds with the theoretical curves in the sense that the impact starts with a large and short pressure pulse and then gradually returns to zero pressure. However, it can be observed that the rise time and the duration of the pulse is larger than predicted by theory. The theory predicts unrealistic infinitely steep pressure pulses with zero rise times. Furthermore, a large difference in the magnitude of the pressure pulses can be noticed, especially when comparing the pressure pulse amplitude as recorded during the experiments with the one calculated from the Wagner and Wienke theory.

In order to better describe the difference in slamming pressure magnitude between the measurements and the theoretical descriptions, the maximum pressure values of the theoretical formulations (2.46), (2.50) and (2.54) should be evaluated. This can be done by first deriving these equations with respect to time, equalizing the obtained formulations to zero, and solving these equations towards time. The obtained solutions give the times which correspond with the maxima of the pressure histories, as function of entry velocity and deadrise angle:

$$t_{p,\max,VK} = \frac{1}{2}\frac{R\sin^2(\theta)\left(1+\sin^2(\theta)\right)}{U} \qquad \textbf{(5.3)}$$

$$t_{p,\max,W} = t_{p,\max,Wi,\theta<45^o} = \frac{1}{16}\frac{R\sin^2(\theta)\left(4+\sin^2(\theta)\right)}{U} \qquad \textbf{(5.4)}$$

Substituting these values in Equations (2.46) and (2.50) gives the pressure peak value as function of entry velocity and deadrise angle according to the theory of von Karman, Wagner and Wienke (for deadrise angles smaller than 45˚):

$$p_{I,C,VK,\max} = \frac{1}{2}\rho U^2\left(1+\frac{1}{\sin^2(\theta)}\right) \qquad \textbf{(5.5)}$$

$$p_{I,C,W,\max} = p_{I,C,Wi,\max,\theta<45^o} = \frac{1}{2}\rho U^2\left(1+\frac{4}{\sin^2(\theta)}\right) \qquad \textbf{(5.6)}$$

At the bottom of the cylinder, where the deadrise angle is 0°, these equations result in infinitely large impact pressures. The reason for this is that the previous theories are based on the assumption that the water is an incompressible fluid. During the initial stages of the impact of the cylinder with the water, the deadrise angle is so small that the wetted area increases faster than the speed of sound in water. This implies a supersonic perturbation travelling over the free surface, allowing the water compressibility to play a role [7-13]. Compressibility should thus be taken into

account during the early stages of the water penetration. This means that the theory of von Karman [4], Wagner [5] and consequently of Wienke [6] are not valid for very small deadrise angles, as was already mentioned in chapter 2. Malleron et al. [12] showed that the validity of these theories is restricted to deadrise angles larger than 4˚. To the author's best knowledge, no theories are available which describe the slamming of a cylinder on the surface of a compressible volume of water. The only theory found which considers the water to be compressible is the von Karman theory for flat plates, which is discussed in section 2.4.2.1.a. This theory gives the impact pressures according to Equation (2.19).

Figure 5-15 shows the impact pressure as function of deadrise angle for an impact velocity of 4.1 m/s according to the cylinder slamming theories of von Karman [4], Wagner [5] and Wienke [6], and the compressible flat plate theory of von Karman [4]. Also the average impact pressure values from this thesis are depicted in the graph. It can be observed that for deadrise angles smaller than 4.25°, the maximum pressure as calculated by Wagner [5] and Wienke [6] is larger than calculated by the compressible flat plate theory of von Karman [4]. However, this is unlikely to happen since the impact pressures calculated by the compressible flat plate theory of von Karman [4] represent the maximum possible impact pressure which may occur at the bottom of the cylinder. Hence, it can be assumed that it is thus for deadrise angles smaller than 4.25° that the water compressibility starts playing a role for cylindrical slamming at the considered impact velocity. This latter value of the deadrise angle is close to the threshold deadrise angle as obtained by Malleron et al. [12].

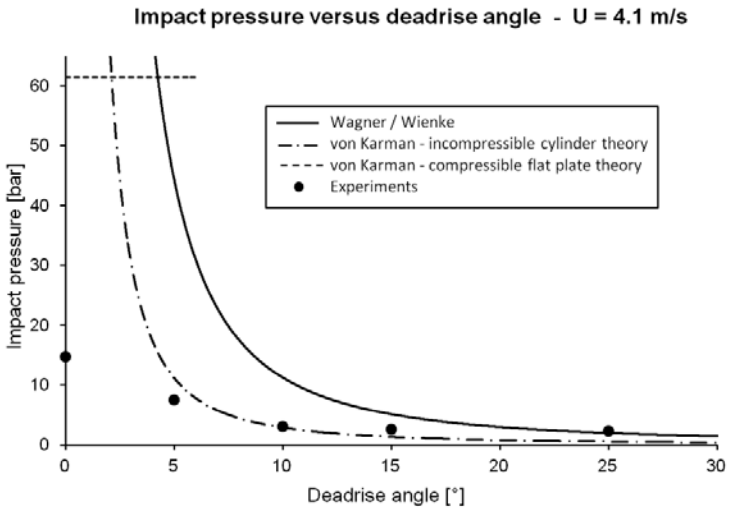

Figure 5-15: The impact pressure during slamming of a horizontal cylinder as function of deadrise angle for an impact velocity of 4.1 m/s

Furthermore, it can be observed from Figure 5-15 that for deadrise angles smaller than 15°, large deviations occur between the experimentally obtained impact pressures and the impact pressures as calculated by Wagner [5] and Wienke [6]. Compared to the theoretical results of von Karman, the experimental values correlate better for deadrise angles larger than 4°.

Concerning experimental studies on rigid cylindrical slamming, Lin and Shieh [2], and Lange and Rung [14] are the only ones found in the available literature which report impact pressures at different deadrise angles during the impact of a horizontal rigid cylinder on a flat water surface. Lin and Shieh [2] used a cylinder with a diameter of 30 cm and 20 cm, while Lange and Rung [14] tested a cylinder with a diameter of 20 cm. Furthermore, Lin and Shieh [2] tested at impact velocities of 0.76 m/s, 1.4 m/s, 1.71 m/s and 1.98 m/s. Lange and Rung [14] only published their results for 2 m/s impact speed. Figure 5-16 compares the pressure results at the bottom of the cylindrical test objects from these experimental studies with the ones obtained in this dissertation for an impact speed of 2 m/s. For the experiments from this thesis, the pressure results at 2 m/s are obtained by interpolation between the results at 1.9 m/s and 2.32 m/s using the fourth order trendline.

It can be observed from Figure 5-16 that for deadrise angles larger than 10°, the three experiment series correspond reasonably well. For deadrise angles smaller than 10°, the impact pressure results from Lin and Shieh [2] start to diverge from the other two experiment series. The difference grows as the deadrise angle decreases. The reason for this has already been mentioned before (see section 4.2.1.1): the data sampling rate of 25 kHz was insufficient to capture the true pressure peak value recorded by the pressure sensors. The reason for the fact that the impact pressure values of Lin and Shieh [2] do correspond well with the other two measurement series for deadrise angles larger than 10° is that for these deadrise angles, the pressure pulse duration increases and becomes less spiky causing a data sampling rate of 25 kHz to be sufficient for measuring the pressure peak values.

The recordings of Lange and Rung [14] have been performed with a data sampling frequency of 96 kHz. This is smaller than the proposed sampling rate of 300 kHz which was determined in section 4.2.1.1 on the basis of a slamming drop test at an impact velocity of 4.1 m/s. For impact pressures corresponding to an impact velocity of 2 m/s and especially for larger deadrise angles, the pressure pulse duration is larger than in the case as treated in section 4.2.1.1 which makes that a data sampling frequency of 96 kHz is sufficient to record the impact pressures depicted in Figure 5-16. The good correspondence between the impact pressures as measured by Lange and Rung [14] and the ones measured in this thesis confirms this.

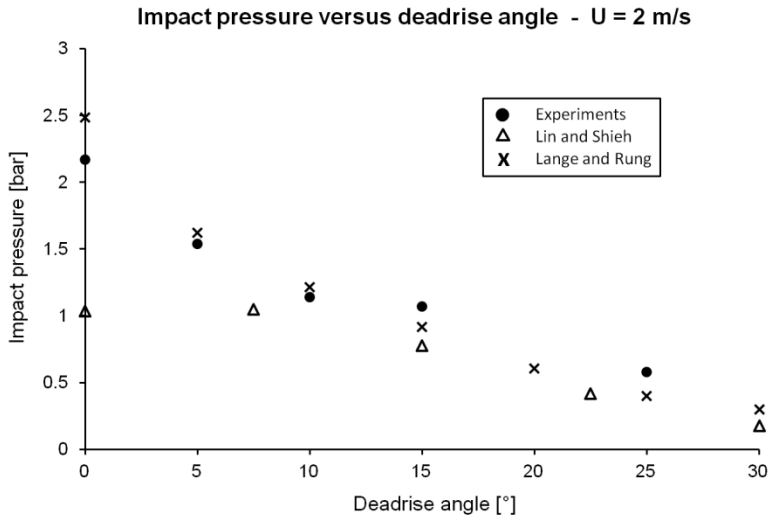

Figure 5-16: Comparison of the impact pressure measurements with the experimental data of Lin and Shieh [2] and Lange and Rung [14] for an impact velocity of 2 m/s

In the following paragraphs, the experimentally obtained impact pressures from this thesis and the ones obtained from the theories of von Karman [4], Wagner [5] and Wienke [6] are compared also for other impact velocities. Since for the considered deadrise angles (up to 25°) the theory of Wienke [6] matches the theory of Wagner [5], both theories will be denoted as the Wagner theory for simplicity. Figure 5-19 (a) – (d) compare the experimentally obtained impact pressures with the theoretically predicted ones, as function of impact velocity for deadrise angles 0°, 5° ,10° and 15°.

The impact pressures measured at the bottom of the cylinder (θ = 0°) are not compared to the cylinder slamming theory of Wagner [5] and von Karman [4] since it is shown previously that these theories are not valid for deadrise angles smaller than 4°. Instead, the compressible flat plate theory of von Karman [4] is used in Figure 5-19 (a). Furthermore, also the experimental impact pressure measurements at 25° are not compared to the mentioned cylinder slamming theories since it was shown by Dobrovol'skaya [15] that due to their blunt body approach both theories are not valid for deadrise angles larger than 20°. The measurements at 25° deadrise angle are thus not taken into consideration in the present comparison.

In Figure 5-19 (a) large differences are found between the compressible flat plate theory of von Karman [4] and the experiments, indicating that the compressible flat plate theory of von Karman [4] is not a good representation of the true impact pressures acting on cylindrical structures during vertical water slamming.

Large differences can also be found between the Wagner theory for cylinder slamming [5] and the experimentally obtained impact pressures for the deadrise angles 5°, 10° and 15°. For these cases, the Wagner impact pressures are much larger than the corresponding experimental ones. When comparing the experimental results to the von Karman theory for cylinder slamming [4], it is observed that the correspondence is much better than for Wagner [5] for the deadrise angles 5° and 10°. This is quite surprising since the theoretical description of Wagner takes the water uprise during water penetration into account, and is thus expected to be more accurate. For the deadrise angle of 15°, the correspondence between von Karman predictions and the experimental recordings is less: the theoretically calculated impact pressures are much smaller than the experimentally recorded ones.

A possible explanation for the large differences found between the experimentally measured impact pressures and the theoretically predicted ones for some of the tested deadrise angles may be the fact that the pressure sensors measure over a certain diaphragm area. This means that the pressure measured at a certain point of the circumference of the cylinder is always an average of the pressures occurring in the adjacent points which correspond to the sensor area. This is not the case for the von Karman [4] and Wagner [5] theory where it is possible to determine the pressure exactly in one point at the circumference of the cylinder.

In order to assess the influence of this effect, the von Karman [4] and the Wagner [5] pressures must be averaged over the sensor area. Therefore, it is first necessary to consider Equations (2.46) and (2.50) at a certain moment of time as function of deadrise angle (by performing a transformation to cylindrical coordinates). As an example, Figure 5-17 shows the pressure profile over the cylindrical surface at the moment that the maximum pressure is reached at 5° deadrise angle for an impact velocity of 4.1 m/s. Averaging the theoretical pressure profiles over the sensor area can be performed as following:

$$p_{I,C,VK/W,avg} = \frac{\int_{\theta}^{\theta+\Delta\theta} p_{I,C,VK/W}\, d\theta}{\Delta\theta} \qquad \textbf{(5.7)}$$

With: $\Delta\theta$ = the angle corresponding with the sensor area [°].

Since the sensors used in this paper have a diaphragm with a diameter of d_{sens} = 5 mm, the angle $\Delta\theta$ can be calculated according to Figure 5-18 as:

$$\Delta\theta = 2\arcsin\left(\frac{d_{sens}/2}{R}\right) = 1.82° \quad \textbf{(5.8)}$$

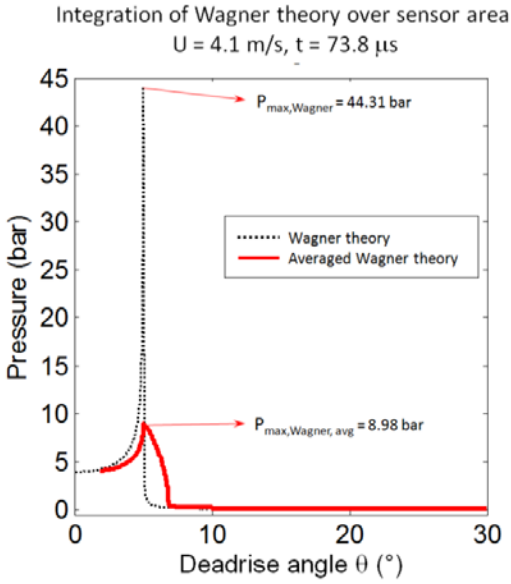

Figure 5-17: Wagner theory and its averaged version as function of deadrise angle for an impact velocity of 4.1 m/s at the moment that the peak value is reached at 5° deadrise angle

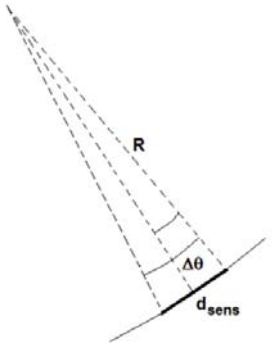

Figure 5-18: The angle Δθ corresponding with the pressure sensor diaphragm

The full red curve in Figure 5-17 shows as an example the averaged Wagner pressure distribution over the cylindrical circumference at the moment that the maximum pressure is reached at 5°. It is found that this new pressure profile has a much smaller peak value. The pressure peak values corresponding to the averaged Wagner and von Karman theories are depicted in Figure 5-19 (a)-(d) as function of impact velocity for the deadrise angles 5°, 10° and 15°.

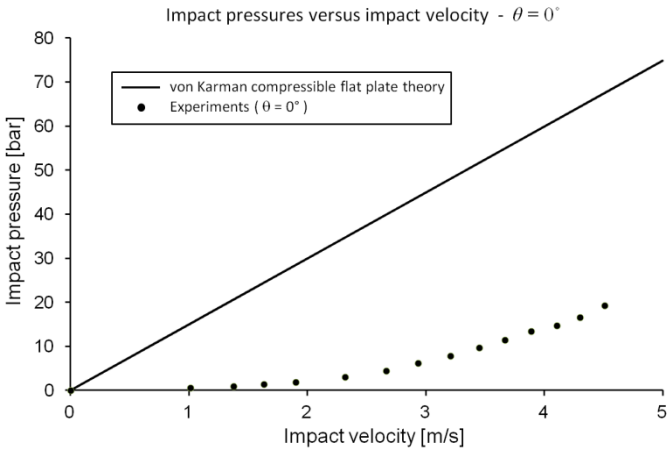
Impact pressures versus impact velocity - θ = 0°
von Karman compressible flat plate theory
Experiments (θ = 0°)
Impact pressure [bar]
Impact velocity [m/s]

(a)

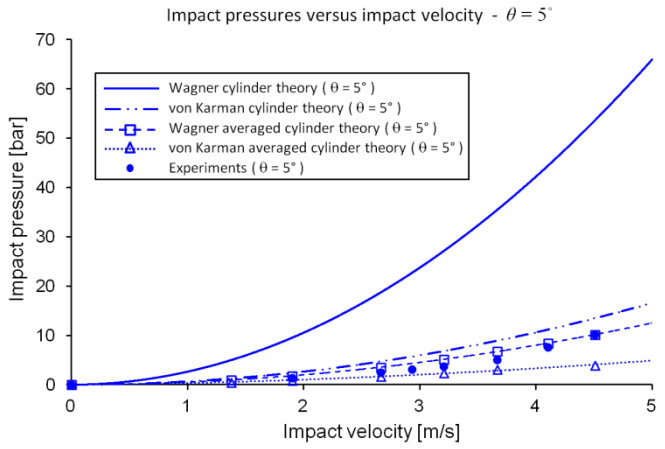
Impact pressures versus impact velocity - θ = 5°
Wagner cylinder theory (θ = 5°)
von Karman cylinder theory (θ = 5°)
Wagner averaged cylinder theory (θ = 5°)
von Karman averaged cylinder theory (θ = 5°)
Experiments (θ = 5°)
Impact pressure [bar]
Impact velocity [m/s]

(b)

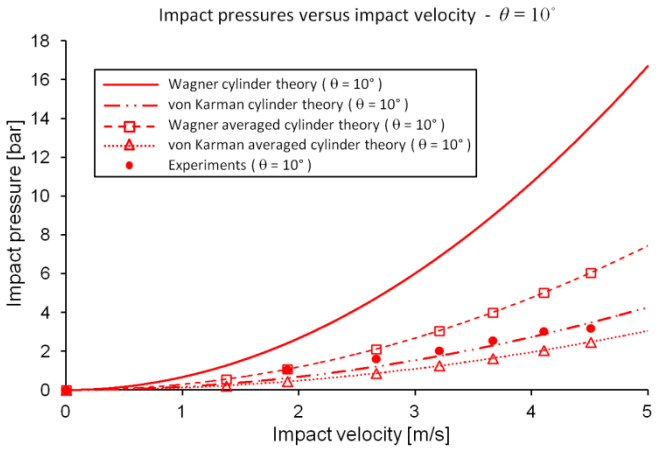
Impact pressures versus impact velocity - θ = 10°
Wagner cylinder theory (θ = 10°)
von Karman cylinder theory (θ = 10°)
Wagner averaged cylinder theory (θ = 10°)
von Karman averaged cylinder theory (θ = 10°)
Experiments (θ = 10°)
Impact pressure [bar]
Impact velocity [m/s]

(c)

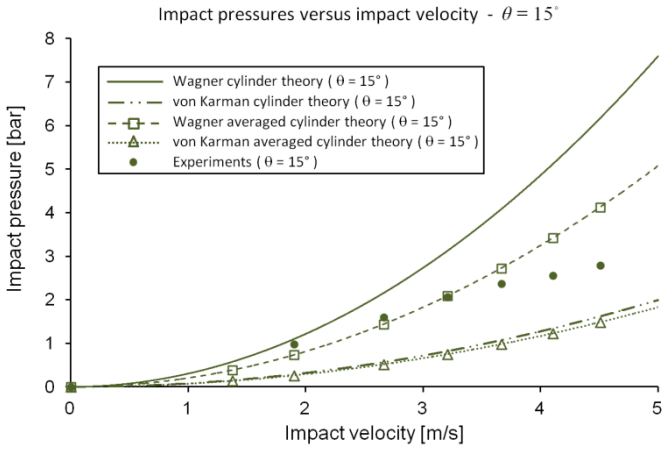

(d)

Figure 5-19: Comparison of the experimentally obtained impact pressures with the theoretically predicted ones as function of impact velocity for the following deadrise angles: 0° (a), 5° (b), 10° (c), 15° (d)

When the averaged von Karman theory is compared with the experimentally obtained impact pressures, it can be observed that there is no correspondence anymore. In contrast with these findings, it is found that the correspondence of the experimental results with the Wagner theory after averaging has improved. However, it is found that the theoretical impact pressures calculated by the averaged Wagner theory are still a bit higher than the experimental values. This latter difference may be explained by the fact that in the theoretical approximations, a constant water entry velocity is assumed while this is not the case in the experiments. In the experiments the body first accelerates under gravity and then decelerates due to the forces acting on it during water impact. However, it has been observed that in the time span of the pressure pulses, the change in velocity is small which makes this effect rather limited (see Figure 5-5).

Another contribution to the difference in impact pressure values between the experiments and the averaged Wagner theory might be the fact that the cylindrical model used during these tests is not theoretically perfect rigid. To investigate this effect, the rigidity of the object has been measured by performing a compression test with the cylinder clamped between the grips of a tensile machine. A stiffness value of 228 N/mm was measured which indicates that this test object can be assumed stiff (as compared to the stiffness values of the deformable cylinders with similar diameter (D = 31.5 cm) – see Table 5-5), but not perfectly rigid. The stiffness of the used cylinder is from that order that it can explain the measured impact pressures to be smaller than the theoretical predicted ones.

It can thus be concluded that the Wagner theory is the best approximation for the true impact pressures travelling over the cylindrical surface during rigid cylindrical water slamming for deadrise angles larger than 4° and smaller than 20°. It may thus also be concluded that the true impact pressures occurring at the cylindrical surface are actually much larger than being measured, since the pressure sensors average the impact pressures over the sensor area. This is an important consideration for design purposes.

5. 2. 2. Impact forces

For industrial purposes, it is much more interesting to determine the impact loads in terms of impact forces, since these can be applied to calculate the maximum stresses in the constructions which are important for design purposes. This is illustrated by the larger number of literature sources focusing on impact forces rather than on impact pressures. In the present section, the slamming forces corresponding to pure rigid cylindrical slamming are assessed from the force recordings for the three types of rigid cylindrical test objects.

5. 2. 2. 1. Force time history

As an example, the recorded impact force for a slamming drop test with the stiffened cylinder for a drop height of 1 m is illustrated in Figure 5-20. It is important to consider that the force from this graph has been obtained by applying the calibration factor for the complete load cell combination together with Equation (4.3) on the raw data, in order to convert the measured force to impact force. Besides this impact force, the graph also depicts the impact pressure at the bottom of the cylinder for the same drop height to indicate the difference in duration and time of occurrence between the two types of load recordings. It is observed that the global force reaches its maximum 3.3 ms later than the pressure and that the load pulse lasts much longer than the pressure pulse. The duration of the force pulse is about 5 ms while for the pressure at the bottom of the cylinder a duration of 200 μs has been measured. The fact that the impact forces are more spread in time indicates that the impact forces build up more gradually than the very localised and short-term impact pressures. This can be explained by the fact that at the very first moment that the cylinder touches the water, the contact between the cylindrical surface and the water is approximately a line contact. The impact pressure is large, but the wetted area is very small. This yields that during the very initial stages of the slamming event almost no impact force is measured although the impact pressure reaches its maximum value at that moment. As the cylinder is then gradually penetrating the water, the wetted area increases and the force grows. At a certain moment the force reaches its maximum value. The wetted area at that moment corresponds with a

submergence up to 30° of the cylindrical circumference, which is illustrated in Figure 5-21.

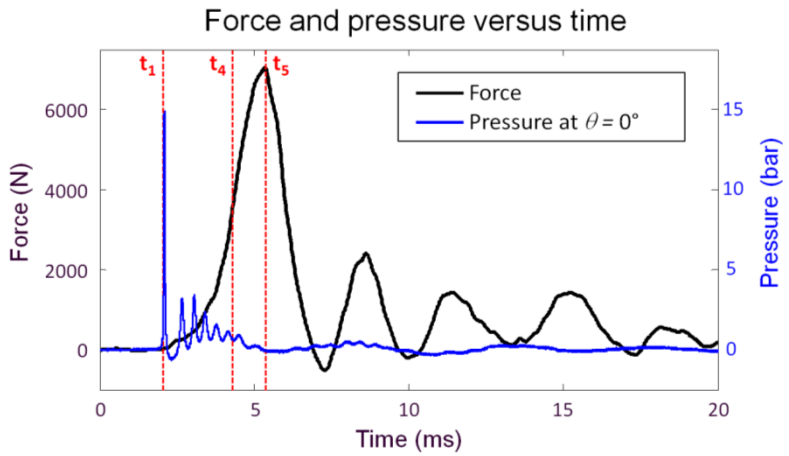

Figure 5-20: Time plot of the impact force and impact pressure at the bottom of the stiffened cylindrical test model for a slamming drop test with a drop height of 1 m

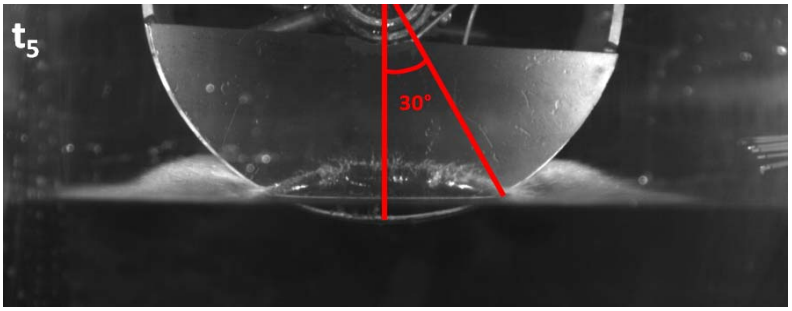

Figure 5-21: Camera image at the time frame of the maximum impact force during a slamming drop test with the stiffened cylindrical test model at a drop height of 1 m

After the first force pulse in the force time history of Figure 5-20, oscillations can be observed similar to the ones which were found in the impact pressure recordings at the bottom of the cylinder. These latter oscillations were allocated to the repeated compression and expansion of the air pocket locally at the bottom of the cylinder. The oscillations observed for the force recordings are spread out in a much larger time frame and have a totally different oscillation frequency. Hence, they cannot be allocated to the effect of the air pocket.

Structural vibrations might explain the oscillations in the force history. To verify this possibility, a frequency analysis was performed on the impactor with the stiffened cylindrical test model. In a first instance, this frequency analysis was

performed numerically on a CAD model, as shown in Figure 3-7. The FEM solver package LS-DYNA was used to calculate the eigenmodes of this model. More details on the details of these simulations can be found in the PhD dissertation of Vepa [16]. A large number of eigenmodes was found, but the most of them comprised structural modes in parts of the structure which have only small effects on the force and pressure measurements (e.g. bending mode of the vertical top structure bar, twisting mode of the horizontal top structure bar). The first mode which was found having a large effect on the force sensor recordings is a vibration mode of the bottom impactor plate at 198 Hz. Figure 5-22 illustrates the deformation mode of the impactor at this frequency for three different time steps. The true deformations are much enlarged in these illustrations in order to visualize the mode shape. Especially the views from the side of the load cell combination plates clearly show that it is the bottom impactor plate which vibrates in this mode. The plate seems to be flapping which causes the plate to deform like a saddle surface.

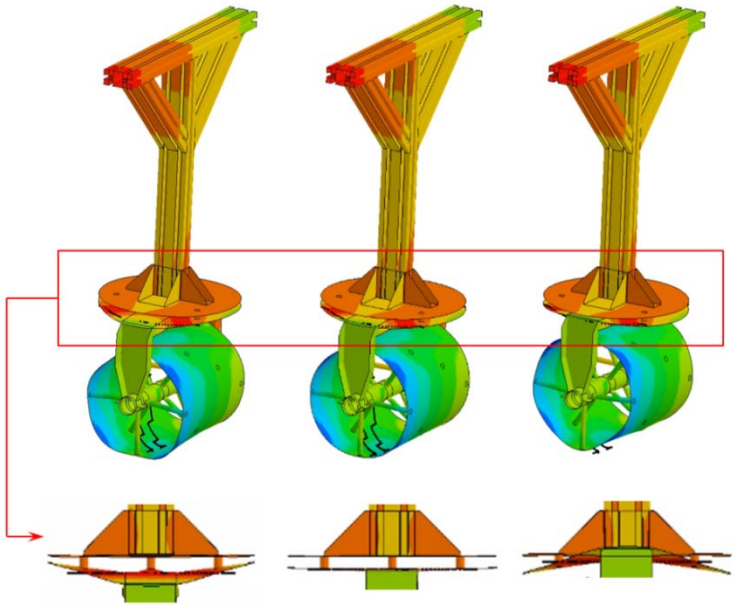

Figure 5-22: Mode shape of the impactor at an eigenfrequency of 198 Hz as calculated by the FEM package LS-DYNA

The largest deformation of the bottom impactor plate in this vibration mode occurs at the locations where the vertical parts of the U-shaped support structure of the cylindrical test model arrive at the bottom impactor plate. This explains why exactly this vibration mode is exited during the tests: it is at these locations that the impact force is introduced on the load cell combination, as is illustrated in Figure 5-23. It is the sudden water impact of the cylinder which most probably triggers the depicted

vibration mode causing an alternate loading and unloading of the force sensors. This reflects in an oscillation in the recorded force which eventually dampens out in time.

Figure 5-23: Illustration of the force introduction on the load cell combination

In order to verify the results from the numerical simulation, an experimental modal analysis was performed on the impactor. For this purpose, a pulse load was generated at different locations of the impactor by means of a short hammer impact while the response of the bottom impactor plate was recorded by means of six accelerometers distributed over the bottom surface of this plate. Figure 5-24 presents the position of these accelerometers. The schematic illustration depicts a view from the underside of the bottom impactor plate.

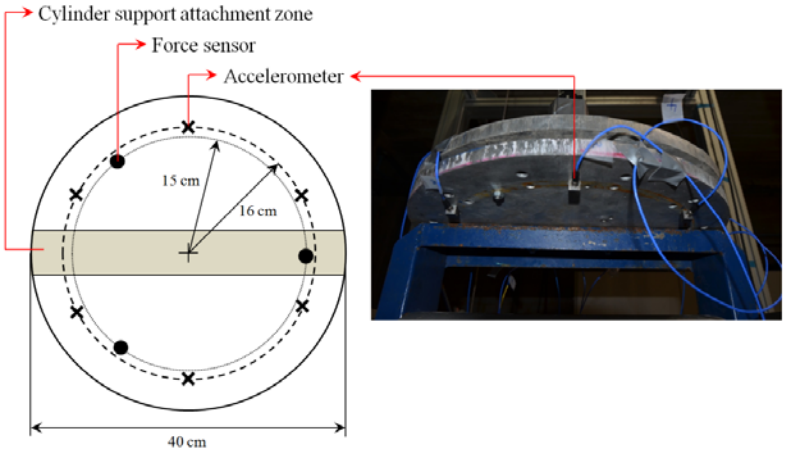

Figure 5-24: Overview of the positions of the accelerometers on the bottom surface of the bottom impactor plate

Hammer impact pulses were generated at seven different locations on the cylindrical surface of the stiffened cylinder and at the underside of the bottom impactor plate. Figure 5-25 shows the average spectral density of the six accelerometers, averaged over the seven experiments performed. A large spike in the spectral density can be observed exactly at the same frequency (198 Hz) as was calculated by the FEM model. This confirms the validity of the FEM model and confirms the presumption that structural vibrations are causing the oscillations in the force recordings.

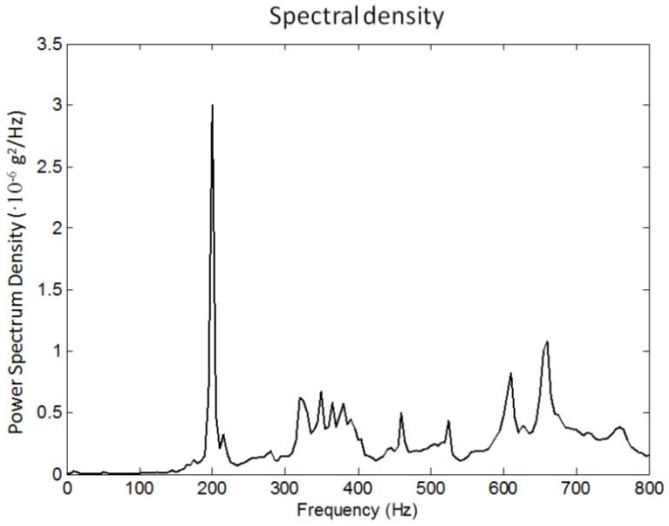

Figure 5-25: Average spectral density of the accelerometer outputs from the modal analysis test

Figure 5-26 shows the spectral density of the force recording as depicted in Figure 5-20. This spectrum shows peaks at frequencies of 30 Hz, 90 Hz, 190 Hz and 300 Hz. It is the large peak value observed at a frequency of 300 Hz which mainly represents the oscillation in the force time history since the period of this oscillation is approximately 3.3 ms as can be extracted from Figure 5-20. The reason for the difference between this oscillation frequency observed during the slamming experiments and the eigenfrequency of 198 Hz which was obtained from the modal analysis and at which the impactor plate is expected to vibrate due to an impact load is not very clear. It is supposed that one of the reasons for this shift in frequency is a difference in boundary conditions of the impactor when it is set up for the modal analysis and when it is penetrating the water during a slamming experiment. Furthermore, it is assumed that also a difference in load inducing instrument (hammer versus water) between both cases might have a contribution to the frequency shift.

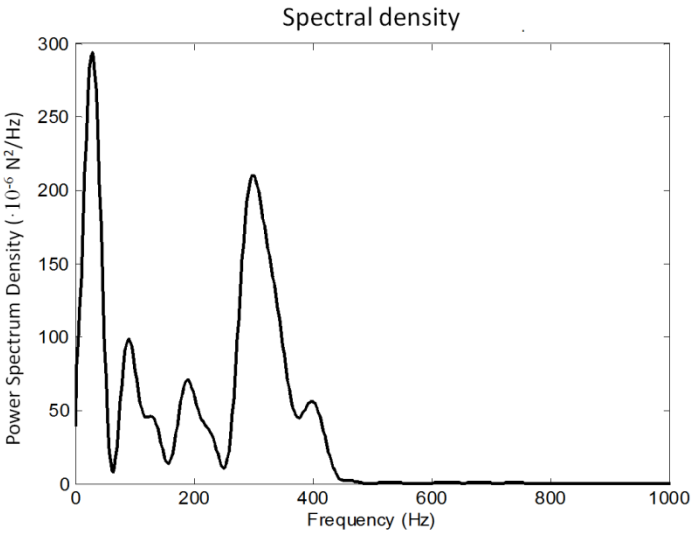

Figure 5-26: Spectral density of the force recording as depicted in Figure 5-20

From the previous paragraphs, it may be thus concluded that the oscillations in the force recordings from the stiffened cylinder are not characteristic to the slamming phenomenon, but are due to structural vibrations in the experimental setup. The forces which are recorded by the force sensors thus do not exactly correspond in this case with the true forces acting on the cylindrical model. The peak values of the force recordings may therefore not be interpreted as the slamming force values acting on this test model in the sense that they do not exactly represent the forces which are introduced purely because of pushing away a certain amount of water (added mass).

The bottom impactor plate vibrations have no consequences for the pressure measurements since oscillations at 198 Hz or 300 Hz have not been observed in these recordings. The vibrations are thus only localized at the bottom impactor plate and are not present in the cylindrical test model.

Although the forces recorded during the water impact of the stiffened cylinder do not represent the true slamming forces acting on this cylindrical model, they do represent the true forces acting inside the impactor construction during the slamming process. This results in the important indication that, due to the impulse character of the slamming impact loads, eigenmodes of a certain part of a structure prone to slamming may be excited, resulting in forces inside the structure which are larger than the forces acting on the interaction surface between the water waves and the structure. The excitation of certain eigenmodes during slamming impact might thus cause larger stresses into the structure than the ones which would be expected only

because of the magnitude of the slamming force. Analogue findings were also reported by Faltinsen [17], Miao [18] and Ionina [19]. In the shipbuilding industry, the vibrations caused by slamming are known under the terminology of springing and whipping [20]. It is only during the past ten years that excessive research has been performed on this springing and whipping effect [21-24]. However, in the recommendation rules made up by classification societies such as Det Norske Veritas (DNV) [25], no design guidelines are yet included which take into account these springing and whipping effects which are sometimes responsible for serious damage, especially in the form of fatigue damage.

A detailed study on the springing and whipping phenomenon and the accompanying loads is not within the scope of this dissertation. The original goal is to determine the difference in pure slamming loads caused by the water impact of rigid and deformable bodies. In order to enable the measurement of these pure slamming loads during the vertical impact of a rigid cylinder, the occurring structural vibrations in the impactor must thus be avoided. It is for this purpose that the plaster and concrete cylindrical test objects as described in section 3.4.1.1.b were developed. Since these test objects were elaborated as cylindrical segments, they could be firmly fixed with their flat side to the bottom impactor plate. As such, the impact forces could be much more distributed over the entire surface of the bottom impactor plate which was necessary to suppress its vibrations.

A time plot of the recorded force for a slamming drop test with the plaster cylindrical test object for a drop height of 1 m (see Figure 5-27) shows that the magnitude of the oscillations has now drastically been reduced. This indicates that the vibrations of the bottom impactor plate are successfully suppressed. However, smaller oscillations are still present which prevent the exact determination of the pure impact force characteristic to cylinder slamming. When compared to the force time history of the stiffened cylindrical test object of Figure 5-20, some other differences can be observed:

- The slamming force pulse caused by the water impact of the plaster cylindrical model rises much faster and the peak value is obtained much earlier than in the case of the stiffened cylindrical test object. The peak value of the force is now obtained at a submergence corresponding with a wetted area up to 16° of the cylindrical circumference (see Figure 5-28).

- The slamming force peak value is smaller than for the case of the stiffened cylindrical test object.

- After the slamming force pulse has occurred, the force does not swing to negative values as was the case for the stiffened cylinder, but oscillates around a

slowly decreasing average positive force value for more than 10 ms. The frequency of this oscillation is smaller as compared to Figure 5-20 for the stiffened cylinder, which confirms that the structure is more rigid than before and thus the vibration of the bottom impactor plate is suppressed (with increasing stiffness, the natural frequency of a system increases – see Equation (2.10)). However, the vibrations are not eliminated completely.

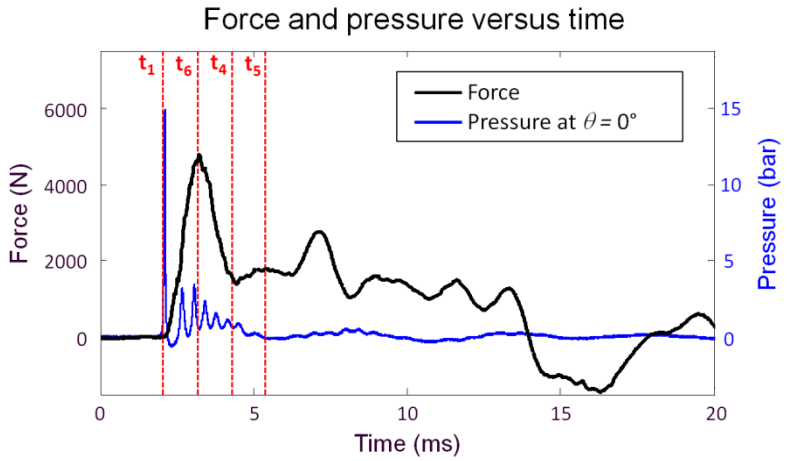

Figure 5-27: Time plot of the impact force recorded during a slamming drop test with the plaster cylindrical segment for a drop height of 1 m, compared to the impact pressure recording measured at the bottom of the stiffened cylindrical test model

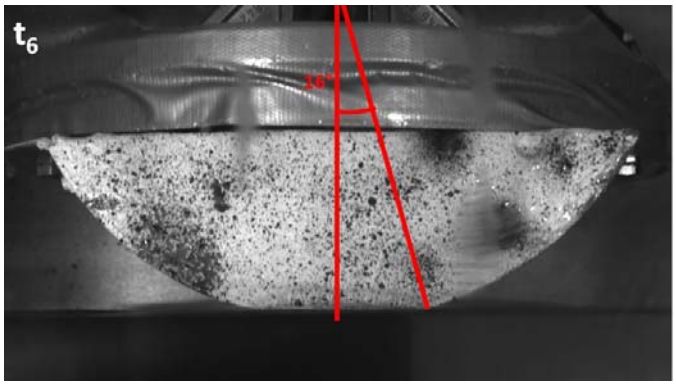

Figure 5-28: Camera image at the time frame of the maximum impact force during a slamming drop test with the plaster cylindrical test model at a drop height of 1 m

At the time t = 14ms, a negative drop in the impact force is recorded. This occurs at the moment that the motion of the test object is stopped by the action of the dampers on the setup. This time moment has been tuned to make it correspond with the

moment of full submergence of the cylindrical segment. The force history after t = 14 ms is thus not relevant anymore.

Impact forces during vertical drop experiments with a rigid cylindrical test object were also recorded by Campbell and Weynberg [26], Miao [18] and Lange and Rung [14]. All of these tests were done with a forced impact at constant entry speed. Campbell and Weynberg [14] used a cylinder with a diameter of 10.2 cm. The length, the wall thickness and the material of the test model were not reported. Miao [18] used a standard PVC pipe of 12.5 cm diameter, 25 cm length and 3.7 mm wall thickness. Lange and Rung [14] used two test models both with a diameter of 20 cm, and with lengths of 50 cm and 70 cm. The materials and the wall thicknesses of the tubes were not specified.

Figure 5-29 shows some typical force histories as published by Campbell and Weynberg [26], Lange and Rung [14] and Miao [18]. Lange and Rung [14] reported a constant impact speed of 3 m/s for the presented data. Campbell and Weynberg [26] and Miao [18] did not report the impact speed corresponding to the depicted force histories. All of the presented force histories are expressed in terms of the dimensionless slamming coefficient, and the time is represented as a dimensionless submergence factor. Furthermore, the force history from Figure 5-27 corresponding to the impact force for the plaster cylinder for an impact velocity of 4.1 m/s has also been included in the graph. Besides the differences in magnitude, it can be observed that all the depicted curves show oscillations at different frequencies. This indicates that the force recordings of the previously mentioned authors were also contaminated with vibrations due to the excitation of one or more eigenmodes in the experimental setup. Especially for the recordings of Campbell and Weynberg [26], which are used as standard values in the DNV guidelines [25], large oscillations are present which also reach large negative values. All this again confirms the importance of the dynamic behaviour of the construction during water slamming.

An accurate recording of the force generated purely by the slamming phenomenon can thus only be performed when eliminating the vibrations of the experimental setup causing oscillations in the measurements. For the constant velocity experiments of Campbell and Weynberg [26] and Miao [18], this issue has been solved by fitting appropriate curves through their oscillatory force time histories. Averaging these curve fits over their entire experimental campaign at different impact speeds resulted in Equations (2.70) and (2.71) for the slamming coefficient as obtained by Campbell and Weynberg [26] and Miao [18] respectively. However, no clear explanations were reported in how exactly they obtained the best fitting curves.

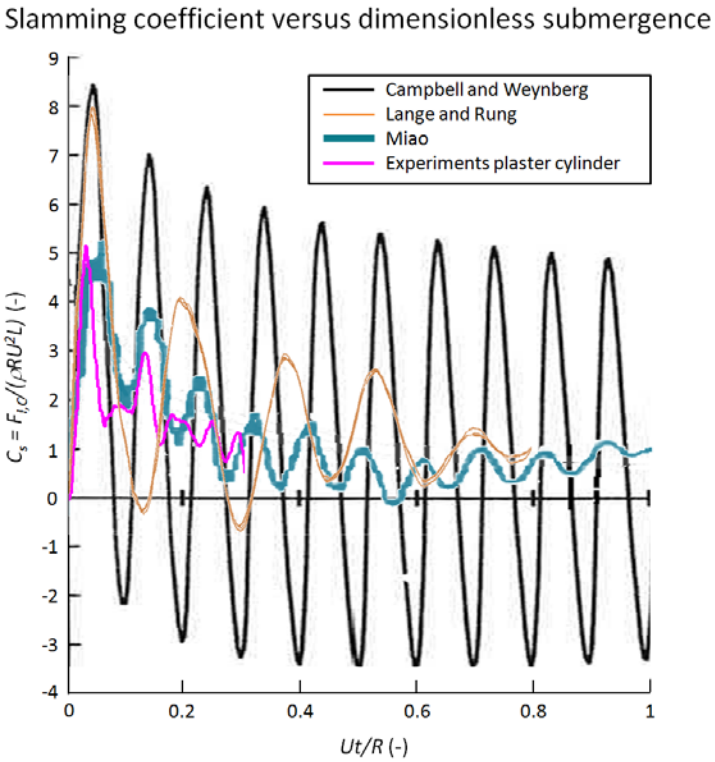

Figure 5-29: The experimentally obtained force time history of the plaster cylinder for an impact speed of 4.1 m/s compared to the experimental results of Campbell and Weynberg [26], Lange and Rung [14] and Miao [18]

A plot of Equations (2.70) and (2.71) as function of dimensionless submergence is shown in Figure 5-30. Also the experimental curve recorded during the impact of the plaster cylindrical test model has been included in this graph. Furthermore, the theoretical slamming coefficients according to von Karman [4] (Equation (2.58)), Wagner [5] (Equation (2.62)), Wienke [6, 27] (Equation (2.62) and (2.64)), Greenhow and Yanbao [28] (Equation (2.65)), Wellicome [29] (Equation (2.66)) and Kaplan and Silbert [30] (Equation (2.69)) elaborated for rigid cylindrical slamming at constant entry speed have been added to complete this diagram. All the plots are valid for an impact speed value of 4.1 m/s. All the plotted empirical and theoretical slamming force time histories do not exhibit oscillations and might thus be a good representation of the pure slamming force.

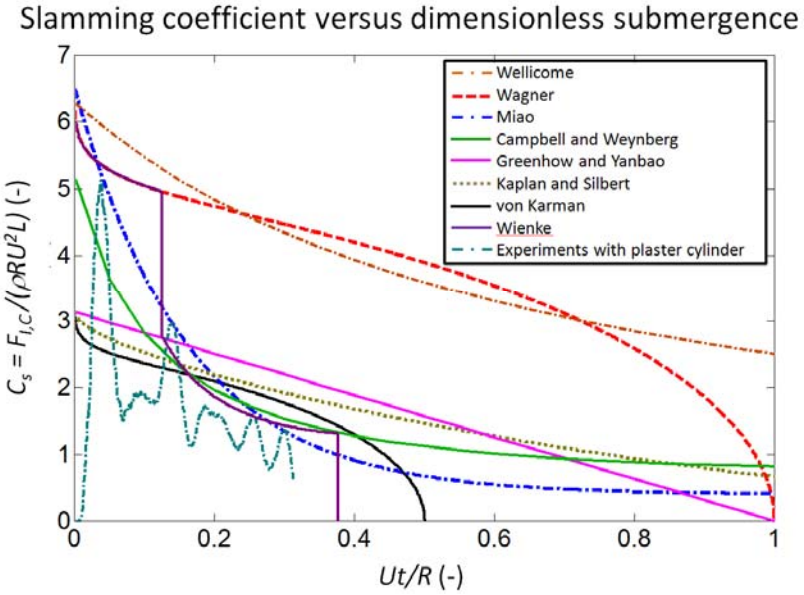

Figure 5-30: The experimentally obtained force time history of the plaster cylinder for an impact speed of 4.1 m/s compared to the empirical relations of Campbell and Weynberg [26] and Miao [18] and the theoretical formulations of Wellicome [29], Wagner [5], Greenhow and Yanbao [28], Kaplan and Silbert [30], von Karman [4] and Wienke [6, 27]

In the previous paragraphs, it was shown that the force results obtained during the slamming drop tests with the concrete and plaster cylindrical test models are the best approach for the pure slamming force corresponding to rigid cylindrical slamming since the structural vibrations were largely suppressed in these tests. The empirical or theoretical equation which is the best description of the true and pure slamming force can thus be identified as the curve which is the best approximation for these latter experimental results. However, no conclusions can yet be drawn from the comparison made in Figure 5-30, because the graph shows the results for only one impact velocity. In order to enable general conclusions, comparisons for other impact velocities are necessary. This is done in the following section, which describes the impact force values of the experiments and the different models as function of impact velocity.

5. 2. 2. 2. Force impact values

Figure 5-31 and Table 5-4 give an overview of the experimentally obtained impact forces for the concrete and plaster test model, as function of impact velocity.

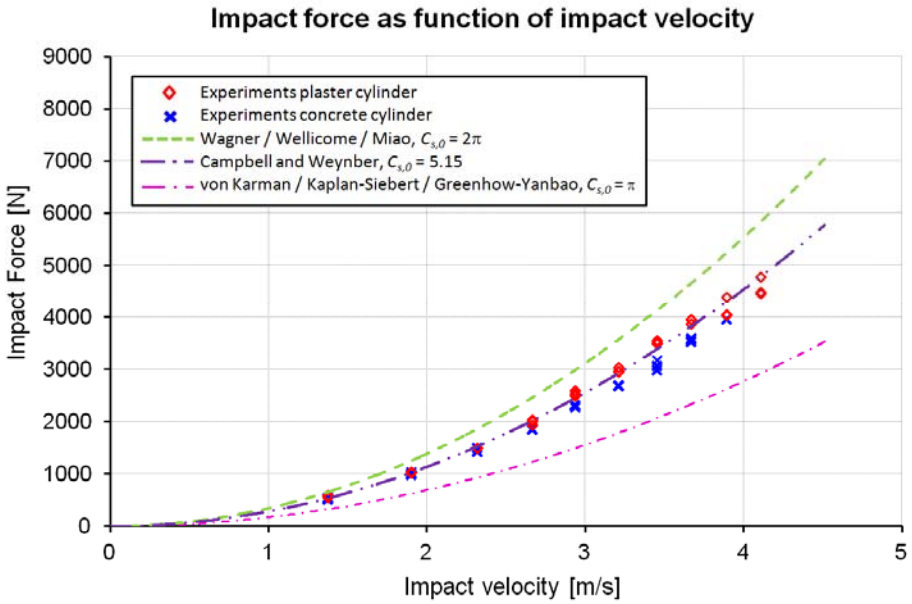

Figure 5-31: Overview of the force peak values as function of impact velocity for the experimental recordings with the plaster and concrete cylindrical test models and as calculated from the empirical and theoretical formulations

Two main observations can be drawn from the plot:

- It can be observed that the results from the plaster and concrete cylindrical test object are very close to each other. Only a slight difference can be observed which is in the range of the scatter for some of the tested impact velocities. Hence, this difference is assumed negligible. This observation confirms the fact that the impact forces for cylindrical slamming are independent from the mass of the cylindrical objects, as was shown in section 5.1 for the mass range of this dissertation.

- If the average force peak values of the experiments are considered as function of the tested impact velocity, then it can be observed that these impact force values follow a second order relationship with respect to the impact velocity for both cylindrical test models.

Table 5-4: Overview of the force peak values as function of impact velocity for the experimental recordings with the concrete and plaster cylindrical test models

H [m]	U_{avg} [m/s]	Impact forces [N]			
		Concrete model		Plaster model	
		$F_{I,C}$ [N]	σ_F [N]	$F_{I,C}$ [N]	σ_F [N]
0	0	0	0	0	0
0.1	1.37	534.22	19.74	571.11	19.46
0.2	1.90	1004.10	31.19	1034.74	5.17
0.3	2.32	1453.72	41.27	1499.76	1.55
0.4	2.66	1850.70	1.28	1994.59	50.77
0.5	2.93	2298.36	26.40	2545.16	45.38
0.6	3.21	2687.60	7.96	2983.61	46.92
0.7	3.45	3092.59	89.69	3428.58	188.16
0.8	3.67	3562.94	43.40	3924.50	45.56
0.9	3.89	3955.82	-	4156.98	206.94
1	4.10	-	-	4580.20	175.36
1.1	4.30	-	-	-	-
1.2	4.51	-	-	-	-

This last conclusion can also be drawn when calculating the slamming coefficients from the impact force values and plotting these as function of impact velocity (see Figure 5-32). This graph shows only little variation of the average slamming coefficients of the concrete and plaster cylinders with a variation in impact velocity. This constant relation indicates a second order relationship between the force peak values and the impact velocity (see Equation (2.58)).

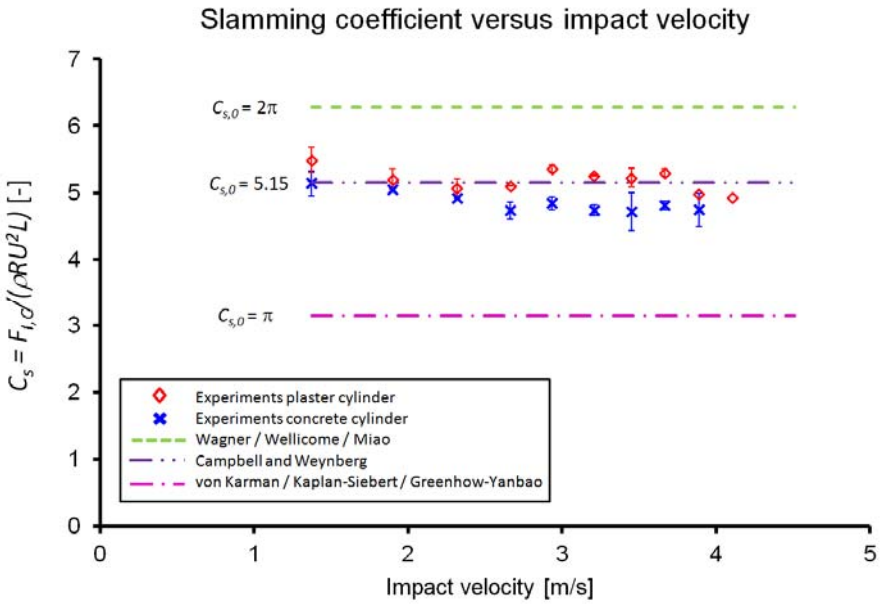

Figure 5-32: Overview of the maximum slamming coefficients as function of impact velocity for the experimental recordings as well as for the empirical and theoretical formulations

The fact that the slamming coefficient calculated from the experimentally recorded impact forces of the two types of cylindrical test objects is more or less constant as function of impact velocity has important consequences for the comparison made in Figure 5-30 concerning the force time histories. It means that this graph is in a reasonable extent representative for all tested impact velocities, since the forces are expressed in terms of the slamming coefficient. Hence, some conclusions can be drawn with respect to the comparison of the experimentally recorded slamming force time histories from this thesis and the empirical and theoretical formulations found in the literature from this graph only.

Therefore, it is important to notice that in Figure 5-30 the theoretical and empirical equations all converge to three kinds of slamming coefficient values for t = 0 ms, which simultaneously correspond to the maximum slamming coefficient values of these empirical and theoretical formulations. For the formulations of Wagner [5], Wienke [6, 27], Wellicome [29] and Miao [18], a maximum initial slamming coefficient $C_{s,0}$ of 2π is found. According to Campbell and Weynberg [26] this initial slamming coefficient is 5.15, and von Karman [4], Kaplan and Silbert [30] and Greenhow and Yanbao calculated an initial slamming coefficient equal to π. These three kinds of maximum slamming coefficients are also plotted in Figure 5-31 (converted to impact force) and Figure 5-32 as function of impact velocity.

From section 5.2.2.1, it was already concluded that the impact forces recorded during the slamming drop tests with the concrete and plaster cylindrical test objects are considered as the best approximation for the pure and undisturbed slamming force inherent to cylinder slamming, since the structural vibrations were largely reduced. However, small oscillations were still present in the force recordings, indicating that the structural vibrations were not completely eliminated. Hence, the maximum slamming coefficient as obtained during the slamming drop tests with the concrete and plaster cylindrical test objects overestimates in a certain extent the maximum slamming coefficient characteristic for pure cylinder slamming due to the oscillations in the recordings. The fact that the slamming coefficient corresponding with the experimental results of the concrete and plaster cylinder more or less corresponds to the slamming coefficient value of 5.15 as empirically obtained by Campbell and Weynberg [26] indicates that the maximum slamming coefficient characteristic for pure cylinder slamming must be smaller than the latter value and certainly smaller than the maximum slamming coefficient value of 2π as predicted by Wagner [5], Wienke [6, 27], Wellicome [29] and Miao [18].

Using the experimental results from this thesis, it is thus not possible to determine the exact value of the maximum slamming coefficient corresponding to pure rigid cylindrical slamming, due to structural vibrations affecting the slamming force measurements. Though, it is possible to calculate an approximate value of the maximum slamming coefficient corresponding to pure rigid cylindrical slamming from the experimental data. This can be done by determining a smooth best fitting curve through the oscillating force recordings from the concrete and plaster cylindrical models, similarly as done by Campbell and Weynberg [26] and Miao [18]. It was decided to fit both a hyperbolic curve and a exponential curve from the same type as used by Campbell and Weynberg [26] and Miao [18] respectively through the force result from Figure 5-30 corresponding to the plaster cylinder. The general equation for the hyperbolic curve and the exponential curve is of the following form (see Equations (2.69) and (2.70)):

$$C_s = \frac{A}{1+\frac{BUt}{R}} + \frac{CUt}{R} \qquad \textbf{(5.9)}$$

$$C_s = A' e^{B'\frac{Ut}{R}} + C' \qquad \textbf{(5.10)}$$

Whereby A, A', B, B', C and C' represent the variables which should be empirically determined. The second terms in these equations represent portions which become only significant after the initial stages of the impact. Since only the initial impact

stages are investigated here, it is not necessary to include these terms in the best fit study. The fitting is thus only done using the first terms by means of a least square method. This fitting technique resulted in the following variables:

$$A = 2.61 \quad ; \quad B = 3.65 \quad ; \quad A' = 2.65 \quad ; \quad B' = 2.93 \qquad \textbf{(5.11)}$$

Figure 5-33 shows the corresponding hyperbolic and exponential fit together with the original force recording from the plaster cylinder for an impact velocity of 4.1 m/s. The graph also shows the theoretical and empirical relations for the maximum slamming coefficient from Campbell and Weynberg [26], Greenhow and Yanbao [28], Kaplan and Silbert [30] and von Karman [4]. It can be observed that both hyperbolic and exponential fits correspond reasonably well and result in an average initial maximum slamming coefficient of 2.63. This value is smaller than the smallest theoretically predicted value of π and is situated in the lower part of the range of reported experimentally obtained maximum slamming coefficients corresponding to cylindrical slamming (see Table 2-1). Although this value does not represent an exact determination of the true maximum slamming coefficient corresponding to pure rigid cylindrical slamming but rather represents an approximate estimation, it shows that the maximum slamming coefficient as determined by Campbell and Weynberg [26] and as used in the DNV standard [25] largely overestimates the true value. However, this does not necessarily indicate that the guidelines concerning cylindrical slamming as provided by the DNV standard [25] are too conservative. After all, a lot also depends on the structural vibrations which are present in the cylindrical constructions. In this respect it is even possible that the loads as predicted by the DNV standard [25] underestimate the true slamming forces acting on marine constructions.

Though, it is a fact that the DNV standard [25] concerning cylinder slamming is based on experiments which are largely affected by structural vibrations. Up to now, it is not exactly known in which extent these vibrations affect the loads purely related to slamming. To improve the current standards, a distinction should be made between the true cylinder slamming loads, purely related to the phenomenon of rapidly pushing away a certain amount of water (added mass), and the possible amplification of these loads due to structural vibrations. The experiments from this thesis cannot provide more information on these two aspects since they are also affected by structural vibrations of the setup, though in a smaller extent. It can only be concluded that the maximum slamming coefficient purely related to water induced rigid cylindrical slamming is situated in a range between 2.63 and 5.15. Further research is necessary to obtain more information and to improve the current guidelines.

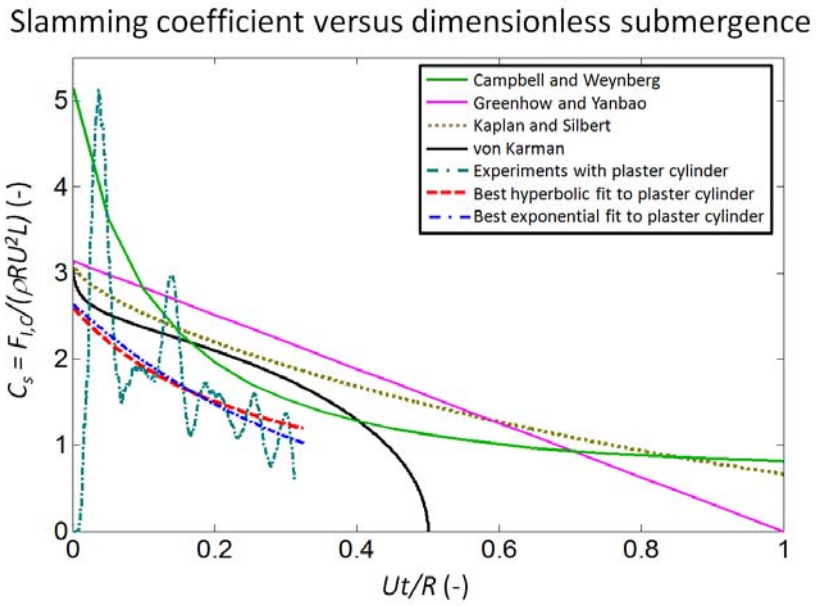

Figure 5-33: The experimentally obtained force time history plaster cylinder for an impact speed of 4.1 m/s compared to its hyperbolic and exponential fit and with the empirical and theoretical relations of Campbell and Weynberg [26], Greenhow and Yanbao [28], Kaplan and Silbert [30] and von Karman [4]

5. 3. Deformable cylindrical test objects

During the experiments with the deformable cylindrical test objects, no pressure measurements could be performed, since a firm installation of the pressure sensors in the thin-walled cylindrical models could not be guaranteed. The next section thus immediately starts with a description of the force recordings.

5. 3. 1. Impact forces

From the experiments done for the rigid cylindrical test objects, it was observed that vibrations of the bottom impactor plate are excited during the slamming impact, causing fluctuations in the force recordings. These vibrations were largely suppressed by elaborating the rigid cylindrical test object as a cylindrical segment of which the flat side is firmly fixed to the bottom impactor plate.

However, for the deformable cylindrical test objects this is not possible since cutting segments out of the deformable cylinders would completely change the boundary conditions of the problem and result in completely different impact load results. Hence, the deformable cylinders are tested in their entire shape and the load is

introduced from the cylinder to the bottom impactor plate through a narrow area which approximates a line contact. Because of the fact that the load is not evenly distributed over the entire bottom impactor plate, vibrations are again allowed to occur.

In order to enable the extraction of the true forces out of the experimentally obtained force recordings, strains are measured on the deformable cylindrical test models by using strain gauges installed on the cylindrical surfaces. The method of extracting the true forces out of the oscillatory force recordings is explained in detail in the following section.

5. 3. 1. 1. Deformable cylindrical test objects with large diameter ($D \geq 31.5$ cm)

5. 3. 1. 1. a. Force time histories

Figure 5-34 shows the force time histories for the six deformable cylindrical test objects with large diameter ($D \geq 31.5$ cm) for slamming drop experiments at an impact speed of 3.74 m/s. The force recordings all start with large oscillations which quickly dampen out in time. For the recordings of cylinder C1, C2 and C4, it can be observed that, besides these initial short term and high frequent oscillations, also an oscillation with a smaller frequency is present. From the depicted graph only, it cannot be verified whether both types of oscillations are due to the deformations of the cylinders or whether they are caused by structural vibrations of the setup.

All the graphs show an abrupt decrease at a time between 60 ms and 80 ms. This force drop occurs when the motion dampers of the setup are activated and the impactor is stopped. The slamming force recordings should thus only be considered before the abrupt force drop.

Although the exact elastic properties of the cylinders were initially not known, it could be observed at first sight that for the deformable cylindrical test objects with smaller wall thickness and thus larger degree of deformability, smaller impact forces were recorded which were more spread in time (e.g. cylinder C1 versus cylinder C3). This corresponds with the expectation that with increasing flexibility of the cylinders more energy is absorbed by the deformation which results in smaller slamming loads, as theoretically approximated in section 2.2.

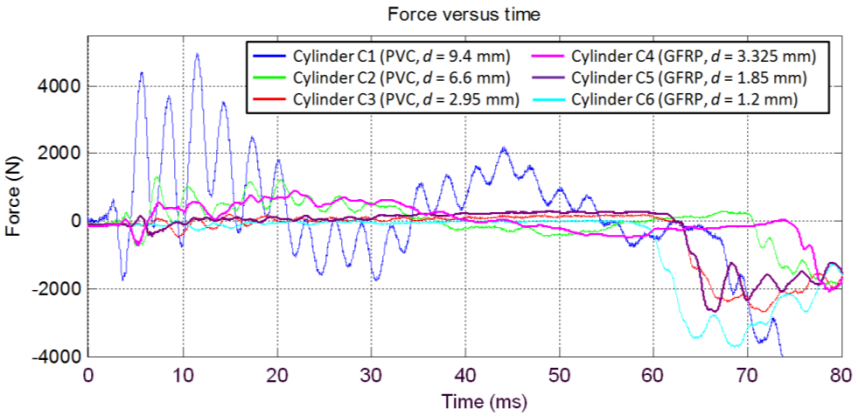

Figure 5-34: The slamming forces of the six deformable cylindrical test objects with large diameter ($D \geq 31.5$ cm) as function of time for slamming drop experiments at an average impact speed of 3.74 m/s

For the very thin-walled cylindrical models C3, C5 and C6, the force recordings are much smaller in magnitude than for the other cylindrical models. They are depicted in Figure 5-35 for a better visualisation. From this graph, it can be observed that, unfortunately, the slamming forces are still increasing at the moment that the motion dampers are activated and the forces abruptly decrease. Hence, no impact force values could be determined for these cylindrical models, except for the recording for cylinder C5 at the smallest tested impact speed (0.92 m/s), since the maximum forces for these tests were reached just before the moment of the damper activation.

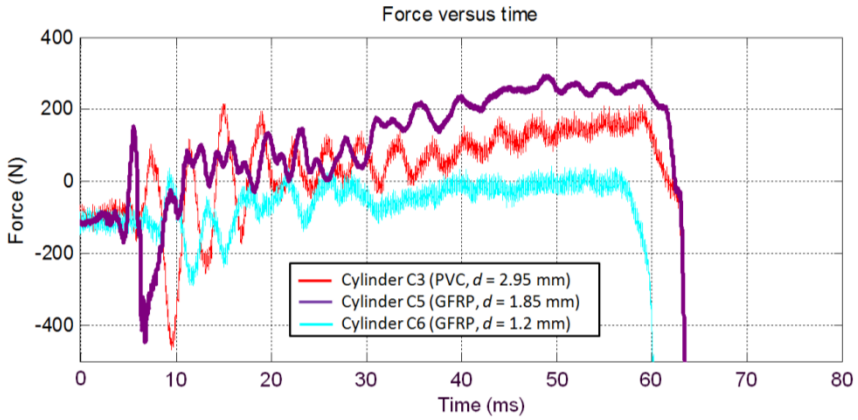

Figure 5-35: The slamming forces of the deformable cylindrical test objects C3, C5 and C6 as function of time for slamming drop experiments at an average impact speed of 3.74 m/s

In order to verify whether the oscillations in the force recordings are due to structural vibrations or whether they are caused by deformations of the test objects, it is interesting to compare the force recordings with the hoop strain measurements performed at the cylindrical surfaces. This is done in Figure 5-36 for the deformable cylinders C1, C2, C4 and C5. From the depicted graphs, it can clearly be observed that the oscillations with the larger frequency in the force recordings are not present in the strain recordings. The deformable cylindrical objects thus do not 'feel' these types of oscillations. Hence, these frequencies are not caused by the deformation of the cylinder, but must be due to structural vibrations of the bottom impactor plate of the load cell combination. The oscillations in the force recordings corresponding to the smaller observed frequency are also present in the strain recordings and are thus generated by an oscillatory deformation of the cylindrical test objects.

In order to extract the true forces acting on the deformable cylindrical test models out of the force recordings, low pass filters can be used which filter out the oscillations at the larger frequencies. The cut-off frequency of these filters can be determined by comparing the frequency content of the force and strain recordings for each of the tested cylinders. As an example, Figure 5-37 shows the amplitude spectrum of the force and strain recording for the test model C1 at an impact speed of 3.74 m/s.

This graph clearly shows a low frequency peak at about 30 Hz which is present both in the force recording and the strain recording. It is at this frequency that the cylindrical model deforms. Besides this latter frequency, the force recording shows also peaks in its amplitude spectrum at frequencies of about 130 Hz and 340 Hz, which are not observed in the amplitude spectrum of the strains. These frequencies are thus inherent to vibrations of the impactor. By the application of a low pass filter with a cut-off frequency of 90 Hz, the oscillations due to the structural vibrations can thus be filtered out from the force recordings. The resulting force time history for the slamming test with cylinder C1 at an impact speed of 3.74 Hz is shown in Figure 5-38 and matches in shape exactly with the strain. The true impact force acting on the deformable cylindrical model can then be determined as the maximum of this filtered force recording.

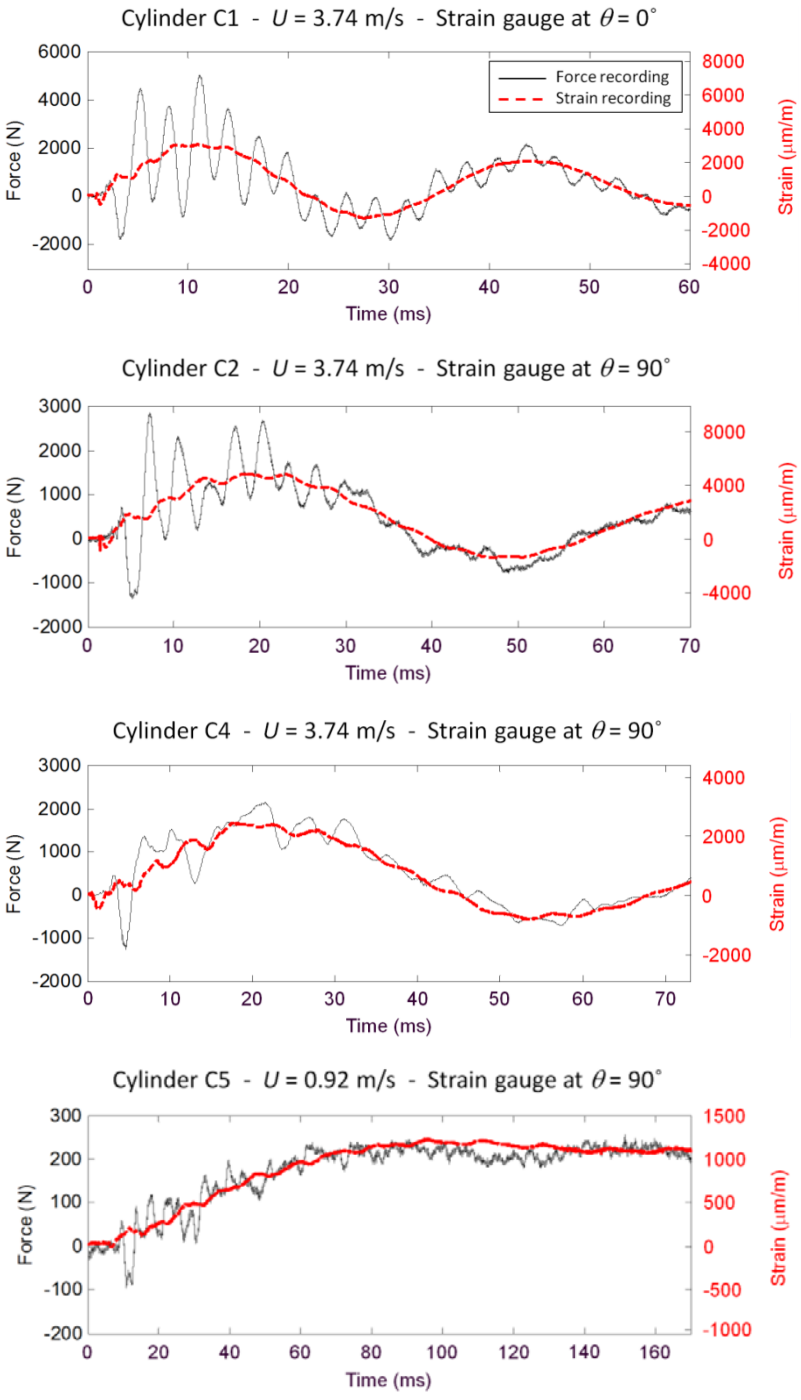

Figure 5-36: Examples of the comparison between the force and strain recordings of the deformable cylindrical test objects C1, C2, C4 and C5

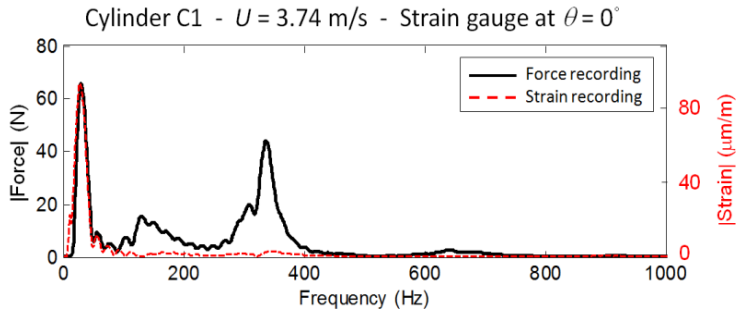

Figure 5-37: Amplitude Fourier spectrum of the force and strain recording for the test model C1 at an impact speed of 3.74 m/s

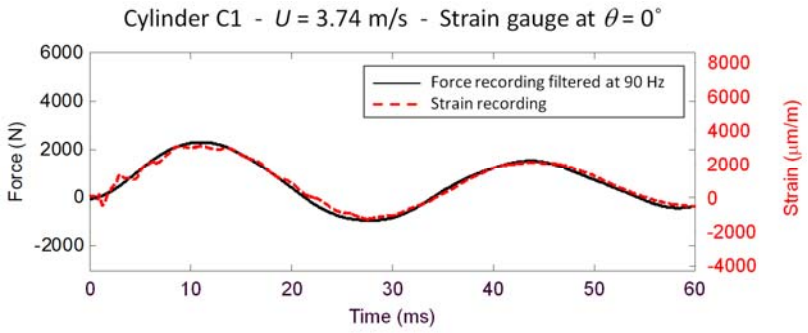

Figure 5-38: Comparison between the force recording filtered with a low pass filter at a cut-off frequency of 90 Hz, and the strain recording of the test object C1 for a slamming experiment at an impact speed of 3.74 m/s

In order to verify the correct value of these impact force values determined from the filtered force recordings, they can be compared with the impact forces obtained directly from the strain measurements. In order to convert the strain measurements to force, additional static compression tests were done on each deformable cylindrical test model. These tests were performed with the same servo-hydraulic Instron machine as described in section 4.3.3.2.b. Figure 5-39 shows the test configuration for the deformable cylinder C1. Two circular plates were used above and below the cylindrical test objects to compress the cylinders under certain (small) displacements. The applied forces, the displacements and the occurring strains at the locations of the strain gauges were measured in order to obtain a relation to convert strain to force.

However, it must be mentioned that the circular plates which were used to compress the cylindrical test models did not cover the complete length of the test models. Hence, these compression tests could not be directly used to find a conversion factor to calculate the force from the strains recorded during the slamming experiments.

In order to solve this problem, two types of numerical simulations were performed by using the finite element solver ABAQUS for each deformable cylindrical test object. In the first simulation case, the real compression tests using the circular compression plates were mimicked. In the second case, a compression test with two compression plates covering the complete length of the cylindrical test models was simulated for each cylinder. Figure 5-40 shows the difference between the two simulation cases for the test model C1. The force versus strain relation necessary to convert the measured strains to slamming forces can be obtained from the second simulation case. However, it was initially not possible to perform these types of numerical calculations since the elastic material properties (elasticity modulus and Poisson's ratio) of the used materials were not provided by the manufacturer and could thus not be introduced in the FEA models.

Figure 5-39: The test configuration for the compression test with cylinder C1

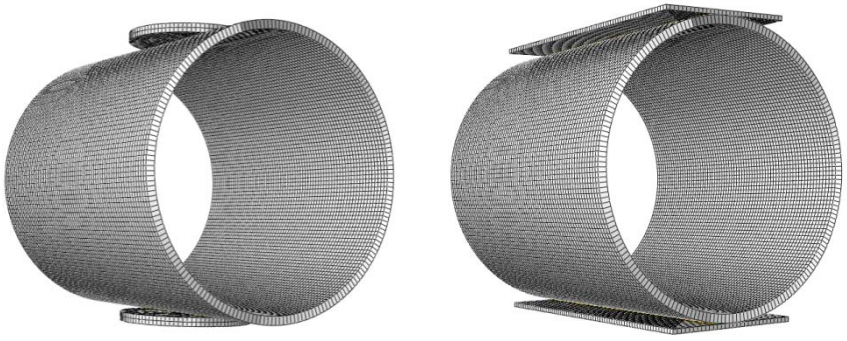

(a) (b)

Figure 5-40: (a) Simulation of the compression test of cylinder C1 with the original circular compression plates; (b) Simulation of the compression test of cylinder C1 with fictive compression plates covering the complete length of the model

For the Poisson's ratio for the deformable cylindrical models with the PVC (C1, C2, C3, C7, C8, C9), PE (C10, C11) and PP (C12) materials, a value has been assigned which is an average of the Poisson coefficient values for several kinds of respectively PVC, PE and PP materials as listed in the material database from the *Cambridge Engineering Selector EduPack* [31]. The value of the Poisson's ratio for the composite cylindrical test objects has been obtained as the average Poisson's ratio for several types of unidirectional glass fibre reinforced composite materials as provided by Degrieck [32]. Since the winding angle of the fabricated composite cylinders is close to 90°, the composite tubes are assumed unidirectional in the hoop direction, and the reported value of the Poisson's ratio is thus assumed valid in this direction. The Poisson's ratio values for the different cylindrical test models are provided in Table 5-5.

In order to determine the elastic moduli of each tube, the numerical simulations of the compression tests with the real compression plates were used. By varying the E-modulus of the tubes in these latter simulations and comparing the corresponding force – displacement relations with the ones observed during the true compression tests, the true E-modulus could be determined. This method is illustrated in Figure 5-41 for cylinder C2. This graph shows both the experimentally recorded as well as the numerically simulated force applied during the compression test of the cylindrical model C2 as function of its indentation. Numerical simulations have been performed for five values of the elasticity modulus. Nonlinear effects were taken into account, and friction between the cylindrical model and the compression plates was neglected. Furthermore, mesh convergence was obtained. From Figure 5-41 it can be observed that for an E-modulus of 3.4 GPa, the simulated force – displacement curve perfectly matches the experimentally obtained relation. From this correspondence, it was concluded that the E-modulus of the PVC material of cylinder C2 is 3.4 GPa. The same procedure has been applied for the other deformable cylindrical test models, except for cylinder C3 and C6, since for these cylinders no impact forces could be determined (the maximum values were not reached during the experiments). Table 5-5 gives an overview of the obtained results.

It can be observed that for cylinders of the same material, other elastic moduli are obtained. For the cylindrical test objects with the PVC, PE and PP materials, all the obtained values are within the range as provided in the *Cambridge Engineering Selector Edupack* [31]. A different E-modulus for tubes of the same materials but other wall thickness means that apparently slightly other material properties are used during the production process depending on the wall thickness of the tubes. For the composite cylinders, the difference in Young's modulus is probably due to the different fibre fraction volume in the fabricated composite.

Table 5-5: Overview of the obtained values for the Poisson coefficients and E-moduli for the different deformable cylindrical test objects

Cylinder	Material	Thickness d [mm]	Diameter D [cm]	Poisson's ratio [-]	E-modulus [GPa]	Cylinder stiffness K_c [N/mm]
C1	PVC	9.4	31.5	0.4	3.2	158.778
C2	PVC	6.6	31.5	0.4	3.4	58.350
C4	GFRP	3.325	32.17	0.3	18.25	43.452
C5	GFRP	1.85	31.87	0.3	22.8	6.084
C7	PVC	4.7	9	0.4	2.58	745.964
C8	PVC	3.15	9	0.4	2.7	230.250
C9	PVC	1.5	8.9	0.4	3	26.840
C10	PE	5.83	9	0.43	1.05	602.110
C11	PE	3.3	9	0.43	1.02	103.099
C12	PP	3.1	9	0.406	1.28	104.525

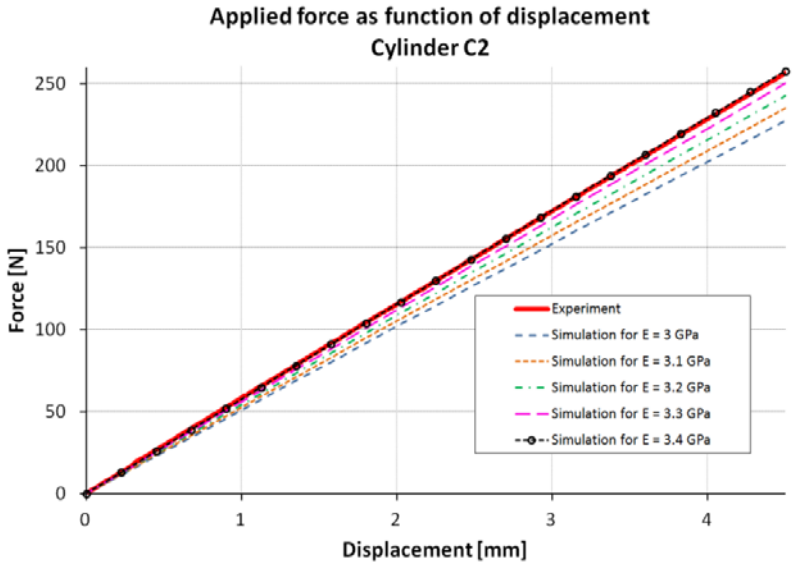

Figure 5-41: Comparison between the experimentally recorded force applied during the compression test of cylinder C2 and the force numerically calculated by the corresponding FEA model for different values of the E-modulus, as function of vertical indentation of the cylindrical model

With the knowledge of the Young's modulus of the test model materials, the finite element calculations on the compression tests with the compression plates covering the complete length of the deformable cylindrical test models could be finalized. These calculations resulted in a relation between the vertical force acting on the cylinders and the strain at the locations of the strain gauges during a vertical indentation of the cylindrical models. These relations can be used to calculate the impact forces from the strains recorded during the slamming experiments. However, it should be taken into account that during the slamming tests, the slamming load is distributed over the wetted area, while in the compression simulations, a force distributed over a narrow area is modelled and the cylinders are thus assumed to deform as an ellipse. Furthermore, it is also important to consider that these force-strain relations are obtained from quasi-static compression experiments while during the slamming experiments the forces and deformations are of a highly dynamic nature.

Figure 5-42 shows the force-strain relation obtained from the compression simulation for the strain gauge at the side ($\theta = 90^{\circ}$) and at the inner surface of tube C2. This graph also shows the force-strain relation as measured during the true compression tests and the corresponding numerical simulations with the true circular compression plates.

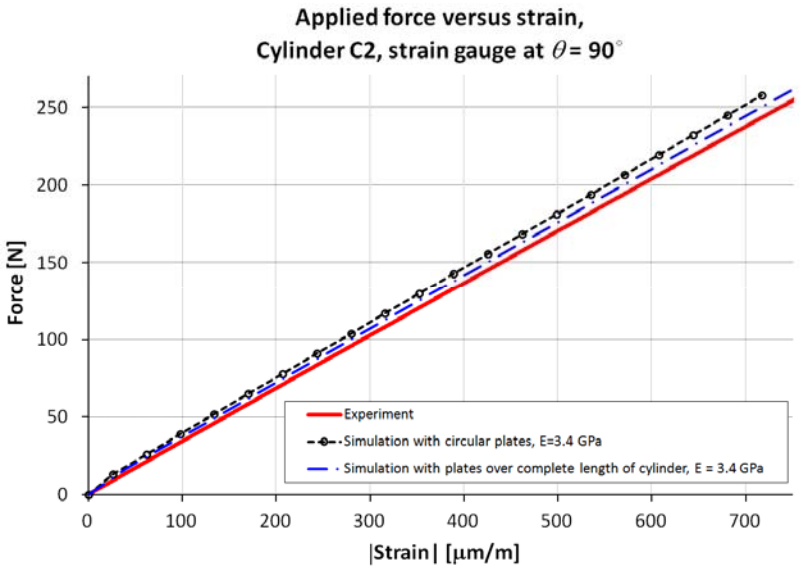

Figure 5-42: Comparison between the experimentally acquired and numerically calculated force-strain relations applicable at the location of the strain gauge at the side ($\theta = 90^{\circ}$) of the inner surface of cylinder C2.

It can be observed that all of the three curves are located closely to each other indicating that in this particular case, the deformation behaviour at the location of the considered strain gauge is quite similar in the case of a compression test with the true circular compression plates as well as in the case of a compression test with the compression plates covering the complete length of the cylinder.

However, this is not always the case. Figure 5-43 shows the same curves as in Figure 5-42, but now for the strain at the bottom of cylinder C4 on the inside of this tube.

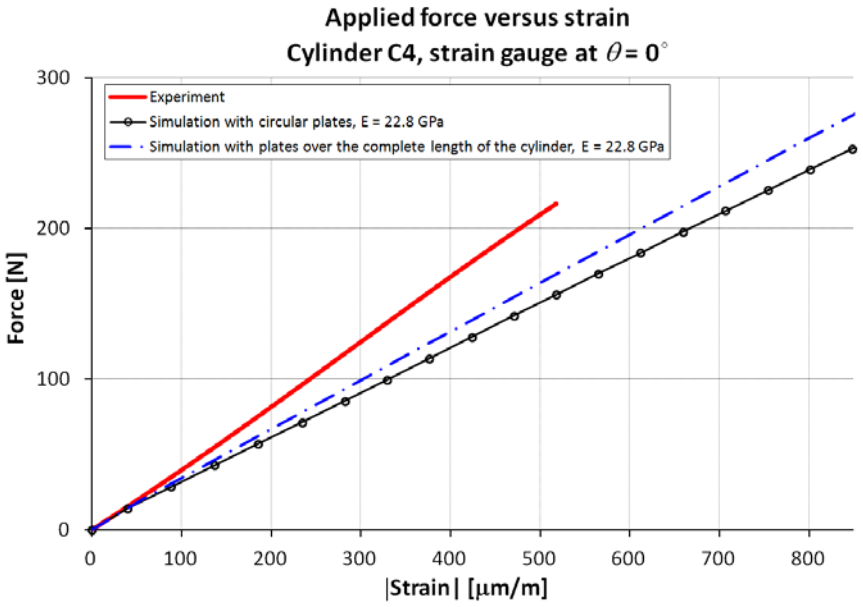

Figure 5-43: Comparison between the experimentally acquired and numerically calculated force-strain relations applicable at the location of the strain gauge at the bottom ($\theta = 0^{\circ}$) of the inner surface of cylinder C4.

Two major observations can be done from this graph:

- First of all, it can be observed that the experimentally obtained force-strain relation at the location of the strain gauge at the bottom of the cylinder is not matching with the numerically obtained relation calculated from its corresponding FEA model. For the same applied vertical force on the cylindrical model, the numerical calculations predict more deformation than which is actually measured. This difference may be due to a misalignment of the strain gauge with respect to the hoop direction and/or errors in the strain gauge fixation, resulting in recorded strains which are smaller than the truly occurring strains which are predicted by the numerical model. This conclusion

can be confirmed by the compression test done for the cylindrical test model C9 of which the force-strain diagram for the strain on the outside of the model for $\theta = 90^{\circ}$ is depicted in Figure 5-44.

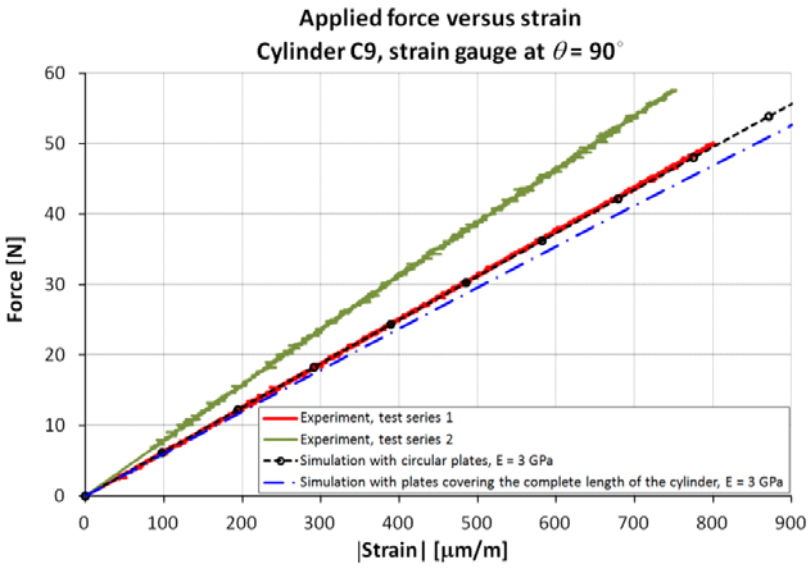

Figure 5-44: Comparison between the experimentally acquired and numerically calculated force-strain relations applicable at the location of the strain gauge at the side ($\theta = 90^{\circ}$) of the inner surface of cylinder C9.

In this graph, two experimental curves can be distinguished, corresponding with two different test series. These test series differ from each other in the sense that after the first test series, the considered strain gauge has been removed and replaced by a new strain gauge after the first one failed after a few tests. Although this second strain gauge was installed on the same position and was of identically the same strain gauge type as the first strain gauge, a large difference was found in the force-strain relationships. This difference can thus only be explained by an error in the strain gauge installation. These errors were observed for a few strain gauges. In order to convert the strains recorded by these particular gauges during the slamming experiments to slamming force, the errors should be taken into account. This is possible by the application of installation correction factors to the slamming strain recordings from the considered strain gauges corresponding with the difference between the experimentally obtained force-strain curves from the compression tests and the numerically obtained force-strain relations from the corresponding FEA models. Only the linear portions of these force-strain relations will be taken into account to determine these correction factors. For example, for the strain

gauge used in the second test series in Figure 5-44, this correction factor can be found by finding a multiplication factor which should be applied to the original force-strain curve to let it correspond with the force-strain relation from the simulation with the circular plates.

- The second important observation which can be done both from Figure 5-43 and Figure 5-44 is a significant difference between the force-strain curve for the compression tests obtained from the numerical simulation involving the truly circular shaped compression plates and the force-strain relation acquired from the numerical simulations using compression plates over the complete length of the cylindrical test models. It has been observed that this is the case for most of the cylindrical test objects. This indicates that there is a difference in deformation behaviour of the cylindrical test objects between the two situations. Hence, for converting the strains recorded during the slamming experiments to impact force, the force-strain relations will be used which correspond to the numerical simulations involving a compression of the cylinders over their entire length.

Using the determined installation correction factors (if appropriate), and applying the considered force-strain conversion relations on the strains recorded during the slamming experiments, then the slamming forces can be calculated from the strain measurements. Figure 5-45 compares the original force recordings, the low pass filtered version of these force recordings (at 90 Hz cut-off frequency) and the slamming forces calculated from the strain recordings for the same examples as depicted in Figure 5-36. A very good correspondence can be observed between the filtered version of the force recordings and the slamming force calculated from the strain recordings for every considered cylindrical object. The following conclusions can hence be drawn:

- First of all, it can finally be concluded that for the deformable cylindrical test objects with large diameter ($D \geq 31.5$ cm) the maximum force values of the filtered version of the force recordings are valid representatives for the slamming impact forces. These impact force values will be considered further in the following sections.

- Furthermore, it can be observed that the force-strain relation obtained from the quasi-static compression simulation apparently can also be used for converting the slamming strain recordings to slamming force. This indicates that for the case of the deformable cylinders, the slamming process can be treated approximately as a quasi-static process in the same deformation mode.

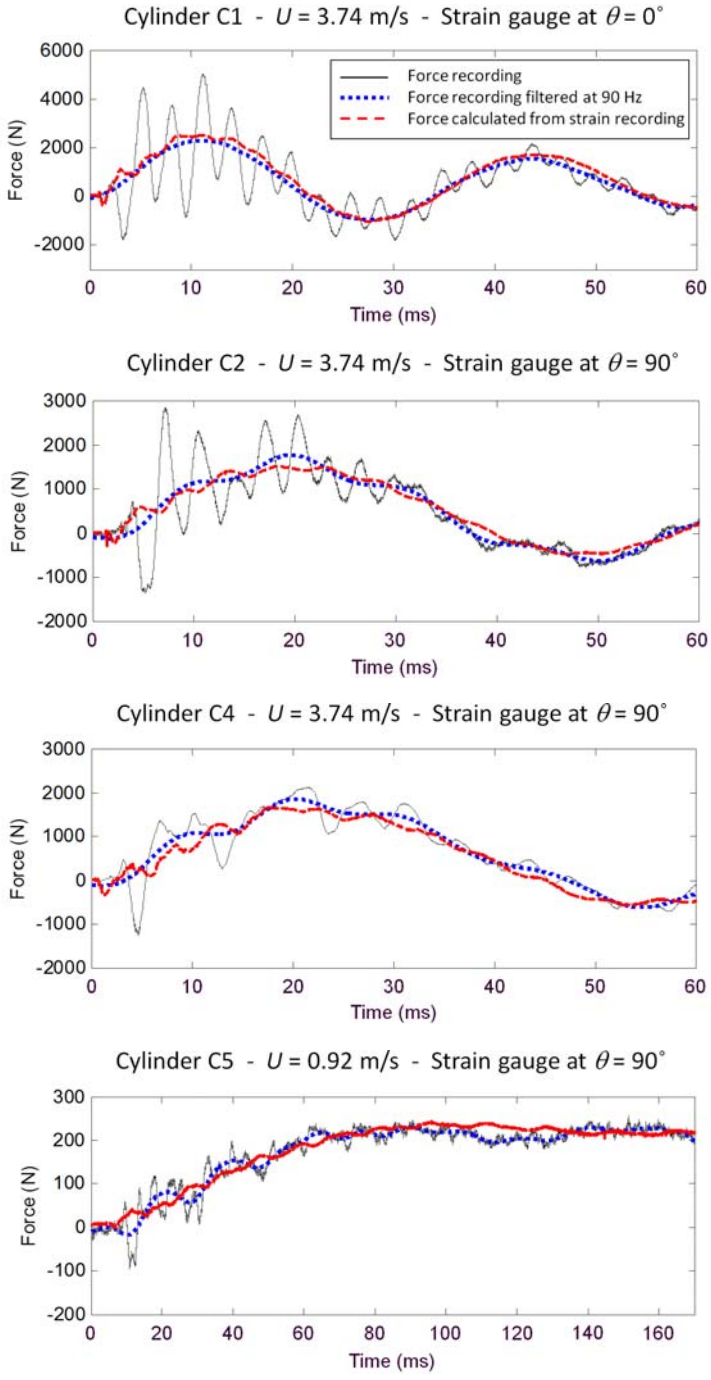

Figure 5-45: Examples of the comparison between the original force recordings, the filtered version of the force recordings and slamming forces calculated from the strain recordings for the deformable cylindrical test objects C1, C2, C4 and C5

- Finally, the fact that the force-strain relation obtained from the compression simulation is a very good approximation for the force-strain relation characteristic for the slamming experiments, indicates that the assumption of the cylinders deforming as ellipses by the action of line forces at the tips of the cylinders is a good approximation of the true deformation pattern of the cylinders and indicates that the true slamming loads may be approximately substituted by a line force when determining the force-strain relation. The fact that the cylindrical objects deform elliptically has also been observed in the PIV measurements from Nila et al. [33].

5. 3. 1. 1. b. Impact force values

Figure 5-46 and Table 5-6 give an overview of the force peak values obtained from the filtered force recordings of the deformable test models with large diameter ($D \geq 31.5$ cm). For the cylindrical models C4 (L = 40 cm) and C5 (L = 39 cm), the impact forces have been adjusted to match the impact forces which would be recorded for a length of 35 cm by a linear interpolation of the force results, to enable a comparison with the other test models (which have a length of 35 cm).

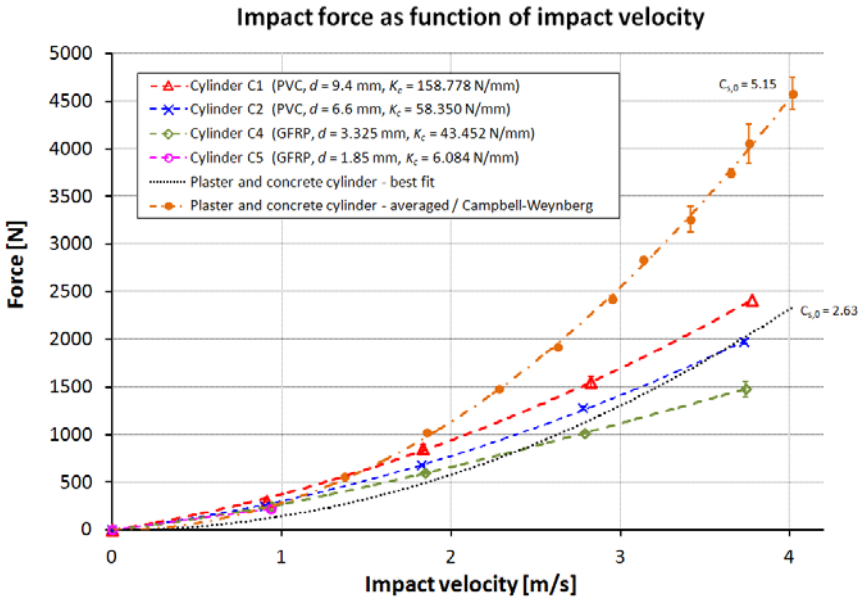

Figure 5-46: Overview of the force peak values obtained from the filtered force recordings of the deformable test models with large diameter ($D \geq 31.5$ cm) as function of impact velocity

Table 5-6: Overview of the force peak values and the scatter obtained from the filtered force recordings of the deformable cylindrical models with large diameter ($D \geq 31.5$ cm)

H [m]	U_{avg} [m/s]	Impact forces [N]							
		Cylinder C1		Cylinder C2		Cylinder C4		Cylinder C5	
		$F_{I,C}$ [N]	σ_F [N]	$F_{I,C}$ [N]	σ_F [N]	$F_{I,C}$ [N]	σ_F [N]	$F_{I,C}$ [N]	σ_F [N]
0	0	0	0	0	0	0	0	0	0
0.051	0.92	305.10	13.61	250.51	6.29	284.47	7.44	223.90	5.64
0.115	1.84	853.25	46.89	680.51	11.78	683.09	9.45	-	-
0.204	2.79	1551.27	56.94	1275.48	17.47	1160.93	10.64	-	-
0.459	3.74	2409.87	-	1975.67	24.07	1688.92	94.77	-	-

The standard deviation of the experiments which is provided in Table 5-6 and Figure 5-46 in terms of error bars is reasonably small compared to the absolute values of the impact velocities. This indicates a good reproducibility of the considered force recordings.

It can be observed that the impact forces again increase quadratically with the impact velocities. However, in contrast with the force results from the rigid cylindrical test objects, the relations are now not pure quadratic but also contain a significant linear term.

The graph also mentions the cylinder stiffness values K_c for the considered deformable cylindrical test objects. This stiffness value does not correspond to the bending stiffness K as presented in chapter 3. The cylindrical stiffness K_c is determined as the slope of the linear part of the force-displacement curves obtained from the numerical compression tests. As such, the stiffness of the cylindrical test objects is not only expressed as function of the elastic properties and the thickness of the cylindrical wall (as would be the case when expressing the stiffness in terms of bending stiffness K), but also as function of the diameter of the cylindrical test objects. This makes it possible to compare the experimental results from cylindrical test objects with a different diameter as function of the degree of flexibility.

When comparing the impact force results from the four types of deformable cylindrical test objects depicted in Figure 5-46, it can be clearly observed that for increasing degree of deformability of the test objects, the magnitude of the impact forces decreases. This behaviour was already observed from the force recordings at an impact velocity of 3.74 m/s in Figure 5-34, and corresponds with findings from

section 2.2. This trend is confirmed by the plot in Figure 5-47 which shows the impact forces as function of the cylinder stiffness K_c of the test objects for the different tested impact velocities. In this diagram, the impact forces seem to increase logarithmically as function of the cylinder stiffness K_c, in the sense that large changes in the impact forces occur with increasing stiffness for small values of the cylinder stiffness and small changes in the impact force are observed for large values of the cylinder stiffness. This behaviour is more pronounced as the impact velocity increases.

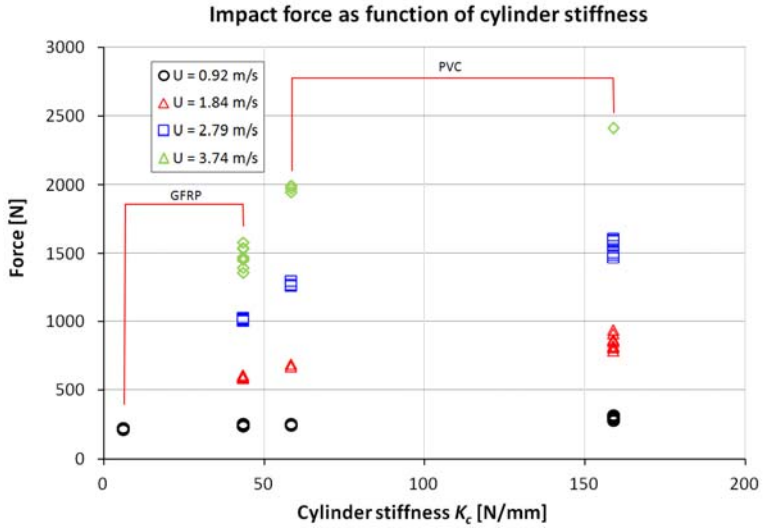

Figure 5-47: Overview of the force peak values obtained from the filtered force recordings of the deformable test models with large diameter ($D \geq 31.5$ cm) as function of flexural stiffness for the four tested impact velocities

Furthermore, the plot of Figure 5-46 also includes the average maximum forces measured during the slamming experiments with the rigid concrete and plaster cylindrical model and corresponding to a maximum slamming coefficient $C_{s,0}$ of 5.15, as well as the maximum forces obtained from the best hyperbolic and exponential fit of these latter force recordings, corresponding to a maximum slamming coefficient of 2.63 as determined in section 5.2.2.2**.** It was concluded in that section that the value of the maximum slamming coefficient purely related to rigid cylinder slamming is situated between the latter two values. However, it can be observed that the impact forces corresponding to a maximum slamming coefficient of 2.63 are very similar to the impact forces measured for the deformable test objects, at least for the tested impact velocities. Moreover, it can be observed that for impact velocities smaller than 2 m/s, the impact forces corresponding to a maximum slamming coefficient of 2.63 are even slightly smaller than the ones

measured for the deformable cylinders. Also for the curve representing the impact forces corresponding to a maximum slamming coefficient of 5.15 it can be observed that the impact force values for impact velocities smaller than 2 m/s correspond to the ones measured for the considered deformable test objects. This is in contradiction with the observed behaviour of the considered deformable cylindrical test objects that larger values for the flexural stiffness K_c result in larger cylinder slamming forces. As such, much larger impact forces would be expected for the rigid cylindrical test objects, but this appears not to be the case. More insight on this aberrant behaviour was gained when comparing the results from the rigid cylindrical test objects and the deformable test objects with large diameter ($D \geq 31.5$ cm) with the ones obtained from the experiments with the deformable cylindrical test objects with small diameter ($D \leq 9$ cm). These are discussed in the next section.

5. 3. 1. 2. Deformable cylindrical test objects with small diameter ($D \leq 9$ cm)

5. 3. 1. 2. a. Force time histories

A graph comparing the force time histories of the deformable cylindrical test objects with small diameter ($D \leq 9$ cm) is provided in Figure 5-48. Similarly as for the case of the deformable cylindrical test models with large diameter ($D \geq 31.5$ cm), a lot of oscillations can be observed with a large variety in frequency values. Again, it is the issue of this section to identify the oscillation frequencies which are the result of vibrations in the setup and which cause errors in the force measurements, and the oscillation frequencies which are caused by the deformation of the cylinder which reflect in the true forces acting upon the cylindrical models.

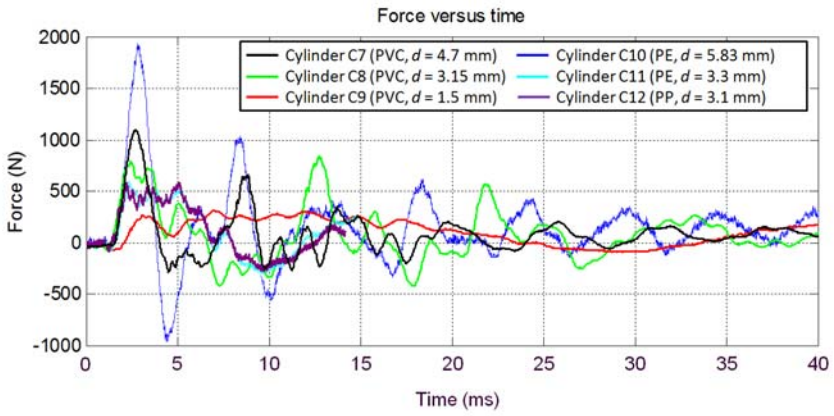

Figure 5-48: The slamming forces of the six deformable cylindrical test objects with small diameter ($D \leq 9$ cm) as function of time for slamming drop experiments at an average impact speed of 3.63 m/s

All the plots from Figure 5-48 stop at the time moment that the motion dampers of the setup are activated to prevent the test models from hitting the bottom of the water tank. It can be observed that for the cylindrical models C11 and C12, this moment was set earlier than for the other cylindrical models. This was necessary for the PIV measurements as described in the PhD dissertation of Nila [3], which were done simultaneously with the current experiments. However, this did not affect the ability to obtain the impact force values from the considered cylindrical test models.

In order to extract the true forces acting on the cylindrical models out of the force measurements, it was again first necessary to compare the raw force recordings with the recordings done by the strain gauges, which are installed in the hoop direction at the surface of the cylindrical models. For all the cylindrical test models described in this section, the strain gauges were installed on the outer surface at the side ($\theta = 90^{\circ}$) of the tubes. It was shown in section 5.3.1.1.a that by investigating the strain recordings, it is possible to indentify the loads which are really 'felt' by the cylindrical models, and to eliminate the frequency content of the force signals which originates from vibrations in the setup.

Figure 5-49 compares the raw force recordings with the forces directly calculated from the strain recordings. The impact forces calculated from the strain recordings are obtained with the same method as was used in section 5.3.1.1.a. Therefore, calculations were performed on numerical models simulating the cylindrical test objects being compressed by plates over their entire lengths. The relation between the strain obtained at the side ($\theta = 90^{\circ}$) and the vertical force applied on these numerical models was used to convert the strain recordings from the slamming experiments to impact force. The material parameters (E-modulus, Poisson's ratio) which were needed as input for the numerical calculations were obtained from the material database of the *Cambridge Engineering selector EduPack* [31] (Poisson's ratio) and from the comparison of the real compression experiments of the cylindrical test objects using circular compression plates with their numerical analogue (Young's modulus). The results of these material parameters are given in Table 5-5. This table also presents the cylinder stiffness values K_c of the considered cylindrical test objects based on the numerically obtained force-displacement characteristics.

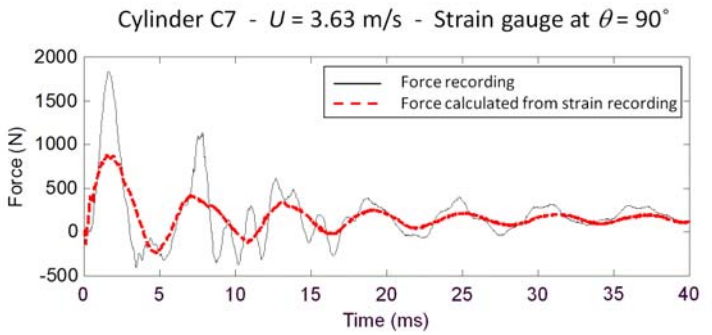
Cylinder C7 - U = 3.63 m/s - Strain gauge at θ = 90°
Force recording
Force calculated from strain recording
Force (N)
Time (ms)

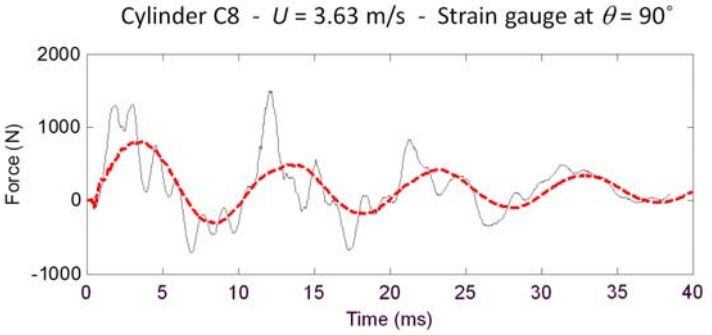
Cylinder C8 - U = 3.63 m/s - Strain gauge at θ = 90°
Force (N)
Time (ms)

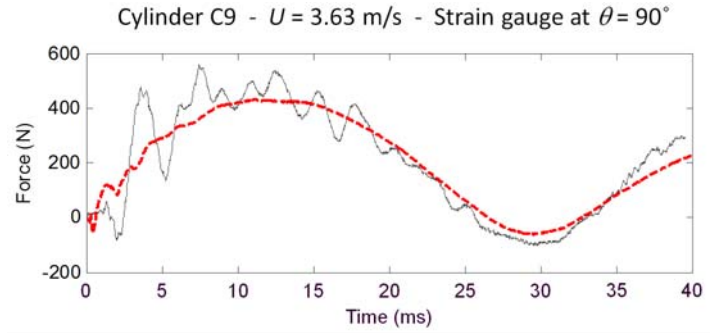
Cylinder C9 - U = 3.63 m/s - Strain gauge at θ = 90°
Force (N)
Time (ms)

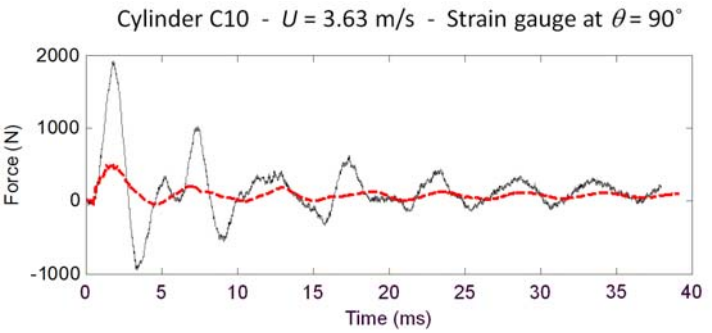
Cylinder C10 - U = 3.63 m/s - Strain gauge at θ = 90°
Force (N)
Time (ms)

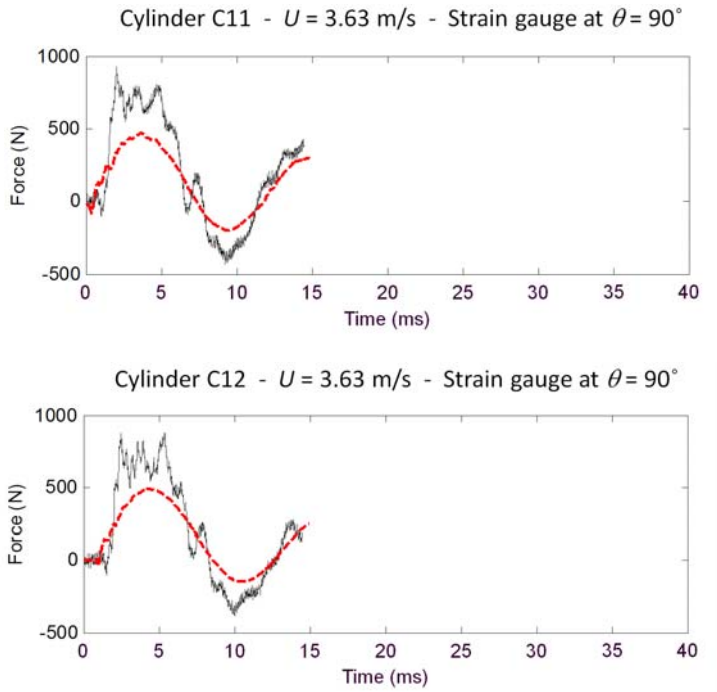

Figure 5-49: Examples of the comparison between the original force recordings and the slamming forces calculated from the strain recordings for the six deformable cylindrical test objects with small diameter

For the cylindrical test models with large diameter ($D \geq 31.5$ cm), the comparison of the raw force measurements with the forces calculated from the strains resulted in the clear understanding that the low-frequency deformations of the cylindrical test models were corrupted with high-frequency oscillations caused by vibrations of the setup. However, for most of the cylindrical test objects with small diameter ($D \leq 9$ cm), it is difficult to make this same observation. Only for cylinder C9, which has the largest deformation time period, it can be observed that an oscillation at a larger frequency is superposed on the oscillation with the frequency at which this cylindrical object really deforms.

In order to investigate the force recordings of the other cylindrical test objects with small diameter more into detail, it was interesting to examine the amplitude Fourier spectra of these recordings. Figure 5-50 compares as an example the amplitude Fourier spectra of the raw force recording and of the force calculated from the strain for the slamming drop experiments at an impact speed of 3.63 m/s for the cylindrical test objects C7 and C9.

It can be observed that for the most deformable test object C9, the amplitude Fourier spectrum of the measured force and the force calculated from the strain correspond reasonably well up to a frequency of 190 Hz. At a frequency of 33 Hz, a large spike in both frequency spectra can be observed which corresponds with the oscillation time period at which this cylindrical test object deforms as can be derived from Figure 5-49. For frequencies larger than 190 Hz, the signal obtained by the force sensors still shows a non-zero frequency content while for the signal obtained from the strain gauge the frequency content disappears gradually. This indicates that the forces are corrupted with oscillations at frequencies larger than 190 Hz which are not observed in the strain recordings. Since the cylindrical test object thus not 'feels' the oscillations at these frequencies, they do not represent true forces acting on the test object and must thus be caused by vibrations of the setup. Hence, they may be eliminated by the means of a low pass filter.

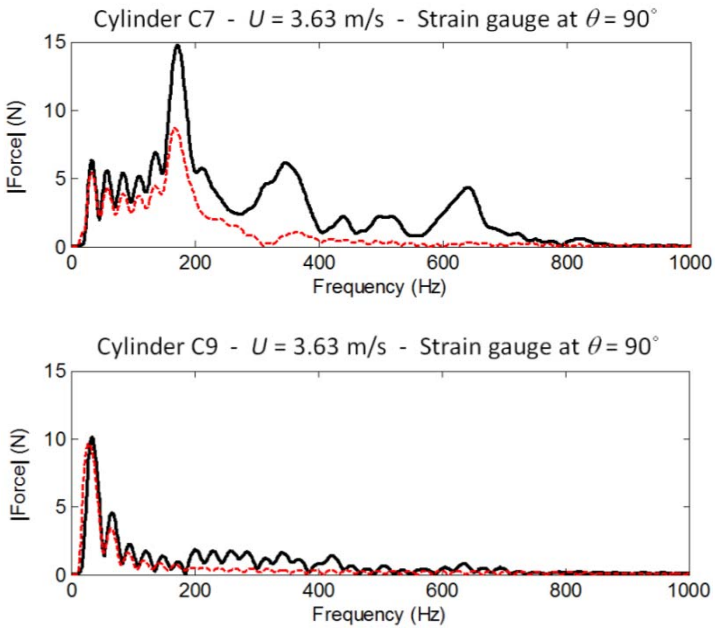

Figure 5-50: Amplitude Fourier spectrum of the original force recording and the force calculated from the strain for the test model C7 and C9 for an impact speed of 3.63 m/s

For the cylindrical test object C7, the Fourier amplitude spectrum from the force recording and from the force obtained from the strain only correspond for small frequencies up to 40 Hz. For the frequency range between 40 Hz and 200 Hz, both amplitude spectra correspond concerning the frequency values of the spikes in the amplitude spectrum, but these spikes do not correspond in amplitudes. For both

spectra, a large spike can be observed at 170 Hz. This corresponds with the main oscillation time period of the deformation pattern of this test object, as can be observed from Figure 5-49. However, a large difference in amplitude of this main amplitude spike can be observed between both amplitude spectra. Finally, for frequencies larger than 170 Hz, the amplitude spectrum of the strain recording gradually diminishes while for the force recordings many other amplitude spikes are observed due to excitations of the eigenfrequencies of the setup.

The large difference in amplitude between the amplitude spectrum from the force recording and from the force calculated from the strain for the frequency range between 40 Hz and 170 Hz explains the difference in magnitude in the force time histories from Figure 5-49 for cylinder C7. Especially the large difference at a frequency of 170 Hz has a large contribution.

This effect was also observed for the other cylindrical test objects with small diameter except for the cylinder C9. Furthermore it was noticed that the considered difference was larger for the cylindrical models with larger stiffness and thus larger deformation frequency. For the stiffest cylindrical models C7 and C10, it can be noticed that the deformation frequencies are in the neighbourhood of the eigenfrequencies of the bottom impactor plate (198 Hz as determined in section 5.2.2.1). It is assumed that due to this correspondence, the bottom impactor plate starts to resonate causing amplified vibrations and consequently amplified force recordings. Though, the attached cylindrical objects do not ‘feel’ these vibrations (cfr. strain recordings from the cylinder C9 and from all the cylinders with large diameters, section 5.3.1.1.a). This most probable explains the large up and down swings of the force signals resulting in large magnitude differences between the force recordings and the forces obtained from the strains. Also the force recordings of the cylindrical models C8, C11 and C12 are affected by resonance, however in a smaller extent since their deformation frequencies are slightly smaller.

All this makes that in the end the impact force values cannot be extracted from the measurements of the force sensors for cylinders C7, C8, C10, C11 and C12 since the signal content which originates from the vibrations of the setup cannot be filtered out of the force recordings because of the overlap of these vibration frequencies with the deformation frequencies. Hence, the impact force values for these cylindrical models will be determined only from the force histories calculated from the strain recordings since these are not affected by the vibrations.

5. 3. 1. 2. b. Impact force values

Figure 5-51 and Table 5-7 provide an overview of the impact force values obtained as the maxima of the forces calculated from the strain recordings for the deformable

cylindrical test objects with small diameter ($D \leq 9$ cm). The table and graph also show that the standard deviation of the measurements is relatively small indicating reproducible measurements.

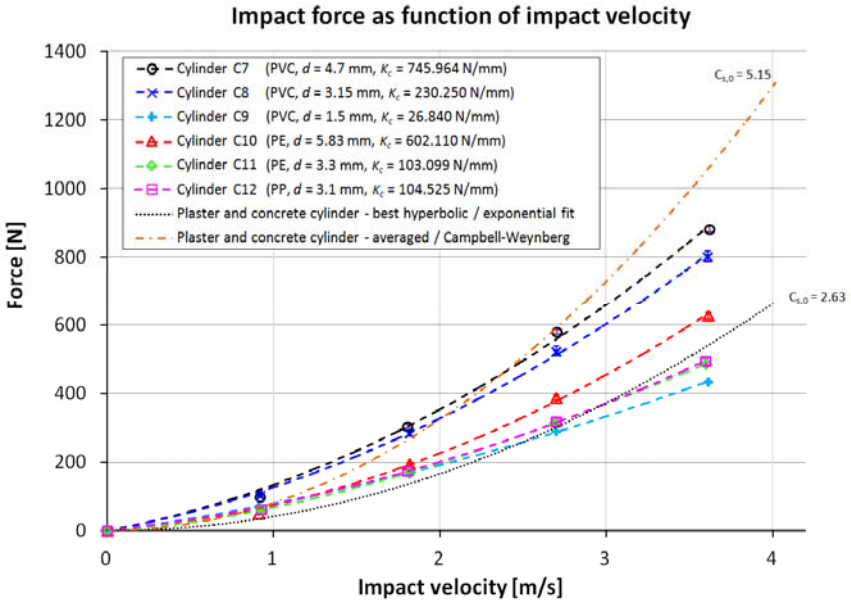

Figure 5-51: Overview of the force peak values obtained from the forces calculated from the strain measurements of the deformable test models with small diameter as function of impact velocity

Similarly as for the case with the deformable cylindrical models with large diameter, it has been observed that the relations between the obtained impact forces and impact velocities are of second order with a significant linear term, which is in contrast with the force-velocity relation for the rigid cylindrical test objects which was purely quadratic without linear term.

A comparison of the impact force values of the six considered deformable cylindrical test objects with small diameter learns that the initial assumption of smaller slamming forces corresponding to test objects with larger degree of deformability is valid for the cylindrical objects C7, C9, C11 and C12. However, this behaviour is not valid when comparing the impact forces obtained for cylinder C8 ad C10. As such, it can be observed that the impact force values of cylinder C8 are larger than the ones of cylinder C10, although its cylinder stiffness is more than 2.5 times smaller.

Table 5-7: Overview of the force peak values obtained from the forces calculated from the strain measurements of the deformable test models with small diameter

H [m]	U_{avg} [m/s]	Impact forces [N]													
		Cylinder C7		Cylinder C8		Cylinder C9		Cylinder C10		Cylinder C11		Cylinder C12	
		$F_{I,C}$ [N]	σ_F [N]	$F_{I,C}$ [N]	σ_F [N]	$F_{I,C}$ [N]	σ_F [N]	$F_{I,C}$ [N]	σ_F [N]	$F_{I,C}$ [N]	σ_F [N]	$F_{I,C}$ [N]	σ_F [N]
0	0	0	0	0	0	0	0	0	0	0	0	0	0
0.051	0.92	98.55	1.93	102.55	3.22	69.60	5.25	51.30	5.36	60.22	1.32	63.07	1.91
0.204	1.81	304.78	5.46	285.06	9.37	167.04	6.05	194.23	5.92	170.62	3.21	175.34	1.23
0.459	2.71	579.89	5.22	523.41	14.14	290.44	2.10	388.51	7.79	312.38	3.25	318.61	1.04
0.815	3.63	882.98	9.21	803.09	14.78	434.59	2.69	628.22	10.12	486.22	5.61	493.57	4.21

This can also be observed from Figure 5-52 which shows the impact force values as function of cylinder stiffness K_c for all the experiments. However, it must be mentioned that both cylindrical objects C8 and C10 are constructed from another material. Hence, this indicates that probably other material parameters might play a major role in the slamming behaviour of cylindrical objects. The fact that also material damping affects the impact loads has already been shown in section 2.2. When regarding the test series for each material type individually, then it can be observed that the initial assumption of larger slamming forces for larger flexural stiffness is valid. This can be observed for the PVC cylinders C7, C8 and C9 as well as for the PE cylinders C10 and C11.

For the cylindrical test objects with large diameter, it was observed that the impact forces vary approximately logarithmically as function of the cylinder stiffness, with the slamming forces increasing rapidly for small cylindrical stiffness values and slightly for larger cylindrical stiffness values. Roughly, a same trend can be identified for the impact forces for the cylindrical test objects with small diameter taking into account that oscillations in this trend might be caused by the effect of other material parameters such as damping (see Figure 5-52). In order to draw final conclusions on this relation, the impact force values of the cylindrical objects with large and small diameter should be compared to each other. This is done in the following section.

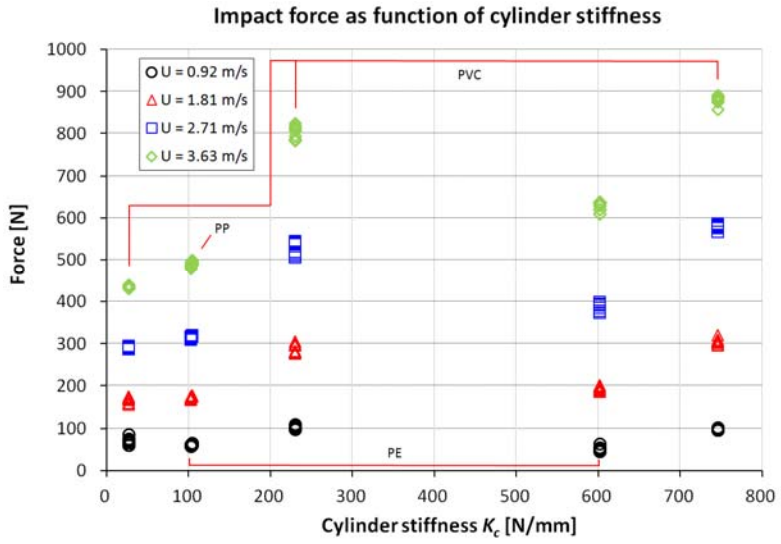

Figure 5-52: Overview of the force peak values obtained from the forces calculated from the strain measurements of the deformable test models with small diameter as function of flexural stiffness for the four tested impact velocities

Finally, similarly as in the previous section, the plot in Figure 5-51 shows the average maximum forces obtained from the recordings with the concrete and the plaster cylindrical test objects (corresponding to the maximum forces as published by Campbell and Weynberg [26]), and the maximum force values according to the best hyperbolic and exponential fits of these latter recordings. The comparison of these curves with the impact forces obtained from the cylindrical test objects with small diameter again learns that the impact forces corresponding to rigid cylindrical slamming are from the same magnitude as for the considered deformable cylinders, which is in contradiction with the initial findings from this thesis (section 2.2). An explanation for this observation is provided in the following section.

5. 3. 1. 3. Comparison of the slamming force results for all cylindrical test objects

In this section, a comparison is made between the slamming force results for all the tested cylindrical models. In order to compare the impact forces measured during the slamming experiments with the deformable cylindrical models with small and large diameter, the impact force results should be rescaled to the same diameter. This issue can also be solved by converting the slamming forces to dimensionless values which are not affected by scaling effects. This is the reason why in many other publications the impact forces are expressed in terms of maximum slamming coefficients. As such, they can be compared with the results from cylinders with other diameters.

Figure 5-53 shows the maximum slamming coefficients (see Equation 2.58) for all the considered deformable cylindrical test objects as function of impact velocity. Also the maximum slamming coefficient corresponding to the slamming experiments with the rigid concrete and plaster cylindrical test objects, as well as the maximum slamming coefficient obtained from the best hyperbolic and exponential fit of these recordings are depicted in the graph.

First of all, it can be observed that in contrast with the results obtained from the rigid cylindrical test objects, the measured slamming coefficients for all the deformable cylindrical test objects generally decrease with increasing impact velocity. This was already observed in the previous sections in the sense that the curves depicting the impact forces versus impact velocity for the deformable test objects were not purely quadratic but also contained significant linear terms which were not observed for the rigid cases. Furthermore, it can again be observed that the maximum slamming coefficient values corresponding to rigid cylindrical slamming are in the same magnitude order as the maximum slamming coefficients obtained for the deformable test objects, which is not as expected when considering that in the previous sections

the impact forces are observed to increase with increasing stiffness in the most cases.

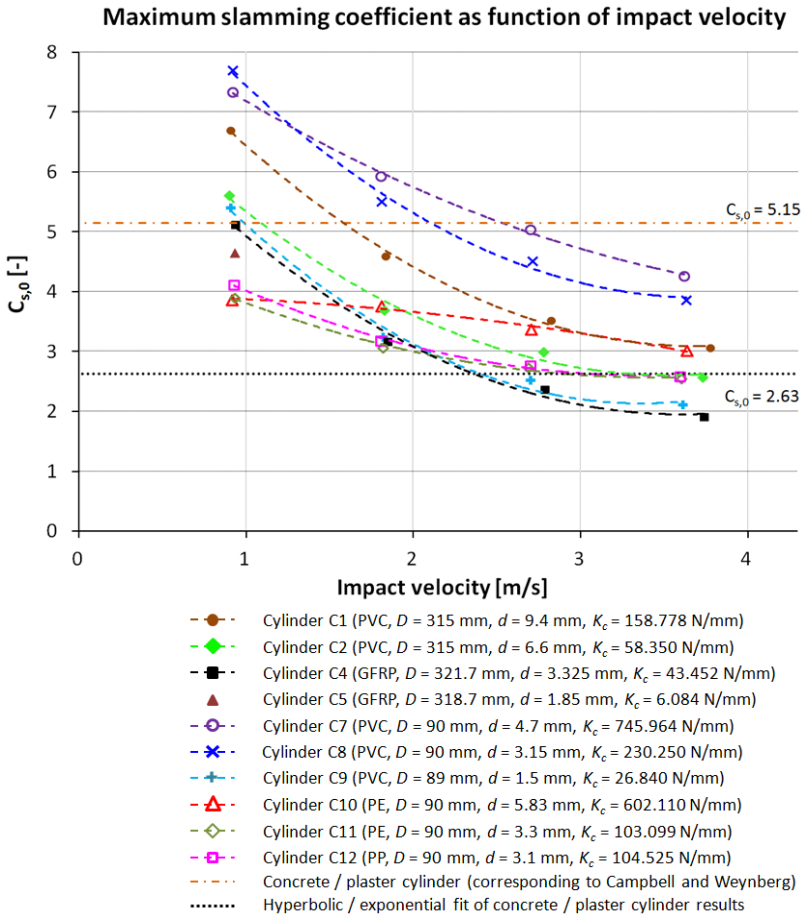

Figure 5-53: Overview of the maximum slamming coefficients of all the deformable test objects as function of impact velocity

To find an explanation for this aberrant behaviour, the original definition of the slamming force is again taken into consideration: the slamming force is defined as the force which is needed to displace a certain mass (volume) of water and can hence be calculated as following [30]:

$$F_{I,C} = \frac{d}{dt}\left(M_w V\right) = V\frac{d}{dt}\left(M_w\right) + M_w\frac{d}{dt}\left(V\right) \qquad \textbf{(5.12)}$$

With:
- M_w = added mass of water as function of water penetration [kg]
- V = velocity of the bottom of the test object [m/s]

For the case of the rigid cylindrical test objects, the speed V at the bottom of the cylindrical objects equals the speed of the upper part of the impactor which is measured by the position encoder, the accelerometer and the DIC technique. The speed versus time history for the stiffened cylindrical test object measured by the DIC technique for a drop height of 1 m is shown in Figure 5-5. Similar velocity profiles are found for the other rigid cylindrical test objects and for other drop heights. It can be observed that the speed hardly changes at impact. The speed V at the bottom of the rigid cylindrical test models can thus be assumed approximately constant in the impact stage of the slamming experiment. In this case, the slamming force can approximately be written as [30]:

$$F_{I,C} = \frac{d}{dt}\left(M_w V\right) = V\frac{d}{dt}\left(M_w\right) = \rho_w RLC_s U^2 \qquad \textbf{(5.13)}$$

The slamming force corresponding to rigid cylindrical slamming thus varies approximately purely quadratically with the impact velocity U as was also observed during the experiments.

For the case of the deformable cylindrical test objects, the impact stage lasts longer than for the rigid cylindrical test objects. In the time span from the first contact of the deformable cylinders with the water till the time moment that the maximum forces are reached, the top part of the structure decelerates significantly. This can be observed from Figure 5-54 which shows the velocity measured during a slamming experiment with cylinder C2 for a drop height of 0.815 m. But it is especially at the bottom of the deformable cylinders that very large decelerations occur due to the deformation of these test objects. Hence, Equation (5.13) is not valid in this case, and the impact force should be calculated from Equation (5.12). This explains why for the case of the deformable cylindrical test models the impact forces do not vary purely quadratically with impact force, and that the corresponding maximum slamming coefficients are not constant as function of impact velocity. The fact that the velocity changes significantly in the impact stages for the deformable cylindrical test objects makes that a comparison of their impact forces with the ones measured for the rigid cylindrical models does not provide relevant information with respect to the relation of the cylindrical slamming forces to the cylinder stiffness. Slamming experiments with the deformable cylinders with a constant entry speed at the bottom of these models should be performed in order to acquire relevant information on this aspect.

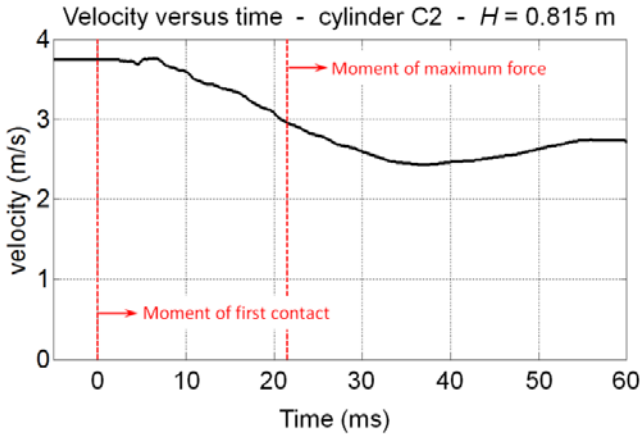

Figure 5-54: Plot of the measured velocity for the cylindrical model C2 for an impact height of 0.815 m

When considering the slamming coefficient versus velocity curves only for the deformable cylindrical test objects in Figure 5-53, then at first sight no straightforward relation can be found between the degree of deformability of the considered deformable cylinders (in terms of cylinder stiffness K_c) and the magnitude of the maximum slamming coefficients. In some cases, it can be observed that more deformable cylinders lead to smaller slamming forces (e.g. cylinder C9 versus cylinder C1), but in other cases the opposite can be observed (e.g. cylinder C10 versus cylinder C8).

However, when investigating the maximum slamming coefficients as function of cylinder stiffness more into detail, then a general trend can be observed. Figure 5-55 shows the maximum slamming coefficients of all the deformable cylindrical test objects as function of the cylinder stiffness K_c, for the four tested impact velocities (average values). With some irregularities taken into account (especially for cylinder C10 with K_c = 602.110 N/mm), a function which evolves logarithmically as function of cylinder stiffness can be observed in the sense that in the range of small cylinder stiffness the maximum slamming coefficients seem to increase rapidly with increasing stiffness, while in the range of large cylinder stiffness the maximum slamming coefficient seems to increase much slower with increasing cylinder stiffness. This trend was already observed in the previous sections when investigating the maximum slamming coefficients for the deformable cylindrical models with large and small diameter individually.

In general, it can thus be concluded that for decreasing cylindrical stiffness, the impact loads also decrease. This indicates that for cylindrical objects introducing deformability in the structure reduces the impact loads since a part of the impact

energy is then absorbed by the deformation of the material. This is certainly the case when introducing deformability by changing only the wall thickness or the diameter of a construction with a fixed material type. As such, it can be observed from Figure 5-56 that for the cylindrical test models made from PVC material a reasonably smooth trend can be observed between the maximum slamming coefficients and the cylinder stiffness without large irregularities. However, if deformability is introduced into a cylindrical structure also by changing its material, then other material parameters such as damping might become important causing an adverse effect than the one being expected (larger instead of smaller slamming loads).

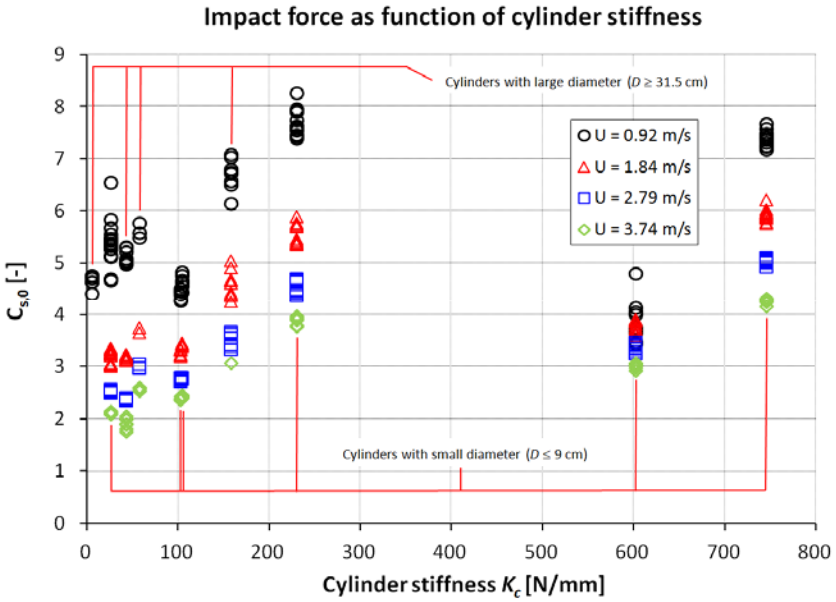

Figure 5-55: Overview of the maximum slamming coefficients of all the deformable test objects as function of flexural stiffness for the four tested impact velocities

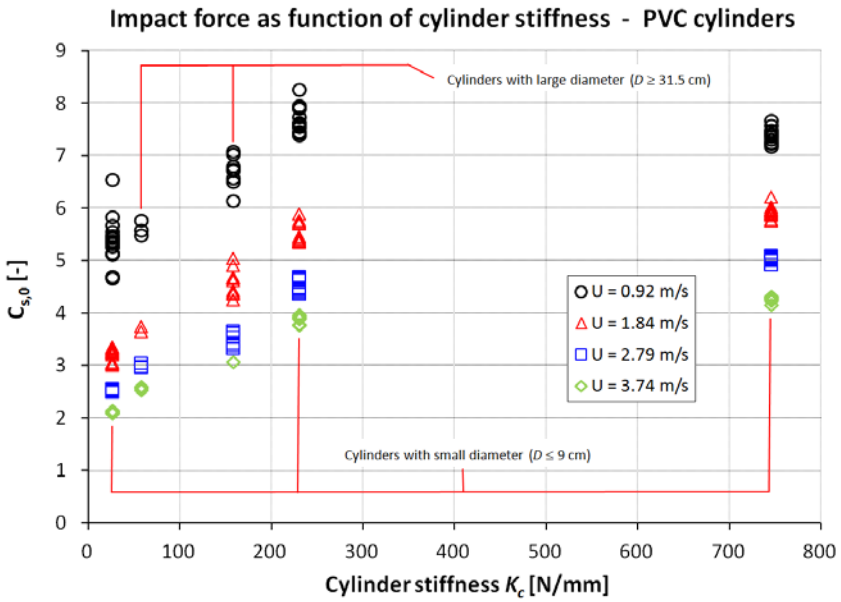

Figure 5-56: Overview of the maximum slamming coefficients of all the PVC deformable test objects as function of flexural stiffness for the four tested impact velocities

5. 3. 2. Maximum hoop strains and stresses

Besides measuring the slamming loads in terms of impact forces, they can also be assessed by evaluating the stresses present in the material. For the deformable cylindrical test objects, it is the stress in the hoop direction which is the most critical. This hoop stress can be evaluated at the locations of the strain gauges by converting the recorded strains at these locations to stress. In order to determine the required conversion factor for this operation, the numerical calculations as presented in section 5.3.1.1.a which simulate a vertical compression of the cylindrical test models over their entire length can be used. Figure 5-57 shows as an example the stress-strain relation at the location of the strain gauges (θ = 90˚) for a vertical indentation of cylinder C7.

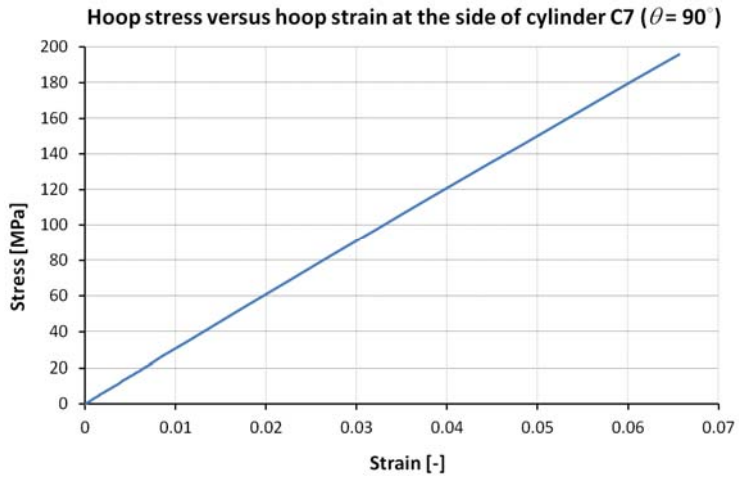

Figure 5-57: The hoop stress – hoop strain relation at the location of the strain gauge at the side of cylinder C7 (θ = 90˚) obtained from numerical calculations

The following sections describe the maximum values of the strains and stresses at the location of the strain gauges for all the deformable cylindrical test objects. The time histories of the strains (and thus also the stresses) were already described in detail in the previous sections.

5. 3. 2. 1. Deformable cylindrical test objects with large diameter ($D \geq 31.5$ cm)

For the deformable cylindrical test objects with large diameter, strains were recorded at two different locations, i.e. at the bottom (θ = 0˚) and at the side (θ = 90˚) of the cylinders, both in the middle of the cylinders' lengths. Figure 5-58, Figure 5-59 and Table 5-8 give an overview of the maximum strain values measured at these locations. Analogous to the force recordings, the maximum strain values could not be recorded during the experiments with the cylinders C3 and C6, since for these test objects the maximum load was not reached at the moment that the motion of the impactor was stopped by the activation of the dampers. For the cylindrical object C5, the maximum strains could only be obtained for the smallest tested impact speed (0.92 m/s).

Furthermore, it must be mentioned that some strain gauges failed quite rapidly due to water infiltrating the protective coatings. As such, no strain measurements could be performed at the side (θ = 90˚) of cylinder C1, and only one measurement per impact speed could be performed by the strain gauge at the side (θ = 90˚) of cylinder C2. For the other strain gauges, three experiments could be performed per drop height.

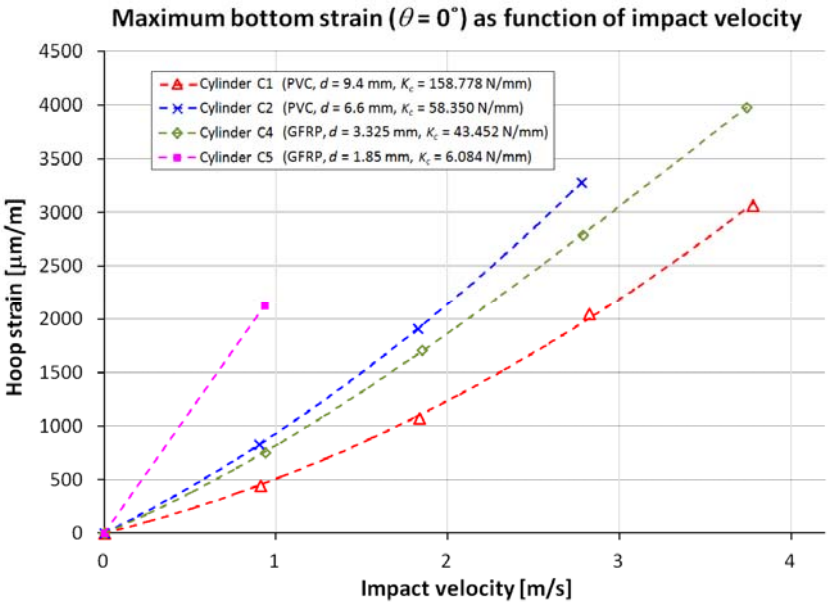

Figure 5-58: Overview of the maximum strain values at the bottom ($\theta = 0^{\circ}$) of the inner surface of the deformable test models with large diameter as function of impact velocity

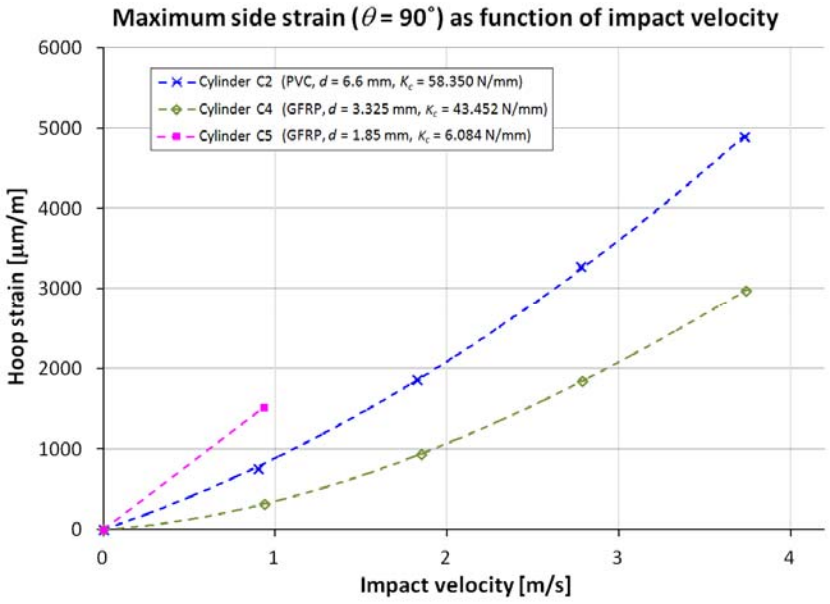

Figure 5-59: Overview of the maximum strain values at the side ($\theta = 90^{\circ}$) of the inner surface of the deformable test models with large diameter as function of impact velocity

Table 5-8: Overview of the maximum strain values at the bottom and side of the inner surface of the deformable test models with large diameter

H [m]	U_{avg} [m/s]	Maximum hoop stress values ε_{max} [μm/m]							
		Cylinder C1		Cylinder C2		Cylinder C4		Cylinder C5	
		bottom	side	bottom	side	bottom	Side	bottom	side
0	0	0	-	0	0	0	0	0	0
0.051	0.92	447	-	828	755	753	323	2129	1520
0.115	1.84	1027	-	1910	1857	1712	937	-	-
0.204	2.79	2049	-	3282	3275	2789	1848	-	-
0.459	3.74	3066	-	-	4894	3980	2978	-	-

At a first glance, no straightforward relation can be found between the maximum strain values and the degree of the cylinder deformability K_c. As such, it can be observed that when comparing the strains at the bottom of cylinders C1 and C2, it is the most deformable cylinder C2 which gives the largest strains, while in the same comparison for cylinders C2 and C4 the most deformable cylinder (C4) gives the smallest strains.

This can be explained by the fact that the maximum hoop strain observed in a deformable cylinder at a certain location does not only depend on the degree of cylinder deformability (which is a combination of the elasticity of the material and of the wall thickness and diameter of the cylinder), but also on the relative distance within the shell thickness direction between the considered location with respect to the neutral surface (where the strains and stresses are zero). Since strain gauges can only be used to measure the strains at the surface of the cylinders, the maximum slamming hoop strains are determined by a combination of both the cylinder stiffness K_c and the cylinder thickness d. A more flexible cylinder (smaller K_c) will deform more during slamming, but will not necessarily be subjected to larger maximum strains.

The same is expected for the stresses calculated from the considered strains. Figure 5-60, Figure 5-61 and Table 5-9 give an overview of the maximum hoop stresses at the locations of the strain gauges, calculated from the previous strain values. Again, no straightforward relation between the maximum hoop stresses and the cylinder stiffness K_c can be found. This confirms the explanation given above.

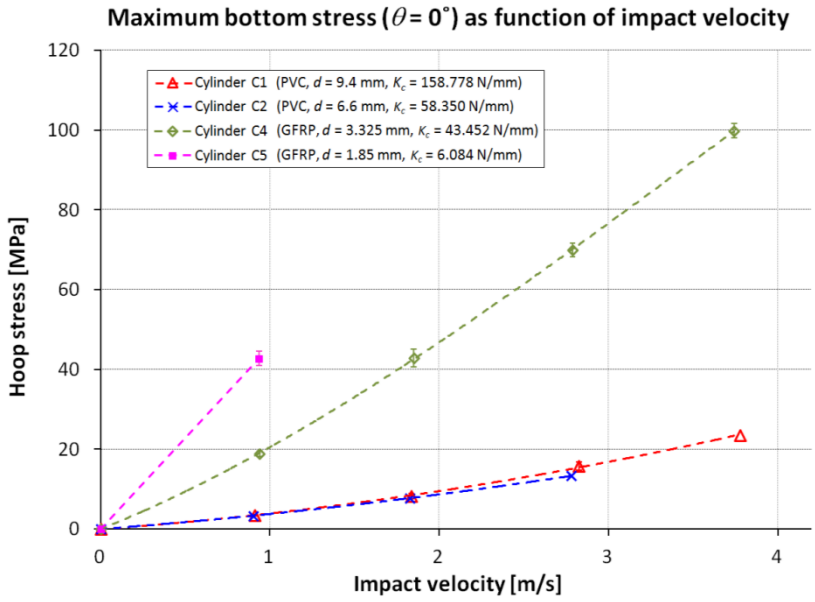

Figure 5-60: Overview of the maximum stress values at the bottom (θ = 0˚) of the inner surface of the deformable test models with large diameter as function of impact velocity

Table 5-9: Overview of the maximum stress values at the bottom and side of the inner surface of the deformable test models with large diameter

H [m]	U_{avg} [m/s]	Maximum hoop stress values σ_{max} [MPa]							
		Cylinder C1		Cylinder C2		Cylinder C4		Cylinder C5	
		bottom	side	bottom	side	bottom	side	bottom	side
0	0	0	-	0	0	0	0	0	0
0.051	0.92	3.44	-	3.36	3.06	18.88	8.09	42.72	30.50
0.115	1.84	8.25	-	7.76	7.52	42.92	23.49	-	-
0.204	2.79	15.77	-	13.33	13.27	69.94	46.20	-	-
0.459	3.74	23.59	-	-	19.82	99.81	73.77	-	-

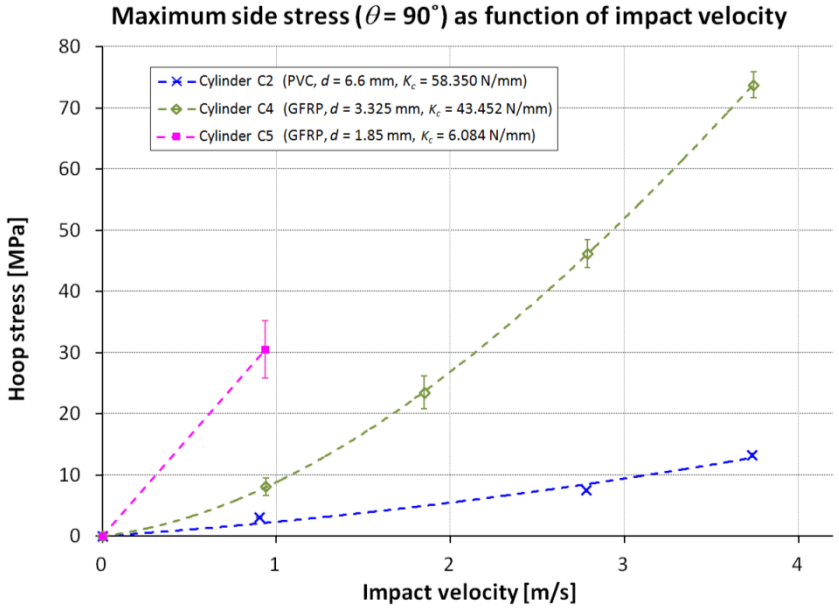

Figure 5-61: Overview of the maximum stress values at the side (θ = 90°) of the inner surface of the deformable test models with large diameter as function of impact velocity

It can thus be concluded that, contrary to the slamming forces, no relevant relations can be found between the maximum stresses and the flexibility degree of the cylindrical test objects. For the deformable cylindrical test objects with small diameter, the same conclusions are expected.

5. 3. 2. 2. Deformable cylindrical test objects with small diameter ($D \leq 9$ cm)

For the deformable cylindrical test objects with small diameter, strains were measured at both sides of the test objects (θ = 90° and θ = -90°), in the middle of the cylinders' lengths. Contrary to the deformable test models with large diameter, no problems were encountered with moist infiltration in the protective coatings of the strain gauges, which makes that for each impact speed at least three slamming tests could be performed. With two strain gauges on each test cylinder, this resulted in at least six strain measurements. Figure 5-62 and Table 5-10 give an overview of the average maximum strain values recorded by the considered strain gauges.

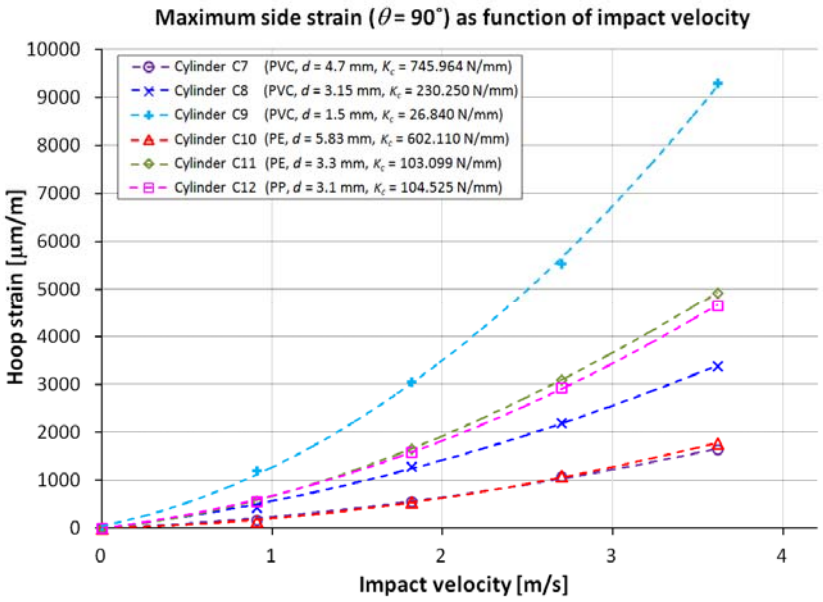

Figure 5-62: Overview of the maximum strain values at the side (θ = ±90˚) of the outer surface of the deformable test models with small diameter as function of impact velocity

Table 5-10: Overview of the maximum strain values at the side of the outer surface of the deformable test models with small diameter

H [m]	U_{avg} [m/s]	Maximum hoop strain values ε_{max} [µm/m]					
		Cyl C7	Cyl C8	Cyl C9	Cyl C10	Cyl C11	Cyl C12
0	0	0	0	0	0	0	0
0.051	0.92	180	434	1202	143	580	565
0.115	1.81	559	1283	3061	542	1664	1590
0.204	2.71	1070	2205	5541	1089	3040	2938
0.459	3.63	1641	3388	9295	1771	4936	4654

Figure 5-63 and Table 5-11 show the corresponding maximum stress values as function of impact velocity. It can be confirmed that also for these test objects, no straightforward relation can be found between the maximum stress values and the cylinder stiffness.

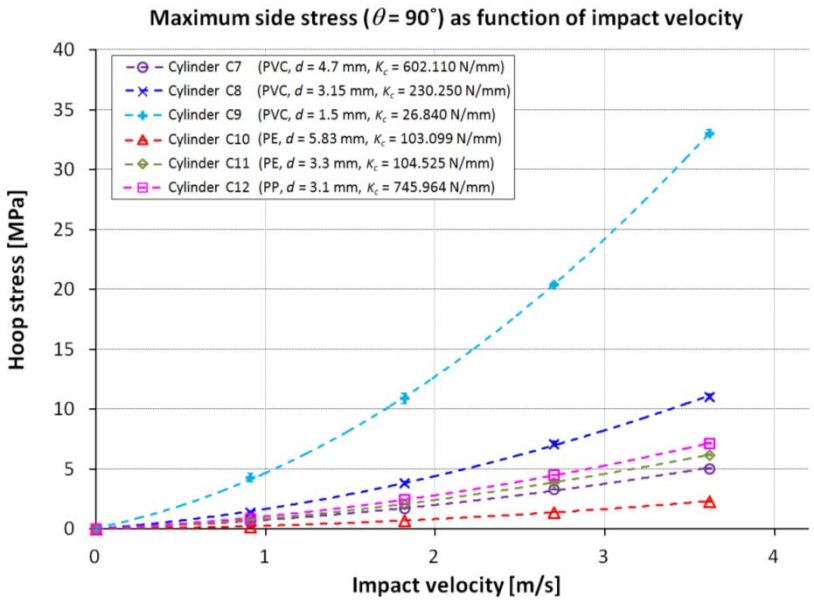

Figure 5-63: Overview of the maximum stress values at the side (θ = 90˚) of the outer surface of the deformable test models with small diameter as function of impact velocity

Table 5-11: Overview of the maximum stress values at the side of the outer surface of the deformable test models with small diameter

H [m]	U_{avg} [m/s]	Maximum hoop stress values σ_{max} [MPa]					
		Cyl C7	Cyl C8	Cyl C9	Cyl C10	Cyl C11	Cyl C12
0	0	0	0	0	0	0	0
0.051	0.92	0.56	1.36	4.29	0.18	0.73	0.87
0.115	1.81	1.72	3.82	10.90	0.70	2.09	2.44
0.204	2.71	3.30	7.10	20.38	1.41	3.89	4.51
0.459	3.63	5.06	11.06	33.06	2.30	6.18	7.14

It can thus be concluded that introducing deformability into a cylindrical structure not necessarily causes a decrease in maximum internal stresses in the cylindrical structure, as was the case for the slamming forces as observed in section 5.3.1

5. 4. Conclusions

This chapter investigates into detail the impact loads corresponding to cylindrical bottom slamming, and searches for a relation between the magnitude of the slamming loads and the deformability of the cylindrical construction in terms of cylindrical stiffness K_c.

A detailed study of the recorded impact pressures during the described slamming experiments showed that cylinder bottom slamming is typically characterized by large local pressures which are very short in duration and which rapidly travel over the cylindrical surface. These pressures occur in the intersection zone of the cylinder with the water, at the location where the water jet is formed.

It was observed that during the very initial stage of a rigid cylinder impact, an air pocket exists locally at the bottom of the cylinder which rapidly disappears. It is shown that this air pocket can most probably be related to the oscillatory pressure history which is observed at the bottom of the cylinder (0°).

A comparison between the measured and theoretically predicted impact pressures for rigid cylindrical bottom slamming learned that the measured pressures are in fact an average of the pressure distribution over the pressure sensor area. The true slamming pressures acting on the rigid cylindrical surface are thus in fact much larger and can be determined from Wagner's extending flat plate theory [5] for deadrise angles between 4° and 20°. For deadrise angles smaller than 4°, the compressibility of the water starts playing a role, and according to the author's best knowledge there is no theory available in the literature which takes this effect into account.

Furthermore, it was shown that during cylindrical slamming, the flow in the longitudinal direction at the edges of the cylinder and its effect on the impact pressures is rather limited. This is an important observation with respect to the ability to extend the obtained impact force results to cylinders with a larger length. Since the effect of the flow in the longitudinal direction is negligible, the impact forces measured on the test objects from this thesis can be extended to cylinders with a larger length by simply multiplying the length of these cylinders by the measured forces per unit length.

The examination of the forces recorded during the cylinder slamming experiments revealed that due to the sudden impact of the test objects with the water, some of the natural frequencies of the setup were excited which caused oscillations in the force recordings. This is an important observation which indicates that also in real marine constructions vibrations might occur due to slamming events which cause forces in

the structure which are larger than the ones which would be expected from the pure slamming loads only.

The vibrations in the setup resulted in the inability to measure the true impact forces corresponding to pure rigid cylindrical bottom slamming. Modifications in the setup successfully suppressed the vibrations, but they could not be totally eliminated. It has been shown that also other experimental studies concerning cylinder bottom slamming dealt with vibrations in the experimental setup. Especially the experimental results from Campbell and Weynberg [26] which are used as a standard in the DNV recommendations [25] have been observed to be significantly affected with vibrations. According to the author's best knowledge, no published material is available in the literature which describes successful experiments on cylindrical bottom slamming. From the experiments performed in this thesis, and the experimental results from the available literature, it may be concluded that the maximum slamming coefficient $C_{s,0}$ corresponding to rigid body slamming, which is approximately independent from the impact velocity, must be situated between 2.63 and 5.15.

For the case of the deformable cylindrical test objects with large diameter ($D \geq 31.5$ cm), the frequency of the vibrations in the setup was significantly larger than the frequency of the true forces (deformations) experienced by the test models. For these cases, the impact forces could hence be extracted from the force recordings by eliminating the force oscillations by means of a low pass filter. Furthermore, the impact forces could also be calculated from the strain which was measured at the cylindrical surface. Therefore, cylindrical compression tests in combination with numerical simulations of these tests were performed in order to find the force-strain relations at the considered locations. For the case of the deformable cylindrical test objects with small diameter ($D \leq 9$ cm), the frequency of the cylinder deformations was in the same range of the frequency of the setup vibrations. This caused resonance at the location of the force transducers and made the force recordings not useful anymore for determining the impact forces. Hence, the impact forces could only be calculated from the strain recordings for these cases.

A comparison of the impact forces measured for the different deformable cylindrical test objects learned that in general the impact loads seem to decrease with decreasing cylindrical stiffness. This confirms the assumption that introducing deformability in the structure reduces the impact loads since a part of the impact energy is then absorbed by the deformation of the material. This is especially the case when comparing cylindrical test objects made from the same material, but with other wall thickness or diameter. In these cases, the slamming forces evolve logarithmically as function of the cylinder stiffness in the sense that the impact forces increase fastly

with increasing cylinder stiffness for small values of this stiffness and increases much slower with increasing rigidity for larger values of the cylinder stiffness. However, when comparing the impact forces between cylindrical test objects of another material it has been noticed that the observation that decreasing cylinder stiffness leads to decreasing impact forces is not always true. This shows that also other material parameters such as damping might have an important effect on the impact forces. A more detailed investigation is necessary to identify these other parameters and their effect on the impact forces.

When comparing the results of the deformable cylindrical test objects with the ones from the rigid cylindrical models and the corresponding theories, then it was observed that in the first case the bottom of the test objects was significantly decelerated at the impact stage of the slamming event, while for the case of the rigid test cases the velocity at the bottom of the test objects could be approximately assumed constant. This difference in slamming conditions makes that a comparison of both results was not relevant since extra slamming force components are generated for the deformable cylinders which are not present in the case of the rigid cylindrical objects.

Finally, it has been observed that no straightforward increasing or decreasing relations could be found between the maximum impact stresses and the cylinder stiffness for the different deformable cylindrical test objects. The reason for this is the fact that besides the cylinder stiffness K_c, the impact stress also depends on the distance in the cylinder thickness direction between the location of the stress (strain) recording and the neutral surface. Introducing deformability into a cylindrical structure not necessarily causes a decrease in maximum internal stresses in the cylindrical structure, as was generally the case for the slamming forces. It is thus possible that introducing deformability to a structure which directly makes contact with the water during a slamming event causes a relief in the forces which are passed on to the structure which lies behind (e.g. a ship's internal structure with respect to its hull), but causes an increase in the maximum stress values internally in the structure.

5. 5. References

[1] S. Victor, "Study of the slamming phenomena occurring on point absorbers: experiments and literature review," Master in Civil Engineering, Department of Civil Engineering, Ghent University, Ghent, 2007.

[2] M.-C. Lin and L.-D. Shieh, "Flow visualization and pressure characteristics of a cylinder for water impact," *Applied Ocean Research,* vol. 19, pp. 101-112, 1997.

[3] A. Nila, "An adaptive PIV method for estimating slamming loads," *PhD dissertation, VUB Brussels, under progress,* 2013.

[4] T. von Karman, "The impact of seaplane floats during landing," *Technical note no. 321, National Advisory Committe for Aeronautics,* 1929.

[5] H. Wagner, "Über Stoß- und Gleitvorgänge an der Oberfläche von Flüssigkeiten," *ZAMM - Journal of Applied Mathematics and Mechanics / Zeitschrift für Angewandte Mathematik und Mechanik,* vol. 12, pp. 193-215, 1932.

[6] J. Wienke and H. Oumeraci, "Breaking wave impact force on a vertical and inclined slender pile--theoretical and large-scale model investigations," *Coastal Engineering,* vol. 52, pp. 435-462, 2005.

[7] E. Campana, A. Carcaterra, E. Ciappi, and A. Iafrati, "Some insights into slamming forces: compressible and incompressible phases," *Proceedings of the Institution of Mechanical Engineers, Part C: Journal of Mechanical Engineering Science,* vol. 214, pp. 881-888, 2000.

[8] I. T. Egorov, "Impact on a compressible fluid," *Technical Memorandum 1413, National Advisory Commitee for aeronautics,* vol. 20, 1956.

[9] A. Iafrati and A. A. Korobkin, "Hydrodynamic loads during early stage of flat plate impact onto water," *Physics of Fluids,* vol. 20, 2008.

[10] A. A. Korobkin, "Bluntbody impact on the fre surface of a compressible liquid," *Journal of Fluid Mechanics,* vol. 263, pp. 319-342, 1994.

[11] A. A. Korobkin and V. V. Pukhnachov, "Initial stage of water impact," *Annual Review of Fluid Mechanics,* vol. 20, pp. 159-185, 1988.

[12] N. Malleron, Y.-M. Scolan, and A. A. Korobkin, "Some aspects of a generalized Wagner model," *22nd International Workshop on Water Waves and Floating Bodies,* pp. 137-140, 2007.

[13] R. Skalak and D. Feit, "Impact on the surface of a compressible fluid," Office of Naval Research, New York1963.

[14] N. A. Lange and T. Rung, "Impact tests in pure and aerated water," presented at the 30th International Conference on Ocean, Offshore and Arctic Engineering, Rotterdam, The Netherlands, 2011.

[15] Z. N. Dobrovol'skaya, "On some problems of similarity flow of fluid with a free surface," *Journal of Fluid Mechanics,* vol. 36, pp. 805-829, 1969.

[16] K. S. Vepa, "Assessing slamming loads using fluid-structure interaction numerical algorithms," *PhD dissertation, Ghent University, under progress,* 2014.

[17] O. M. Faltinsen, "Water impact loads and dynamic response of horizontal circular cylinders in offshore structures," in *9th annual Offshore Technology Conference*, Houston, Texas, 1977, pp. 191 - 123.

[18] G. Miao, "Hydrodynamic forces and dynamic responses of circular cylinders in wave zones," *PhD dissertation, Norwegian University of Science and Technology,* 1988.

[19] M. F. Ionina, "Penetration of an elastic circular cylindrical shell into an incompressible liquid," *Journal of Applied Mechanics and Technical Physics,* vol. 40, 1999.

[20] O. Faltinsen, *Hydrodynamics of High-Speed Marine Vehicles*: Cambridge University Press, 2006.

[21] O. M. Faltinsen, "Hydroelastic slamming," *Journal of Marine Science and Technology,* vol. 5, pp. 49-65, 2000.

[22] O. M. Faltinsen, *Hydrodynamics of high-speed marine vehicles*, 1 ed.: Cambridge University Press, 2005.

[23] S. E. Hirdaris and P. Temarel, "Hydroelasticity of ships: recent advances and future trends," *Proceedings of the Institution of Mechanical Engineers Part M-Journal of Engineering for the Maritime Environment,* vol. 223, pp. 305-330, Aug 2009.

[24] K. Iijima, T. Yao, and T. Moan, "Structural response of a ship in severe seas considering global hydroelastic vibrations," *Marine Structures,* vol. 21, pp. 420-445, Oct 2008.

[25] Det Norske Veritas, "Environmental conditions and environmental loads," *Classification notes no. 30.5,* 2010.

[26] J. M. C. Campbell and P. A. Weynberg, "Measurements of parameters affecting slamming," in *Report No. 440*, Wolfson Unit for Marine Technology, Southampton, United Kingdom, 1980.

[27] J. Wienke, *Druckschlagbelastung auf schlanke zylindrische bauwerke durch brechende wellen*, 2001.

[28] M. Greenhow and L. Yanbao, "Added masses for circular cylinders near or penetrating fluid boundaries—review, extension and application to water-entry, -exit and slamming," *Ocean Engineering,* vol. 14, pp. 325-348, // 1987.

[29] J. M. C. Campbell, J. F. Wellicome, and P. A. Weynberg, "An investigation into wave slamming loads on cylinders," *Wolfson Marine Craft Unit Report No. 317,* 1977.

[30] P. Kaplan and M. H. Silbert, "Impact forces on platform horizontal members in the splash zone," in *Offshore Technology Conference*, Houston, 1976, p. Paper No. OTC 2498.

[31] Granta, "Cambridge Engineering Selector Edupack: Material database."

[32] J. Degrieck, "Composieten," *Master course, Ghent University,* 2013.

[33] A. Nila, S. Vanlanduit, K. S. Vepa, D. Van Nuffel, and W. Van Paepegem, "Strain and force measurements during hydroelastic impact of deformable bodies using image feature tracking techniques," *Submitted to Measurement Science and Technology,* 2013.

Chapter 6

Flat plate slamming

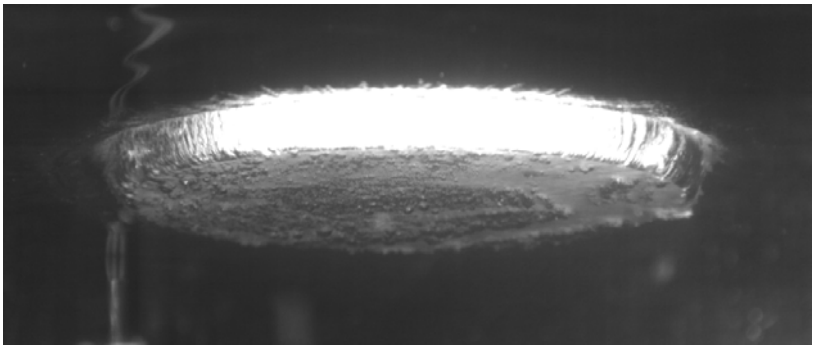

Overview

In this chapter, the effect of the deformability on the impact loads acting during horizontal flat plate slamming on a calm water surface is investigated. Therefore, it was first investigated if mass effects can play a role with respect to the comparison of the impact force results from the different test plates. The chapter further continues with a detailed description of the flat plate slamming process and thoroughly compares the impact forces, impact strains and impact stresses obtained for the different plate test models. Next, conclusions are drawn with respect to the effect of the deformability on the impact loads during flat plate slamming. The chapter ends with the description of a slamming test with a particular flat plate test object, which introduces a new and promising technique for measuring slamming loads.

6. 1. Effect of the flat plate mass on the slamming pressures and forces

In the previous chapter, it was shown that during the drop weight impact tests with the cylindrical test objects, the measured impact pressures and forces are not affected by the mass of these objects in the mass range which was applicable.

For the case of the flat plates, which are discussed in the present chapter, it is important to consider the same study before presenting the experimental results from the different flat plate test models and comparing them with each other. It was

theoretically shown by Verhagen [1] in 1969 that for a two-dimensional rigid flat plate (a rigid plate modeled as a line slamming on a two-dimensional volume of water) the impact pressures present at the surface of the plate during drop weight impact tests depend on the mass of that plate. Figure 6-1 shows this theoretical relation between the maximum impact pressure in the centre of a two-dimensional plate with a half width l of 0.2 m and a sort of dimensionless plate mass, valid for a drop weight impact test with a drop height of 0.2 m. It can be observed that if the plate mass increases, the impact pressure at the surface of the plate increases and eventually converges to a maximum value.

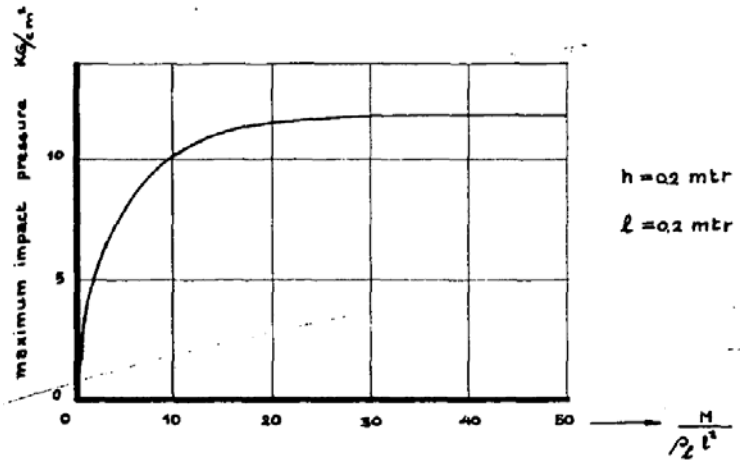

Figure 6-1: Theoretical maximum impact pressure under a theoretically rigid two-dimensional plate (l = 0.2 m) as function of the dimensionless mass of the plate for a drop height of 0.2 m [1]

The fact that this relation is theoretically found for the impact pressures at the bottom of a rigid two-dimensional plate makes that such type of relation is also theoretically valid for the impact forces obtained for the plates tested in this chapter. However, since these plates are not all rigid and the flow for these plates is three-dimensional, it is not possible to derive this theoretical force versus mass relation from the curve provided in Figure 6-1. Moreover, it must be mentioned that Verhagen [1] only validated his theoretical force-mass relation for values of $M/(\rho_l l^2) < 1$, which represents only a very small portion of the curve in Figure 6-1. All this makes that it is thus not exactly clear to which extent a variation in mass affects the impact forces for the considered plates.

The impactor masses corresponding to the different test plates are provided in Table 6-1. It can be observed that the range in which these masses vary is significantly smaller than for the case of the cylindrical test objects. The impactor

masses vary only slightly around an average value of 25.95 kg. Although a relation as depicted in Figure 6-1 may be applicable on the measured slamming pressures and forces, it is assumed that the mass differences among the different test plates of this thesis are not of that order to have large effects on the pressure and force results. Hence, it is assumed that the recordings from the different test plates may be compared with each other.

Table 6-1: Impactor masses for the deformable test plates

Plate	Plate mass [kg]	Impactor mass [kg]
Sandwich panel	1.65	23.94
Bottom impactor plate	6.3	23.00
P1 (Steel, d = 5 mm)	3.08	28.80
P2 (Steel, d = 1.97 mm)	1.28	27.00
P3 (Steel, d = 1 mm)	0.70	26.42
P4 (Aluminium, d = 1.02 mm)	0.29	26.01
P5 (Ertalon, d = 5.1 mm)	0.79	26.51
P6 (Ertalon, d = 2.1 mm)	0.27	25.99
P7 (Ertalon, d = 1.1 mm)	0.17	25.89
	Average	25.95

6. 2. Rigid flat plate test objects

The impact loads acting on rigid horizontal plates during vertical slamming on a flat water surface were intended to be measured in this thesis in two ways: by measuring local impact pressures and global impact forces. To enable local pressure recordings at the bottom of a horizontal rigid plate, the circular composite sandwich panel test object was used. Only for this test object enough space could be provided to enable the installation of the pressure transducers. Hence it is the only flat plate test object for which slamming pressures are measured. The next section describes the slamming experiments on this test model.

6. 2. 1. Sandwich panel

The sandwich panel test object is characterized by a small weight and a large flexural stiffness K (see section 3.4.2.1.b) to prevent the plate from bending under the slamming loads. However, attention should be paid to the fact that the E-modulus in the thickness direction is 36 times smaller than the E-modulus in the

directions in the plane of the plate (E_{33} = 800 MPa). It was estimated in section 3.4.2.1.b that this did not cause significant deformations in the thickness direction under the expected slamming loads which would affect the slamming behaviour.

Slamming experiments were performed, but they resulted in peculiar observations. As such, it was observed that during the initial stages of the slamming impact two pressure pulses and force pulses were measured by each of the pressure and force sensors. The larger the impact velocities, the better that the two pulses in the pressure and force recordings could be distinguished. Figure 6-2 and Figure 6-3 illustrate respectively the impact pressures and the impact force recorded during a slamming experiment of the sandwich test panel at a drop height of 0.8 m, which clearly show two pressure and force slamming peaks.

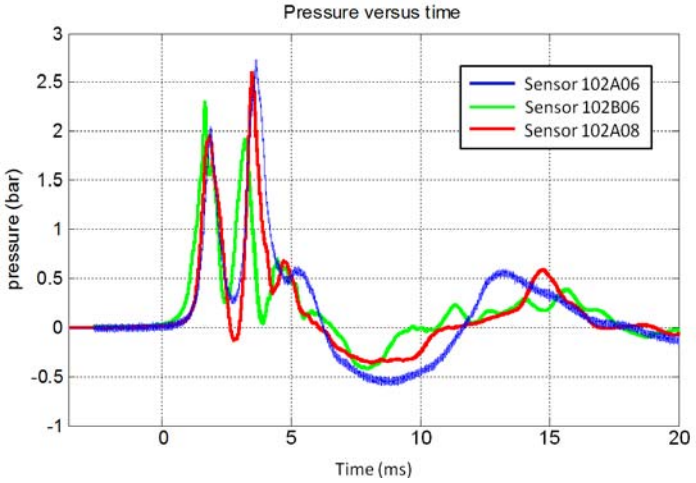

Figure 6-2: Pressure time history recorded by the three pressure sensors during the slamming test of the sandwich panel test object with a drop height of 0.8 m

It was initially unclear what was the physical reason for this second pressure and force pulse. In order to verify a possible contribution of the deformation of the test plate in the thickness direction, it was compressed under a static load in a hydraulic compression machine with a magnitude which is similar to the maximum impact forces as measured during the experiments (14 kN). It has been observed in these tests that the inner foam core of the sandwich panel compresses considerably more than can be calculated from the E-modulus in the thickness direction as provided by the manufacturer (7.06 μm). Hence, it can be concluded that this latter value for E_{33} as provided by the manufacturer is not a good estimation of the true value.

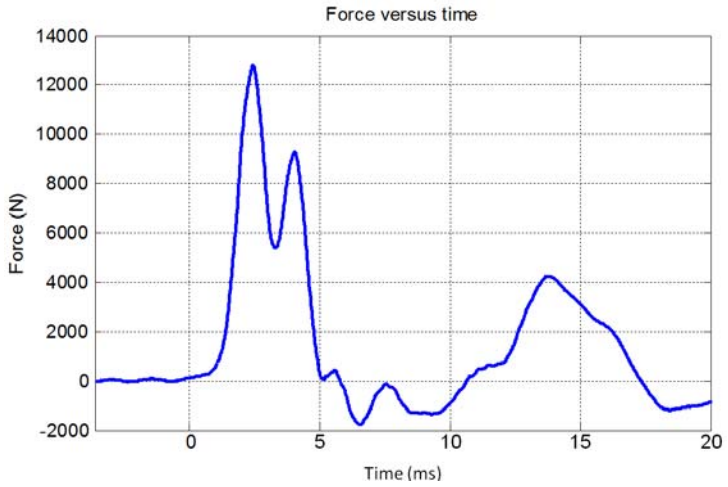

Figure 6-3: Force time history recorded by the force sensors during the slamming test of the sandwich panel test object with a drop height of 0.8 m

This deformation of the test plate unavoidably affects the impact load measurements. It may explain the two impact pulses in the sense that the deformation of the plate in the thickness direction causes an intermediate relief of the impact loads just after the first contact of the plate with the water. The measured impact pressures and forces are consequently not representative for the impact loads which typically occur during rigid flat plate slamming. Hence, the slamming pressure and force values for this test object are not described further in this chapter.

The flat plate test object consisting of the bottom plate of the load cell combination is a full Aluminium plate of which the deformation through the thickness can be considered negligible. Together with its large value for the flexural stiffness K, this test object is thus a better representation of a rigid flat plate. The results for this test object are presented in the next section.

Before doing so, the camera images recorded by the high speed camera from the slamming event for a few experiments with the sandwich panel are investigated more into detail, since they help in understanding the subsequent stages in the slamming process. They are the only few camera images taken from the slamming impact of the flat plate test objects since this camera was also continuously needed for measuring the impact velocity using the DIC technique. However, they can also provide information for the other flat plate test objects since the different physical phenomena related to the slamming event are similar for all flat plate test objects.

For measuring the physical phenomena occurring at the underside of the tested plate, the camera was positioned at the window of the water tank looking to the underside

of the plate under the water level. A schematic view depicted in Figure 6-4 clarifies this configuration. Due to the shallow angle between the camera direction and the water level, the water surface acted as a mirror and the test object could not be observed in the moments before the impact, when it was located above the water surface. This resulted in an exact estimation of the moment of first water contact (first image where the object becomes visible).

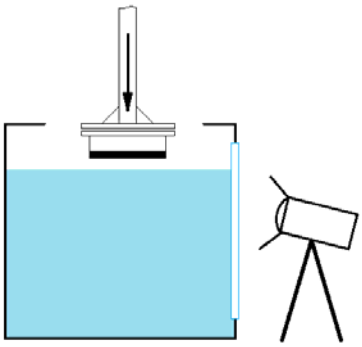

Figure 6-4: Schematic view of the camera position during the impact videos of the sandwich panel test plate

Figure 6-5 presents a sequence of high speed images showing the initial stages of the slamming impact for a slamming experiment with the sandwich panel. For the image taken at the moment of the first contact of the test plate with the water surface (t_0 = 0 ms), only the edges of the plate are visible while the zone inside these edges still has a black colour. This demonstrates that within the edges of the plate, the water surface remains quasi untouched indicating that air is entrapped between the plate surface and the water surface, while the edges of the plate already make contact with the water surface. This observation corresponds with the theoretical description of Verhagen [1] as was already schematically presented in chapter 2 (see Figure 2-13). Verhagen [1] theoretically explained this phenomenon by the very rapid air flow which is generated in the instances just before the impact in the small gap between the test plate and the water surface. Small surface waves elevated above the free water surface resulting from this rapid air flow were assumed to make first contact with the test plate and to entrap the air within the plate edges. The initial small surface waves could not be observed in this dissertation, but experimental evidence for their existence was already provided by Oh. et al. [2]. A high speed image recording depicting the initial surface in their 2D experimental setup is illustrated in Figure 6-6.

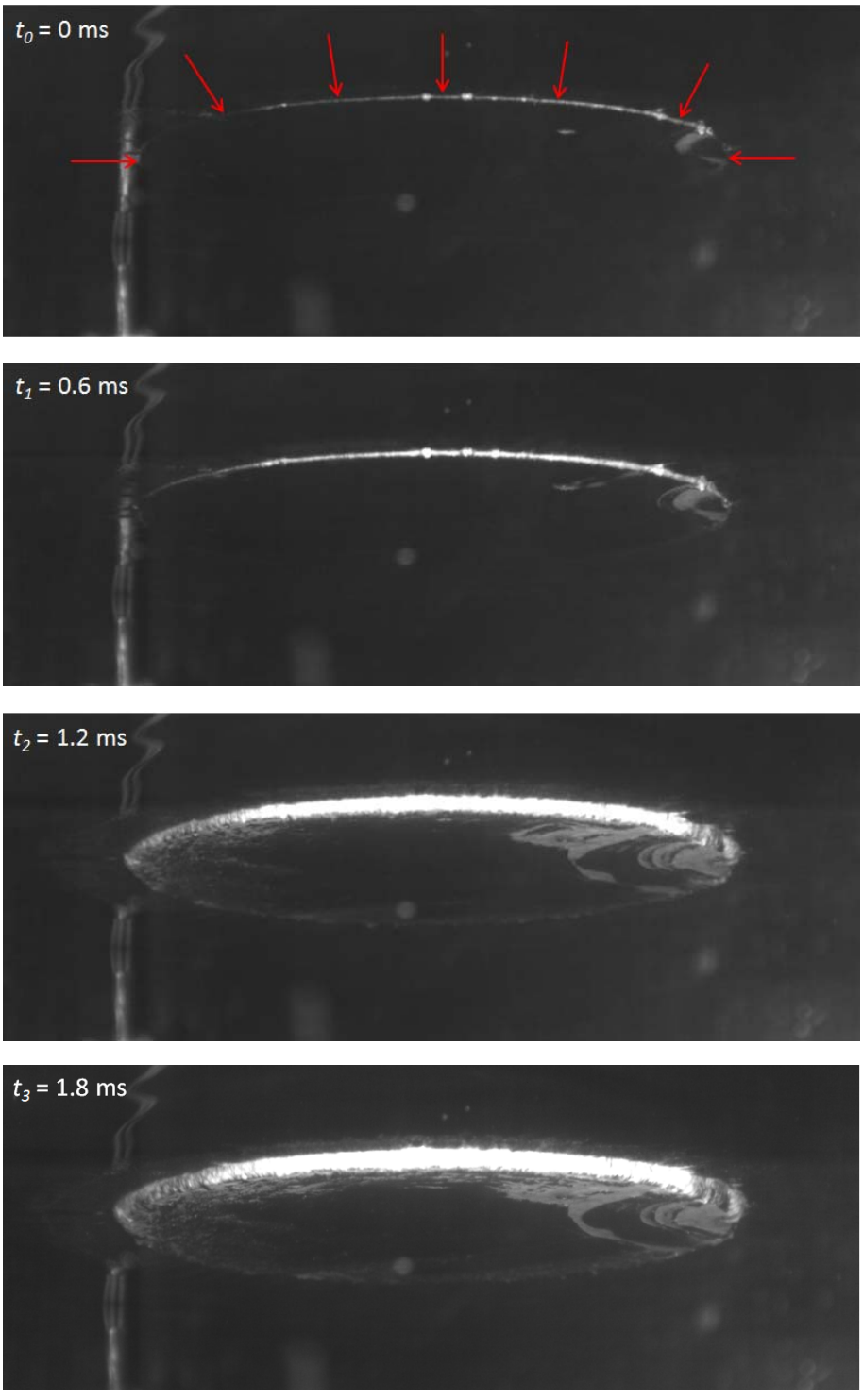
t_0 = 0 ms
t_1 = 0.6 ms
t_2 = 1.2 ms
t_3 = 1.8 ms

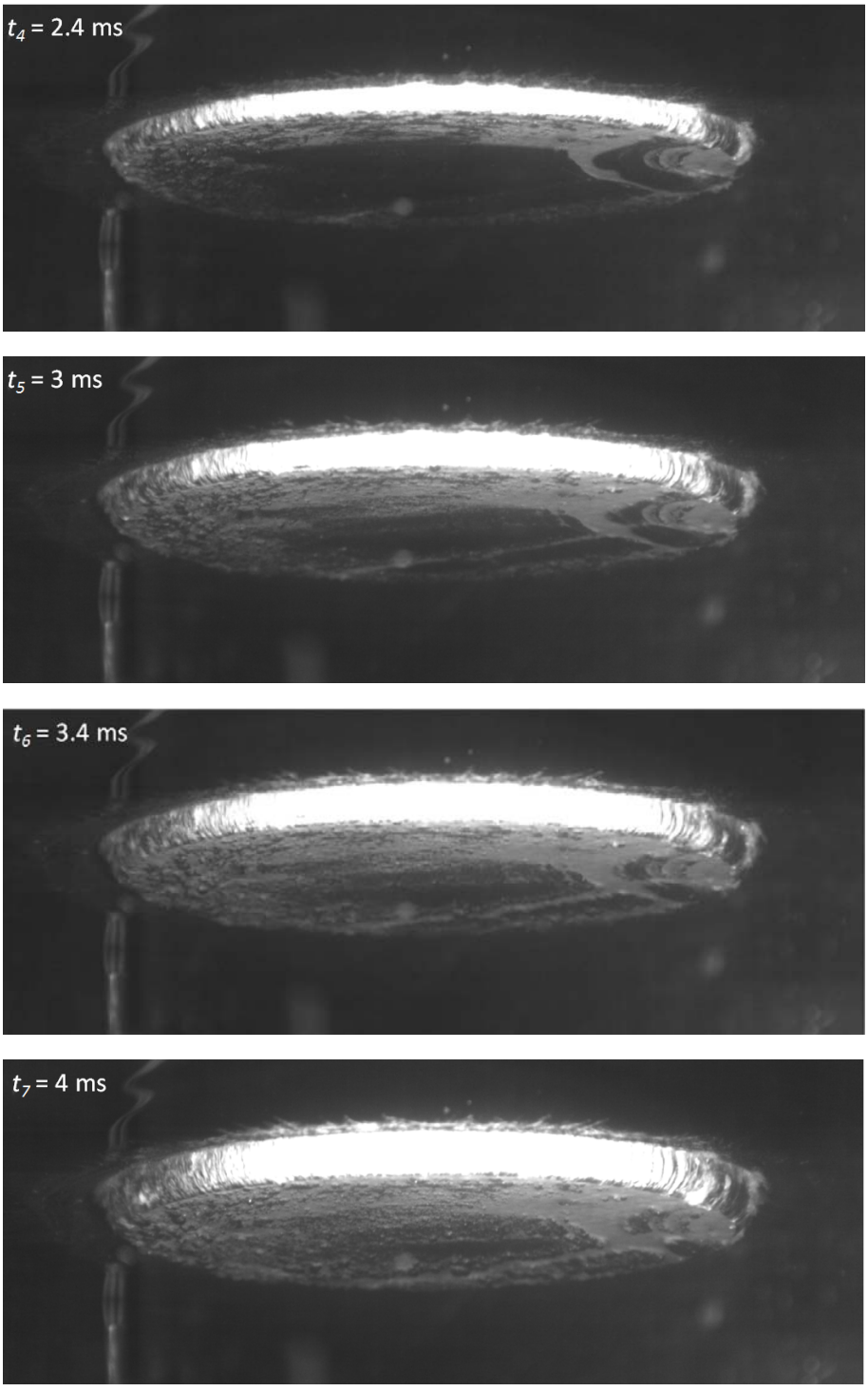
t_4 = 2.4 ms
t_5 = 3 ms
t_6 = 3.4 ms
t_7 = 4 ms

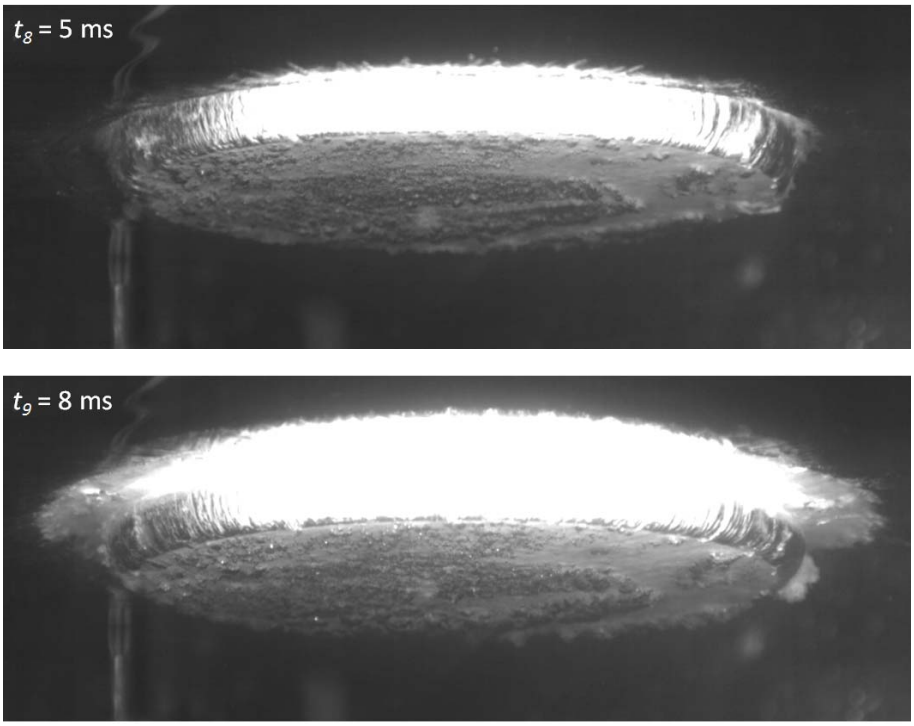

Figure 6-5: Sequence of high speed video images for the initial stages of the slamming impact of the sandwich panel test object for a drop height of 0.5 m

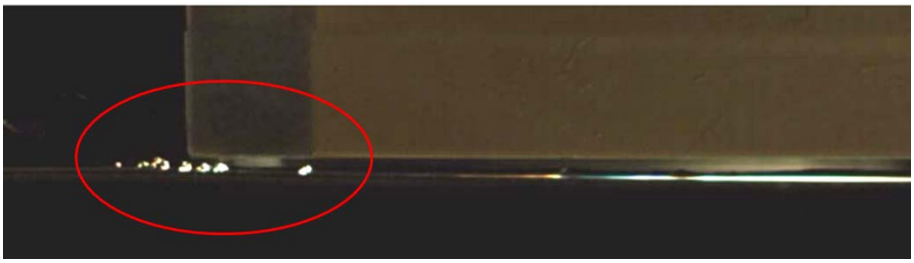

Figure 6-6: The presence of initial surface waves before the water impact of a flat plate [2]

According to Verhagen [1], the sudden stop of the air flow at the moment that the initial surface waves make contact with the plate causes a pressure shock wave in the enclosed air pocket propagating from the edges to the centre of the plate. This causes the air pocket to break up into smaller air bubbles. This is exactly what is observed during the experiments in this dissertation. The subsequent camera images in Figure 6-5 clearly show the black air pocket under the plate to gradually break up into smaller air bubbles. This process progresses from the edges to the centre of the

plate. The time duration of this process is approximately 4 ms and it is in this time span that a pressure and force pulse builds up and disappears again.

An initial air pocket entrapment and a subsequent implosion of this air pocket thus characterize the two main stages of rigid flat plate slamming. With this knowledge, the results obtained from the slamming experiments with the bottom impactor plate will be interpreted carefully in the following section.

6. 2. 2. Bottom impactor plate

For the bottom impactor plate, only slamming forces are recorded. The following section describes in detail the time evolution of these recorded forces.

6. 2. 2. 1. Force time history

Figure 6-7 depicts the force time history for a vertical slamming experiment with the bottom impactor plate dropped from a height of 0.4 m. At the moment that the plate makes the first contact with the water surface (t = 0 ms), the force smoothly starts increasing in the very initial stage of the impact. This very initial small increase in the force is most probable due to the compression of the air pocket entrapped at the moment of the first contact of the plate with the water. It is only after 1 ms, when the implosion of the air pocket propagates from the edges of the plate towards the centre that the impact force evolves into a steep pulse.

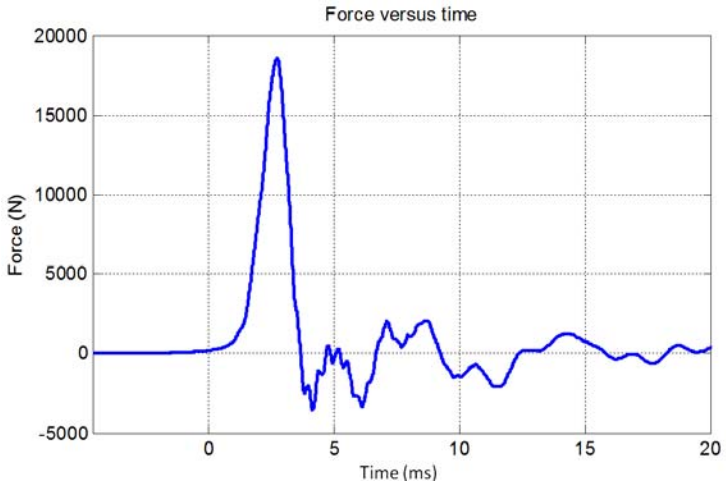

Figure 6-7: Force time history corresponding to a slamming test with the bottom impactor plate at a drop height of 0.4 m

After a time span of about 3 ms, the force pulse reaches its maximum value. This force pulse contains only one peak instead of the two which were observed for the

sandwich test panel. This confirms the assumption that the deformation of the sandwich panel through the thickness is responsible for the two distinguished pressure and force peaks.

After this force maximum, the force decreases rapidly as the implosion process ends at the centre of the test plate. Next, some small and irregular force oscillations are observed for a time span of 20 ms before the force comes back to the zero level. It can be observed that during this last stage, the force reaches negative values. These are most probably caused by the rapid deceleration of the test object as a result of the impact force pulse, as is depicted in Figure 6-8 in terms of a large drop in the velocity of the test object. The discrepancy between the instantly decreased velocity of the test object and the velocity of the volume of water which has been accelerated in the instances just after the impact is assumed to create a pressure under the plate which is smaller than the atmospheric pressure resulting in a negative force. The large deceleration of the flat plate test object also shows that a clear distinction should be made between flat plate slamming experiments accelerated under gravity which are largely decelerated at impact and experiments with forced constant velocity. A comparison of the current results with experimental results from constant velocity slamming experiments would not provide relevant information.

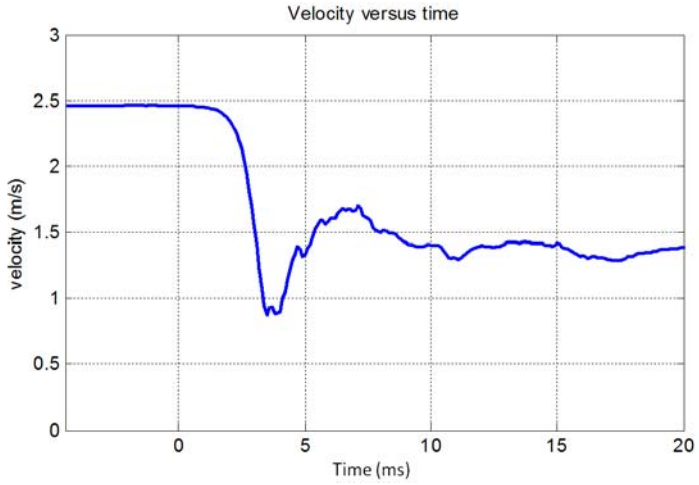

Figure 6-8: Velocity as function of time corresponding to the considered slamming test with the bottom impactor plate for a drop height of 0.4 m

Verhagen [1] also performed slamming drop experiments for a rigid flat plate test model accelerated under gravity (variable velocity). Instead of measuring impact forces, impact pressures in the centre of the plate were presented in the corresponding work. Figure 6-9 presents the pressure time history which was published by Verhagen [1] for a slamming experiment with a drop height of 0.4 m.

A good agreement can be observed with the impact force depicted in Figure 6-7, in the sense that both recordings start with a smooth increase which evolves into a steep pressure pulse, and finally rapidly decrease towards negative values. However, it must be considered that the pressure is measured locally, while the force represents the global response. Since the pressure under the plate is not uniform during the impact, but rather evolves as a pressure wave which rapidly propagates from the edges to the centre of the plate, the impact pressure and impact force cannot by compared directly in magnitude to each other by simply dividing the force by the plate area. The recorded slamming force must be considered at each time moment as the instant integration of the pressures present at the bottom of the test plate.

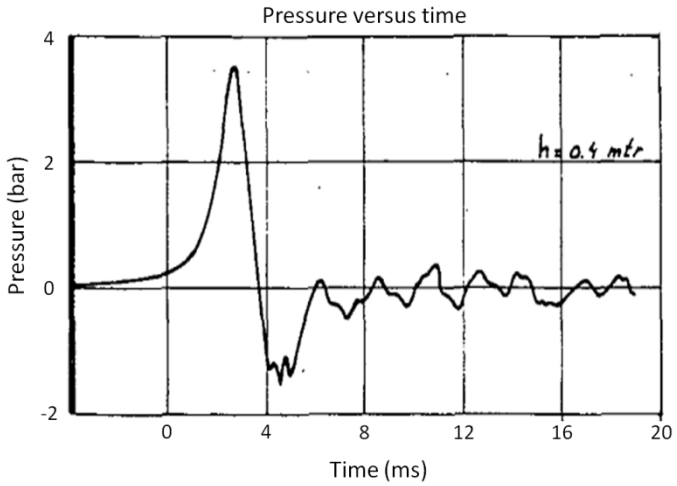

Figure 6-9: Pressure recorded at the centre of a rigid test plate corresponding to a slamming experiment with a drop height of 0.4 m according to Verhagen [1]

6. 2. 2. 2. Impact force values

Figure 6-10 and Table 6-2 give an overview of the impact forces measured during the slamming experiments with the bottom impactor plate. Drop heights ranging from 0.05 m to 1.3 m were tested. Figure 6-10 presents the results for every performed test while Table 6-2 gives the average impact force values per tested drop height together with the standard deviation.

Compared to the magnitude of the impact force values, the overall scatter is reasonably small. Only for impact speeds larger than 4 m/s, the scatter becomes more significant. However, considering the overall reasonable dispersion, the force recordings can be assumed very reproducible.

A quadratic relation including a linear term can be found between the impact force values and the impact velocities. This indicates an approximate linear relationship between the impact forces and the drop height since the square of the impact velocity is directly proportional to the drop height (see Equation (4.10)).

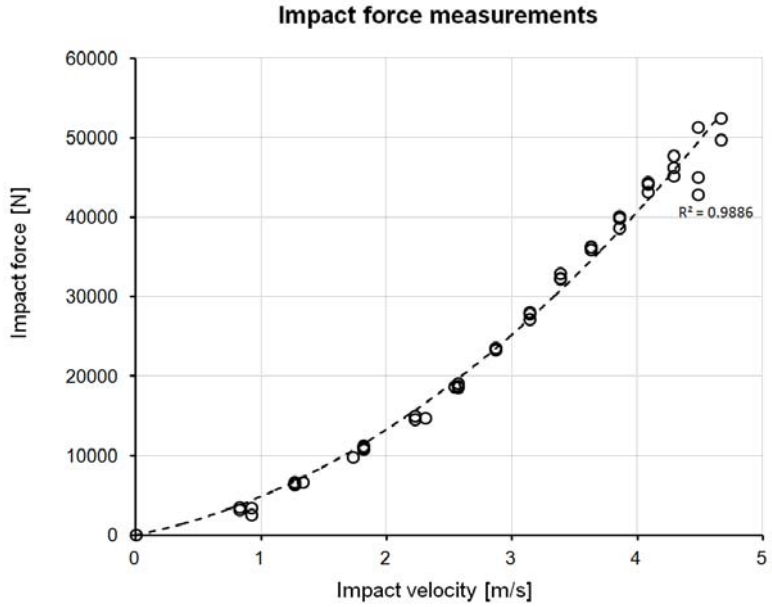

Figure 6-10: Overview of the measured impact force values for the impactor bottom plate as test object

Extremely large impact force values can be observed, especially at larger impact velocities, which are much larger than initially expected during the design of the impactor load cell plates (see section 3.2.2). A static uniformly distributed load on the bottom impactor plate corresponding with the maximum obtained impact force (51.1 kN) would result in a deflection of 1.92 mm it the middle of the plate when the plate would be simply supported at its edges (see Equation (3.2)). This deflection does not occur in reality since the slamming forces are of a highly dynamic nature and the plate is not supported at its edges, but it indicates at least that the deformation of the impactor bottom plate might play a role during the slamming process. This makes that the bottom impactor plate may not be regarded as a rigid flat plate test object. Hence, in the next paragraphs, it will be considered as a very stiff but non-rigid test plate among the other deformable test plates. The results for these latter plates are discussed in the next section.

Table 6-2: Overview of the measured impact force values for the impactor bottom plate as test object

H [m]	U_{avg} [m/s]	Impact forces $F_{I,P}$ [N]	σ_F [N]	Equivalent average pressure $p_{I,P}$ [bar]
0	0	0	0.0	0.000
0.05	0.83	3344.7	225.9	0.266
0.054	0.92	3016.9	670.7	0.240
0.1	1.26	6460.5	184.5	0.514
0.115	1.33	6692.1	-	0.533
0.19	1.73	9874.9	-	0.786
0.2	1.81	11031.1	202.9	0.878
0.3	2.23	14844.4	265.7	1.181
0.319	2.31	14777.6	-	1.176
0.4	2.57	18816.6	266.9	1.497
0.406	2.54	18663.7	-	1.485
0.5	2.87	23480.9	106.0	1.869
0.6	3.14	27714.5	446.1	2.205
0.7	3.38	32526.8	417.0	2.588
0.8	3.63	36191.9	209.6	2.880
0.9	3.86	39559.2	776.0	3.148
1	4.08	43937.4	655.4	3.496
1.1	4.29	46411.9	1245.6	3.693
1.2	4.48	46412.8	4424.4	3.693
1.3	4.67	51101.1	1915.8	4.066

6. 3. Deformable flat plate test objects

For the deformable plate test objects as introduced in section 3.4.2.2, only force measurements will be described since no pressure recordings could be done on these types of objects. Inserting pressure sensors into the test objects would largely affect the deformations of the plates. Moreover, some of the plates were too thin to guarantee a firm fixture of the pressure sensors.

6. 3. 1. Impact forces

6. 3. 1. 1. Force time history

Figure 6-11 shows the force time histories for the different deformable test plates for slamming experiments with a drop height of 0.4 m. The impact force as recorded during the same experiment for the impactor bottom plate has also been included in this graph. For the Aluminium test plate P4, permanent deformations were observed at this drop height and the results are hence excluded from the graph.

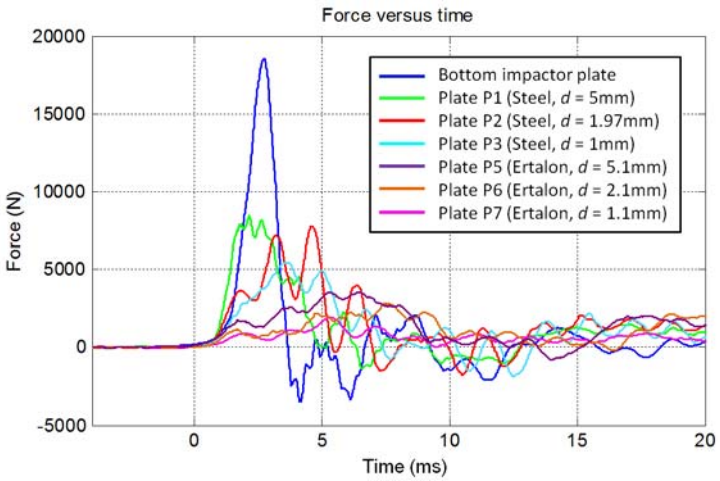

Figure 6-11: Force time histories for the deformable test plates measured during slamming experiments with a drop height of 0.4 m

A large difference can be observed between the force time evolutions of the deformable plates and the one obtained for the impactor bottom plate. The first ones are characterized by highly oscillatory force histories with different types of frequencies which are not observed in the last case. These oscillations are also observed in the strains measured on the deformable plates. Figure 6-12 shows for example a comparison between the force recording and the strain measurement in the centre of the steel plate P2 for a drop height of 0.4 m. The same oscillation frequencies can be identified in both curves. However, the ratio of the magnitudes of the pulses with respect to each other is not the same for both measurements.

Furthermore, it can be observed in Figure 6-11 that generally, as the bending stiffness K of the plate decreases (see Table 3-8), the frequency of the force fluctuations decreases and the force pulses become more spread in time. At the same time, the force magnitudes decrease with decreasing bending stiffness. However, one exception is noticed for the ertalon plate P5 with thickness d = 5.1 mm.

Although it's bending stiffness K is larger than the one for the steel plate P3 with thickness d = 1 mm, it has a smaller force amplitude. A more detailed discussion on the force magnitudes follows in the next section.

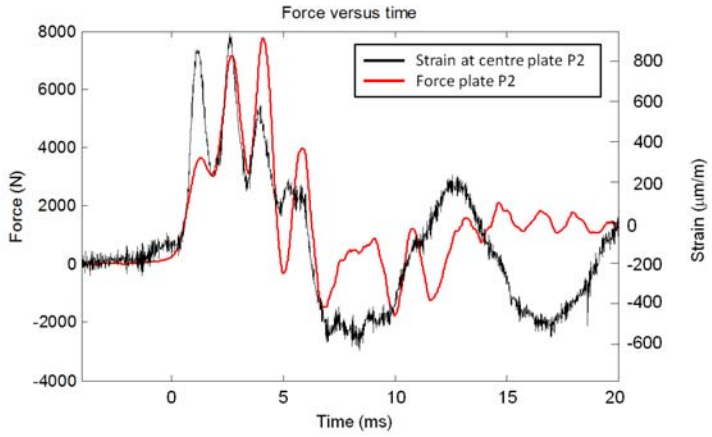

Figure 6-12: Comparison between the force recording and the strain measurement at the centre of plate P2 for a drop height of 0.4 m

The oscillations in the force recordings are different from the ones observed in the forces measured in chapter 5 for cylindrical slamming in the sense that the oscillations are now also present in the strains measured on the test plates, which was not the case for the cylindrical test objects. This indicates that at impact the oscillations in the forces are caused by vibrations in the test plates rather than vibrations in the bottom impactor plate, which were the reason for the oscillations in the force recordings of the cylindrical test models. The vibrations in the bottom impactor plate are in the case of the flat plates suppressed since the load acting on this plate is axisymmetric in contrast to an asymmetric loading which was the case for the cylindrical slamming tests. The oscillations in the force recordings are therefore in this case caused by an excitation of the eigenfrequencies of the plates themselves. This has also been observed in experiments and numerical simulations done by Faltinsen et al [3] (see also further in Figure 6-19) and it explains why for smaller values of the flexural stiffness K the frequency of the vibrations decrease. After all, the fundamental natural frequency of a construction given by Equation (2.10) is proportional to the square root of the stiffness.

The observed vibrations cause oscillatory deformations in the plate which result in a non-uniform pressure distribution under the plate. The recorded forces can be considered as an average of these local pressures over the entire area of the plate. Hence, they do not exactly represent the loads which are experienced by the plate material itself during water impact. They are more closely related to the loads which

are experienced by the structure supporting the plate material during water slamming.

This can be compared with the case of an elastic hull and the framework which supports the hull panels. The recorded forces can give an idea on the loads which act on the support structure, and can be helpful in its design. However, they give no direct information on the loads which might be experienced by the hull panels themselves. The loads which are experienced by the plate material are best described in terms of internal stresses, as has also been done by Faltinsen et al. [3]. These can be calculated from the measured strains on the plate. In the next sections, both force peak values and stress peak values will be discussed.

6. 3. 1. 2. Force impact values

This section investigates the impact force values which are recorded during the slamming experiments with the deformable plates into more detail. Figure 6-13 and Table 6-3 present the average values of the recorded impact forces for three slamming experiments per drop height as function of impact velocity.

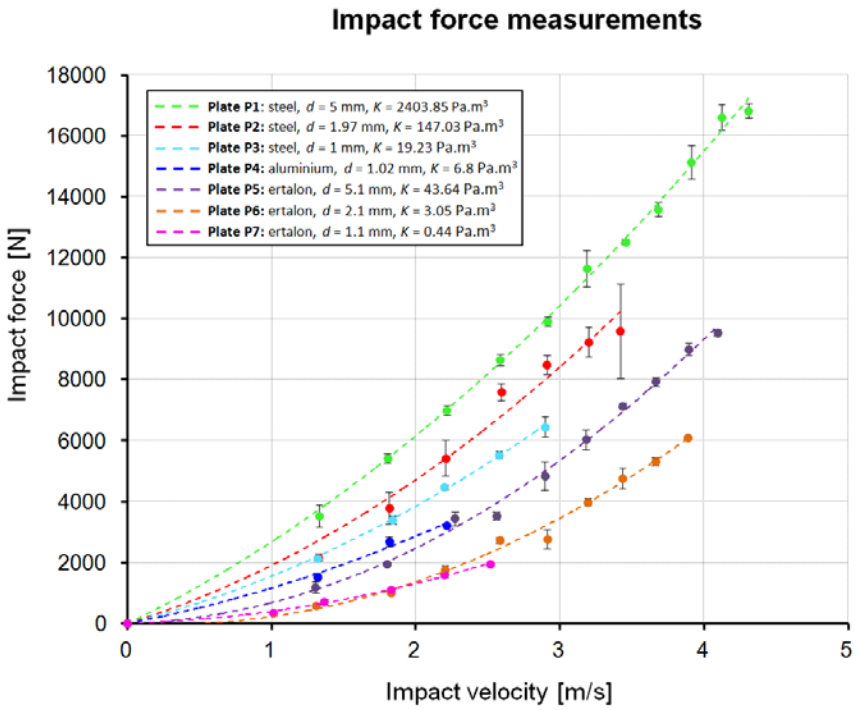

Figure 6-13: Overview of the measured impact force values for the deformable test plates

Table 6-3: Overview of the measured impact force values for the deformable test plates

H [m]	U_{avg} [m/s]	Impact forces $F_{I,P}$ [N]						
		P1	P2	P3	P4	P5	P6	P7
0	0	0	0	0	0	0	0	0
0.05	1.01	-	-	-	-	-	-	355.09
0.1	1.32	3530.85	2170.52	2136.16	1533.63	1963.63	1013.01	706.59
0.2	1.82	5425.13	3788.40	3405.66	2682.04	1963.63	1013.01	1102.50
0.3	2.21	6988.14	5429.15	4482.17	3217.12	3443.31	1761.75	1603.81
0.4	2.57	8652.42	7589.86	5534.36		3524.70	2730.99	1946.22
0.5	2.90	9915.53	8494.99	6453.52		4845.13	2776.15	
0.6	3.19	11648.17	9242.97			6045.91	3986.30	
0.7	3.44	12522.59	9598.01			7134.58	4770.74	
0.8	3.67	13587.10				7933.51	5319.12	
0.9	3.89	15136.11				8998.83	6095.00	
1	4.11	16603.39				9548.37		
1.1	4.31	16825.44						

The impact velocities provided in Table 6-3 represent the average impact velocities of all the experiments with the deformable test plates for each tested drop height. Furthermore, Figure 6-13 also depicts the standard deviation on these average forces. The numeric values of these standard deviations are provided in Table 6-4. With a few exceptions, it can be concluded that the scatter in the results is small enough to have reproducible measurements.

For the stiffest plates a maximum drop height of 1.1 m was applied. For the other ones, the drop height was increased until permanent deformation could be observed. That is the reason why the number of tested drop heights is not the same for the different test plates. After all, testing plates which are already permanently deformed will result in totally different impact loads, since the air cushion at the start of the impact event will have another shape.

Comparing the impact forces among the different deformable plates leads to the observation that in the most cases, a decreasing flexural stiffness K of a plate results in smaller impact forces. This corresponds with the expectation that with increasing flexibility of the plates more energy is absorbed by the deformation which results in smaller slamming loads, as theoretically described in section 2.2. However, it can be

observed that this is not the case for every plate. As such, it can be observed that although the bending stiffness of the ertalon plate P5 is larger than the ones of the steel plate P3 and the aluminium plate P4, its impact forces are smaller than for the two latter cases. This situation also occurs between the ertalon plates P6 and P7 for small drop heights.

Table 6-4: Overview of the standard deviation of the measured impact force values for the deformable test plates

H [m]	U_{avg} [m/s]	σ_F [N]						
		P1	P2	P3	P4	P5	P6	P7
0	0	0	0	0	0	0	0	0
0.05	1.01	-	-	-	-	-	-	3.87
0.1	1.32	362.39	123.25	92.24	124.25	182.45	60.28	93.08
0.2	1.82	167.01	523.57	127.50	162.55	53.30	33.26	25.42
0.3	2.21	158.22	597.32	76.63		219.39	145.86	91.51
0.4	2.57	187.79	264.87	122.63		128.72	87.48	
0.5	2.90	163.12	318.24	322.07		470.05	320.52	
0.6	3.19	609.51	489.93			325.67	123.06	
0.7	3.44	85.87	1552.27			98.10	342.55	
0.8	3.67	231.75				135.97	129.13	
0.9	3.89	556.11				198.74	54.51	
1	4.11	416.69				113.02		
1.1	4.31	226.75						

It can be observed that the trend of decreasing impact forces with decreasing plate's flexibility is more valid when considering the impact forces only per material type (e.g. steel plates, ertalon plates). This indicates that besides the degree of deformability also other materials parameters might significantly affect the impact forces during flat plate slamming. This was also observed in the previous chapter for the case of deformable cylindrical slamming. The fact that material damping has an influence on the impact loads has already been illustrated in section 2.2. Furthermore, since the deformability and thus the stiffness of a material is closely related with the eigenfrequencies of that material, it is clear that also these eigenfrequencies have an effect on the slamming loads. This can be understood when considering that other eigenfrequencies result in other vibration patterns in the

plate and thus other slamming pressure distributions under the plate at impact, eventually resulting in other global impact forces.

The impact force results from the deformable plates can now also be compared to the impact forces corresponding to the much stiffer bottom impactor plate. However, a direct comparison of the force values is difficult since the bottom impactor plate has a significantly larger area than the deformable plates. It was theoretically shown by Verhagen [1] that the maximum impact pressure under the plate is hardly affected by the plate area (see Figure 6-14). Hence, it is assumed that this is also the case for the impact forces per unit area which correspond to the average pressure under the plate at the moment that the global force reaches its maximum. The impact forces measured with test plates of different area can thus be compared to each other by dividing the forces by the area of the corresponding plates.

Figure 6-15 compares the average impact force values per unit area for all the tested flat plate test objects. It can be observed that the impact force values obtained for the bottom impactor plate are significantly larger than the impact forces obtained for the deformable test plates, especially for larger impact velocities. This corresponds with the general trend observed among all the deformable test plates and especially among the deformable test plates of the same material, namely that more rigid structures lead to larger impact forces.

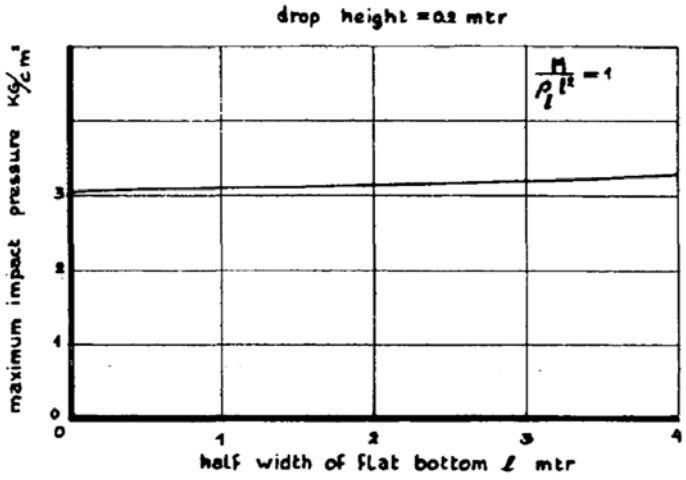

Figure 6-14: Maximum slamming impact pressure as function of the half width of a rectangular flat plate for a drop height of 0.2 m as obtained by Verhagen [1]

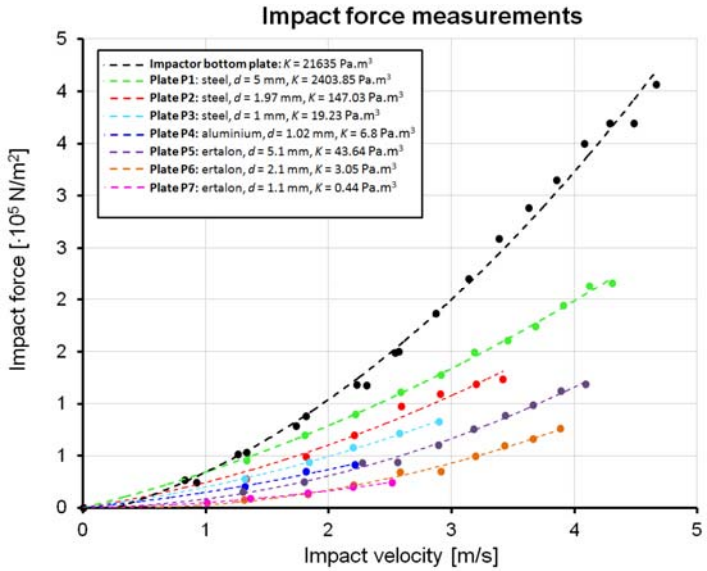

Figure 6-15: Comparison of the average impact forces per unit area of the impactor bottom plate and the deformable test plates

Figure 6-16 plots the average impact forces per unit area for all the tested plates as function of the flexural stiffness for three values of the tested impact velocities. It can be noticed that for small values of the flexural stiffness up to approximately 200 Pa.m^3, the impact forces generally increase very fast with decreasing flexibility. For plates which are stiffer than 200 Pa.m^3, the force versus stiffness curve flattens quickly and the impact forces increase much less with decreasing plate's flexibility. The impact forces thus seem to vary logarithmically as function of the flexural stiffness of the plates. A similar trend was observed for the case of the deformable cylindrical test models in the previous chapter.

This logarithmic trend can be confirmed when presenting the flexural stiffness on a logarithmic basis (see Figure 6-17). Except for some small irregularities, linear relationships can be recognized in these graphs. The small irregularities can be attributed, as already previously discussed, to the effect of other material parameters such as damping and eigenfrequencies.

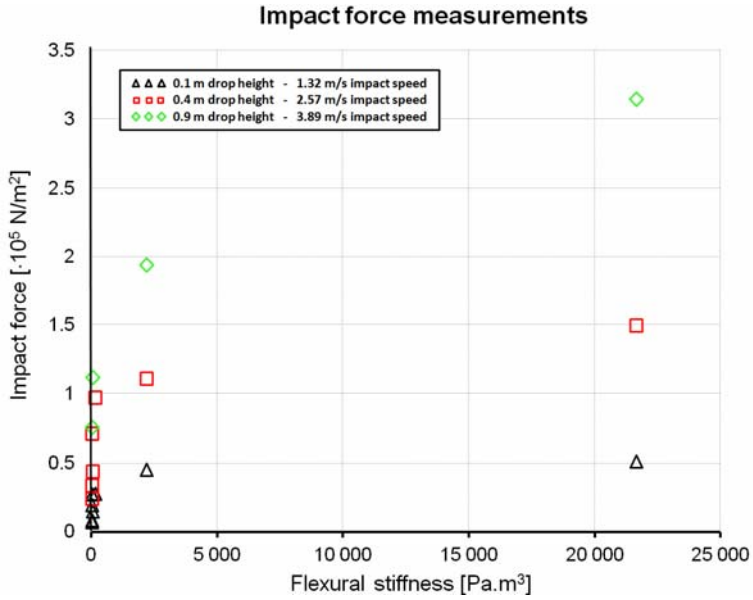

Figure 6-16: Overview of the average impact forces as function of plate stiffness for three tested impact velocities

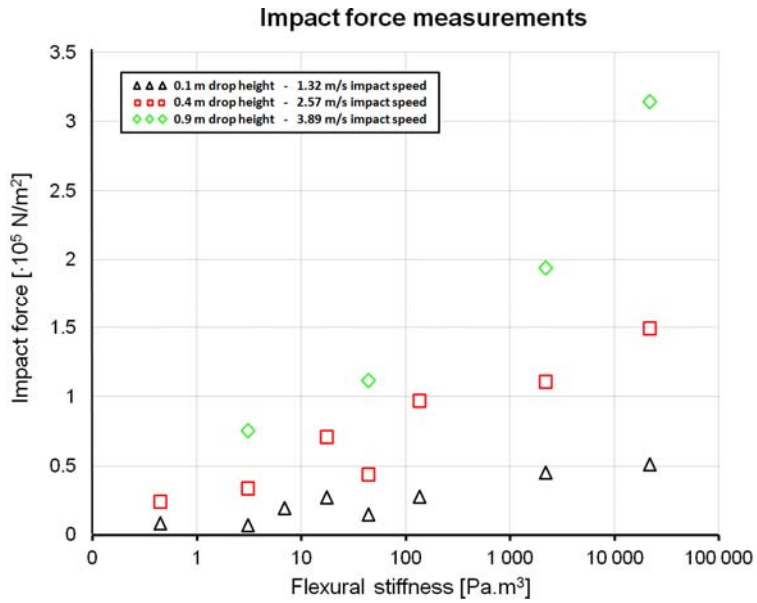

Figure 6-17: Overview of the average impact forces as function of plate stiffness for three tested impact velocities, with the flexural stiffness presented on a log scale

6. 3. 2. Impact strains and stresses

Similarly as in the case of the deformable cylindrical test objects, the slamming loads can also be determined in terms of impact stresses internally in the test plates. In the current section, the recorded impact strains and stresses are discussed and the effect of the plate flexibility on the slamming stresses in investigated.

6. 3. 2. 1. Strain and stress time histories

The typical shape of the strain time histories of the measured strains has already been described in section 6.3.1.1. It was observed that the strains and thus also the stresses showed many oscillations at various frequencies, indicating that the deformable plates are prone to vibrations during the water impact. This can also be observed from Figure 6-18 which shows the strain recordings of the four strain gauges which are installed on the ertalon plate P7 for a drop height of 0.4 m. This graph also shows that the vibrations rapidly decay (after 9 ms in the graph) and the plate thereafter starts deforming at a smaller frequency which corresponds to a normal deflection of the plate. Furthermore it can be noticed that the strain is maximum in the centre of the plate and decreases for increasing radial distance from the plate's centre.

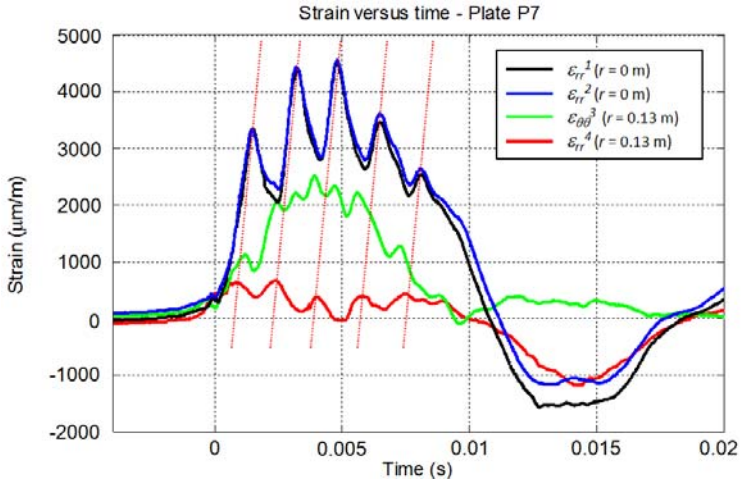

Figure 6-18: Strain recordings of the four strain gauges installed on the plate P7 (ertalon plate, d = 5 mm) for a drop height of 0.4 m

It can also be observed that the vibration pattern in the plate is dependent on the strain gauge location. Furthermore, for the strain gauges measuring the strain in radial direction it can be noticed that the time span between the successive strain pulses is the same (indicated by dashed red lines), but these pulses occur earlier for

the strain gauge close to the edge of the plate. This indicates that the vibrations of the plate originate at the edges and propagate to the centre of the plate, which corresponds with the way that the pressure wave generated at impact propagates in the air pocket.

These types of vibrations and corresponding oscillatory strain recordings were also observed in experiments and numerical simulations done by Faltinsen et al. [3]. Figure 6-19 shows the strain as function of time at the centre of a rectangular steel plate with a flexural stiffness of K = 8960 Pa·m^3 for a drop height of 0.5 m as presented by Faltinsen et al [3].

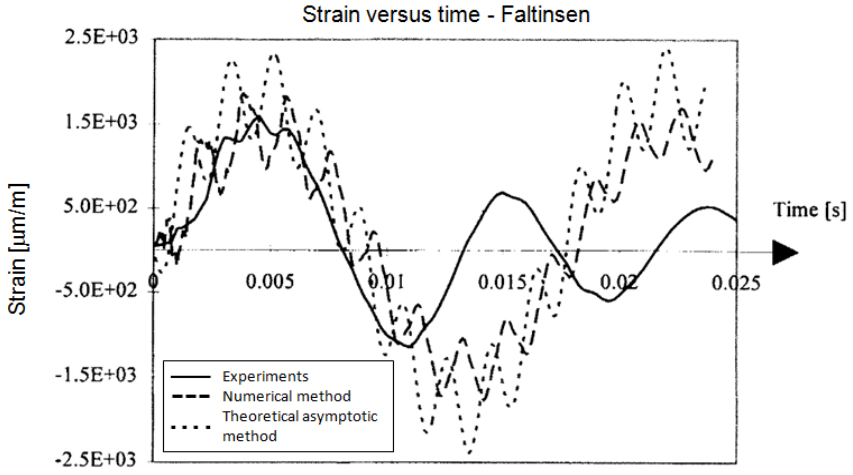

Figure 6-19: Strain as function of time in the centre of a steel plate with K = 8960 Pa·m^3 for a drop height of 0.5 m, presented by Faltinsen et al. [3]

The solid line shows the experimental recording while the broken and the dotted line show respectively the results from a numerical simulation and a theoretically asymptotic method. Low frequency as well as high frequency oscillations can be identified in the results, similarly to the measurements from the current thesis. Furthermore, it can be observed that the oscillations with large frequency, which are caused by an excitation of one of the eigenfrequencies of the plate, rapidly dampen out in the experiments while this is not the case for the numerically and theoretically obtained solution. This rapid decay of the larger frequencies is also noticed in the experiments from the present dissertation.

6. 3. 2. 2. Strain and stress impact values

In order to obtain an overview of the maximum strains and stresses in the tested plates, only the strain recordings in the centre of the plates (r = 0 m) are considered since the strains and the stresses reach the largest values at this position.

Figure 6-20 and Table 6-5 show the average maximum strains measured in the centre of the test plates as function of impact velocity. Each point in the graph represents an average of the strains measured by the two strain gauges in the centre for all the experiments performed at the considered impact speed. For most of the tested plates, three drop tests could be performed for each drop impact velocity. However, the large deformations of some plates caused the encapsulations of the strain gauges to loosen a bit and enabled moist affecting the strain measurements. The affected recordings have been eliminated from the test results. Eventually, this resulted in a reduced number of measurements and a lack of strain recordings for some plates at some impact velocities.

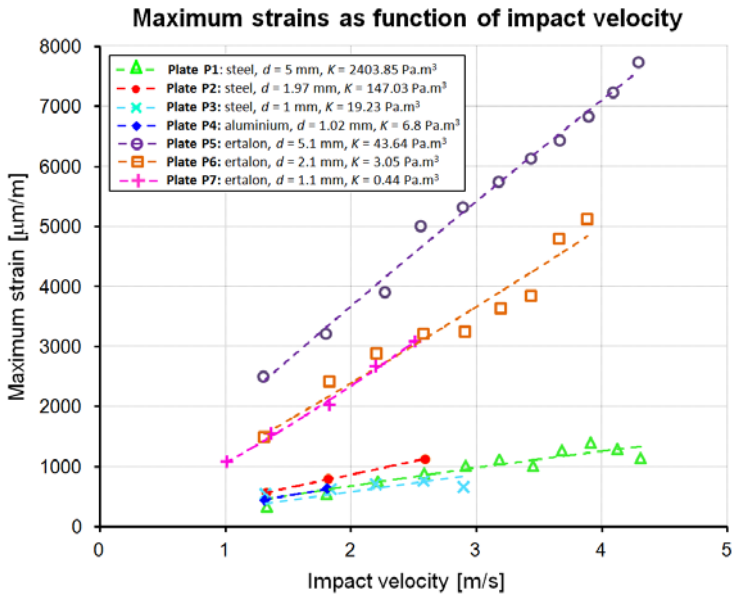

Figure 6-20: Overview of the maximum strains for the deformable test plates as function of impact velocity

For most of the tested plates, it seems that the maximum strains follow an approximate linear relationship with the impact velocity. When comparing the impact strain results among the different test plates, it can observed that no straightforward increasing or decreasing relation can be found between the maximum strains and the flexural stiffness K of the plates. In some cases, it can be

observed that a more deformable plate results in larger maximum strains (e.g. plate P2 with respect to P1) while in other cases the opposite can be found (e.g. plate P6 versus P5). A plate which deforms more during the slamming experiments does thus not necessarily exhibit larger maximum strains. Two effects play a role here:

- Similarly as in the case of the deformable cylinders, it must be noticed that the strain recorded by the strain gauges does not only depend on the flexibility degree of the considered plate, but also on its thickness. If two plates have the same value of the flexural stiffness *K*, but another plate thickness *d*, they will exhibit the same deformation, but the strain recorded at the surface of the thicker plate will be larger than for the other one.
- Furthermore, it has been observed that the plates are prone to vibrations, and the deformation patterns are thus more complicated than expected just by bending under a uniform pressure. Due to these vibrations, it is possible that locally larger strains are observed for plates with smaller flexural stiffness.

Table 6-5: Overview of the maximum strain values for the deformable test plates

H [m]	U_{avg} [m/s]	Maximum strain at plate centre ε_{rr} [μm/m]						
		P1	P2	P3	P4	P5	P6	P7
0	0	0	0	0	0	0	0	0
0.05	1.01	-	-	-	-	-	-	1078.05
0.1	1.32	336.74	562.44	541.22	442.87	2500.02	1496.41	1547.89
0.2	1.82	545.19	800.29	625.31	637.35	3208.67	2414.30	2027.85
0.3	2.21	749.12	-	709.52		3907.02	2884.71	2679.32
0.4	2.57	885.36	1130.03	770.11		4626.56	3213.60	3083.63
0.5	2.90	1014.11		664.65		4966.61	3247.97	
0.6	3.19	1119.48				4645.81	3628.88	
0.7	3.44	1014.92				4999.13	3839.28	
0.8	3.67	1274.86				5324.83	4791.95	
0.9	3.89	1396.20				5745.26	5125.60	
1	4.11	1291.78				6124.88		
1.1	4.31	1145.06				6429.97		

All this makes that also for the maximum impact stresses no straightforward relation with respect to the plate deformability is applicable. This is verified in the following paragraphs.

The stress at a certain radius from the centre of a circular plate can be calculated from the local strain by using Hooke's law:

$$\sigma_{rr} = -\frac{E}{1-\nu^2}\left[\varepsilon_{rr} + \nu\varepsilon_{\theta\theta}\right]$$
$$\sigma_{\theta\theta} = -\frac{E}{1-\nu^2}\left[\varepsilon_{\theta\theta} + \nu\varepsilon_{rr}\right] \quad \textbf{(6.1)}$$

Since the radial and circumferential strain component is the same in the centre of the plate, the same applies for the stresses which simplify to:

$$\sigma_{rr} = \sigma_{\theta\theta} = -\frac{E}{1-\nu}\varepsilon_{rr} \quad \textbf{(6.2)}$$

Figure 6-21 and Table 6-6 give an overview of these average maximum stresses which occur in the deformable plates as function of impact velocity.

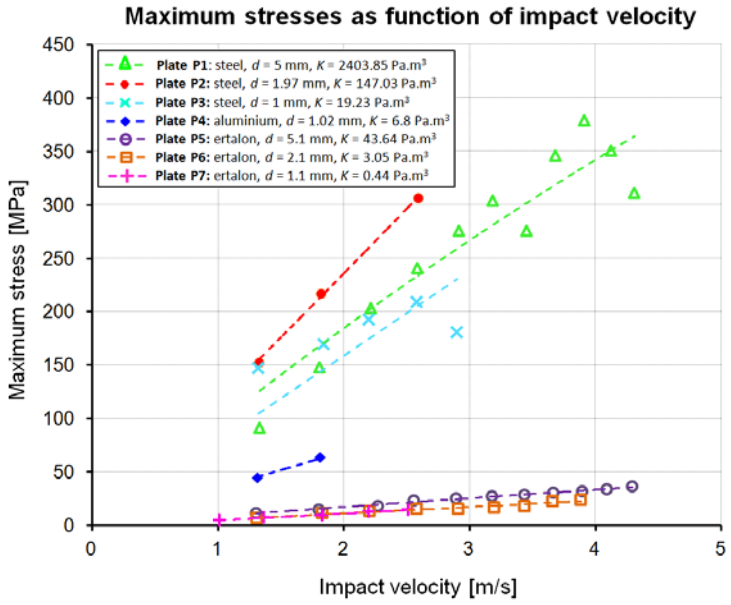

Figure 6-21: Overview of the maximum stresses for the deformable test plates as function of impact velocity

All the depicted experimental results are obtained in the elastic region of the plate deformations, meaning that no permanent deformations could be observed for the considered tests. This indicates that the yield stress for the stainless steel plates, the Aluminium plate and the ertalon plates should be larger than respectively 380 MPa,

64 MPa and 37 MPa. Although the exact properties of the used materials were not provided by the manufacturer, these latter values represent realistic lower limits for the yield stress of the considered materials.

Table 6-6: Overview of the maximum stress values for the deformable test plates

H [m]	U_{avg} [m/s]	Maximum stress at plate centre σ_{rr} [MPa]						
		P1	P2	P3	P4	P5	P6	P7
0	0	0	0	0	0	0	0	0
0.05	1.01	-	-	-	-	-	-	5.08
0.1	1.32	91.40	152.66	146.90	44.29	11.79	7.05	7.30
0.2	1.82	147.98	217.22	169.73	63.73	15.13	11.38	9.56
0.3	2.21	203.33	-	192.58		18.42	13.60	12.63
0.4	2.57	240.31	306.72	209.03		23.57	15.15	14.54
0.5	2.90	275.26		180.41		25.10	15.31	
0.6	3.19	303.86				27.08	17.11	
0.7	3.44	275.48				28.87	18.10	
0.8	3.67	346.03				30.31	22.59	
0.9	3.89	378.97				32.18	24.16	
1	4.11	350.63				34.05		
1.1	4.31	310.80				36.45		

A comparison of the maximum stresses among the different test plates again leads to the conclusion that no straightforward increasing or decreasing trend can be found between the maximum impact stresses and the flexural stiffness of the plates. On the other hand, it was found that generally for flat plate slamming the slamming forces decrease with increasing plate deformability. Similarly to the cylindrical deformable test objects, this indicates that it can thus occur that when increasing the flexibility of a plate in a marine construction (e.g. hull panel), the slamming forces which are passed on to the support structure decrease, but the stresses in the plate material increase.

6. 4. Hopkinson based flat plate slamming experiments

In section 6.2.2.2, it was observed that the slamming forces acting on the impactor bottom plate during vertical slamming drop experiments were so large that deformation of this plate under the slamming loads could play a role in the slamming behaviour. The corresponding force measurements are hence considered

as a good estimate but not an exact representation of the impact forces characteristic for rigid flat plate slamming. However, it is interesting to measure the exact impact force values corresponding to rigid flat plate slamming in order to estimate the maximum impact forces which are expected during flat plate slamming. In order to approximate the impact of a theoretically rigid plate, a quite different type of test object with a different type of measuring technique was developed, which is discussed in this section.

6. 4. 1. Description of the method and materials

To ensure the rigidity, a cylindrical rod with a flat circular bottom was chosen as test object (length d = 69 cm; radius R = 4.35 cm). This specimen can be considered as a rigid flat plate with a thickness which is almost eight times larger than its diameter. Plastic was chosen as material of the bar in order to limit the weight (4.65 kg).

The impact forces during slamming of this test model were not measured by the force sensors, but by using the Hopkinson technique [4], which was already described in section 4.3.3.2.a. In this technique, stress waves in long bars are measured by measuring the longitudinal strain waves using strain gauges. The stress and strain waves are this time generated by the water impact during the slamming drop tests. By applying Equation (4.7) on the measured strain waves ε_i travelling through the test object, the impact force can be calculated.

One strain gauge is placed in the longitudinal direction close to the middle of the bar's length (at 36 cm as seen from the bottom of the bar) to measure the compressive strain wave which propagates with the speed of sound of the bar's material from the bottom till the top of the test bar. However, attention should be paid to the fact that this compression wave reflects at the top of the bar into a tensile wave which then propagates downwards with the speed of sound. If the length of the bar is not long enough, then the possibility exists that the compressive and tensile wave interfere at the location of the strain gauge. This means that the compressive wave has not yet passed the strain gauge completely before the tensile wave arrives at the location of the strain gauge. This depends on the speed of sound of the bar's material and the duration of the strain pulse. However, since the exact material properties were initially not known, it was initially not possible to verify whether this situation could occur.

In order to determine the velocity of sound of the bar's material, a second strain gauge was mounted close to ¾ from the bar's length (at 55 cm as seen from the bottom). The speed of sound could then be calculated from the time difference between the strain wave passages at the two strain gauges and the distance between the two strain gauge locations. Figure 6-22 depicts as an example the strain

recordings of the two strain gauges for a slamming test with a drop height of 2.09 m which shows the time lag between the two strain gauges Δt. An average value of 91.34µs has been obtained for Δt from seven slamming experiments.

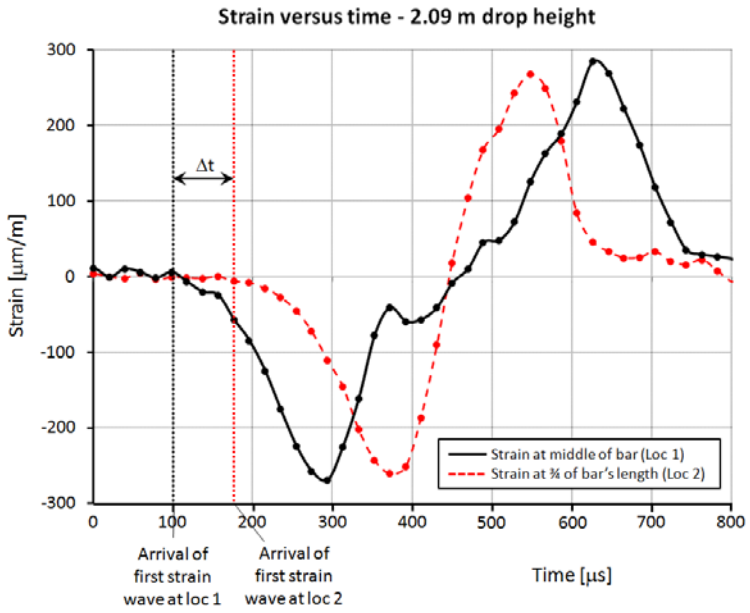

Figure 6-22: Comparison between the strains measured by the two strain gauges installed on the test bar for a slamming test with a drop height of 2.09 m

Together with a distance of 190 mm between both strain gauges, this gives an average value of 2078 m/s for the velocity of sound γ_{bar} for the material of the test bar. This value can subsequently be used for calculating the elasticity modulus E of the material according to the following relationship:

$$E = \gamma_{bar}^2 \rho_{bar} \tag{6.3}$$

The density ρ_{bar} of the test bar can be calculated from its mass and its dimensions. A density ρ_{bar} of 1134 kg/m^3 has been obtained which results in an E-modulus of 4.9 GPa.

With the knowledge of the speed of sound of the bar's material, it can be calculated that the time which is needed for a strain wave to arrive at the middle strain gauge, reflect at the top of the bar and arrive again at this strain gauge is 318 µs. This interval is longer than the time which the strain pulse generated by the water impact needs to reach its maximum value at the location of the middle strain gauge (+/- 220 µs), as can be observed in Figure 6-22. Consequently, it can be concluded

that the maximum strain recorded at the middle strain gauge has not been affected by interference. The slamming impact force can thus be calculated from the maximum strain recorded by the middle strain gauge.

A photograph of the complete test bar indicating the position of the two strain gauges is shown in Figure 6-23. The strain gauges themselves are not visible since they are covered with a rubber coating in order to avoid water contact.

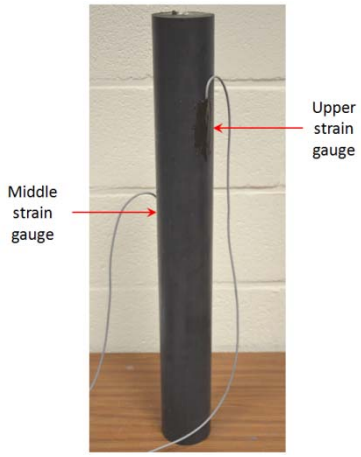

Figure 6-23: The plastic rod as a flat plate test object

6. 4. 2. Experimental results

During the slamming experiments, the test bar was allowed to fall freely after it was released at a specified drop height. The impactor was thus not used to guide the test object. Hence, the impact velocities were not affected by friction between the impactor wheels and the rails of the slamming setup. The impact speed U of the bar can thus be approximated by Equation (4.10).

During the preliminary experiments, it appeared very difficult to realize a horizontal impact of the flat bottom of the bar with the calm water surface since little disturbances at the moment of release caused the bar to tilt during the free fall and to hit the water with the bottom surface making a certain angle with the water surface. A solution of this problem was obtained by releasing the test bar by means of burning a small rope at which the bar was initially suspended before the test. A remarkably reproducible horizontal impact was obtained this way. Figure 6-24 depicts a sequence of high speed images for the slamming experiment with a drop height of 2.09 m which shows the horizontal impact of the bar's bottom surface.

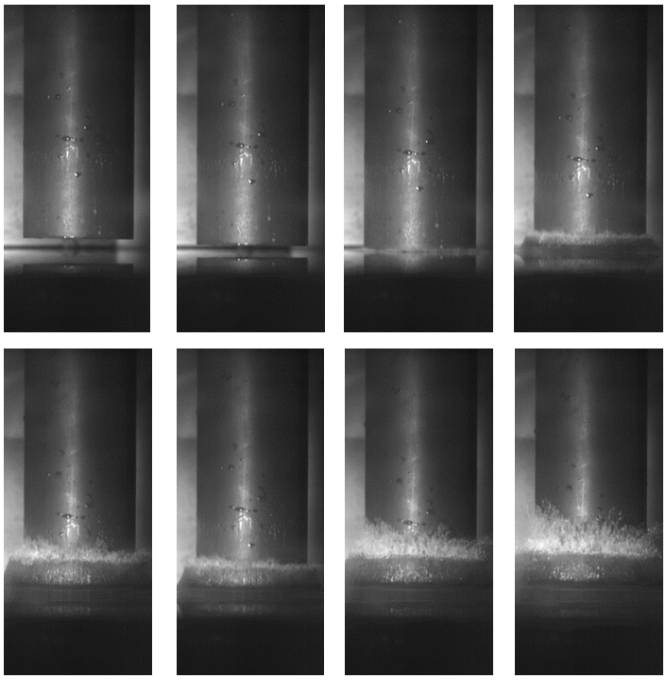

Figure 6-24: Sequence of high speed images for the water impact of the test bar

Figure 6-25 shows the strain as function of time recorded by the middle strain gauge for a slamming experiment with a drop height of 2.09 m. This graph clearly shows the subsequent negative compression and positive tension strain waves which travel back and forth in the test bar with its velocity of sound. It can be observed that the amplitude of the strain pulses decreases with elapsed time due to damping of the material. At the same time, it can be noticed that the duration of the pulses increase. This is caused by interference between the strain waves passing back and forth at the location of the middle strain gauge. A closer view of the first compression strain pulse which is not affected by interference can be observed in Figure 6-22.

By evaluating the maximum absolute values of these first compression strain waves for all the performed experiments and applying Equation (4.7) on these values, the impact forces on the rigid bar can be calculated. Figure 6-26 and Table 6-7 give an overview of these impact forces for seven slamming experiments. Although only seven impact tests were performed for this test object, it can be observed that the impact forces seem to vary quadratically as function of the impact velocity, as was also observed for the impact forces obtained for the impactor bottom plate.

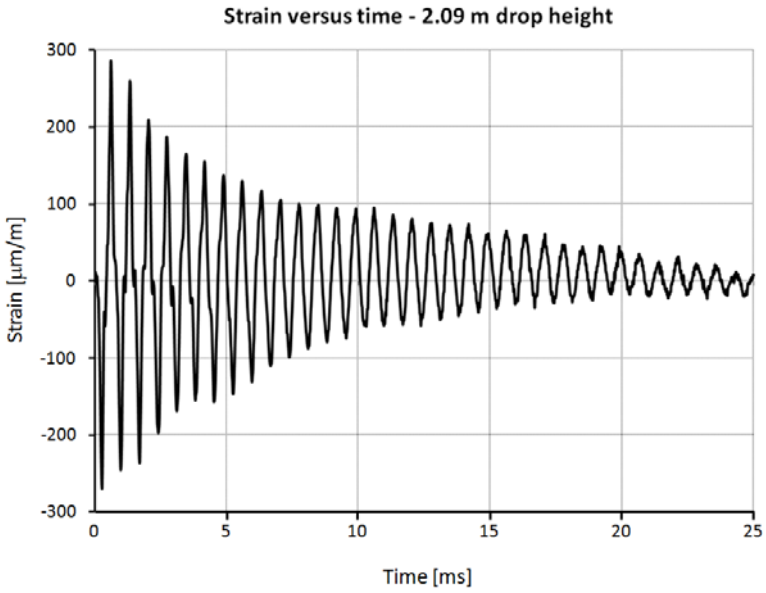

Figure 6-25: Strain as function of time measured at the middle of the rigid bar for a slamming experiment with a drop height of 2.09 m

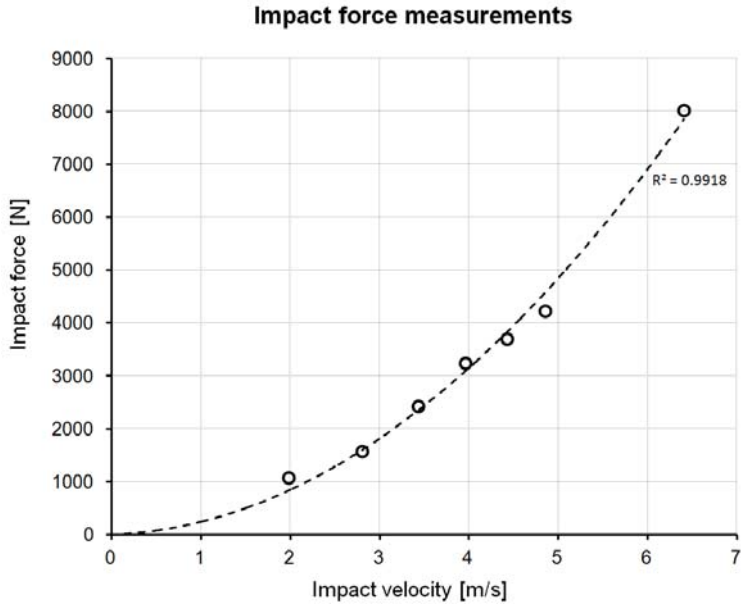

Figure 6-26: Overview of the recorded impact forces for the rigid test bar

Table 6-7: Overview of the recorded impact strains and forces for the rigid test bar

H [m]	U_{avg} [m/s]	$\varepsilon_{t,max}$ [μm/m]	$F_{I,P}$ [N]
0	0	0	0
0.2	3.08	27.73	1063.33
0.4	1.28	45.54	1562.27
0.6	0.70	81.14	2420.92
0.8	0.29	111.31	3242.46
1	0.79	123.27	3701.50
1.2	0.27	137.61	4215.15
2.09	0.17	275.46	8023.80

A comparison of the impact forces obtained for this test bar with the ones obtained for the other test plates can again be done by presenting the impact forces in terms of forces per unit area. Figure 6-27 plots all the obtained results together. It can be observed that the impact forces for the test bar are larger than for all the other plates which corresponds with the observations done in section 6.3.1.2, namely that the slamming forces during flat plate impact increase as the rigidity increases. However, the difference between the impact forces recorded for the test bar and the ones measured for the stiff bottom impactor plate is larger than expected since it was observed in Figure 6-16 that the impact forces measured for the bottom impactor plate are already located on the flattened part of the force versus stiffness curve.

A few effects may play a role in this respect:

- First of all, it is expected that a disturbed flow at the edges of the test bar bottom plays an important role. Although this effect may only be applicable on a small zone near the bottom edges (see Figure 5-10 for the case of cylindrical slamming [5]), this zone is relatively large when compared to the area of the test bar bottom and hence most probably influences the corresponding slamming loads in a large extent.
- Furthermore, since the area of the test bar bottom is very small as compared to the area of the other test plates, it is assumed that the air might escape much easier from under the test bar than in the case of the other test plates. Hence, the softening effect of the air cushion might disappear resulting in larger slamming loads.
- Finally, it must be mentioned that with a mass of 4.65 kg, the test bar differs much in weight with the other test plates (average mass of 25.95 kg). Hence, mass effects may play a role.

All this makes that a direct comparison of the impact force results from the test bar and the other test plates is difficult and it most probable explains the large unexpected differences in the impact force values between the impactor bottom plate and the test bar. A comparison of the impact forces recorded during the experiments with the test bar with the ones measured for the other flat plate test objects is thus not relevant in the framework of finding a relation between the slamming forces and the degree of plate flexibility.

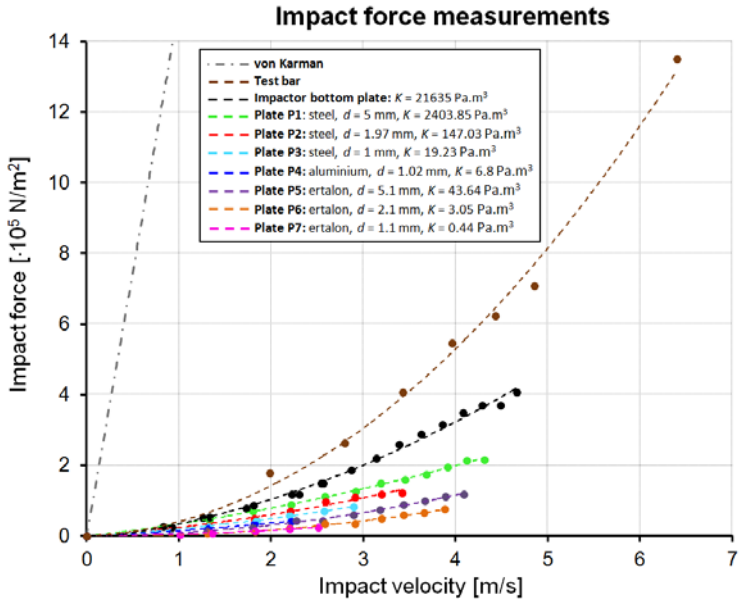

Figure 6-27: Comparison of the average impact forces per unit area of the impactor bottom plate and the deformable test plates

The graph from Figure 6-27 finally also compares the experimentally obtained slamming forces with the ones predicted by von Karman [6] for rigid flat plate slamming (Equation (2.19)). It can be observed that these theoretically predicted impact forces are much larger than the experimentally obtained ones. This large difference can be explained by the fact that von Karman [6] did not take the air cushion into account which has a large effect on the impact loads during flat plate slamming. Hence, it can be concluded that the flat plate theory of von Karman is not a good representation for the true impact loads acting during flat plate slamming.

6. 5. Conclusions

This chapter described the process of horizontal flat plate slamming on a calm water surface and investigated the effect of deformability of the plate under consideration on the slamming loads.

High speed camera images showed that the first stage of the impact of a horizontal plate on a calm water surface typically consists of the entrapment of an air pocket at the moment of first contact of the plate with the water. In a second stage, a pressure wave is generated by the sudden air flow stop at the moment of the air pocket entrapment, which propagates from the edges to the centre of the plate and which causes the air pocket to break up into many smaller air bubbles. It is during this stage that a large slamming force pulse builds up.

For significantly flexible plates, it has been observed that this force pulse is prone to oscillations which are caused by vibrations of the test plate due to an excitation of its eigenfrequencies. This again demonstrates the importance of structural vibrations during slamming events (cfr. springing and whipping of ships). In this case, it is not the structure supporting the objects under consideration which is excited, but the objects themselves which are excited.

It has been observed that the slamming forces generally increase as the flexibility of the plates, expressed in terms of flexural stiffness K, decreases. This indicates that as the flexibility of plates increases, more energy is absorbed by the deformation of the plates, and hence smaller impact loads are observed. Furthermore, it is noticed that for small values of the plates' flexural stiffness (< 200 Pa.m^3) the impact forces increase much faster with decreasing flexibility than for plates with larger values for the bending stiffness. The impact forces thus generally vary logarithmically with the flexural stiffness.

When the impact force versus stiffness relation is investigated in the range of small bending stiffness values, it is observed that also damping of the plate material and the excited eigenfrequencies have an effect on the impact forces. However, this effect is not as large as the effect of the deformability on the impact forces.

For the maximum strains and stresses in the plates caused by the slamming impact, no straightforward relation with respect to the plate deformability is present as was the case for the impact forces. As such, it is possible that when increasing the flexibility of a plate in a marine construction (e.g. hull panel), the slamming forces which are passed on to the support structure decrease, but the internal stresses in the plate material increase.

Finally, an attempt has been done for measuring impact forces on an approximately perfectly rigid test plate, in the form of a test bar with a 'thickness' which is much larger than its diameter. For recording the impact forces, a new measuring technique based on the Hopkinson principle was used. This appeared to be a promising technique for measuring slamming forces. However, the force results obtained with this test bar could not be thoroughly compared with the other test results. Edge flow effects, a reduced air cushion and mass effects were assumed to have an important effect on the test results.

6. 6. References

[1] J. H. G. Verhagen, "The impact of a flat plate on a water surface," *Journal of Ship Research,* pp. 211-223, 1967.

[2] S. H. Oh, S. H. Kwon, and J. Y. Chung, "A close look at air pocket evolution in flat impact," *24th International Workshop on Water Waves and Floating Bodies,* 2009.

[3] O. Faltinsen, J. Kvålsvold, and J. Aarsnes, "Wave impact on a horizontal elastic plate," *Journal of Marine Science and Technology,* vol. 2, pp. 87-100, 1997.

[4] B. Hopkinson, "A method of measuring the pressure produced in the detonation of high explosives or by impact of bullets," *Philosofical Transactions of the Royal Society,* vol. A, pp. 437-456, 1914.

[5] A. Nila, "An adaptive PIV method for estimating slamming loads," *PhD dissertation, VUB Brussels, under progress,* 2013.

[6] T. von Karman, "The impact of seaplane floats during landing," *Technical note no. 321, National Advisory Committe for Aeronautics,* 1929.

Chapter 7

Conclusions and future research

7. 1. Conclusions

The current PhD dissertation deals with the experimental investigation of the effect of structural flexibility on the magnitude of slamming pressures and forces. It comprises a complete analysis, starting from the selection and validation of the appropriate instrumentation and a selection of the test objects, towards a description and discussion of the experimental results.

Two main parts may be distinguished throughout this thesis. In the first part, provisions and preparations are made for the experiment series performed in this thesis (chapter 1-4), while in the second part, the considered experimental results are presented and analyzed (chapter 5-7).

A part of the preparation process consisted of performing a complete literature review on water slamming in general and on cylinder and flat plate slamming in particular, since these were the two types of test models used in this thesis. A complete but concise review on the available slamming theories elaborated throughout the years has been presented. According to the author's best knowledge, this has never been presented before.

The preparation process also included a selection of the appropriate experimental instrumentation for performing the considered slamming experiments. The following state-of-the-art instrumentation, of which the characteristics were selected well-considered, were chosen:

- Dynamic pressure transducers
- Dynamic force transducers
- Accelerometer
- Position encoder
- Strain gauges
- High speed camera (DIC technique)

During some of the experiments, it was useful to visualize the water or air flow during water penetration of one of the test models. The following instrumentation has therefore been used:

- High speed camera
- Particle image velocimetry
- Smoke machine

All this instrumentation was acquisitioned with state-of-the-art data acquisition systems. A trigger was used at the moment that the test object touched the water surface in order to synchronize all the recorded signals.

In order to verify the proper working and an appropriate handling of the transducers, and to guarantee a correct interpretation of their recordings, a rigorous validation procedure was elaborated. For the dynamic pressure and force transducers, this validation process consisted in the first place in an identification of all the external parameters affecting these types of recordings. In this way, measurement guidelines could be developed which should be followed in order to enable correct and reliable pressure and force recordings. For the dynamic pressure transducers, the following guidelines were elaborated:

- The sampling rate of the data acquisition system of the pressure sensors should be chosen sufficiently high in order to obtain the peak value of the pressure pulses. Especially when performing pressure measurements at small deadrise angles, a data sampling rate of at least 300 kHz should be used.
- The pressure sensors should be precisely flush mounted. Flush mounting can be verified by confirming the absence of water bubbles or turbulences at the sensor diaphragms during water impact by using a high speed camera.
- Pressure sensors using a preloaded piezocrystal should be adjusted to the water temperature before an experiment can be performed to prevent parasitic pressures in the pressure signals. Alternatively, sensors based on other sensing technologies can be used.
- The object surface should be dry before testing.
- The water surface should be completely calm at the start of each experiment.

For the dynamic force sensors, the following guidelines were developed:

- The sampling frequency of the acquisition system for measuring slamming forces should be chosen larger than 8 kHz to enable a reliable measurement of the peak value of the slamming force pulses.
- The installation of the force sensors should be performed exactly as is recommended in the mounting instructions. Any change with respect to the standard installation should be calibrated precisely. The preloading of the force sensors during installation is also vital in order to ensure the output linearity. In

this dissertation, three identical dynamic force transducers were used which were clamped between two circular Aluminium plates and configurated in an equilateral triangle with the centre of gravity of the impactor lying on the vertical axis through the midpoint of this triangle. Since this installation did not meet the standard installation as considered by the manufacturer, a calibration of the aforementioned load cell combination was performed.

- It is important to consider the initial force step caused by releasing the impactor when evaluating the slamming force peak value. This initial force should be subtracted from the impact force since it is not a part of the slamming event.
- Finally, it is essential to understand that the impact force acting on the test object differs from the force output of the sensors due the distribution of the impactor mass above and below the force transducers. A mass conversion factor should be applied on the force recordings in order to obtain the slamming force acting at the bottom of the test object.

According to the author's best knowledge, no such guidelines were ever presented before. The aforementioned work may thus be very useful for future research.

In the second place, the validation of the pressure and force transducers consisted of a calibration with respect to a reference pressure and force. The main difficulty in this calibration process is that the generated reference pressure and force pulses must be short enough to prevent the dynamic pressure and force transducers discharging significantly in the considered time period due to their dynamic character. For the pressure transducer, a successful calibration technique was developed based on an existing static calibration instrument in series with a valve. For the dynamic force transducers, a new and promising calibration method was elaborated based on the split Hopkinson pressure bar setup. The great advantage of this technique is that the reference instruments (i.e. strain gauges) are easy to calibrate, which is not the case for the reference instruments used with existing calibration techniques for dynamic force sensors.

For the accelerometer, the position encoder and the DIC technique, another validation method was used. A validation of these instruments could be performed by comparing the position, velocity and force signals obtained or calculated from each of their recordings. A good correspondence was observed among the different sensor types. The fact that thus different sensors record the same data indicates that they all work properly and correctly.

With the experimental instrumentation validated, slamming experiments could be performed. It was decided to perform these experiments on two main types of test objects, namely on horizontal cylinders and horizontal circular flat plates. These two object types were found to be the easiest available in rigid as well as in deformable condition, with the deformable objects being available in various flexibility degrees.

The flexibility of the deformable test objects was varied by changing the material and the material thickness (tube wall thickness / flat plate thickness). For the deformable cylindrical test objects, the cylinder flexibility could also be changed by varying the tube diameter. In this thesis, two main diameter values are applied for the deformable cylindrical test models, i.e. close to 31.5 cm and close to 9 cm.

It was expected that for the flat plate test objects, an air cushion would be formed during the initial stages of the slamming events affecting the impact loads, and thus also affecting the relation between the impact loads and the degree of flexibility of the test models. This initial air cushioning effect was not expected to occur during the slamming experiments with the cylindrical test objects. Hence, it was decided to start the experimental campaign with slamming experiments performed on the cylindrical test models.

A detailed study of the recorded impact pressures during the slamming experiments with the cylindrical test objects showed that cylinder bottom slamming is typically characterized by large local pressures which are very short in duration and which rapidly travel over the cylindrical surface. These pressures occur in the intersection zone of the cylinder with the water, at the location where the water jet is formed.

In contrast with the initial expectations, it was observed that during the very initial stage of a rigid cylinder impact, an air pocket exists locally at the bottom of the cylinder which rapidly disappears. It is shown that this air pocket is most probably the reason for oscillations in the pressure history at the bottom of the cylinder (0°). At other deadrise angles, these oscillations were not observed.

A comparison between the measured and theoretically predicted impact pressures for rigid cylindrical bottom slamming learned that the measured pressures are in fact an average of the pressure distribution which is really applied over the pressure sensor area. The true slamming pressures acting on the rigid cylindrical surface are thus in fact much larger and can be determined from Wagner's extending flat plate theory [1] for deadrise angles between 4° and 20°. For deadrise angles smaller than 4°, the compressibility of the water starts playing a role, and according to the author's best knowledge there is no theory available in the literature which takes this effect into account.

Furthermore, it was shown that during cylindrical slamming, the effect of the flow in the longitudinal direction of the cylinder on the impact pressures is rather limited. This is an important observation with respect to the ability to extend the obtained impact force results to cylinders with a larger length. If the effect of the flow in the longitudinal direction is neglected, then the impact forces measured on the test objects from this thesis can be extended to cylinders with a larger length by simply multiplying the length of these cylinders by the measured forces per unit length.

The examination of these forces recorded during the cylinder slamming experiments revealed that due to the sudden impact of the test objects with the water, some of the natural frequencies of the setup were excited which caused oscillations in the force recordings. This is an important observation which indicates that also in real marine constructions vibrations might occur due to slamming events which cause forces in the structure which are larger than the ones which would be expected from the pure slamming loads only.

The vibrations in the setup resulted in the inability to measure the true impact forces corresponding to pure rigid cylindrical bottom slamming. Modifications in the setup successfully suppressed the vibrations, but they could not be totally eliminated. It has been shown that also other experimental studies concerning cylinder bottom slamming dealt with vibrations in the experimental setup. Especially the experimental results from Campbell and Weynberg [2] which are used as a standard in the DNV recommendations [3] have been observed to be significantly affected with vibrations. According to the author's best knowledge, no published material is available in the literature which describes successful experiments on cylindrical bottom slamming. From the experiments performed in this thesis, and the experimental results from the available literature, it may be concluded that the maximum slamming coefficient $C_{s,0}$ corresponding to rigid body slamming, which is approximately independent from the impact velocity, must be situated between 2.63 and 5.15.

For the case of the deformable cylindrical test objects with large diameter ($D \geq 31.5$ cm), the frequency of the vibrations in the setup was significantly larger than the frequency of the true forces (deformations) experienced by the test models. For these cases, the impact forces could hence be extracted from the force recordings by eliminating the force oscillations by means of a low pass filter. Furthermore, the impact forces could also be calculated from the strain which was measured at the cylindrical surface. Therefore, cylindrical compression tests in combination with numerical simulations of these tests were performed in order to find the force-strain relations at the considered locations. For the case of the deformable cylindrical test objects with small diameter ($D \leq 9$ cm), the frequency of the cylinder deformations was in the same range of the frequency of the setup vibrations. This caused resonance at the location of the force transducers and made the force recordings not useful anymore for determining the impact forces. Hence, the impact forces could only be calculated from the strain recordings for these cases, which were not affected by the vibrations at the location of the force transducers.

A comparison of the impact forces measured for the different deformable cylindrical test objects learned that in general the impact loads seem to decrease with decreasing

cylindrical stiffness. This confirmed the assumption that introducing deformability in the structure reduces the impact loads since a part of the impact energy is then absorbed by the deformation of the material. This is especially the case when comparing cylindrical test objects made from the same material, but with other wall thickness or diameter. In these cases, the slamming forces evolve logarithmically as function of the cylinder stiffness in the sense that the impact forces increase fastly with increasing cylinder stiffness for small values of this stiffness and increases much slower with increasing rigidity for larger values of the cylinder stiffness. However, when comparing the impact forces between cylindrical test objects of different materials it has been noticed that the observation that decreasing cylinder stiffness leads to decreasing impact forces is not always true. This shows that also other material parameters such as damping might have an important effect on the impact forces. A more detailed investigation is necessary to identify these other parameters and their effect on the impact forces.

When comparing the results of the deformable cylindrical test objects with the ones from the rigid cylindrical models and the corresponding theories, then it was observed that in the first case the bottom of the test objects was significantly decelerated at the first stage of the slamming event, while for the case of the rigid test cases the velocity at the bottom of the test objects could be approximately assumed constant. This difference in slamming conditions makes that a comparison of both results was not relevant since extra slamming force components are generated for the deformable cylinders which are not present in the case of the rigid cylindrical objects.

In light of investigating the relation between the slamming loads and the degree of structural flexibility, also the impact stresses inside the material were examined. However, no straightforward relation between the impact stresses and the cylinder stiffness could be identified. The fact that besides the cylinder stiffness, the strain and stress recordings also depend on the thickness of the cylindrical tubes is the reason for this observation. It is thus not clear beforehand whether introducing deformability into a structure by selecting another material, changing the tube wall thickness or changing the diameter would increase or decrease the maximum impact stresses. It might thus occur that introducing deformability to a cylindrical structure which directly makes contact with the water during a slamming event causes a relief in the forces which are passed on to the structure which lies behind but an increase in the maximum stress values internally in the structure (e.g. a ship’s internal structure with respect to its hull).

Concerning the slamming experiments on the flat plate test objects, high speed camera images confirmed that the first stage of the impact of a horizontal plate on a

calm water surface typically consists of the entrapment of an air pocket at the moment of first contact of the plate with the water. This air pocket is the result of air which could not escape in the stages just before the first water contact from the gap between the flat plate and the water surface. Once this air is entrapped by the plate and the air flow is suddenly stopped, a pressure wave is generated which propagates from the edges to the centre of the plate and which causes the air pocket to break up into many smaller air bubbles. Also this phenomenon has been recorded by the high speed camera. It is during this stage that a large slamming force pulse builds up.

For significantly flexible plates, it has been observed that this force pulse is prone to oscillations which are caused by vibrations of the test plate due to an excitation of its eigenfrequencies. This again demonstrates the importance of structural vibrations during slamming events (cfr. springing and whipping of ships). However, in contrast with the cylindrical test objects, it is in this case not the structure supporting the objects under consideration which is excited, but the objects themselves which are excited.

Similarly to the case of the deformable cylindrical test objects, it has been observed that the slamming forces acting on the flat plate models generally increase as the flexibility of the plates, expressed in terms of flexural stiffness K, decreases. This indicates that as the flexibility of the plates increases, more energy is absorbed by the deformation of the plates, and hence smaller impact loads are observed. Furthermore, it is noticed that for small values of the plates' flexural stiffness (< 200 $Pa.m^3$) the impact forces increase much faster with decreasing flexibility than for plates with larger values for the bending stiffness. The impact forces thus generally vary logarithmically with the flexural stiffness. This also corresponds with the observations done for the cylindrical test models.

When the impact force versus stiffness relation was investigated in the range of small bending stiffness values, it was observed that also damping of the plate material and the excited eigenfrequencies have an effect on the impact forces. This corresponds again with the observations done for the cylindrical test objects. However, this effect is not as large as the effect of the deformability on the impact forces.

An attempt was also made for measuring impact forces on an approximately perfectly rigid test plate, in the form of a test bar with a 'thickness' which is much larger than its diameter. For recording the impact forces, a new measuring technique based on the Hopkinson principle was used. This appeared to be a promising technique for measuring slamming forces. However, the force results obtained with this test bar could not be thoroughly compared with the results from the other test

plates. Edge flow effects, a reduced air cushion and mass effects were assumed to have an important effect on the measurements.

Finally, for the maximum strains and stresses in the plates caused by the slamming impact, no straightforward relation with respect to the plate deformability could be found as was the case for the impact forces. As such, it was concluded that it is possible that when increasing the flexibility of a plate in a marine construction (e.g. hull panel), the slamming forces which are passed on to the support structure decrease, but the internal stresses in the plate material increase.

Recapitulatory, from both experimental test campaigns (cylindrical and flat plate test models), the following main conclusions concerning the effect of structural flexibility on the slamming loads can be drawn:

- Introducing flexibility into a marine structure which is prone to water slamming causes in the most cases a relief of the impact forces which are passed on to the construction supporting the structure which is in direct contact with the water.

- This relation seems to be proportional to the logarithm of the stiffness degree, in the sense that in the range of small stiffness values (large flexibility), the impact forces increase fast with increasing stiffness, while for larger stiffness values (small flexibility), the impact forces increase much slower with increasing stiffness.

- This trend is not always the case for the internal stresses acting in the material of the structure which is in direct contact with the water slamming. Introducing deformability may also cause an increase in the internal stresses in the considered structure. For the internal stresses, no straightforward relation with respect to the structural flexibility is present.

- Besides the flexibility of a structure, also other material parameters may have an effect on the magnitude of the slamming loads (e.g. damping). Introducing flexibility by changing to another (less stiff) material may hence also cause an increase in the recorded slamming forces. However, the effect of these material parameters on the impact forces is much smaller that the effect of the structural flexibility.

7. 2. Future work

This thesis revealed some interesting topics which are necessary to investigate further in future research. These items are listed below:

- One of the main issues dealt with in the current research was the presence of vibrations during the experiments due to an excitation of some of the eigenfrequencies of the setup. For some of the slamming experiments, the vibration frequencies were in the same order as the frequencies of the true slamming loads, which made accurate recordings difficult or impossible. As such, it was observed that the impact force measurements obtained from the rigid cylindrical test model were affected by vibrations in such a way that they could only be estimated in a large force range and thus a large uncertainty was applicable on these recordings. It has been shown that this problem was also encountered by other researchers, but this did not prevent them from publishing their results and drawing conclusions from inaccurate results. It is the challenge for future research to improve the drop weight slamming setup in such a way that the eigenfrequencies of the setup, of which some are inevitably excited during a slamming event due to its highly dynamic character, are far away from the frequencies which are characteristic for the true water slamming loads. By filtering the frequencies due to vibrations out of the load recordings, the true slamming loads can be then obtained. The most straightforward way to improve the setup in order to meet the previous objective consists of making the setup much more rigid to shift the eigenfrequencies of the setup towards much larger zones. The complete construction for the setup must therefore be altered. The following measures may be taken to achieve the objective:
    - Using heavy and massive construction elements
    - Applying multiple and strong anchorings of the setup towards massive walls and floors
    - Performing a numerical modal analysis of the planned setup with all its details to verify the eigenfrequencies and iterate this process until a setup is designed which meets the requirements.
- It was concluded from this thesis that among the different material parameters, it is not only the flexibility in terms of material stiffness which affects the slamming loads, but also other material parameters have an important effect. As such, it was observed that also material damping plays an important role in this respect. However, the precise effect of these other material parameters was out of the scope of this research. The identification of the other parameters affecting

the slamming loads and a detailed investigation of their effect on these loads may thus be considered as an important item for future research.

- It was observed in section 6.4.2 that in the case of flat plate slamming, it is most probable that the magnitude of the slamming loads depend on the mass of the plate. However, a precise analysis was not performed since all the considered test objects for the flat plate slamming experiments were similar in mass. It might be interesting for future research to precisely investigate the effect of the mass on the slamming loads for the case of flat plate slamming. This would enable the extrapolation of the obtained results from this thesis towards other plate masses.
- The current research presents the onset towards the investigation of the effect of structural flexibility on the slamming loads by means of experimental test campaigns on simple object geometries. It might be interesting for future research to extend the current study to more complex, realistic and large scale constructions in order to more accurately predict the effect of deformability on the slamming loads for more specific constructions.
- Finally, it must be mentioned that the experiments in this thesis are performed with smooth experimental test models. It might be expected that the slamming loads might be different when using significantly rough test objects. An investigation of the effect of the surface roughness on the impact loads is hence suggested for future research.

7. 3. References

[1] H. Wagner, "Über Stoß- und Gleitvorgänge an der Oberfläche von Flüssigkeiten," *ZAMM - Journal of Applied Mathematics and Mechanics / Zeitschrift für Angewandte Mathematik und Mechanik,* vol. 12, pp. 193-215, 1932.

[2] J. M. C. Campbell and P. A. Weynberg, "Measurements of parameters affecting slamming," in *Report No. 440*, Wolfson Unit for Marine Technology, Southampton, United Kingdom, 1980.

[3] Det Norske Veritas, "Environmental conditions and environmental loads," *Classification notes no. 30.5*, 2010.

Appendix A

Experimental study on the effect of water properties on the slamming loads

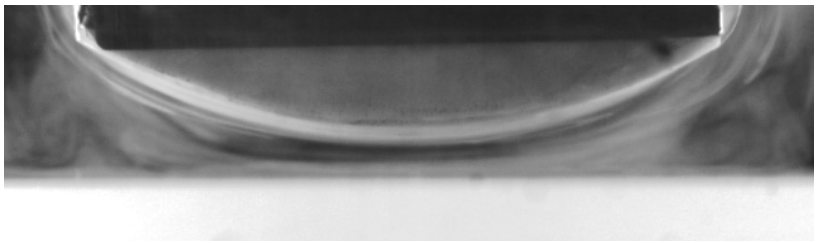

Overview

In this appendix, instead of examining the effect of the structural properties of the impacting body on the slamming loads, the effect of the water properties on the slamming loads will be investigated. Three water properties will therefore be varied, i.e. the density/salinity of the water, the level of water surface tension and the level of aeration. A test setup smaller than the one used in the previous chapters will be applied. By comparing the results from this setup with the ones from the previous setup, an extra validation of some of the measurements done in the previous chapters will be performed. In the first stage of this appendix, the background for this study and the working method will be explained. In the second stage, the experimental results are described in detail and conclusions are drawn from these results.

A. 1. Background

In the previous chapters, it has been shown that the magnitude of the impact loads is dependent on the material parameters of the structure which is subjected to water slamming. Not only the degree of deformability, which is dependent on the stiffness of the material, but also the material damping and the eigenmodes of the structure (which are also closely related to the material's stiffness) affect the impact loads.

Besides, it can be assumed that the physical properties of the second component participating in the slamming process, i.e. the water, may also have an influence on the slamming loads. One of the water characteristics with the largest natural variation is the water density ρ_l. For fresh liquid water, the density of water at atmospheric pressure is maximum at 4°C, and reaches a value of 999.97 kg/m^3 [1]. If the temperature changes, the density decreases. For fresh water at 30°C and at an

atmospheric pressure the water density is 995.65 kg/m^3 [1]. Besides the water temperature, also the water salinity has an effect on the water density. The sea-surface water salinity varies between 31 g salt per liter water and 39 g salt per liter water around the globe [2]. The average is 35 g salt per liter water which is also the average salinity of the North Sea [3]. Due to this salinity distribution, and due to the sea-surface temperature distribution, the water density of the earth's major oceans varies between 1020 kg/m^3 and 1028 kg/m^3 [2]. Figure A-1 shows the distribution of the earth's sea-surface salinity, temperature and density.

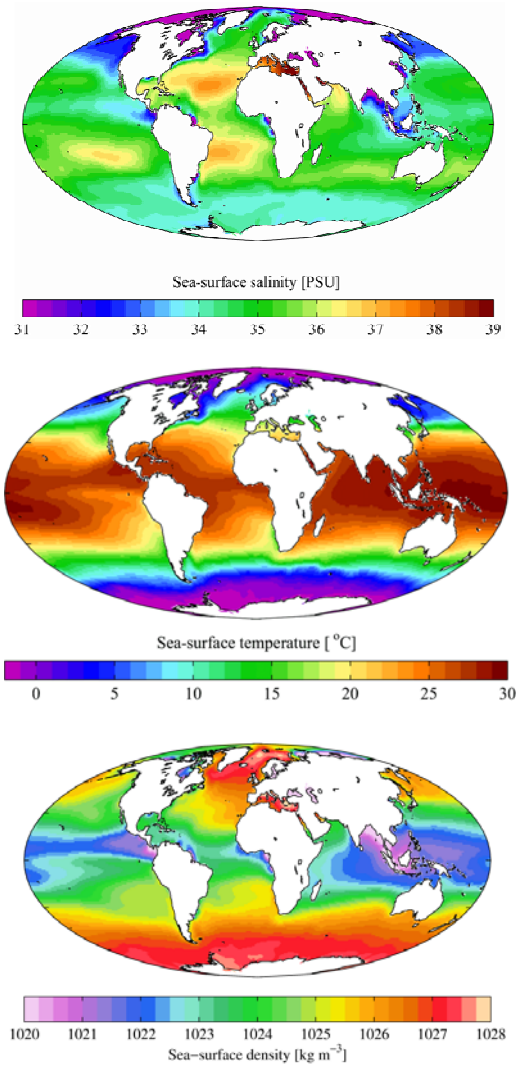

Figure A-1: The distribution of the earth's sea-surface salinity, temperature and density [2]

Another water parameter which may have an influence on the impact loads during water slamming is the water surface tension τ. The surface tension is defined as the property of the surface of a liquid to resist an external force. It is the result from an imbalance of molecular forces in a liquid. The fact that at the surface of a liquid the molecules are not surrounded completely by other fluid molecules makes that due to the cohesive attraction a net force applies on these molecules directed inwards in the fluid resulting in a pressure difference at the fluid boundary and a tension in the first layer of fluid molecules [4]. The tension forces are parallel to the fluid surface and are expressed as force per meter (N/m) or dyne per centimeter (= 1 dyn/cm = 0.001 N/m).

In natural environments, the water surface tension can vary according to the water temperature and the water salinity [5]. The temperature is hereby the dominating parameter. In standard conditions (25°C and atmospheric pressure), fresh water is characterized by a surface tension of 72.5 N/m. The graph in Figure A-2 shows that the surface tension decreases as the water temperature increases and the salinity decreases. Besides the effect of temperature and salinity also chemical pollution of the water (oil spill) can affect the surface tension of parts of ocean and lakes and therefore possibly affect the magnitude of the loads which are generated during slamming events.

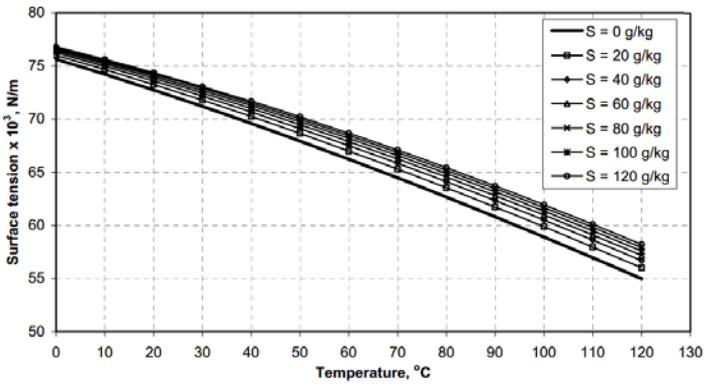

Figure A-2: The water surface tension as function of water temperature and water salinity [5]

The last important parameter which can have an effect on the magnitude of the slamming loads and which is investigated in this appendix is the gas content of the water in the sense of air bubbles being present in the water top layer. Slamming on aerated water occurs for example during ditching of an aircraft. It has been reported in earlier studies [6, 7] that ventilation occurring between the bottom of the aircraft

and the water during such water landing events, results in a significant amount of air bubbles being sucked underneath the aircraft fuselage.

In this appendix, the sensitivity of the impact loads on the water density, the surface tension and the presence of air bubbles in the water will be investigated. The method of working is presented in the next section.

A. 2. Materials and methods

A. 2. 1. Experimental test setup and test object

For the experiments performed in this appendix, some of the water properties will be changed by adding additives to normal tap water. In order to limit the amount of additives necessary for obtaining certain water properties, it was necessary to restrict the volume of water in the test basin. Hence, another smaller test drop test setup containing a smaller water basin is applied. It is the experimental drop setup from the Department of Materials Science and Engineering from Ghent University which has been used as depicted in Figure A-3.

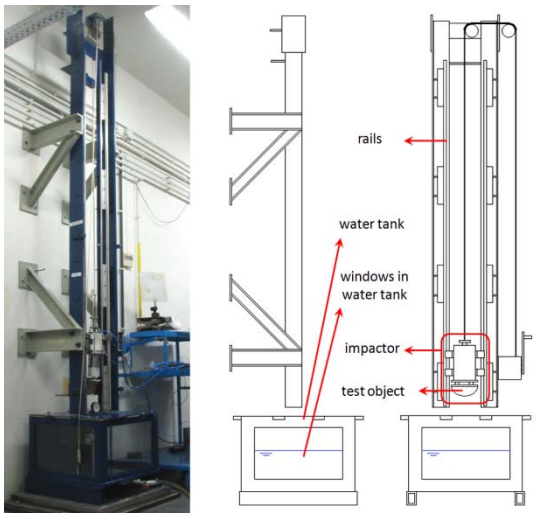

Figure A-3: The experimental drop setup used in current appendix

This setup has already been successfully used in earlier studies dealing with impact on solid structures [8, 9], and has been described in detail in these works. It is mainly based on the same working principle as the test setup which is described in chapter 3. It consists of two vertical rails of 2 m long and an impactor assembly which slides over these rails with roller bearings. At the bottom of the setup, a water

tank with a width and length of 59 cm and a height of 34 cm is provided which is thus much smaller than the water basin used in the previous chapters.

Using a smaller water tank indicated that no large test objects could be used. Hence, a small cylindrical segment, with a radius of 15 cm, a width of 15 cm and a length of 20 cm has been used to perform the experiments in this appendix. It was manufactured as a fully casted polyurethane epoxy model and assumed as a rigid model. The test model was selected to be cylindrical to avoid large air pocket effects on the slamming loads. Figure A-4 depicts the small scale cylindrical test object.

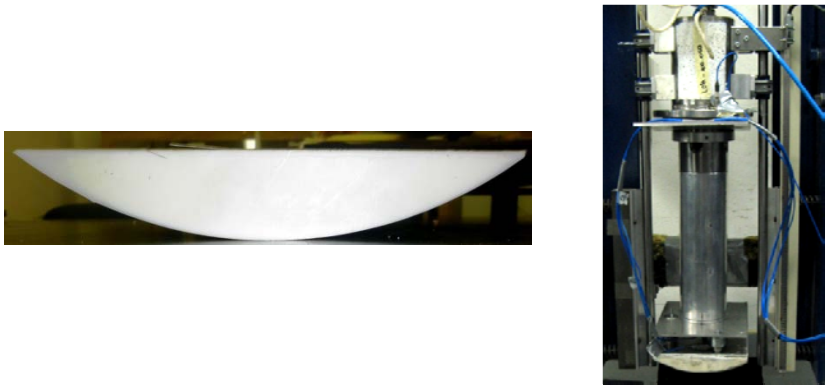

(a) (b)

Figure A-4: The small scale cylindrical test object (a) and the test object attached to the impactor of the small scale test setup.

The diameter of this test object is close to the diameter of the rigid cylindrical test objects from chapter 5 (31.5 cm), which makes it easy to compare the results obtained from the current appendix with the ones acquired in chapter 5. In this way it is possible to validate both slamming setups and the working method.

Furthermore, the same instrumentation has been used as described in chapter 3. One pressure sensor (type 102A08) is placed in the centre of the cylindrical segment to measure the local pressures at the bottom of the cylindrical segment. Three force transducers (type 201B05) have been installed in a similar configuration as described in section 3.2.2, clamped between 2 small Aluminium plates in order to record the global slamming forces. Furthermore, the same accelerometer, position sensor and high speed camera are applied as described in chapter 3. Also the same data acquisition system and trigger process have been used.

A. 2. 2. Test procedure

In order to find out the effect of the water density, the water surface tension and the air content of the water on the magnitude of the slamming loads, slamming experiments are first performed with tap water in normal conditions (20° C and atmospheric pressure). These results are subsequently compared with the results from the previous chapters in order to validate the experimental setups and the working method. Hence, they can be used as a reference for the experiments with changed water properties. It was verified that, by measuring the mass of a certain volume of water used for these initial experiments, the density for normal tap water at 20° C is 998 kg/m^3.

A. 2. 2. 1. Effect of the water density/salinity on the slamming loads

The effect of the density of the water on the slamming loads has been investigated by adding salt to the water volume. Three levels of water salinity levels have been realized. In a first stage, salt was added to the water tank in order to obtain a salinity of 35 g salt per litre water, which is the average salinity of the earth's oceans. Furthermore, also salinity levels of 150 and 300 g per litre water were tested. This last salinity level approaches the saturation level of salt in water which has been determined as being 360 g per litre water [10]. The measured water densities corresponding to the three tested salinity levels are provided in Table A-1.

Table A-1: The water densities corresponding to the different levels of tested salinity

Salinity [g/l]	Density [kg/m^3]
0	998
35	1025
150	1076
300	1149

During the latter tests, the temperature was kept constant at 20°C. It can be observed from Figure A-2 that at this temperature also the surface tension changes by varying the salinity of the water. However, it has been assumed that this change in surface tension only due to a change in salinity at 20°C is rather limited which makes its possible effect on the impact loads negligible.

A. 2. 2. 2. Effect of the water surface tension on the slamming loads

To investigate the effect of the water surface tension on the impact loads, a commercial dish soap was added to the water. It is known that these types of soaps act as very good surfactants, i.e. additives that reduce the surface tension of a fluid [11]. Such surfactants are usually organic compounds containing both a hydrophobic (repelled from water) group and a hydrophilic (attracted to water) group. When the surfactant molecules are present at the surface of the water, than the water insoluble hydrophobic groups typically extend out the water phase, directed towards the air phase, while the water soluble hydrophilic groups remain in the water phase. This alignment of the surfactant molecules modifies the surface properties of the water-air interface and causes a reduction of the surface tension. Figure A-5 shows the typical alignment of a molecule of a popular soap surfactant at the water surface.

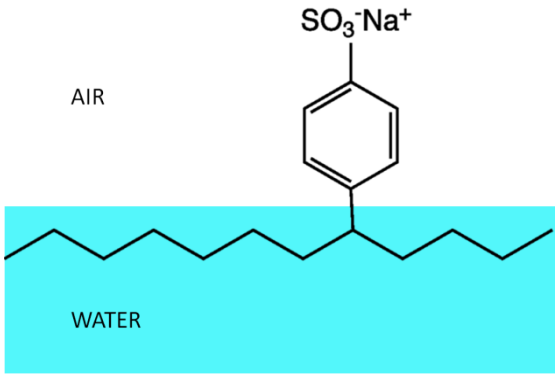

Figure A-5: Typical alignment of a molecule of a popular soap surfactant at the water surface

During the experiments with the reduced water surface tension, an amount of 400 g dish soap was added to the volume of water. This was assumed satisfactory for reducing the surface tension drastically. However, the exact amount of surface tension reduction could not be measured.

A. 2. 2. 3. Effect of water aeration on the slamming loads

Finally, for investigating the sensitivity of the slamming loads on the level of water aeration, air bubbles were initiated in the water tank by introducing compressed air at the bottom of the water tank. Therefore, an air inlet with a non-return valve was provided in the centre of the bottom plate of the water tank. Figure A-6 shows the air inlet and some air bubbles generated in the water tank. Analogue experiments were performed by Lange [12].

Figure A-6: Air bubbles generated in the water tank

A. 3. Experimental results

In the present section, the slamming pressures and slamming forces recorded during the slamming drop tests in the different types of water will be investigated in detail. Firstly, the experiments performed in normal tap water will be discussed and compared with the experimental results obtained in chapter 5. Next, they will be compared with the ones recorded for the experiments with the changed water properties

A. 3. 1. Slamming experiments in tap water

A. 3. 1. 1. Impact pressures

Slamming experiments were performed in tap water for drop heights up to 0.5 m. Figure A-7 shows the recorded pressure at the bottom of the cylindrical polyurethane test object for a drop height of 0.3 m which corresponds to an impact velocity of 2.27 m/s. The graph also shows the impact pressure which was recorded at the bottom of the stiffened cylindrical test object from chapter 5 for a drop height of 0.3 m. A good correspondence can be observed in shape as well as in magnitude between the first slamming pressure peak of both time series. However, after this first slamming pressure peak, both curves deviate from each other in the sense that the pressure history measured for the polyurethane test object does not exhibit pressure oscillations as the ones which are observed for the pressure time history of the stiffened cylindrical test object.

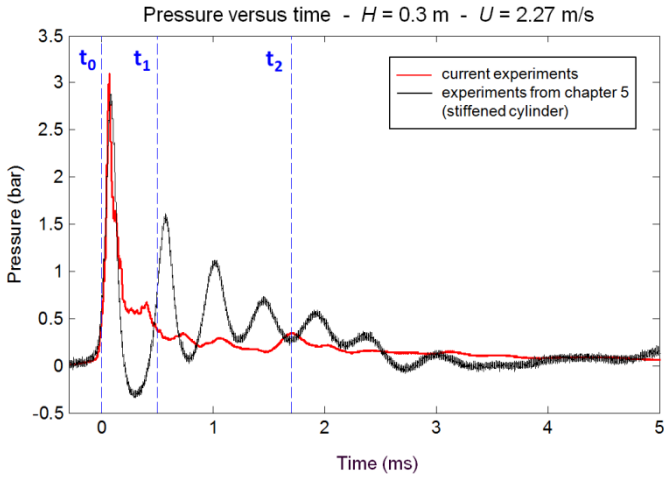

Figure A-7: The slamming pressure as function of time at the bottom of the polyurethane cylindrical segment and at the stiffened cylinder for an impact velocity of 2.27 m/s

It was shown in section 5.2.1.1 that these oscillations are most probably caused by a small air pocket which is formed in the initial stages of the impact at the bottom of the cylinder which rapidly disappears. However, this air pocket cannot be observed on camera images taken from the underside of the polyurethane test object during the initial stages of the impact (see Figure A-8 at a time t_1 = 0.5 ms after the first contact of the test object with the water). Only a large number of smaller air bubbles can be observed at the underside of the test object. This explains why no pressure oscillations are present in the pressure history of the polyurethane test object and confirms that the presence of an air pocket in the initial stages of the impact at the bottom of a slamming cylinder is closely related to the pressure oscillations which are observed at the bottom of this cylinder. A possible reason for the absence of the air pocket during the experiments with the polyurethane test object may be the fact that this test object is only a segment of a cylinder, and therefore has a limited width compared to a complete cylinder. This can be understood from Figure A-9, which presents a sequence of high speed images taken from the impact of the polyurethane test object with the air flow visualized by means of smoke. It can be observed that before the moment of first contact, the smoke is compressed under the cylinder and pushed aside, and finally escapes along the side of the test object. The fact that the air can escape along the sides of the test object makes that it can escape more rapidly and that finally, at the moment of first contact, all air has been evacuated under the test object and no air pocket can be formed.

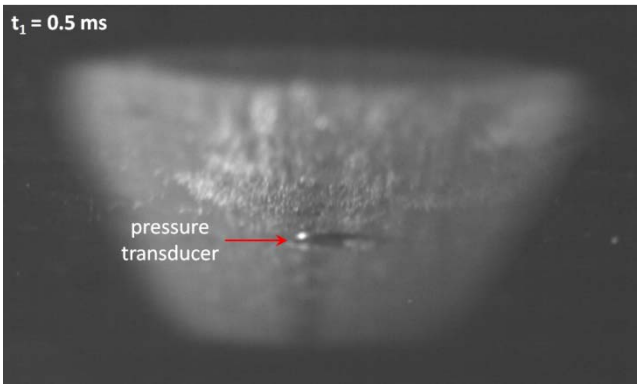

Figure A-8: Camera image from the underside of the polyurethane cylindrical test object at a time t_1 = 0.5 ms after the initial contact of the test object with the water

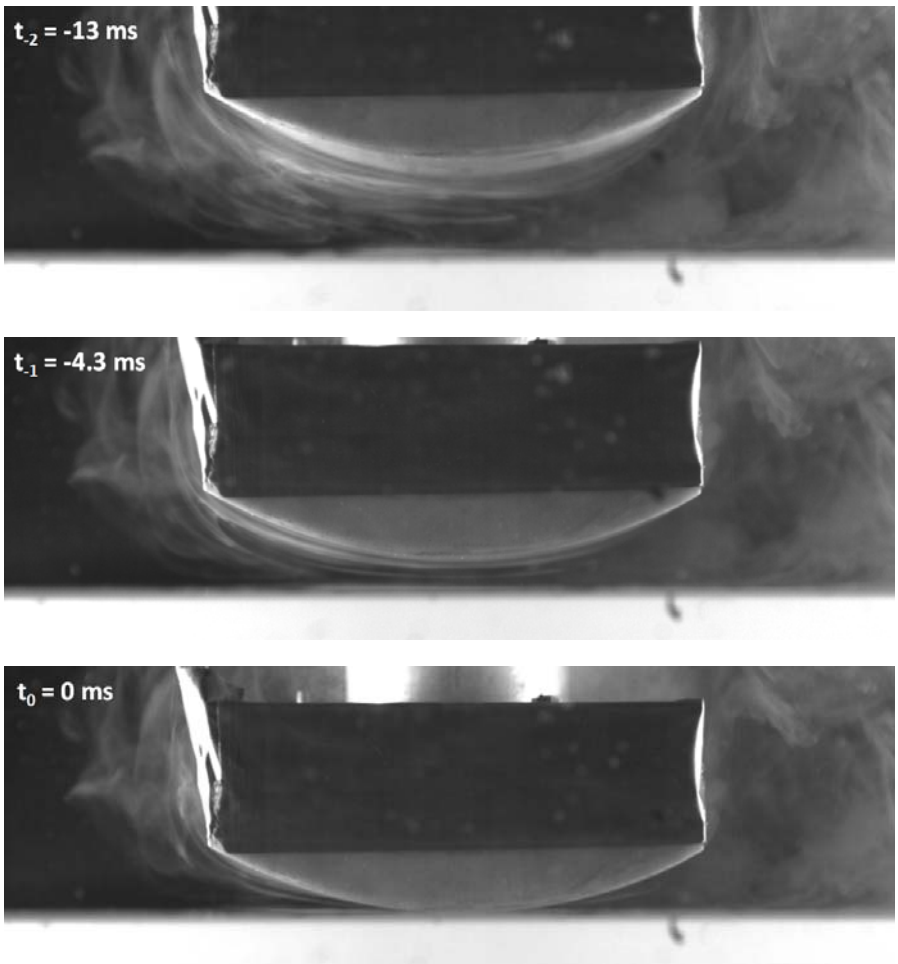

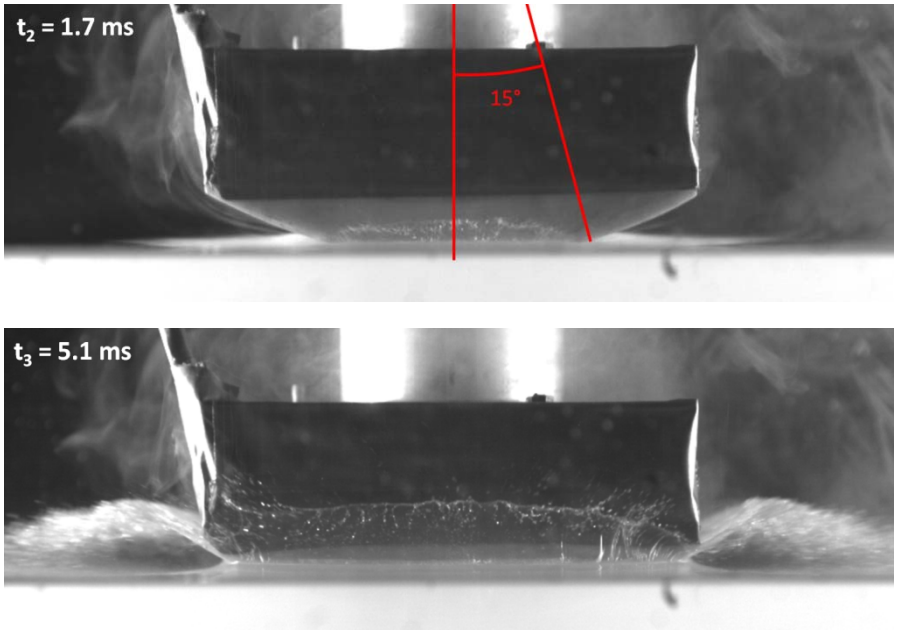

Figure A-9: Sequence of high speed images from the slamming impact of the polyurethane cylindrical test object

Table A-2 and Figure A-10 give an overview of the average maximum pressures measured at the bottom of the polyurethane cylindrical test object during the performed slamming drop experiments. For every drop height, at least three experiments were carried out per drop height. The standard deviation on the results indicates that the test results are reproducible.

Table A-2: Overview of the impact pressures and impact forces measured for the polyurethane cylindrical test object

H [m]	U_{avg} [m/s]	Impact pressures		Impact forces	
		$p_{I,C}$ [bar]	σ_p [bar]	$F_{I,C}$ [N/m]	σ_F [N/m]
0	0	0	0	0	0
0.1	1.34	1.07	0.076	1843.41	126.65
0.2	1.90	2.19	0.016	3413.89	30.83
0.3	2.28	3.30	0.522	4800.93	183.95
0.4	2.58	3.52	1.020	5776.44	112.35
0.5	2.93	5.69	0.201	7143.37	156.16

Figure A-10 also depicts the average impact pressures recorded at the bottom of the stiffened cylinder as described in section 5.2.1.2. It can be observed that the slamming pressure values for both cylindrical test objects correspond very well. This indicates that in the case of cylinder slamming, the very small and thin air layer just at the bottom of the cylinder in the initial stages of the impact apparently has no effect on the magnitude of the first slamming pressure pulse. Hence, it will also not affect the slamming impact forces. The good correspondence between both experiment series is a validation for both experimental setups and the working method used in this dissertation.

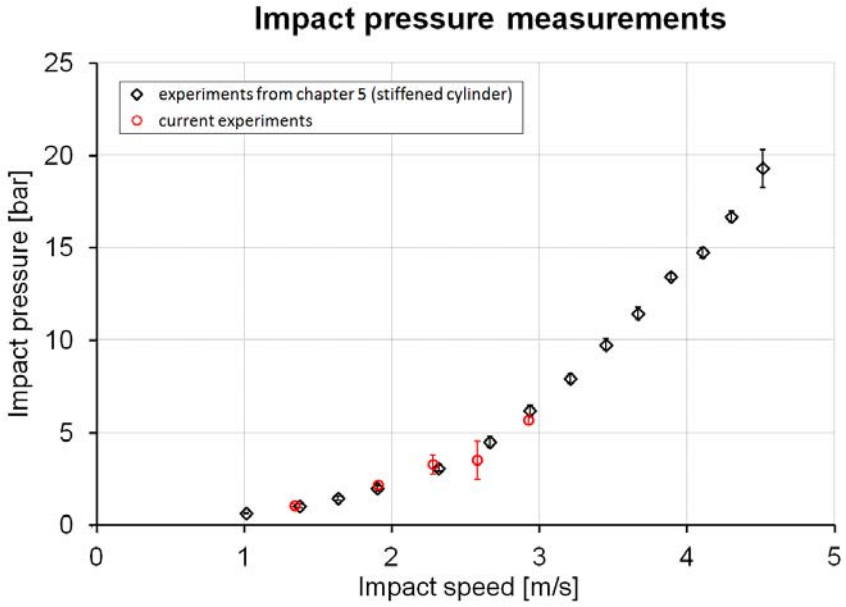

Figure A-10: Comparison between the impact pressures measured with the polyurethane cylindrical test object and with the stiffened cylindrical test object from chapter 5

A. 3. 1. 2. Impact forces

Figure A-11 shows the time series of the slamming force measured during the impact of the polyurethane test object for a drop height of 0.3 m, compared to the corresponding slamming force recording of the plaster cylindrical test object from chapter 5. Both recordings are expressed in terms of force per unit length to account for the fact that both test objects have a different length. The duration of the force recording of the polyurethane test object is much shorter than the other one, since at time t_3 (5.1 ms) the polyurethane test object is already fully submerged and the force

history after this moment is thus not representative anymore for the slamming of a rigid cylinder (see also Figure A-9).

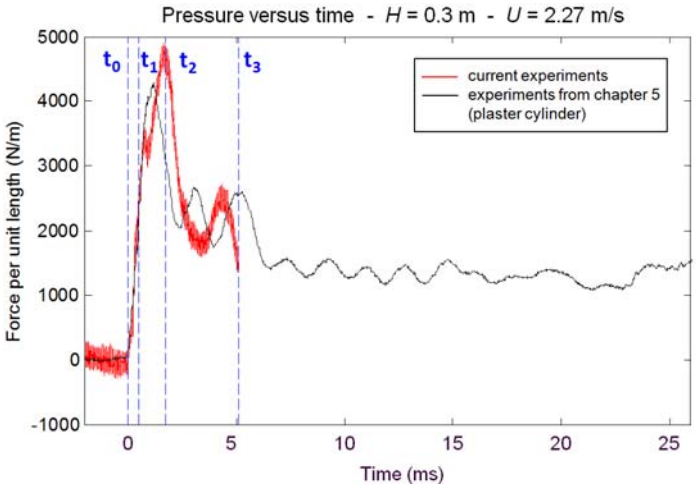

Figure A-11: The slamming force as function of time for the polyurethane cylindrical segment and for the stiffened cylinder for an impact velocity of 2.27 m/s

It can be observed that both force time histories correspond very well in the sense that they both start with a steep and large force pulse which lasts for a few milliseconds and then gradually evolve into an oscillating force. However, a little difference in slamming force magnitude and oscillation frequency can be noticed.

The fact that also the force recordings for the polyurethane test object show oscillations indicates that, similarly as for the measurements from chapter 5, eigenfrequencies of the upper part of the impactor are excited by the slamming impact and affect the force recordings. However, the frequency of the oscillations corresponding to the force recordings of the polyurethane test object is larger than the frequency of the force oscillations corresponding to the experiments with the plaster and concrete cylinder. This indicates that other eigenfrequencies play a role and thus explains why also a small force magnitude difference can be observed.

Figure A-12 and Table A-2 show the average maximum slamming force values determined for each tested drop height for the polyurethane cylindrical segment compared to the average values obtained from Figure 5-27 for the plaster and concrete cylinder. It can be observed that for every drop height, the maximum forces obtained from the polyurethane test object are slightly larger than the ones obtained from the plaster and concrete cylindrical segments, which makes that the corresponding maximum slamming coefficient is also slightly larger, and thus larger

than the maximum slamming coefficient corresponding to pure rigid cylindrical bottom slamming (see section 5.2.2.2).

However, the fact that the forces measured during the slamming experiments with the polyurethane test object do not exactly represent the slamming forces characteristic for pure rigid cylindrical bottom slamming, does not limit the ability to investigate the effect of water density/salinity, water surface tension and water aeration level on the slamming forces. During these test series, the experimental setup and thus its eigenfrequencies remain the same since only the properties of the water are changed. Hence, the way in which the excited eigenfrequencies affect the slamming forces is consistent in every test series, and the results from the different test series can be compared with each other. Changes in the impact force values from the different test series due to variations in water properties then also indicate changes in the impact forces corresponding to pure cylindrical bottom slamming. A comparison of the impact force and impact pressure values from the different test series is done in the next section.

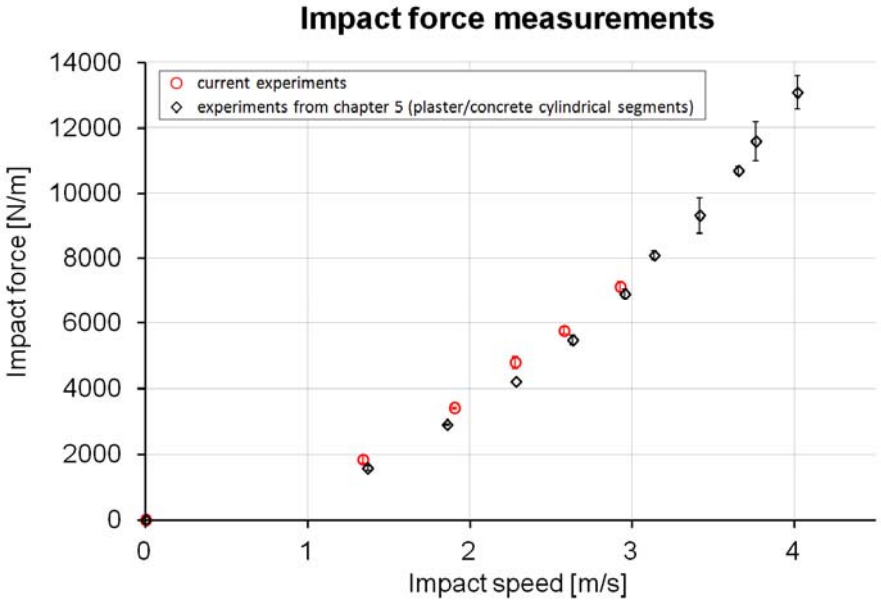

Figure A-12: Comparison between the impact forces measured with the polyurethane cylindrical test object and with the stiffened cylindrical test object from chapter 5

A. 3. 2. Slamming experiments in water with changed properties

In order to determine the effects of the considered water properties on the slamming loads of the cylindrical test object, the impact forces and impact pressures obtained at a drop height of 0.3 m are compared among the different cases. For each test case, at least ten experiments were performed at this drop height.

Figure A-13 and Figure A-14 give an overview of respectively the measured impact pressures and impact forces for all the tests involved. The average values and standard deviation of the slamming pressure and forces for every test case are provided in Table A-3.

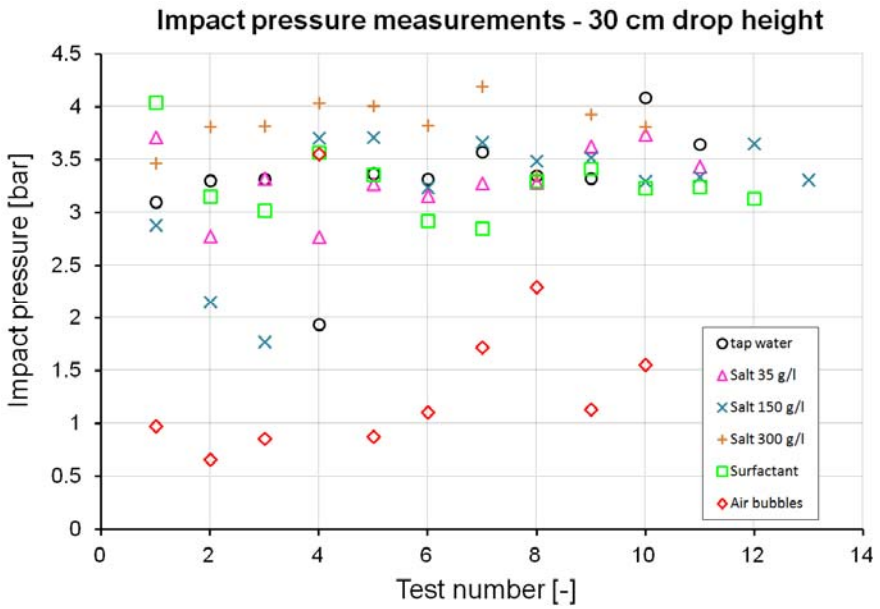

Figure A-13: Overview of the impact pressure values obtained at a drop height of 0.3 m for the different test cases

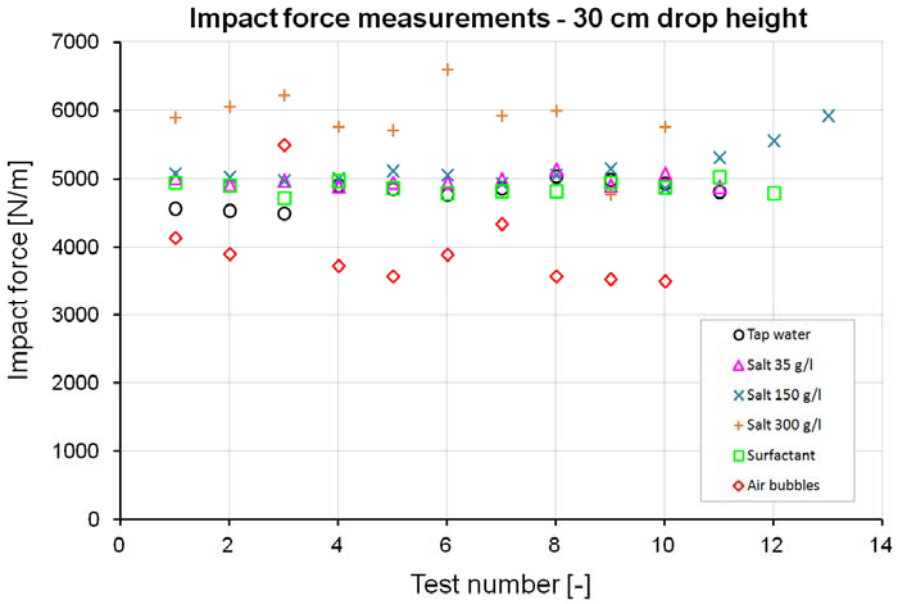

Figure A-14: Overview of the impact force values obtained at a drop height of 0.3 m for the different test cases

Table A-3: Overview of the impact pressures and impact forces measured for the polyurethane cylindrical test object

Test case	Impact pressures		Impact forces	
	$p_{I,C}$ [bar]	σ_p [bar]	$F_{I,C}$ [N/m]	σ_F [N/m]
Normal slamming	3.30	0.522	4800.93	183.95
Salt 35 g/l	3.31	0.324	4971.67	126.65
Salt 150 g/l	3.21	0.605	5201.98	321.75
Salt 300 g/l	3.82	0.25	5873.84	466.78
Surface tension	3.27	0.318	4877.61	89.73
Air bubbles	1.47	0.879	3972.51	602.99

A. 3. 2. 1. Effect of the water density/salinity on the impact loads

When comparing the impact force values from Figure A-14 for the test cases with the normal tap water and the test cases with the different levels of salinity, it can be observed that it is only for the case of a salinity of 300g/l that the impact forces are significantly larger than the values obtained for the test case with normal tap water.

The same can be observed concerning the impact pressures depicted in Figure A-13, however, this effect is less pronounced since the impact pressures are prone to a larger scatter than the impact forces. From Table A-3 it can be observed that the average impact force values for the test cases with a salinity level of 35 g/l and 150 g/l are also larger than the average impact force value for the test case with the normal tap water, but the differences are close to the scatter level of these force results. Hence, it is assumed that the effect of the salinity on the impact forces for these two salinity levels is negligible.

From these findings it can thus be concluded that in the complete range of realistic ocean densities (minimum 995.65 kg/m^3 for fresh water at 30° C and maximum 1028 kg/m^3 for salt water at -2°C), the density has no effect on the magnitude of the slamming forces and slamming pressures. It is only for larger, unrealistic variations in water density that a significant effect of the density on the impact loads can be observed.

A. 3. 2. 2. Effect of the water surface tension on the impact loads.

When comparing the experimental results for the test case with the reduced water surface tension with the ones obtained for the test case with the normal tap water, no significant differences can be found in the impact pressures as well as in the impact forces. This indicates that the surface tension has no effect on the magnitude of the slamming loads.

This can be understood when considering that the slamming loads are generated because the structure suddenly pushes away a volume of fluid with a certain mass (added mass) which was before at rest. The impact force can thus be calculated as the inertia of this particular fluid mass (see Equation (2.66)). The fluid volume affected by the slamming impact will be the same no matter what is the magnitude of the surface tension. Hence, also the impact forces and pressures are the same independently from the magnitude of the surface tension.

A. 3. 2. 3. Effect of water aeration on the slamming loads

It can be observed both from Figure A-13 and Figure A-14 that the slamming loads for the test case with the aerated water are significantly smaller than for the test case with the normal tap water. This has also been observed in the study performed by Lange [12]. Lange [12] contributed this reduction to the compressibility of the introduced air bubbles.

A detailed investigation of the high speed images taken from the slamming experiments in the test case with the aerated water showed that an increased

compressibility of the water-air mixture is not the only reason for the slamming load reduction. It can be observed on the images that the air bubbles cause waves when they reach the water surface (see Figure A-15).

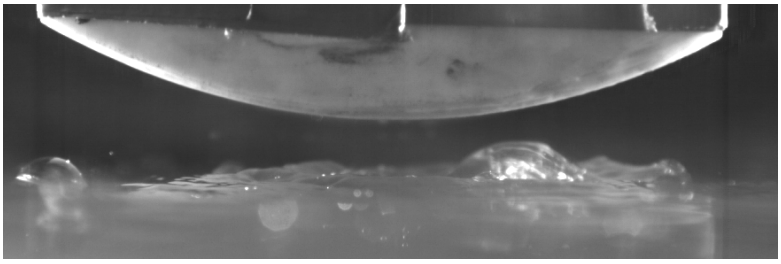

Figure A-15: Water waves due the air bubbles reaching the water surface

This causes a completely different slamming of the cylindrical test object with the water surface, whereby the test object penetrates the water surface more gradually as is the case for slamming on a calm water surface. The local deadrise angle at the moment of impact is hence not zero which might have a large effect on the slamming loads as was shown in section 4.2.1.5. It is thus assumed that the reduction of the impact loads is due to a combination of the compressibility of the introduced air and the presence of small waves on the water surface generated by the air bubbles.

A. 4. Conclusions

In this appendix, the effects of the water density/salinity, the water surface tension, and the effect of water aeration on the slamming loads acting on a rigid cylindrical test object have been investigated. Therefore, a smaller experimental setup has been used with a smaller water tank which makes it possible to easily vary the properties of the volume of water. Impact loads were measured in terms of impact pressures at the bottom of the cylindrical test object and global impact forces.

Experiments with normal tap water at 20˚C gave similar experimental results as recorded during the previous chapters with the original experimental setup. This correspondence can be considered as a validation of both experimental setups and as a validation of the working method applied throughout this complete dissertation.

Concerning the effect of water density on the slamming loads, it has been observed that in the range of realistic ocean water densities, the density has a negligible effect on the impact loads corresponding to the considered cylindrical test object. Only for unrealistic water densities, corresponding to unrealistic salinity levels or unrealistic water temperatures, the impact loads are significantly affected.

Furthermore, it has been observed that the water surface tension has no effect on the slamming loads. After all, the volume of water which is displaced by the cylindrical test object at impact is the same, no matter what the magnitude of the surface tension is.

Finally it is observed that the presence of air bubbles does matter during slamming of a cylindrical body. Introducing air bubbles causes a reduction of the slamming loads. It is assumed that this reduction is due to a combination of the compressibility of the introduced air and the presence of small waves on the water surface generated by the air bubbles.

A. 5. References

[1] D. R. Lide, "CRC Handbook of Chemistry and Physics (70th Edition)," 1990.

[2] National Oceanographic Data Center (NODC). *World Ocean Atlas 2009*. Available: www.nodc.noaa.gov

[3] G. Lacroix, K. Ruddick, J. Ozer, and C. Lancelot, "Modelling the impact of the Scheldt and Rhine/Meuse plumes on the salinity distribution in Belgian waters (southern North Sea)," *Journal of Sea Research*, vol. 52, pp. 149-163, 9// 2004.

[4] U. S. Gekwu, *Effect of Temperature and Impurities on Surface Tension of Crude Oil*, 2010.

[5] M. H. Sharqawy, J. H. Lienhard, and S. M. Zubair, "Thermophysical properties of seawater: a review of existing correlations and data," *Desalination and Water Treatment*, vol. 16, pp. 354-380, 2010/04/01 2010.

[6] H. Streckwall, O. Lindenau, and L. Bensch, "Aircraft ditching: a free surface / free motion problem," *Archives of Civil and Mechanical Engineering*, vol. 7, pp. 177-190, // 2007.

[7] H. Climent, L. Benitez, F. Rosich, F. Rueda, and N. Pentecote, "Aircraft ditching numerical simulation," *25th International Congress of the Aeronautical Sciences*, 2006.

[8] S. De Pauw, "Experimental and Numerical Study on Window Glass Fitted with Safety Window Film," *PhD dissertation, Ghent University*, 2010.

[9] S. Palanivelu, "Energy Absorption of Crushable Tubes for Protective Structures under Static, Impact and Blast Loading," *PhD dissertation, Ghent University*, 2011.

[10] J. W. Hill and R. H. Petrucci, *General Chemistry, 2nd Edition*, 1999.

[11] M. J. Rosen and J. T. Kunjappu, *Surfactants and Interfacial Phenomena*, 2012.

[12] N. A. Lange and T. Rung, "Impact tests in pure and aerated water," presented at the 30th International Conference on Ocean, Offshore and Arctic Engineering, Rotterdam, The Netherlands, 2011.

About the author

Curriculum vitae

Diederik Van Nuffel was born on April 9th, 1985. Based on his interest in science and technology, he started his education in mechanical engineering at Ghent University after he graduated from secondary school in 2003. After successfully performing his bachelor thesis in 2007, dealing with the development of a 'weigh-in-motion' system for the determination of a driving vehicle's weight, he confirmed his technical interest by choosing the option of 'mechanical construction' for his master studies. During these two years of masters, he decided to gain some practical and international experience by performing two internships abroad (Eurolift, Croatia – elevator construction; StatoilHydro, Norway – oil and gas industry). Finally, when he successfully finished his master thesis in 2009, dealing with experimental lab scale water slamming experiments on composite egg-shaped buoys for wave energy convertors, he obtained the degree of Master in Mechanical Engineering.

Driven by his interest in scientific research, and determined in solving the problems that he encountered during his master thesis, he decided to continue his master thesis in the form of a PhD which is presented in the underlying dissertation. During these four years of research, he gained a lot of specified technical, but also much personal knowledge.

At the current moment, he decided to leave the academic world and broaden his technical knowledge after four years of specialization. On January 1st of 2014, he stepped into the nuclear industry and started a job as Nuclear Safety Analyst in the Belgian technical support organization (BelV) of the Federal Agency for Nuclear Control (FANC).

During his doctoral study, the author has written and contributed to a number of publications and has participated in a number of national and international congresses, of which an overview is given below.

List of publications

Publications in international journals of the Science Citation Index (SCI):

[2013-A1-1] Van Nuffel D., Vepa K.S., De Baere I., Degrieck J., De Rouck J., Van Paepegem W. (2013), Study on the parameters influencing the accuracy and reproducibility of dynamic pressure measurements at the surface of a rigid body during water impact, Accepted for *Experimental Mechanics*, 53*(2), p.131-144*

[2014-A1-1] Van Nuffel D., Vepa K.S., De Baere I., Lava P., Kersemans M., Degrieck J., De Rouck J., Van Paepegem W. (2014), A comparison between the experimental and theoretical impact pressures acting on a horizontal quasi-rigid cylinder during vertical water entry, Accepted for *Ocean Engineering*

[2014-A1-2] Van Nuffel D., Vepa K.S., De Baere I., Lava P., Degrieck J., De Rouck J., Van Paepegem W. (2014), An experimental and theoretical study on the impact loads acting on a horizontal quasi-rigid cylinder during vertical water entry, Submitted to *Marine Structures*

[2014-A1-3] Nila A., Vanlanduit S., Vepa K.S., Van Nuffel D., Van Paepegem W. (2014), An adaptive PIV method for estimating slamming loads during water entry of elastic bodies, Submitted to *Measurement Science and Technology*

[2014-A1-4] Nila A., Vanlanduit S., Vepa K.S., Van Nuffel D., Van Paepegem W. (2014), Strain and force measurements during hydroelastic impact of deformable bodies using image feature tracking techniques, Submitted to *Measurement Science and Technology*

Publications in conference proceedings

[2009-C1-1] Van Nuffel D. (2009), Experimental study of the slamming wave impact on deformable composite structures, *10e UGent-FirW Doctoraatssymposium*, Ghent, Belgium, p. 268-269

[2010-C3-1] Van Nuffel D., De Baere I., Van Paepegem W., Degrieck J. (2010), An experimental study on repetitive slamming wave impact on deformable composite structures, *SAMPE Benelux student seminar 2010: book of abstracts*, Nijverdal, The Netherlands, p.17-18

[2010-C1-1] Van Nuffel D. (2010), Pressure measurement on the surface of a rigid cylindrical body during slamming wave impact, *11e UGent-FirW Doctoraatssymposium*, Ghent, Belgium, p. 123

[2010-C1-2] Van Nuffel D., Vepa K.S., De Baere I., Degrieck J., Van Paepegem W., Vierendeels J. (2010), Slamming wave impact on a rigid cylindrical body: comparison of experimental research and numerical simulation, *14th European Conference on Composite Materials*: *proceedings*, Budapest, Hungary

[2011-P1-1] Van Nuffel D., Vepa K.S., De Baere I., Degrieck J., De Rouck J., Van Paepegem W. (2011), Pressure measurement on the surface of a rigid cylindrical body during slamming wave impact, *30thInternational Conference on Ocean, Offshore and Arctic Engineering: proceedings vol 6: Ocean Engineering*, Rotterdam, The Netherlands, p. 303-312

[2011-P1-2] Vepa K.S., Van Nuffel D., Van Paepegem W. , Degroote J., Vierendeels J. (2011), Comparative study of slamming loads on cylindrical structures, *30thInternational Conference on Ocean, Offshore and Arctic Engineering: proceedings vol 7: CFD and VIV: Offshore Geotechnics*, Rotterdam, The Netherlands, p. 279-286

[2011-C1-1] Van Nuffel D., Vepa K.S., De Baere I., Degrieck J., De Rouck J., Van Paepegem W. (2011), Parameters affecting the pressure measurements on the surface of a rigid cylindrical body during water slamming impact, *26th International Workshop on Water Waves and Floating Bodies (IWWWFB26): proceedings*, Athens, Greece, p. 193-196

[2011-C1-2] Vepa K.S., Van Nuffel D., Van Paepegem W. (2011), Pressure predictions during water entry of a 2D rigid cylinder using SPH method, *26th International Workshop on Water Waves and Floating Bodies: proceedings (IWWWFB26)*, Athens, Greece, p. 197-200

[2011-C1-3] Vepa K.S., Van Nuffel D., Van Paepegem W., Degrieck J. (2011), Numerical study of composite structures subjected to slamming loads using Smoothed Particle Hydrodynamics (SPH), *8th International Conference on Structural Dynamics: Proceedings*, Leuven, Belgium, p. 3077-3082

[2011-C1-4] Nila A., Vanlanduit S., Vepa K.S., Van Nuffel D., Van Paepegem W., Degroote J., Vierendeels J. (2011), High speed particle image velocimetry measurements during water entry of rigid bodies, *9th International Symposium on Particle Image Velocimetry: proceedings*, Kobe, Japan

[2012-P1-1] Van Nuffel D., Vepa K.S., De Baere I., Degrieck J., De Rouck J., Van Paepegem W. (2012), Experimental study on the impact loads acting on a horizontal rigid cylinder during vertical water entry, *31st International Conference on Ocean, Offshore and Arctic Engineering*, Rio de Janeiro, Brazil, p. 67-76

[2012-P1-2] Vepa K.S., Van Nuffel D., Van Paepegem W., Degrieck J. (2012), Fully coupled time domain modeling of 3D floating bodies and mooring systems in regular and irregular sea states, *31st International Conference on Ocean, Offshore and Arctic Engineering*, Rio de Janeiro, Brazil, p. 401-406

[2012-P1-3] Van Nuffel D., Peirs J., De Baere I., Verleysen P., Degrieck J., Van Paepegem W. (2012), Calibration of dynamic piezoelectric force transducers using the Hopkinson bar technique, *15th International Conference on Experimental Mechanics: proceedings*, Porto, Portugal, p. 341-342

[2012-P1-4] Van Nuffel D., De Baere I., De Rouck J., Degrieck J., Van Paepegem W. (2012), An experimental comparison of vertical water entry between a rigid cylindrical body and a deformable cylindrical composite shell, *15th International Conference on Experimental Mechanics: proceedings*, Porto, Portugal, p. 607-608

[2012-P1-5] Kersemans M., Van Paepegem W., Van Nuffel D., Luyckx G., De Baere I., Zastavnik F., Gu J., Sol H., Van Den Abeele K., Degrieck J. (2012), Polar scan technique for material characterization and identification of new operating regimes, *15th International Conference on Experimental Mechanics: proceedings*, Porto, Portugal, p. 85-86

[2012-C1-1] Van Nuffel D., Vepa K.S., De Baere I., De Rouck J., Van Paepegem W., Degrieck J. (2012), Slamming wave impact on cylindrical structures: model tests including a rigid and deformable cylinder, *4th International Conference on the*

Application of Physical Modeling to Port and Coastal Protection: proceedings, Ghent, Belgium, p. 137-146

[2012-C1-2] Nila A., Vanlanduit S., Vepa K.S., Van Nuffel D., Van Paepegem W., Degroote J., Vierendeels J. (2012), High speed particle image velocimetry measurements during water entry of rigid and deformable bodies, *16th International Symposium on Applications of Laser Techniques to Fluid Mechanics: proceedings*, Lisbon, Portugal, p. 1-11